Statistical optics methods for generating, simulating, and characterising emission from relativistic electron beams

Dissertation

zur Erlangung des Doktorgrades an der Fakultät
für Mathematik, Informatik und Naturwissenschaften
Fachbereich Physik
der Universität Hamburg

vorgelegt von
Andrei Trebushinin

Hamburg
2024

The work presented in this thesis was completed at the FEL Physics group
at the European X-Ray Free-Electron Laser Facility GmbH

Supervised by Dr. Svitozar Serkez, Dr. Gianluca Geloni,
and Prof. Dr. Alexander Lichtenstein

Gutachter/innen der Dissertation:	Prof. Dr. Alexander Lichtenstein Prof. Dr. Jom Luiten
Zusammensetzung der Prüfungskommission:	Prof. Dr. Markus Drescher Prof. Dr. Alexander Lichtenstein Prof. Dr. Jom Luiten Dr. Gianluca Geloni Dr. Svitozar Serkez
Vorsitzende/r der Prüfungskommission:	Prof. Dr. Markus Drescher
Datum der Disputation:	25.02.2025
Vorsitzender des Fach-Promotionsausschusses PHYSIK:	Prof. Dr. Wolfgang J. Parak
Leiter des Fachbereichs PHYSIK:	Prof. Dr. Markus Drescher
Dekan der Fakultät MIN:	Prof. Dr.-Ing. Norbert Ritter

Declaration on Oath

I hereby declare and affirm that this doctoral dissertation is my own work and that I have not used any aids and sources other than those indicated.

If electronic resources based on generative artificial intelligence (gAI) were used in the course of writing this dissertation, I confirm that my own work was the main and value-adding contribution and that complete documentation of all resources used is available in accordance with good scientific practice. I am responsible for any erroneous or distorted content, incorrect references, violations of data protection and copyright law or plagiarism that may have been generated by the gAI.

Monday 26th August, 2024

Signature of doctoral candidate

Acknowledgement

Back in the summer of 2017, I showed up to my optics oral exam armed with a laser pointer from Aliexpress and a vague plan to impress the examiner by demonstrating diffraction using my own hair. To my surprise, the examiner ran with it, immediately asking me to estimate the thickness of my hair and the coherence length of the laser based on the diffraction pattern. The result: a solid *khorosho* (4 out of 5) — my only non-*otlichno* (5 out of 5) that semester.

Years later, I ended up writing my entire PhD thesis on statistical optics. Apparently, life decided I still owed optics some proper homework — and this time, I finally did it, with a bit more confidence and a lot more support.

Before I thank those I met during my doctoral studies, I want to express my gratitude to all the teachers at my alma mater who put a lot of effort into teaching, challenging us, and helping to lay the foundation for everything that followed — including that very thesis.

First and foremost, I want to thank my supervisors — Svitozar Serkez, Gianluca Geloni, and Alexander Lichtenstein — as well as Evgeny Saldin, who informally supported me throughout my doctoral studies.

Svitozar, thank you for guiding me since the DESY Summer School and for sharing your distinctive scientific approach — a blend of visual thinking, simulations, and classic limit-case reasoning — which has helped strengthen my physical intuition. I truly enjoyed our time doing and discussing physics together. Thank you for your patience, clarity, and support.

Gianluca, thank you for the scientific freedom and for encouraging me to follow my own research ideas. Your gentle mentoring and rigorous mathematical approach to physics taught me the value of structure without rigidity.

Evgeny, thank you for your mentorship. Since our first email exchange in 2017, your explanations — especially in statistical optics — have helped shape my thinking and approach to science. I appreciate your willingness to share your experience and perspective.

I express my gratitude to **Alexander Lichtenstein** for his academic guidance and support throughout my PhD.

Along the way, I met friends who shaped this journey just as much.

I am deeply grateful for the friendship of **Tatyana Yuryevna Mikhaylova** and her husband **Sergey Gilev**. Their travels to the very corners and heights of this world are a reminder that there's always more to discover. Tatyana Yuryevna shared her love for mathematics, the legacy of her father Yuri B. Rumer, stories of adventures — and poetry, which I still have to learn to appreciate.

Thanks to **Agnes** & **Heiko Menz** for welcoming me to Germany and for being such warm and hospitable landlords. Your kindness made me feel at home in a new land.

Thanks to my Hamburg friends — **Ivan Rybin**, for always keeping the spark alive and motivating me when I needed it; **Dima Potorochin** and **Masha Potorochina**, for all the fun we shared, the support, and our cocktail evenings in Blankenese — moments that kept the balance right. Thanks to **Giovanni Perosa**, who joined our group after the submission of this thesis, and with whom we spent joyful hours discussing physics.

Thanks to the people who helped me explore new hobbies: **Masha** and **Sergey**, for being a strong team as we completed the *Alta Via 2* in the *Dolomites* — one of the most memorable journeys of recent years. Thanks to **Igor** for introducing me to rock climbing — and to my climbing partner **Anton** for the soft catches. I was also inspired by the films of Harmen Hoek, which encouraged me to take my camera, set off on long-distance hikes across Europe, and

begin documenting my own journeys.

And finally, to my family, I want to thank my mama and papa, **Tatiana** and **Evgeny**. They've always believed in me, supported all my endeavours, and did everything they could to give me a good education. Thank you for building such a strong and loving family, and for giving me two wonderful younger brothers — **Nikita** and **Grisha**.

And to **Katya**, whom I met at the very beginning of this PhD journey — thank you for your love, kindness, and unwavering support.

Zusammenfassung

Synchrotronstrahlungsquellen und Freie-Elektronen-Laser haben das Studium von Materie und biologischen Systemen revolutioniert, indem sie einzigartige Kombinationen von Strahlungspuls-Eigenschaften bieten. Obwohl sich diese beiden Arten von Einrichtungen grundlegend in Bezug auf Zeitmaßstäbe, Kohärenzeigenschaften und (Spitzen-)Brillanz unterscheiden, bietet jede eine außergewöhnliche Mischung dieser Merkmale. Die Kombination aus Kohärenz, kurzer Pulsdauer und hohem Photonfluss, die für beide Quellentypen charakteristisch ist, ermöglicht beispiellose experimentelle Möglichkeiten über ein breites Spektrum von Photonenergien. Diese fortschrittlichen Fähigkeiten bringen jedoch auch neue Herausforderungen bei der Charakterisierung und numerischen Modellierung dieser Strahlung mit sich. Eine Verbesserung unseres Verständnisses der Strahlungsdiagnosetechniken und die Entwicklung neuer Simulationsmethoden könnten den Weg für innovative Ansätze zur Verbesserung der Pulseeigenschaften ebnen.

Ich beginne meine Dissertation mit der Untersuchung des Potenzials zur Entwicklung neuer theoretischer Modelle zur Beschreibung teilweise kohärenter Quellen, wobei ein besonderer Schwerpunkt auf der Strahlung von relativistischen Elektronenstrahlen liegt. Zu diesem Zweck schlage ich eine Reihe numerisch effizienter Algorithmen vor, die darauf ausgelegt sind, individuelle statistische Instanzen des Strahlungsfeldes zu simulieren. Diese Algorithmen sind hochgradig vielseitig und effizient und in der Lage, Strahlung von einer Vielzahl von Quellen zu simulieren, von vollständig inkohärenten bis hin zu teilweise kohärenten Systemen, einschließlich thermischer Quellen, Synchrotronstrahlung und sogar Freie-Elektronen-Laser-Strahlung mit komplizierten Wigner-Funktionsverteilungen.

Insbesondere bietet einer der entwickelten Algorithmen eine neue Perspektive auf die Synchrotronstrahlung. Auf dieser Grundlage schlage ich eine Methode zur Messung der Kohärenzlänge der Synchrotronstrahlung an Linearbeschleuniger-Einrichtungen wie dem Europäischen XFEL vor, die einen nicht-interferometrischen Ansatz verwendet. Durch die direkte Detektion der Strahlung nach der Monochromatisierung und die Anwendung der Autokorrelationsanalyse kann die Kohärenzlänge ohne Interferenzschema bestimmt werden. Diese Messung zeigt auch, dass die monochromatisierte transversale Verteilung der Synchrotronstrahlung aus Spitzen besteht. In der Praxis dient diese Methode als neues Diagnosetool zur Bestimmung der transversalen Elektronenstrahlgröße an Freie-Elektronen-Laser-Einrichtungen, wobei das van Cittert-Zernike-Theorem genutzt wird, um die transversale Kohärenzlänge mit der Elektronenstrahlgröße in Beziehung zu setzen.

Als nächstes konzentriere ich mich auf die Struktur der virtuellen Quelle der Undulatorstrahlung von einem einzelnen Elektron. Obwohl die Undulatorstrahlung im Resonanzfall typischerweise als eine einzelne Taille an der Position der virtuellen Quelle betrachtet wird, zeigen genauere Untersuchungen feinere Details. Es gibt zwei charakteristische Längen, die mit der Undulatorstrahlung verbunden sind: die Gesamtlänge des Geräts und die Periodenlänge. Diese Skalen entsprechen den Strahlungsbildungsdauern und stehen in direktem Zusammenhang mit der Beugungsgröße der Strahlung. In diesem Teil untersuche ich die weniger erforschten Besonderheiten der virtuellen Quelle, die mit der Undulatorperiodenlänge verbunden sind.

Abschließend beschreibe ich einen numerischen Code zur Simulation der Synchrotronstrahlungserzeugung unter dem Einfluss von Wellenleitereffekten. Diese Effekte treten typischerweise im Infrarotfrequenzbereich auf und werden von den metallischen Elementen der Strahllinien beeinflusst, die immer vorhanden sind. Ich führte verschiedene Kreuzprüfungen des entwickelten Codes durch, indem ich ihn mit dem Synchrotron Radiation Workshop-Code für Freiraumszenarien und mit analytischen Ausdrücken für praktische Fälle mit zirkularen Wellenleitern verglich. Diese Forschung trägt zur Entwicklung von Strahllinien für THz-Pump-X-ray-Probe-Experimente an Freie-Elektronen-Laser-Einrichtungen bei. Der letzte Teil der Dissertation enthält numerische Berechnungen für einen Iriswellenleiter, der für den THz-Strahlungstransport durch die Strahllinien von Freie-Elektronen-Lasern entwickelt wurde.

Abstract

Synchrotron radiation sources and free-electron lasers have revolutionised the study of matter and biological systems by providing unique combinations of radiation pulse characteristics. Although these two types of facilities differ fundamentally in terms of pulses time scales, coherence properties, and (peak) brilliance, each offers an exceptional mix of these features. The combination of coherence, short pulse duration, and high photon flux, characteristic of both types of sources, delivers unparalleled experimental capabilities across a wide range of photon energies. However, these advanced capabilities also introduce new challenges in both the characterisation and numerical modelling of this radiation. Improving our understanding of radiation diagnostics techniques and developing new simulation methods could pave the way for innovative approaches to enhance pulse properties.

I begin my thesis by exploring the potential for developing new theoretical models for describing partially coherent sources, with a particular focus on radiation from relativistic electron beams. To this end, I propose a set of numerically efficient algorithms designed to simulate individual statistical instances of the radiation field. These algorithms are highly versatile and efficient, capable of simulating radiation from a range of sources, from fully incoherent to partially coherent systems, including thermal sources, synchrotron radiation, and even free-electron laser radiation with complicated Wigner function distributions.

In particular, one of the developed algorithms offers a new perspective on synchrotron radiation. Building on this, I propose a method for measuring the coherence length of synchrotron radiation at linear accelerator facilities, such as the European XFEL, using a non-interferometric approach. By detecting radiation directly after monochromatization and employing auto-correlation analysis, the coherence length can be determined without the need for an interference scheme. This measurement also reveals that the monochromatized transverse distribution of synchrotron radiation consists of spikes. In practice, this method serves as a novel diagnostic tool for determining the transverse electron beam size at free-electron laser facilities, leveraging the van Cittert-Zernike theorem to relate the transverse coherence length to the electron beam size.

Next, I focus on the virtual source structure of undulator radiation from a single electron. Although undulator radiation in resonance is typically considered to have a single waist at the virtual source position, closer inspection reveals finer details. There are two characteristic lengths associated with undulator radiation: the overall device length and the period length. These scales correspond to the radiation formation lengths and are directly related to the diffraction size of the radiation. In this part, I examine the less-studied peculiarities of the virtual source associated with the undulator period length.

Finally, I describe a numerical code for simulating synchrotron radiation generation in the presence of waveguide effects. These effects typically arise in the infrared frequency range and are influenced by the metallic elements of the beamlines, which are always present. I conducted various cross-checks of the developed code, comparing it with the Synchrotron Radiation Workshop code for free-space scenarios and with analytical expressions for practical cases involving circular waveguides. This research contributes to the development of radiation beamlines for THz pump – X-ray probe experiments at free-electron laser facilities. The final part of the thesis includes numerical calculations for an iris waveguide designed for THz radiation transport through the beamlines of free-electron lasers.

Contents

1 Introduction **1**

2 Gaussian random field generators for simulating partially coherent radiation **5**
2.1 Introduction . . . 5
2.2 Classification of random processes . . . 6
2.2.1 Stationarity and ergodicity . . . 8
2.2.2 Gaussian random processes . . . 9
2.2.3 Quasi-stationary approximation . . . 11
2.2.4 Wiener-Khinchin theorem for quasi-stationary processes . . . 12
2.3 Transverse coherence properties of quasi-stationary sources . . . 14
2.3.1 Introducing transverse domain . . . 14
2.3.2 Practical importance of the spectral domain . . . 15
2.3.3 Cross-spectral density function at the source and quasi-homogeneity . 15
2.3.4 Propagation law for cross-spectral density function in free space . . . 16
2.3.5 The van Cittert-Zernike theorem . . . 17
2.3.6 Fourier transform of cross-spectral density . . . 18
2.4 Coherence properties of synchrotron radiation . . . 20
2.4.1 Cross-spectral density functions for synchrotron radiation . . . 21
2.4.2 Consistency of quasi-stationary approximation and Wiener–Khinchin theorem for synchrotron radiation . . . 24
2.4.3 Quasi-homogeneity approximation for synchrotron radiation . . . 24
2.5 SERVAL: stochastic emission rapid evaluator . . . 25
2.5.1 Heuristic approach I: homogeneous/stationary sources. Paper I. . . . 26
2.5.2 Heuristic approach II: quasi- homogeneous/stationary sources. Paper II. 38
2.5.3 Coherence properties of SASE FEL radiation . . . 52
2.5.4 Heuristic approach III: non- homogeneous/stationary sources. . . . 54
2.5.5 Attosecond-at-Harmonic: limits of SERVAL applicability. Paper III. . . 60
2.6 Conclusion . . . 69

3 Direct observation of spike structure of synchrotron radiation for transverse electron beam size measurement **71**
3.1 Introduction . . . 71
3.2 Underlying theory . . . 73
3.2.1 Qualitative estimations . . . 73
3.2.2 Quantitative estimations . . . 74
3.3 Simulation . . . 75
3.4 Experimental results . . . 79
3.5 Outlook and discussion . . . 81
3.6 Conclusion . . . 82

4 Peculiarities of undulator virtual source distribution 85
4.1 Introduction . . . 85
4.2 Synchrotron radiation from a single electron in free space . . . 86
4.2.1 Helmholtz equation . . . 86
4.2.2 Solution of the paraxial approximation of the Helmholtz equation . . . 89
4.3 Undulator radiation virtual source . . . 90
4.3.1 Analytical expression for the field of undulator radiation . . . 91
4.3.2 Source peculiarities as a result of Wigner function propagation . . . 91
4.3.3 Undulator virtual source wiggling . . . 94
4.4 Conclusion . . . 97

5 Generation of synchrotron radiation within a waveguide 99
5.1 Introduction . . . 99
5.2 Boundary conditions and Green's function integral . . . 100
5.3 Numerical implementation . . . 102
5.4 Code cross-checks . . . 102
5.4.1 Free space Green's function . . . 103
5.4.2 Circular waveguide Green's function . . . 109
5.5 Conclusion . . . 111

6 Propagation of THz radiation in an iris waveguide 113
6.1 Introduction . . . 113
6.2 Iris line theory . . . 114
6.3 Analysis of radiation propagation at 3 THz . . . 117
6.3.1 In-coupling condition . . . 118
6.3.2 Wave packet enlargement . . . 119
6.3.3 Optimization of iris line dimensions for 0.3 – 30 THz . . . 119
6.4 Estimation of tolerances . . . 120
6.5 Out-coupling from the source and in-coupling into the iris line . . . 122
6.5.1 Mirror-based propagation line . . . 122
6.5.2 Design of a beam expander . . . 123
6.6 Discussion and conclusion . . . 124

7 Summary 127

8 Publications 129

A Free space propagation 131

B Brightness of undulator radiation 133

C Choice of the noise for SERVAL algorithms 135

D Y-Polarisation Component of Undulator Radiation: SRW and SRinWGuide 137

E Stellar intensity interferometer photo overlaid with spiky distribution 139

List of Figures 141

References 147

Chapter 1
Introduction

My thesis is presented as a collection of research projects conducted during my studies on synchrotron radiation sources and free-electron lasers. While each project focuses on a specific aspect, they are all united by a common objective: to provide an advanced understanding of the characteristics of radiation pulses. This includes the exploration of their properties, modeling techniques, and generation methods, with particular emphasis on coherence.

The advent of synchrotron radiation sources [1] and high-gain free-electron lasers [2]–[4], has significantly advanced capabilities in material and life sciences [1], [5]–[15]. These radiation sources are designed as facilities to serve the scientific community. Consequently, the pulses impinging on users' samples must be thoroughly characterised and adjusted according to specific experimental requirements. Modern synchrotron radiation sources are undergoing magnetic lattice upgrades to maximise radiation brilliance and achieve higher degrees of transverse coherence of the emitted radiation across a broader *X-rays* frequency range. Accurate characterisation of coherence and ensuring its proper propagation are crucial for effectively delivering the unique properties from the source location down to the users' samples. Regarding pulse duration, synchrotron radiation pulses are typically constrained by the electron beam duration. At synchrotrons, the pulse duration is on the order of picoseconds [16]–[21], and only in exceptional cases can it be further reduced [22], [23] for users' applications. Hence, synchrotron radiation is generally poorly coherent in the longitudinal direction.

When discussing the coherence properties of free-electron lasers, it is important to note that while these are nearly fully coherent in the transverse domain, the longitudinal domain contains many "modes" within a radiation pulse [24] for the nominal self-amplified spontaneous emission (SASE) mode of operation. Free-electron lasers rely heavily on high peak current to achieve high gain. This is accomplished through a multistage compression system [25], which reduces the effective electron beam duration down to tens of femtoseconds, e.g. [26]. Special techniques can further reduce the lasing part of the beam to the sub-femtosecond level [27]–[31], effectively increasing longitudinal coherence. Additionally, seeding techniques provide almost full longitudinal coherence and enhance the spectral flux density of the radiation pulses. Both efforts to increase coherence and reduce pulse duration have garnered significant interest within the user community [32]–[34]. Furthermore, free-electron laser radiation may exhibit large frequency chirps [35], [36], which frequently behaves non-linearly [37]. This is a result of the longitudinal phase space of the electron beam being imprinted onto the radiation structure. All the aforementioned properties of the radiation must be properly characterised and simulated, leading to a better understanding physics process behind that will progress the development of more advanced pulse characteristics.

In **Chapter 2**, I present a set of numerical algorithms for modeling partially coherent fields. As advances in synchrotron radiation sources and free-electron lasers continue to push the boundaries of research, the need for accurate and efficient numerical methods to describe

and predict radiation coherence properties has become increasingly critical. It provides researchers with powerful tools for conducting comprehensive and computationally-efficient numerical experiments. These simulations allow for the testing of hypotheses without the complexities and constraints of physical experimentation. Furthermore, they play a pivotal role in the development of new facilities, thereby enhancing our understanding and expanding capabilities in material and life sciences.

The developed algorithms are universal for describing random fields and can be applied to different kinds of sources: thermal, synchrotrons, and free-electron lasers. These sources share the same statistical characteristics and are described as Gaussian random processes, with a few exceptions for radiation from special modes of operation of free-electron lasers. Normally, modeling a partially coherent source and the corresponding radiation pulse requires accurately accounting for the radiation from the single electrons of the source [38]–[41] or applying mode decomposition methods [42]–[45]. I propose an alternative treatment of the problem: by knowing the radiation ensemble averaged intensities and auto-correlation function, one can easily retrieve a single statistical instance of the random field. These instances are well-suited for numerical propagation to study the influence of optical systems on the final pulse properties. The proposed set of algorithms is also numerically efficient, requiring the generation of random samples of complex white noise, which are then restricted by appropriate mathematical supports in both direct and reciprocal domains. Moreover, the proposed algorithms can be applied well beyond physical optics applications to simulate various Gaussian stochastic processes.

I describe the application of the algorithms in different scenarios: in **Paper I** I show a simulation the image formation properties of a pinhole camera installed at a synchrotron, **Paper II** demonstrates the application of an algorithm for simulating partially coherent radiation from undulators, and in Section 2.5.4 I summarise their applications and extends it to radiation with arbitrary Winger function distributions like free-electron laser radiation. Additionally, in this Section, I provide a historical reference and numerically replicate Thomas Young's original experiment from 1803. **Paper III** goes beyond the limits of applicability of the algorithms and primarily demonstrates the experimental generation of sub-femtosecond pulses using a novel method called attoseconds-at-harmonics, which deals with non-Gaussian statistics.

The study of the coherence properties of synchrotron radiation continues in **Chapter 3** with the experimental demonstration of its fluctuating structure in the transverse dimension and measurements of the coherence length. In linear accelerator machines, the length of the electron beams is much shorter than that at synchrotrons and is on the order of tens of femtoseconds. This, in turn, means that in hard X-ray the number of spikes in the spectrum that fall within the typical monochromator bandwidth, such as Si (111), amounts to only dozens. This unique parameters allow one to retrieve the transversely spiky synchrotron radiation distribution upon monochromatization. The typical width of the spikes in the spatial domain is proportional to the transverse coherence length of the radiation.

I present results of such measurement, first conducted at the European XFEL using the monochromator so-called "K-monochromator" [46] paired with the spontaneous radiation imager "SR-imager" [47], which are designed for precise determination of the undulator K-values at the European XFEL. The experiment was conducted using radiation from a single undulator cells at SASE1 beamline of the European XFEL. I developed a data analysis procedure that can retrieve the auto-correlation function even from overwhelmingly noisy data

with a signal-to-noise ratio of much less than unity. The practical value of such measurements is in possibility to relate the width of the auto-correlation function to the transverse electron beam size, following the generalized van Cittert-Zernike theorem [48]–[50]. This provides an efficient tool for electron beam diagnostics for the long undulators of free-electron laser facilities. To validate the method, I collected different data sets under varying conditions of the electron beam optics. The results showed that the detected signal varied in accordance with the expected changes in the beta function, confirming the reliability of the approach.

Chapter 4 is devoted to the investigation of the undulator virtual source, revealing unexpected fine details in its structure. A very intriguing feature of the undulator virtual source was first noticed in [51] remarking the appearance of singular points in the radiation distribution located at both ends of the undulator, under the resonance approximation. Going beyond this approximation, a fine structure appears, that can be considered from the perspective of the radiation diffraction size. In this context, there are two typical radiation formation lengths for undulator radiation, and the formation length is naturally related to the radiation diffraction size. The longer formation length is associated with the undulator length and appears under the resonance approximation. However, there is also a shorter formation length related to the undulator period length, which is hidden in the finer structures of the virtual source structure. I studied the virtual source both under resonance conditions and out of resonance, highlighting the source peculiarities related to this shorter formation length. In this thesis, I propose two experimental setups to verify these peculiarities.

Another use of synchrotron radiation is the generation of powerful THz radiation pulses [52]. This is especially relevant in combination with an excellent X-ray source for conducting pump-probe experiments at free-electron laser facilities [52]. In **Chapter 5**, I describe a method for simulating synchrotron radiation that accounts for waveguide effects, which is particularly important for the highly divergent THz wavelength range. This method has been implemented in a simulation code that is essential for developing special insertion devices for dedicated THz radiation beamlines, for example those that are being developed at free-electron laser facilities [53]–[56].

In the developed code, I used the Green's function method, which allows for various boundary conditions, once the Green's function of the system is known. I conducted numerous cross-checks that demonstrate the feasibility of the Green's function method for calculating synchrotron radiation fields. I used a well-known code called Synchrotron Radiation Workshop [38] to validate the integration process for the Green's function method in free space. Then, I cross-checked my code with the results for a circular waveguide Green's function against the limiting case of free space and the analytical solution for a real-life case. This study was then continued in **Chapter 6** with a proposal for a conceptual design of a THz radiation propagation beamline for THz pump – X-ray probe experiments at free-electron laser facilities [55]–[58].

In particular, I studied methods for propagating THz radiation over hundreds of meters from the generation point to the experimental hall of the European XFEL using a device called iris waveguide [55], [57], [58]. I numerically estimated the performance of a propagation line based on this waveguide, where radiation is confined within a metallic tube and spatially filtered by periodically placed apertures. This leads to a mode selection process where, after a long propagation distance, the fundamental mode, a the Bessel function, is observed. This fundamental mode propagates with low losses. I also explored the use of a mirror-based system to out-couple radiation from the source and direct it into the iris line, ensuring optimal

matching conditions.

Each chapter provides the necessary theoretical background, context, and motivation for the conducted research, offering a broader perspective on the addressed problems. I hope this work will contribute to the advancement of light source development and user experiments.

Chapter 2

Gaussian random field generators for simulating partially coherent radiation

2.1. Introduction

In undergraduate optics courses, the focus is typically on abstract plane wavefronts entering optical systems rather than on the sources of electromagnetic radiation themselves. This simplification facilitates the study of the impulse response functions of optical systems, wavefront propagation techniques, diffraction effects, etc. At the next level of complexity, it becomes essential to consider the coherence properties of radiation sources and how these properties propagate through optical systems. Such radiation sources with finite coherence can be described as a sum of single emitters with random phases. This view can be extended by broadening the bandwidth of the emitted wavelength, thus additionally introducing temporal (or longitudinal) coherence. Radiation sources typically comprise numerous spatially distributed emitters contributing to the emission process, spatial (or transverse) coherence comes into play. As the number of emitters becomes exceedingly large, it becomes impractical to describe these sources deterministically, leading to their characterization as random sources. In such scenarios, the theory of statistical optics offers an ideal framework for describing the behavior of electromagnetic fields emitted by such sources. Examples of random sources include thermal sources like stars and light bulbs, as well as radiation from ultra-relativistic particle bunches, such as synchrotron radiation and self-amplified spontaneous emission of free-electron lasers (SASE FEL). These sources can be described in terms of statistical optics [59], [60], and a common feature among these sources is their adherence to the statistics of Gaussian processes, except for several cases of special modes of FEL operation.

There are several methods for simulating statistical optics phenomena. The most frequently applied methods in the synchrotron radiation and FEL communities are Monte Carlo-based simulations and mode decomposition methods [42]–[44], [61]–[64]. The methods referred to as Monte Carlo-based, such as Synchrotron Radiation Workshop (`SRW`) [38] and `Genesis 1.3` [65], simulate radiation based on first principles. In some cases, when the statistical properties of a random process are known in advance, a field distribution of the random process can be emulated in a very fast and numerically efficient way.

In this chapter, I present a method for simulating Gaussian random processes based on computationally efficient algorithms that leverage the properties of Gaussian random noise. I refer to these algorithms as `SERVAL` (**S**tochastic **E**mission **R**apid e**VAL**uator). These algorithms shapes the field distribution by multiplying the Gaussian white noise distribution with specifically chosen mathematical supports in the reciprocal domains. I designed these methods exclusively for Gaussian random fields – multidimensional Gaussian random processes. However, there is potential to extend these methods to non-Gaussian statistics, as

demonstrated in [66]. Although these algorithms were developed for simulating synchrotron radiation sources and SASE FELs, they can be easily extended to all electromagnetic fields that are stochastic and follow Gaussian random process statistics.

Describing these methods necessitates an introduction to the fundamentals of statistical optics theory, which I present earlier in this chapter. I begin with general definitions of random processes and their properties. Delving into the concepts of stationarity and ergodicity, I discuss differences in statistical averaging of radiation events: averaging *over* time versus *across* different statistical realizations. Then I introduce the central theoretical concept for this thesis – Gaussian random processes. Subsequently, I present the theory for quasi-stationary sources in a manner similar to that used in [59], [60] for stationary sources.

I provide a proof of a generalized form of the Wiener-Khinchin theorem. This generalization accounts for the quasi-stationarity of a source and relates the finite duration of the pulse to its spectral coherence properties. From the *longitudinal* coherence properties of radiation, I transition to its *transverse* domain and offer a derivation of the generalized van Cittert-Zernike theorem following [50].

After this, I discuss the coherence properties of synchrotron and SASE FEL radiation, along with well-established methods for simulating these types of radiation sources. Towards the end, I present `SERVAL` algorithms for simulating partially coherent radiation. Each algorithm is first presented through heuristic considerations, that are then extended to applications in simulation problems: bending magnet radiation, undulator radiation, and FEL SASE radiation, as represented in **Papers I**, **II**, and in Section 2.5.4. Finalizing this Chapter, I present an experimental method for generating sub-femtosecond level pulses at FEL facilities, presented in **Paper III**; statistics of these pulses deviates from Gaussian behavior. This result showcases that the proposed algorithms should be applied thoughtfully to each considered case.

2.2. Classification of random processes

In this section, I will introduce the basic notation and concepts of statistical optics. I primarily follow the textbooks [59], [60] with slight modifications to encompass quasi-stationary sources in the theory. The material presented here is shortened to the bare minimum, and more details can be found in [59], [60]. I start by defining different types of averages: over time and across different statistical realization and then introduce the concept of stationarity and ergodicity. This is followed by a definition of a complex Gaussian process, which plays a central role for the random processes. Finally, I discuss quasi-stationary approximation for describing synchrotron radiation and SASE FEL.

A real-valued random process X consists of statistical realizations $x^{[k]}$, each of which is numbered $1, 2, \ldots, k$. Unlike a random variable, a random process X depends on time – $X(t)$. The process is random, meaning that the exact value of a random variable $x^{[k]}(t_0)$ at the specific moment in time t_0 cannot be predicted in advance. An objective way to make predictions about a statistical process over time is to define averages. Realistically, an observer is able to measure the process only over a finite time interval $[-T/2, T/2]$. So, one writes the

following definition of a *time average*:

$$[x^{[k]}(t)]_T = \frac{1}{T}\int_{t-T/2}^{t+T/2} x^{[k]}(t')dt', \tag{2.1}$$

One can expect that $[x^{[k]}(t)]_T$ will fluctuate from measurement to measurement when T is rather small. To mitigate this one should extend the time interval $[-T/2, T/2]$ reasonably large, i.e. $T \to \infty$. This naturally lead to the *full-time average* value:

$$\overline{x^{[k]}} = \lim_{T\to\infty}[x^{[k]}(t)]_T, \tag{2.2}$$

which does not depend either on t and T[1], but can depend on chosen k-th realisation of the process X. *Time auto-correlation function* can be defined also as time averaged integral in the following form:

$$[x^{[k]}(t_1)x^{[k]}(t_2)]_T = \frac{1}{T}\int_{t-T/2}^{t+T/2} x^{[k]}(t+t_1)x^{[k]}(t+t_2)dt \tag{2.3}$$

and the full-time average is:

$$\overline{x^{[k]}(t_1)x^{[k]}(t_2)} = \lim_{T\to\infty}[x^{[k]}(t_1)x^{[k]}(t_2)]_T, \tag{2.4}$$

where t_1 and t_2 are time delays. All higher-order time auto-correlation function

$$\overline{x^{[k]}(t_1)x^{[k]}(t_2)\dots x^{[k]}(t_n)} \tag{2.5}$$

up to n-th order can be introduced by analogy. Time averages are important when describing the temporal behavior of a given statistical realization, while it is possible to define different type of statistical averages based on averages across different realizations. For this, it is convenient to define the joint probability density functions of a random process:

$$p_{x,m}(x_1, x_2, \dots, x_m; t_1, t_2, \dots, t_m), \tag{2.6}$$

which is probability of finding the values $x_1, x_2, \dots, x_m$ at the times $t_1, t_2 \dots, t_m$ correspondingly when measuring a realisation of the process X. The joint probability density function is used for calculation of the joint moments. For example, when $m = 1$ one obtains:

$$\langle x(t)\rangle \equiv \int x_1 p_{x,1}(x_1, t_1)dx_1, \tag{2.7}$$

and similarly for the second-order moment:

$$\langle x(t_1)x(t_2)\rangle = \iint x_1 x_2 p_{x,2}(x_1, t_1, x_2, t_2)dx_1 dx_2, \tag{2.8}$$

[1] If T is indeed large.

which is called the first-order temporal auto-correlation function.

In principle, to fully describe a process, one needs to know all higher-order auto-correlation functions[2]. However, in practice, it is often not possible. In this case, one can utilise another useful but equivalent definition of the ensemble averaging. If one collects a reasonably large statistical ensemble: $x^{[1]}(t), x^{[2]}(t), \ldots, x^{[N]}(t)$, then the ensemble average can be defined as the following:

$$\langle x(t) \rangle = \lim_{N \to \infty} \frac{1}{N} \sum_{i=1}^{N} x^{[i]}(t) \tag{2.9}$$

and the same for the first-order temporal auto-correlation function:

$$\langle x(t_1) x(t_2) \rangle = \lim_{N \to \infty} \frac{1}{N} \sum_{i=1}^{N} x^{[i]}(t_1) x^{[i]}(t_2), \tag{2.10}$$

and so on for higher-order correlation functions. These definitions are fully equivalent to Eqs. 2.7, 2.8 but the latter are much more useful in practice. This only requires measurements of the realizations themselves without any *a priori* knowledge about the process. In this thesis, I will mostly rely on definitions in Eqs. 2.9, 2.10 for practical calculations.

2.2.1. Stationarity and ergodicity

Identifying properties that classify random processes and establishing governing laws is always essential. In this subsection, I will introduce two important concepts in statistical optics: stationarity and ergodicity. These concepts classify a process based on its behaviour *over* time and *across* different realisations of the process.

A process is called stationary if all its joint probability density functions have the following property:

$$p_{x,m}(x_1, t_1, x_2, t_2, \ldots x_m, t_m) = p_{x,m}(x_1, t_1 + T, x_2, t_2 + T, \ldots x_m, t_m + T) \text{ for all } T \tag{2.11}$$

The choice of T is arbitrary here and one can set it to be $T = t - t_1$ and finds that, for example, the auto-correlation function depends only on the times delays difference $t_2 - t_1$:

$$\langle x(t_1) x(t_2) \rangle = \iint x_1 x_2 p_{x,2}(x_1, t_1, x_2, t_2) dx_1 dx_2 =$$
$$\iint x_1 x_2 p_{x,2}(x_1, t, x_2, t + t_2 - t_1) dx_1 dx_2 = \langle x(t) x(t + t_2 - t_1) \rangle \tag{2.12}$$

and equivalently:

$$\langle x(t) x(t + t_2 - t_1) \rangle = \lim_{N \to \infty} \frac{1}{N} \sum_{i=1}^{N} x^{[i]}(t) x^{[i]}(t + t_2 - t_1) \tag{2.13}$$

[2] I will use the term auto-correlation function, correlation function, or simply correlation to refer to this quantity further in the thesis, unless specified otherwise.

for all t values, so the auto-correlation depends only on the delays difference. This definition in Eq. 2.11 is also called *strict-sense stationarity* because it requires that all orders of the joint probability function follow this definition. In practice, when one is interested only in the average and the first-order auto-correlation function, a weaker definition can be used. If these two quantities are stationary, the process is called *wide-sense stationarity*.

There are two conceptual ways to define averages in statistical optics: *over* time and *across* different realizations. In general, these averages should be different, but there is a specific type of process for which two averages are equivalent. This type of processes are called *ergodic*. Writing the definition for this explicitly:

$$\lim_{N\to\infty}\frac{1}{N}\sum_{i=1}^{N}x^{[i]}(t)=\lim_{T\to\infty}\frac{1}{T}\int_{t-T/2}^{t+T/2}x^{[k]}(t')dt' \tag{2.14}$$

for any t and k-th realization of the process, T should be large enough. And the same can be written for the auto-correlation function:

$$\lim_{N\to\infty}\frac{1}{N}\sum_{i=1}^{N}x^{[i]}(t+t_1)x^{[i]}(t+t_2)=\lim_{T\to\infty}\frac{1}{T}\int_{t-T/2}^{t+T/2}x^{[k]}(t'+t_1)x^{[k]}(t'+t_2)dt' \tag{2.15}$$

again for any t and taken k-th realization.

To state that a process is ergodic in full sense, one must verify similar equalities for all higher-order correlation functions of the process. However, there is a specific type of process called a Gaussian random process, where once the first-order correlation function is known, all higher-order correlations can be expressed through it using moment theorem for Gaussian processes. Therefore, if a process is Gaussian random process and adheres to the definition in Eq. 2.15 then the process is indeed ergodic in full sense.

2.2.2. Gaussian random processes

In this thesis I mostly consider Gaussian random processes. Expressing this kind of statistics in mathematical terms, a random processes $X(t)$ is called Gaussian if probability to find a realization of $X(t)$ between to values x and $x+dx$ is described by the normal distribution:

$$p(x)=\frac{1}{\sqrt{2\pi}\sigma}e^{-x^2/2\sigma^2}, \tag{2.16}$$

at any points of time. Here p is as usual probability density function, σ is the dispersion of the normal distribution. It is always convenient to work with an analytic representation of a signal for representing most of physical process. So, one can introduce a definition of the *complex* Gaussian random process: $Z=X+iY$, where both processes X and Y have the same dispersion σ. So, the probability density function for $p(z)$:

$$p(z)=p(x)p(y)=\frac{1}{2\pi\sigma^2}e^{-(x^2+y^2)/2\sigma^2}, \tag{2.17}$$

which can be transformed using polar coordinates $x = A\cos(\phi)$ and $y = A\sin(\phi)$ to the following:

$$p(z) = p(A, \phi) = \frac{A}{2\pi\sigma^2} e^{-A^2/2\sigma^2}. \tag{2.18}$$

This distribution is called the *Rayleigh probability distribution*. In the last equation, the

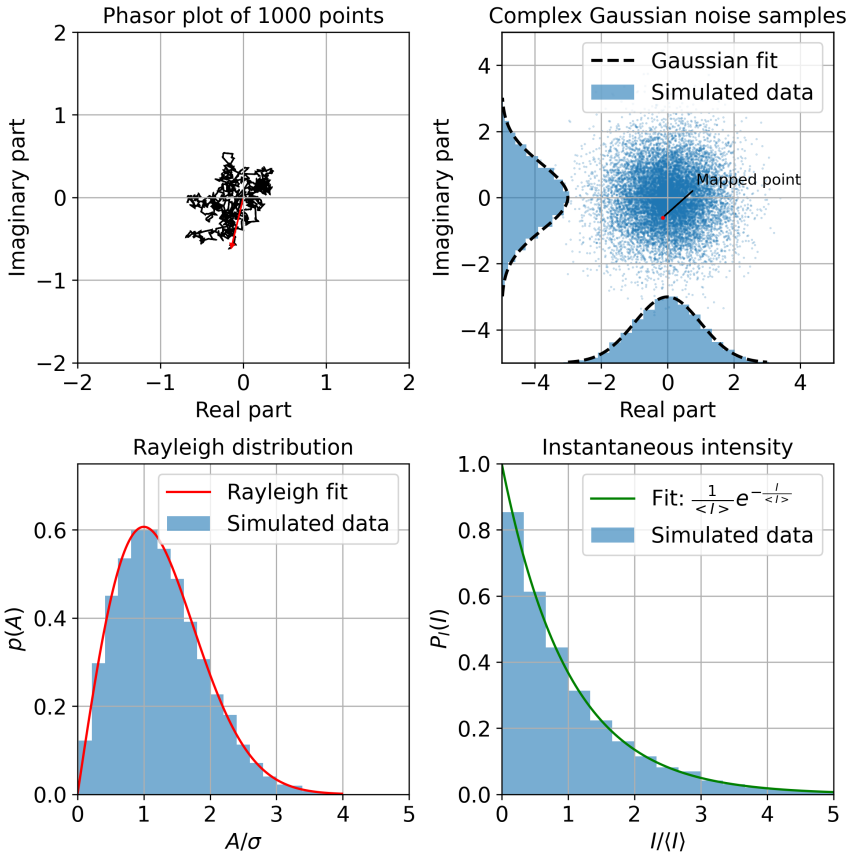

Figure 2.1: Gaussian random process statistics. The upper left subplot represents the sum of random phasors, resulting in a sample of a Gaussian random process shown on the complex plane. The upper right subplot shows 10^4 samples plotted on the complex plane, with zero mean and unit variance; the red dot corresponds to the sample in the upper left. The lower left shows the resulting Rayleigh distribution, and the lower right shows the instantaneous intensity of the simulated samples.

dependence on ϕ is not presented explicitly, which implies that the phase is distributed uniformly for all values ($0 \leq \phi \leq 2\pi$), i.e.:

$$p(\phi) = \frac{1}{\sqrt{2\pi}}. \tag{2.19}$$

One can also consider probability density function for the *instantaneous intensity*:

$$I(t) = A^2(t) \tag{2.20}$$

and using the law for probability functions transformations one obtains the negative exponential distribution:

$$p(I) = \frac{1}{\langle I \rangle} e^{-I/\langle I \rangle}, \tag{2.21}$$

where $\langle I \rangle = 2\sigma$.

Discussing important properties of Gaussian processes, one can notice that *a Gaussian random process remains Gaussian after linear filtering*. Let's say $u(t)$ is a Gaussian process and $h(t, \xi)$ is some time-response filter, then:

$$v(t) = \int_{-\infty}^{\infty} h(t, \xi) u(\xi) d\xi \tag{2.22}$$

$v(t)$ is also a Gaussian process.

Another very useful property of Gaussian processes is that higher-order moments can be expressed using the first- and second-order moments. This means that as soon as the first- and second-order moments are known, the process is fully determined in terms of its statistical moments. *Thus, any wide-sense stationary Gaussian process is actually strictly stationary.*

Gaussian random processes play a fundamental role in describing synchrotron radiation, SASE FEL, and, more generally, statistical processes. From this point forward, I will assume that the processes discussed in this thesis possess Gaussian statistics, with several exceptions described separately. Now, I will focus on extending the definition of stationarity to a broader class of processes to account for the time-confined nature of synchrotron radiation and SASE FEL.

2.2.3. Quasi-stationary approximation

Although many day-to-day sources of radiation can be categorized as stationary and/or ergodic, numerous processes are constrained in time, such as synchrotron radiation and SASE FEL. In principle, these are non-stationary processes. Developing a generalized theory for non-stationary processes and deriving practical laws is very challenging. Nevertheless, there is a class of sources that can be described similarly to stationary ones, but accounting for their finite nature in time. Such sources are referred to as quasi-stationary, and certain types of synchrotron radiation and FEL SASE can be described by this classification. As the name suggests, quasi-stationary processes share most of the statistical properties with stationary ones, but they start and finish at specific points in time. *Quasi-stationary processes appear to be stationary only within a certain interval of time, which is much smaller than their overall duration.* At this point, I will slightly deviate from the usual presentation of statistical optics concepts, which is formulated for stationary processes only, as in [59], [60], and focus on the properties of quasi-stationary processes. I will first introduce the theory of quasi-stationarity without links to real physical processes to present its general properties and establish a relation to the stationary theory. Since quasi-stationarity is just a useful approximation, it is always necessary to demonstrate that a real physical process follows these properties and justify the assumptions, which I will show for synchrotron radiation in Section 2.4.

I denote a polarisation components of an electric field in time domain or just the "field" as $E(t)$, which is analytic representation of some real-valued electric field[3]. I also assumes that

[3] I will redefine $E(t)$ to be a real-valued function in Chapters 4 and 5.

the field $E(t)$ follows Gaussian statistics as a complex valued random process. An ensemble averaged intensity of this field will be:

$$I(t) = \langle |E(t)|^2 \rangle = \lim_{N\to\infty} \frac{1}{N} \sum_{i=1}^{N} E^{[i]}(t) E^{*[i]}(t), \tag{2.23}$$

where * denotes complex conjugate operation. $I(t)$ is the ensemble averaged radiation intensity (time envelope), which depends on time. The time auto-correlation function can be presented as ensemble average following the definition from Eq. 2.10:

$$\Gamma_t(t_1, t_2) = \langle E(t_1) E^*(t_2) \rangle = \lim_{N\to\infty} \frac{1}{N} \sum_{i=1}^{N} E^{[i]}(t_1) E^{*[i]}(t_2), \tag{2.24}$$

which is adopted for the complex-valued process. The auto-correlation function $\Gamma_t(t_1, t_2)$ now can be normalised:

$$\gamma_t(t_1, t_2) = \frac{\langle E(t_1) E^*(t_2) \rangle}{\sqrt{\langle |E(t_1)|^2 \rangle \langle |E(t_2)|^2 \rangle}} = \frac{\Gamma_t(t_1, t_2)}{\sqrt{I(t_1) I(t_2)}} \tag{2.25}$$

and rewritten as:

$$\Gamma_t(t_1, t_2) = \gamma_t(t_1, t_2) \sqrt{I(t_1) I(t_2)}. \tag{2.26}$$

This is still general representation of $\Gamma_t(t_1, t_2)$ and now I will introduce the concept of quasi-stationary. If the width of $\gamma_t(t_2, t_1)$ remains constant over the intensity distribution, then it depends only on the time difference $t_2 - t_1$:

$$\Gamma_t(t_1, t_2) = \gamma_t(t_2 - t_1) \sqrt{I(t_1) I(t_2)}. \tag{2.27}$$

The radiation sources that have this kind of auto-correlation function can be refer to as quasi-stationary. However, there is a "stronger" definition of quasi-stationarity. If one assumes that the width $\gamma_t(t_2 - t_1)$ is much smaller than the scale of $I(t)$, which on practice means that a pulse is many coherent lengths long, then one ends up with even simpler factorised expression:

$$\Gamma_t(\bar{t}, \Delta t) = \gamma_t(\Delta t) I(\bar{t}), \tag{2.28}$$

where I introduced new set of variables $\bar{t} = (t_1 + t_2)/2$ and $\Delta t = t_2 - t_1$. This representation of a radiation sources is to some extent similar to quasi-homogeneity in the transverse domain introduced in [50], [59], which I will discuss later in this thesis. To my best knowledge, there are only a few mentions [67], [68] of Eq. 2.28 in optics community and authors of [69] resulted in this expression for synchrotron radiation.

2.2.4. Wiener-Khinchin theorem for quasi-stationary processes

Here I will demonstrate that temporal correlation function in Eq. 2.28 can be used to derive a similar to the well-known Wiener-Khinchin theorem relation but for quasi-stationary radiation pulse. I define the Fourier transform of the field $E(t)$ to the *frequency domain* as

$$\bar{E}(\omega) = \int_{-\infty}^{\infty} E(t) e^{i\omega t} dt \tag{2.29}$$

and corresponding inverse Fourier transform back to the *time domain*:

$$E(t) = \frac{1}{2\pi}\int_{-\infty}^{\infty} \bar{E}(\omega)e^{-i\omega t}d\omega. \tag{2.30}$$

I write spectral auto-correlation function for two frequencies ω_1 and ω_2 and substitute Eq. 2.29 in it:

$$\Gamma_\omega(\omega_1,\omega_2) = \langle \bar{E}(\omega_1)\bar{E}^*(\omega_2)\rangle = \iint_{-\infty}^{\infty} \langle E(t_1)E^*(t_2)\rangle e^{i(\omega_1 t_1 - \omega_2 t_2)}dt_1 dt_2, \tag{2.31}$$

where I brought the ensemble averaging under the integral sign. Then using the expression in Eq. 2.28 and substituting this in Eq. 2.31 I obtain:

$$\Gamma_\omega(\omega_1,\omega_2) = \iint_{-\infty}^{\infty} \gamma_t(t_2-t_1)I\left(\frac{t_1+t_2}{2}\right)e^{i(\omega_1 t_1 - \omega_2 t_2)}dt_1 dt_2. \tag{2.32}$$

At this point it makes sense to exchange variables t_1, t_2 for $\Delta t, \bar{t}$ and, by analogy, ω_1, ω_2 for $\Delta\omega, \bar{\omega}$. With this variables exchanges, it is now evident that the integral factorises:

$$\Gamma_\omega(\bar{\omega},\Delta\omega) = \int_{-\infty}^{\infty} \gamma_t(\Delta t)e^{i\bar{\omega}\Delta t}d\Delta t \int_{-\infty}^{\infty} I(\bar{t})e^{-i\Delta\omega\bar{t}}d\bar{t} = G(\bar{\omega})\bar{f}(\Delta\omega). \tag{2.33}$$

At first, one can see that the spectral auto-correlation function $\Gamma_\omega(\bar{\omega},\Delta\omega)$ consist of spectral density function $G(\bar{\omega})$:

$$G(\bar{\omega}) = \int_{-\infty}^{\infty} \gamma_t(\Delta t)e^{i\bar{\omega}\Delta t}d\Delta t, \tag{2.34}$$

and spectral correlation function $\bar{f}(\Delta\omega)$:

$$\bar{f}(\Delta\omega) = \int_{-\infty}^{\infty} I(\bar{t})e^{-i\Delta\omega\bar{t}}d\bar{t}, \tag{2.35}$$

which can be viewed as normalised version of $\Gamma_\omega(\bar{\omega},\Delta\omega)$.

The derivation of Eq. 2.33 is very similar to the one done for stationary theory, where it comes to the original Wiener-Khinchin theorem. There is one difference: the time auto-correlation function is presented in the form given in Eq 2.28. Eq. 2.33 includes $I(t)$, which signifies the finite nature of the radiation pulse. According to the more general representation of the Wiener-Khinchin theorem, this intensity distribution is now related to the spectral correlation function $\bar{f}(\Delta\omega)$ via an inverse Fourier transform (Eq. 2.35). The result in Eq. 2.33 will be referred to as the Wiener-Khinchin theorem in application to *quasi-stationary processes* [69]. Due to the symmetry of Fourier transform operation, the inverse relations of Eqs. 2.34, 2.35 must also hold.

For consistency of the narrative, the original results of the Wiener-Khinchin theorem can be obtained for a *stationary process* by simply setting the intensity envelope to remain constant along the pulse: $I(\bar{t}) = C$

$$\left\langle \bar{E}\left(\bar{\omega} + \frac{\Delta\omega}{2}\right)\bar{E}^{*}\left(\bar{\omega} - \frac{\Delta\omega}{2}\right)\right\rangle = C\int_{-\infty}^{\infty}\gamma_t(\Delta t)e^{i\bar{\omega}\Delta t}d\Delta t\int_{-\infty}^{\infty}e^{-i\Delta\omega\bar{t}}d\bar{t} = G(\bar{\omega})\delta(\Delta\omega). \tag{2.36}$$

Thus, the spectral correlation function of an infinitely long pulse becomes infinitely narrow, reducing to a Dirac delta function: $\delta(\Delta\omega)$. One can recognize that the radiation spectral density, or just spectrum, is related to the auto-correlation function via a Fourier transform. Both expressions in Eqs. 2.33 and 2.36 play an essential role in coherence theory on an equal footing with the van Cittert-Zernike theorem, which I present in the next section.

2.3. Transverse coherence properties of quasi-stationary sources

Previously, I only considered sources in the time-frequency domain pair, while real fields exist in a three-dimensional space. In this section, I will introduce transverse variables into the auto-correlation function. Then, I will classify the types of sources in terms of the factorizability of the cross-spectral density function, in a manner very similar to what I have done for the longitudinal domain. After this, I will provide a derivation of the van Cittert-Zernike theorem and its generalised version for quasi-homogeneous sources. This chapter will be the last one on the general laws of statistical optics, and it will be followed by practical applications in the theory of synchrotrons and free-electron lasers.

2.3.1. Introducing transverse domain

In the previous section, I ignored transverse coordinates, which corresponds to a signal being effectively observed through a pinhole. As I consider optical phenomena, not many of them can be fully described with only time or frequency domains – the signal's propagation direction – but also require taking into account transverse coordinates and respective domains. Therefore, the expressions I previously provided should be adjusted accordingly to correctly reflect the statistical properties in the transverse dimensions of the real fields.

Eq. 2.33 should hold regardless of the presence of the transverse domain. To introduce them, I assume that the radiation pulse shape $I(\bar{t})$ does not depend on transverse coordinates $\vec{r}$. This, in practice, implies the absence of a pulse-front tilt in space-time or angular dispersion in inverse-space-frequency domains. For convenience, I need to redefine $I(\bar{t})$ to $f(\bar{t})$. Thus, all the dependence on transverse variables is in the normalized temporal auto-correlation function γ_t. So, I rewrite Eq. 2.33 in the following form:

$$\Gamma_{\omega}(\vec{r}_1, \vec{r}_2, \bar{\omega}, \Delta\omega) = \int_{-\infty}^{\infty}\gamma_t(\vec{r}_1, \vec{r}_2, \Delta t)e^{i\bar{\omega}\Delta t}d\Delta t\int_{-\infty}^{\infty}f(\bar{t})e^{-i\Delta\omega\bar{t}}d\bar{t} = G(\vec{r}_1, \vec{r}_2, \bar{\omega})\bar{f}(\Delta\omega). \tag{2.37}$$

This representation results in the appearance of the cross-spectral density function $G(\vec{r}_1, \vec{r}_2, \bar{\omega})$ in a manner similar to that done for stationary sources in, for example, [60] but now $\bar{f}(\Delta\omega)$ describes the finite width of spectral correlation.

Actually, $\Gamma_\omega(\vec{r}_1, \vec{r}_2, \bar{\omega}, \Delta\omega)$ also depends on radiation position along the propagation coordinate z:

$$\Gamma_\omega(z, \vec{r}_1, \vec{r}_2, \bar{\omega}, \Delta\omega) = G(z, \vec{r}_1, \vec{r}_2, \bar{\omega})\bar{f}(\Delta\omega), \tag{2.38}$$

where $G(z, \vec{r}_1, \vec{r}_2, \bar{\omega})$ can be written for a given frequency ω as the following :

$$G(z, \vec{r}_1, \vec{r}_2, \omega) = \langle \bar{E}(z, \vec{r}_1, \omega)\bar{E}^*(z, \vec{r}_2, \omega)\rangle \tag{2.39}$$

The same dependence on z follows for $\Gamma_t(z, \vec{r}_1, \vec{r}_2, \bar{t}, \Delta t)$:

$$\Gamma_t(z, \vec{r}_1, \vec{r}_2, \bar{t}, \Delta t) = \gamma_t(z, \vec{r}_1, \vec{r}_2, \Delta t)f(\bar{t}). \tag{2.40}$$

2.3.2. Practical importance of the spectral domain

The fields I have described are random, which in practice means that they fluctuate both in the time-frequency domain as well as in the transverse pair of domains. These fluctuations have typical distributions described by $\gamma_t(z, \vec{r}_1, \vec{r}_2, \Delta t)$ in the time domain and $\bar{f}(\Delta\omega)$ in the frequency domain. I will refer to these fluctuations of the field as spikes – a term commonly accepted in the FEL community.

Describing a quasi-stationary process is experimentally challenging in the time domain, especially when dealing with radiation pulses from relativistic electron beams. They occur so quickly that even reliably detecting the start and end of a given realization is difficult. Additionally, reconstructing the time domain of these fields and resolving spikes is typically not feasible. On the contrary, analyzing the frequency domain and measuring the spectrum of the radiation is a much more approachable problem. Thus, the spectral auto-correlation function $\Gamma_\omega(z, \vec{r}_1, \vec{r}_2, \bar{\omega}, \Delta\omega)$, the cross-spectral density function $G(z, \vec{r}_1, \vec{r}_2, \bar{\omega})$, and $\bar{f}(\Delta\omega)$ are of great practical use for synchrotron radiation and SASE FEL application.

In this section, I assumed that the field follows Gaussian statistics, which implies that the correlation functions in Eqs. 2.38 and 2.40 are sufficient to calculate all higher-order correlation functions and fully describe this statistical process. In the next section, I will introduce the concept of quasi-homogeneity and present propagation laws for $G(z, \vec{r}_1, \vec{r}_2, \bar{\omega})$.

2.3.3. Cross-spectral density function at the source and quasi-homogeneity

The normalized version of the cross-spectral density function has the following form:

$$g(z, \vec{r}_1, \vec{r}_2, \omega) = \frac{G(z, \vec{r}_1, \vec{r}_2, \omega)}{\sqrt{\bar{I}(z, \vec{r}_1, \omega)\bar{I}(z, \vec{r}_2, \omega)}}, \tag{2.41}$$

where z is the distance along the propagation axis and $z = 0$ corresponds to the source position. Writing this at the source position and expressing G through g:

$$G(0, \vec{r}_1, \vec{r}_2, \omega) = g(0, \vec{r}_1, \vec{r}_2, \omega)\sqrt{\bar{I}(0, \vec{r}_1, \omega)\bar{I}(0, \vec{r}_2, \omega)}, \tag{2.42}$$

Now, I assume that the width of $g(0, \vec{r}_1, \vec{r}_2, \omega)$ does not change across the intensity distribution, which means that this function depends only on the coordinates difference:

$$G(0, \vec{r}_1, \vec{r}_2, \omega) = g(0, \vec{r}_2 - \vec{r}_1, \omega)\sqrt{\bar{I}(0, \vec{r}_1, \omega)\bar{I}(0, \vec{r}_2, \omega)}, \tag{2.43}$$

This kind of radiation source is called quasi-homogeneous according to [59]. In the same way as was done for defining quasi-stationarity, one can simplify the expression and make further assumptions on the width of the $g(0, \vec{r}_2 - \vec{r}_1, \omega)$ function to be much smaller than the radiation envelope $I(0, \vec{r}, \omega)$, again exactly similarly as was done for the longitudinal domain in Eq. 2.28 :

$$G(0, \vec{\bar{r}}, \Delta\vec{r}, \omega) = g(0, \Delta\vec{r}, \omega)\bar{I}(0, \vec{\bar{r}}, \omega), \tag{2.44}$$

where I introduced $\Delta\vec{r} = \vec{r}_2 - \vec{r}_1$ and $\vec{\bar{r}} = (\vec{r}_1 + \vec{r}_2)/2$. In the limit case of fully incoherent sources this expression is reduced to:

$$G(0, \vec{\bar{r}}, \Delta\vec{r}, \omega) = \bar{I}(0, \vec{\bar{r}}, \omega)\delta(\Delta\vec{r}), \tag{2.45}$$

where $\delta(\Delta\vec{r})$ is the Dirac delta function. Aside of incoherent sources, this definition also applies to the cases when the resolution of an optical system cannot resolve $g(\Delta\vec{r}, \omega)$, [59].

2.3.4. Propagation law for cross-spectral density function in free space

Another essential problem in coherence theory concerns the calculation of coherence properties upon the propagation of radiation through an optical system. By its nature, a single statistical realisation of a field from a random process behaves identically to any other field and can be propagated in the same way, adhering to the wave equation. One effective method to calculate the field and its statistical properties upon propagation is to directly apply the corresponding wave optics propagator – or a sequence of propagators – through the optical system. This approach is extremely practical, especially in numerical simulations, and is used in well-known codes for simulating synchrotron radiation, such as `SRW` [38]. An alternative approach for calculating coherence properties is to derive the corresponding wave equations for the propagation of the cross-spectral density function. This not only results in the propagation law but also in a very useful theorem that relates the cross-spectral density function with the source intensity distribution, called the van Cittert-Zernike theorem.

One seeks the $G(z, \vec{r}_1, \vec{r}_2, \omega)$ cross-spectral density distribution at z in the S' plane, assuming that the distribution $G(0, \vec{r}'_1, \vec{r}'_2, \omega)$ in the source plane S, where $z = 0$, is known. This problem is described by a system of two Helmholtz equations on cross-spectral density with respect to $\vec{r}_1$ and $\vec{r}_2$, as shown, for example, in [60]. The solution of the system is expressed as an integral:

$$G(z, \vec{r}_1, \vec{r}_2, \omega) = \left(\frac{k}{2\pi}\right)^2 \iint_{S'} G(0, \vec{r}'_1, \vec{r}'_2, \omega)\frac{e^{ik(R_2 - R_1)}}{R_1 R_2}\cos(\theta_1)\cos(\theta_2)dr'_1 dr'_2. \tag{2.46}$$

The geometry of the problem is depicted in Fig. 2.2, where O' is the origin of the coordinates, lying in the S' plane, and $\vec{r}'_1, \vec{r}'_2$ are in this plane. Vectors $\vec{r}_1, \vec{r}_2$ correspond to the observation positions in plane S. R_1 and R_2 are defined as follows:

$$R_{1,2} = \sqrt{z^2 + |\vec{r}_{1,2} - \vec{r}'_{1,2}|^2} \tag{2.47}$$

The integral in this equation can be evaluated once the cross-spectral density function $G(0, \vec{r}'_1, \vec{r}'_2, \omega)$ is known. However, there is a simpler expression available when one adopts the

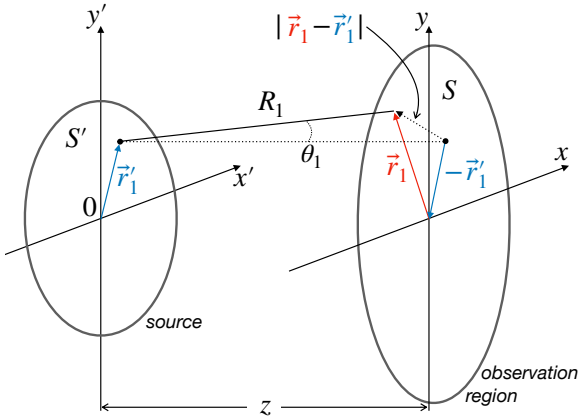

Figure 2.2: Schematic representation of the geometry for Eq. 2.46. The parameter R_2 is represented in the same way.

quasi-homogeneous approximation for describing a radiation source resulting in well-known van Cittert-Zernike theorem.

Historically, the van Cittert-Zernike theorem was formulated using Huygens' principle, leading to an expression that relates the mutual intensity function with the radiation intensity distribution at the source [48], [49]. The cross-spectral density function $G(z, \vec{r}_1, \vec{r}_2, \omega)$ obeys the same propagation laws as the mutual intensity function $J(\vec{r}_1, \vec{r}_2) = g_t(\vec{r}_1, \vec{r}_2, \Delta t = 0)$, which is shown in [59], [60]. I will continue to present the results for the theorem using the cross-spectral density.

2.3.5. The van Cittert-Zernike theorem

Eq. 2.46 is general and can be applied to any field to calculate its cross-spectral distribution upon propagation over distance z. This integral can be further simplified to derive a more practical relation for specific types of sources, namely fully incoherent and partially coherent sources under the quasi-homogeneous approximation introduced in Eqs. 2.44 and 2.45.

Assuming the paraxial approximation and that the cross-spectral density function is observed in the far zone ($z \gg 1$), one can write the following expression for the mutual intensity function based on Eq. 2.46, where dependence on angles $\theta_{1,2}$ is neglected:

$$G(z, \vec{r}_1, \vec{r}_2, \omega) = \left(\frac{k}{2\pi}\right)^2 \iint_{S'} G(0, \vec{r}'_1, \vec{r}'_2, \omega) \frac{e^{ik(R_2 - R_1)}}{R_1 R_2} d^2 r'_1 d^2 r'_2, \tag{2.48}$$

here $R_{1,2}$ can be further simplified using the relations:

$$\begin{aligned} R_{1,2} &\approx z + \frac{|\vec{r}'_{1,2} - \vec{r}_{1,2}|^2}{2z} \\ R_1 R_1 &\approx z^2 \end{aligned} \tag{2.49}$$

Using the first relation in Eq. 2.49, I explicitly write $R_2 - R_1$:

$$R_2 - R_1 = \frac{1}{2z}\left(|\vec{r}_2|^2 - 2|\vec{r}_2 \cdot \vec{r}_2'| + |\vec{r}_2'|^2 - |\vec{r}_1|^2 + 2|\vec{r}_1 \cdot \vec{r}_1'| - |\vec{r}_1'|^2\right), \tag{2.50}$$

where:

$$\begin{gathered} |\vec{r}_2|^2 - |\vec{r}_1|^2 = 2\vec{\bar{r}} \cdot \Delta\vec{r} \\ |\vec{r}_2'|^2 - |\vec{r}_1'|^2 = 2\vec{\bar{r}}' \cdot \Delta\vec{r}' \\ |\vec{r}_1 \cdot \vec{r}_1'| - |\vec{r}_2 \cdot \vec{r}_2'| = -\vec{\bar{r}} \cdot \Delta\vec{r}' - \vec{\bar{r}}' \cdot \Delta\vec{r}. \end{gathered} \tag{2.51}$$

Then I substitute this in Eq. 2.48 and obtain:

$$G(z, \vec{\bar{r}}, \Delta\vec{r}, \omega) = \left(\frac{k}{2\pi}\right)^2 \frac{e^{i\frac{k}{z}\vec{\bar{r}}\cdot\Delta\vec{r}}}{z^2} \iint_{\mathcal{S}'} G(0, \vec{\bar{r}}', \Delta\vec{r}', \omega) e^{-i\frac{k}{z}(\vec{\bar{r}}\cdot\Delta\vec{r}' + \Delta\vec{r}\cdot\vec{\bar{r}}')} d\vec{\bar{r}}' d\Delta\vec{r}' \tag{2.52}$$

Here, the term $2\vec{\bar{r}}' \cdot \Delta\vec{r}'$ was neglected in the exponent under condition $\vec{\bar{r}}' \cdot \Delta\vec{r}'/(\lambda z) \ll 1$, which applies to the far zone assumption made earlier. Using the representation of fully incoherent source and substituting this in Eq. 2.52 one obtains:

$$G(z, \vec{\bar{r}}, \Delta\vec{r}, \omega) = \frac{e^{i\frac{k}{z}\vec{\bar{r}}\cdot\Delta\vec{r}}}{(\lambda z)^2} \iint_{\mathcal{S}'} \bar{I}(0, \vec{\bar{r}}', \omega)\delta(\Delta\vec{r}') e^{-i\frac{k}{z}(\vec{\bar{r}}\cdot\Delta\vec{r}' + \vec{\bar{r}}'\cdot\Delta\vec{r})} d\vec{\bar{r}}' d\Delta\vec{r}' =$$

$$\boxed{\begin{gathered}\text{van Cittert-Zernike theorem} \\ = \frac{e^{i\frac{k}{z}\vec{\bar{r}}\cdot\Delta\vec{r}}}{(\lambda z)^2} \int_{\mathcal{S}'} \bar{I}(0, \vec{\bar{r}}', \omega) e^{-i\frac{k}{z}\vec{\bar{r}}'\cdot\Delta\vec{r}} d\vec{\bar{r}}'\end{gathered}} \tag{2.53}$$

This is the original result of the van Cittert-Zernike theorem but the theorem can be extended for a quasi-homogeneous source representation under Eq. 2.44. Again using the integral in Eq. 2.52 and substituting in it the expression from Eq. 2.44 I obtain:

$$G(z, \vec{\bar{r}}, \Delta\vec{r}, \omega) = \frac{e^{i\frac{k}{z}\vec{\bar{r}}\cdot\Delta\vec{r}}}{(\lambda z)^2} \iint_{\mathcal{S}'} g(0, \Delta\vec{r}', \omega)\bar{I}(0, \vec{\bar{r}}', \omega) e^{-i\frac{k}{z}(\vec{\bar{r}}\cdot\Delta\vec{r}' + \vec{\bar{r}}'\cdot\Delta\vec{r})}\, d\vec{\bar{r}}'\, d\Delta\vec{r}' =$$

$$\boxed{\begin{gathered}\text{generalised van Cittert-Zernike theorem} \\ = \frac{e^{i\frac{k}{z}\vec{\bar{r}}\cdot\Delta\vec{r}}}{(\lambda z)^2} \int_{\mathcal{S}'} g(0, \Delta\vec{r}', \omega) e^{-i\frac{k}{z}\vec{\bar{r}}\cdot\Delta\vec{r}'}\, d\Delta\vec{r}' \int_{\mathcal{S}'} \bar{I}(0, \vec{\bar{r}}', \omega) e^{-i\frac{k}{z}\vec{\bar{r}}'\cdot\Delta\vec{r}}\, d\vec{\bar{r}}'\end{gathered}} \tag{2.54}$$

2.3.6. Fourier transform of cross-spectral density

One can derive a similar dependence of the cross-spectral density in the inverse space – for angular frequencies. For this, I define the transverse domain Fourier transform for the field $\bar{E}(\vec{r}, \omega)$ as follows:

$$\hat{\bar{E}}(\vec{k}_\perp, \omega) = \iint_{-\infty}^{\infty} \bar{E}(\vec{r}, \omega) e^{i\vec{k}_\perp \cdot \vec{r}} d\vec{r}, \tag{2.55}$$

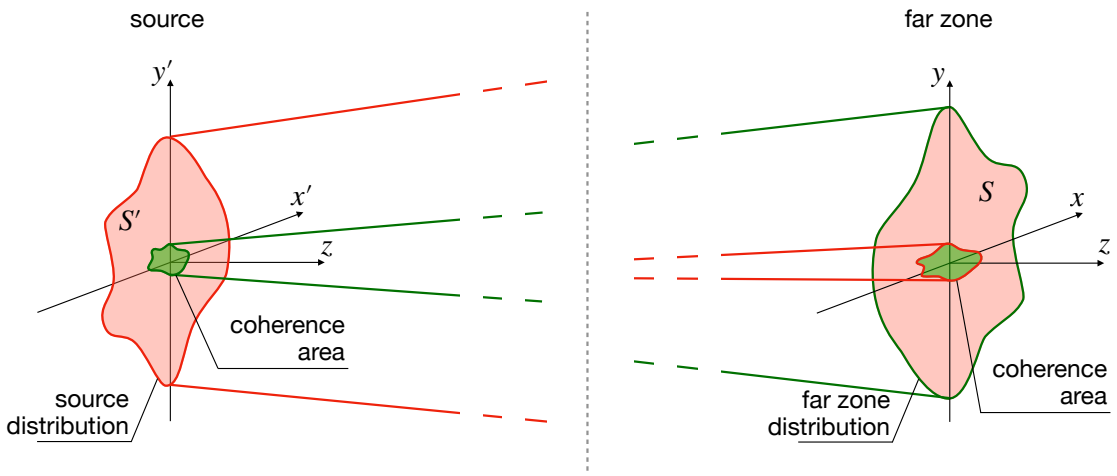

Figure 2.3: Schematic representation of the geometry used for the generalized van Cittert–Zernike theorem.

and the corresponding inverse Fourier transform:

$$\bar{E}(\vec{r},\omega) = \frac{1}{4\pi^2}\iint_{-\infty}^{\infty} \hat{E}(\vec{k}_\perp,\omega)e^{-i\vec{k}_\perp\cdot\vec{r}}d\vec{k}, \tag{2.56}$$

where I have defined the transverse component of the wave vector as $\vec{k}_\perp$. Then, by writing the cross-spectral density in the inverse space domain:

$$\begin{aligned}\hat{G}(0,\vec{k}_{\perp 1},\vec{k}_{\perp 2},\omega) &= \langle \hat{E}(0,\vec{k}_{\perp 1},\omega)\hat{E}^*(0,\vec{k}_{\perp 2},\omega)\rangle = \\ &= \iiiint_{-\infty}^{\infty} \langle \bar{E}(0,\vec{r}_1,\omega)\bar{E}^*(0,\vec{r}_2,\omega)\rangle e^{i(\vec{k}_{\perp 1}\cdot\vec{r}_1-\vec{k}_{\perp 2}\cdot\vec{r}_2)}d\vec{r}_1 d\vec{r}_2\end{aligned} \tag{2.57}$$

and as usual introducing a new set of variables $\vec{\bar{k}}_\perp = (\vec{k}_{\perp 1}+\vec{k}_{\perp 2})/2$, $\Delta\vec{k}_\perp = \vec{k}_{\perp 1}-\vec{k}_{\perp 2}$, analogous to $\vec{\bar{r}} = (\vec{r}_1+\vec{r}_2)/2$, $\Delta\vec{r} = \vec{r}_1-\vec{r}_2$, and factorising the integrals correspondingly:

$$\begin{aligned}\hat{G}(0,\vec{\bar{k}}_\perp,\Delta\vec{k}_\perp,\omega) &= \iiiint_{-\infty}^{\infty} g(0,\Delta\vec{r},\omega)\bar{I}(0,\vec{\bar{r}},\omega)e^{-i(\vec{\bar{k}}_\perp\cdot\Delta\vec{r}+\Delta\vec{k}_\perp\cdot\Delta\vec{\bar{r}})}d\vec{\bar{r}}d\Delta\vec{r} = \\ = \iint_{-\infty}^{\infty} g(0,\Delta\vec{r},\omega)e^{-i\vec{\bar{k}}_\perp\cdot\Delta\vec{r}}d\Delta\vec{r} &\iint_{-\infty}^{\infty} \bar{I}(0,\vec{\bar{r}},\omega)e^{-i\Delta\vec{k}_\perp\cdot\vec{\bar{r}}}d\vec{\bar{r}} = \hat{I}(0,\vec{\bar{k}}_\perp,\omega)\hat{g}(0,\Delta\vec{k}_\perp,\omega).\end{aligned} \tag{2.58}$$

As one can see, this result is very similar to the formulation of the van Cittert-Zernike theorem, but it is written for the cross-spectral density at the source in the inverse space domain. The clear similarity between Eq. 2.58 to Eq. 2.54 arises from the fact that the free space propagator

essentially acts as a Fourier transform, which holds true in the far-zone approximation. The only difference lies in the quadratic phase factor in Eq. 2.54.

The van Cittert-Zernike theorem in Eq. 2.53 and its generalized version in Eq. 2.54 along with the expression for the inverce space in Eq. 2.58, provide practical relations between the source distribution and the coherence spot in the far zone/inverse space, as well as between the coherence spot at the source and the radiation size in the far zone/inverse space. This leads to the intuitive understanding that large features of radiation at the source (source size distribution) transform into small features in the far zone/inverse space (coherence spot), and vice versa. Clearly, Eq. 2.58 is now a full twin in the mathematical sense of the Wiener-Khinchin theorem for quasi-stationary sources in Eq. 2.33. I will use both Eqs. 2.58 and 2.33 for shaping the field using `SERVAL`. Both relations are essential for applications to synchrotron radiation, which I will consider in the next section.

2.4. Coherence properties of synchrotron radiation

In this section, I will explore the theory of synchrotron radiation coherence, following the framework presented in [69]. This framework results in practical expressions for calculating the correlation function that are well-suited for numerical implementation. This numerical implementation resembles Monte Carlo-like methods, where the contribution from each particle is calculated separately and then summed up. This is discussed in detail in the corresponding sections of **Paper II**. Based on the theory developed in this section, I will provide the theoretical reasoning and introduce algorithms for calculating radiation using Gaussian field generators based on complex white Gaussian noise later in the chapter. First, I present an algorithm for fully incoherent radiation and demonstrate its application in **Paper I**, focusing on the image formation properties of a pinhole camera at a synchrotron facility. Then, I extend it to the case of partially coherent radiation and present the results in **Paper II**, followed by Section 2.5.4, where I consider an algorithm for generating radiation with an arbitrary Winger function distribution. Each development stage of the algorithm will be preceded by a dedicated "heuristic" section, outlining the idea behind the algorithms.

The classical textbook on statistical optics [60] provides a wave equation for radiation from a fluctuating scalar source in the following form:

$$c^2\nabla^2 E(\vec{r},t) - \frac{\partial^2 E(\vec{r},t)}{\partial t^2} = -4\pi c^2 Q(\vec{r},t). \tag{2.59}$$

It then provides an expression for propagating the radiation from the source based on the propagation law of the correlation function. This means that the correlation function at some position along the optical axis can be expressed as an integral using the correlation function of the source.

$$\Gamma_Q(\vec{r}_1,\vec{r}_2,t_1,t_2) = \langle Q(\vec{r}_1,t_1)Q^*(\vec{r}_2,t_2)\rangle. \tag{2.60}$$

This calculation is complicated by the fact that the nature of $Q(\vec{r},t)$ remains obscured. For example, to describe a thermal source, radiation must be calculated using quantum mechanics, making it unclear how to properly present the wave equation in Eq. 2.59.

Fortunately, synchrotron radiation from a relativistic electron beam is governed solely by classical electrodynamics, allowing for writing an explicit equation in the same manner as

Eq. 2.59 but accounting for the electron beam:

$$c^2\nabla^2\vec{E}(\vec{r},t) - \frac{\partial^2\vec{E}(\vec{r},t)}{\partial t^2} = -4\pi c^2\vec{\nabla}(-e)\sum_{i=1}^{N_e}\delta(\vec{r}-\vec{r}_i'(t)) + 4\pi(-e)\sum_{i=1}^{N_e}\frac{\partial(\vec{v}_i(t)\delta(\vec{r}-\vec{r}_i'(t)))}{\partial t}. \quad (2.61)$$

This equation represents a stochastic partial differential equation where the right-hand side depends on random variables, such as the coordinates and velocities of electrons within the electron beam phase space. Essentially, the initial conditions are random, representing a "snapshot" of the electron beam phase space at a given "0" time. Solving this equation in the context of stochastic partial differential equations demands substantial analytical effort, if not impossible at the current moment.

This problem can be simplified by employing the superposition principle of electrodynamics, as the equation for a single electron can easily be solved. One can obtain the final solution for the field by summing up the contributions from all electrons. In numerical simulations, this approach requires solving $N_e \times N_b$ equations for single electrons, where N_e is the number of electrons[4] and N_b is the number of statistical realizations. Nevertheless, analytically, this approach can lead to very useful and practical equations for the coherence properties of synchrotron radiation.

2.4.1. Cross-spectral density functions for synchrotron radiation

This section mainly follows the reasoning given in [69]. As it has been discussed, the field from the whole electron beam can be written as the sum of the fields from individual electrons:

$$E_b(z,\vec{r},t) = \sum_{k=1}^{N_e} E(\vec{\eta}_k,\vec{l}_k,z,\vec{r},t-t_k). \quad (2.62)$$

The electric field E here is the electric field emitted by a single electron, N_e is the number of electrons in the electrons beam. $\vec{\eta}_k, \vec{l}_k$ is an electron deflection angle and transverse offset with respect to the optical axis and t_k – arrival time of the k-th electron with respect to some reference time. These three variables are random and statistically independent. It is more practical to consider this field in the frequency domain:

$$\bar{E}_b(z,\vec{r},\omega) = \sum_{k=1}^{N_e} \bar{E}(\vec{\eta}_k,\vec{l}_k,z,\vec{r},\omega)e^{i\omega t_k}. \quad (2.63)$$

and obtaining ensemble averaged intensity from this:

$$\bar{I}_\omega(z,\vec{r},\omega) = \langle \bar{E}_b(z,\vec{r},\omega)\bar{E}_b^*(z,\vec{r},\omega)\rangle. \quad (2.64)$$

Writing the cross-spectral density function of the field $\bar{E}_b$:

$$\Gamma_\omega(z,\vec{r}_1,\vec{r}_2,\omega_1,\omega_2) = \langle \bar{E}_b(z,\vec{r}_1,\omega_1)\bar{E}_b^*(z,\vec{r}_1,\omega_2)\rangle, \quad (2.65)$$

[4]This number is actually immense; however, it can be substituted by a smaller number that represents 'macro'-electrons, as used in `SRW` and `Genesis 1.3 v2`, for example.

I notice, that Eq. 2.64 and Eq. 2.65 can be used directly for calculating the radiation intensity distribution and its coherence properties. This approach is very time- and computational resource-consuming, as it requires first calculating individual statistical realizations and then averaging these realizations over the entire statistical ensemble. I refer to this approach as the Field Addition Method (FAM), which I considered more closely in **Paper II**. However, anticipating the following narrative: *Summation of the fields of single electrons can be reduced to the summation of their intensities*.

Now, I assume that the length of the electron beam $\sigma_T c$ is much larger than the wavelength, so $\omega\sigma_T \gg 1$. This leads to the approximation that the phase in the exponent in Eq. 2.63 is distributed uniformly in the interval $(0, 2\pi)$. The case when the electron beam length is small compared to the radiation wavelength – $\omega\sigma_T \ll 1$ – refers to an effect called coherent synchrotron radiation (CSR), which I do not consider in this thesis. With these assumptions, one can show that the field $\bar{E}_b(z, \vec{r}, \omega)$ actually follows complex Gaussian random process statistics, which can be proven with the help of the central limit theorem.

Substituting Eq. 2.63 in Eq. 2.65 I obtain:

$$\Gamma_\omega(z, \vec{r}_1, \vec{r}_2, \omega_1, \omega_2) = \left\langle \sum_{m,n=1}^{N_e} \bar{E}(\vec{\eta}_m, \vec{l}_m, z, \vec{r}, \omega_1)\bar{E}^*(\vec{\eta}_n, \vec{l}_n, z, \vec{r}, \omega_2)e^{i(\omega_1 t_m - \omega_2 t_n)} \right\rangle, \tag{2.66}$$

then, I extract the sum over the same indexes and obtain:

$$\begin{aligned}\Gamma_\omega(z, \vec{r}_1, \vec{r}_2, \omega_1, \omega_2) = &\sum_{m=1}^{N_e} \langle \bar{E}(\vec{\eta}_m, \vec{l}_m, z, \vec{r}, \omega_1)\bar{E}^*(\vec{\eta}_m, \vec{l}_m, z, \vec{r}, \omega_2)e^{i(\omega_1-\omega_2)t_m}\rangle + \\ &\sum_{m\neq n} \langle \bar{E}(\vec{\eta}_m, \vec{l}_m, z, \vec{r}, \omega_1)\bar{E}^*(\vec{\eta}_n, \vec{l}_n, z, \vec{r}, \omega_2)e^{i(\omega_1 t_m - \omega_2 t_n)}\rangle.\end{aligned} \tag{2.67}$$

One may notice that the ensemble average can be written as the following:

$$\langle e^{i\omega t_k}\rangle = \int_{-\infty}^{\infty} f(t_k)e^{i\omega t_k}dt_k = \bar{f}(\omega), \tag{2.68}$$

following the definition of the ensemble averaging in Eq. 2.7. So, I rewrite Eq. 2.67 using Eq. 2.68:

$$\begin{aligned}\Gamma_\omega(z, \vec{r}_1, \vec{r}_2, \omega_1, \omega_2) = &\sum_{m=1}^{N_e} \langle \bar{E}(\vec{\eta}_m, \vec{l}_m, z, \vec{r}, \omega_1)\bar{E}^*(\vec{\eta}_m, \vec{l}_m, z, \vec{r}, \omega_2)\rangle \bar{f}(\omega_1 - \omega_2) + \\ &\sum_{m\neq n}^{N_e} \langle \bar{E}(\vec{\eta}_m, \vec{l}_m, z, \vec{r}, \omega_1)\bar{E}^*(\vec{\eta}_n, \vec{l}_n, z, \vec{r}, \omega_2)\rangle \bar{f}(\omega_1)\bar{f}(-\omega_2).\end{aligned} \tag{2.69}$$

The second term corresponds to cross-correlation of radiation from different electrons. As I assumed that the electron beam length is long compared to the radiation wavelength, this means that the width of $\bar{f}(\omega)$ is much smaller than the radiation bandwidth and the product $\bar{f}(\omega_1)\bar{f}(-\omega_2)$ rapidly goes zero for the frequencies larger than the spectral coherence length.

So, I can neglect this term and obtain:

$$\Gamma_\omega(z,\vec{r}_1,\vec{r}_2,\omega_1,\omega_2) = \sum_{m=1}^{N_e}\langle\bar{E}(\vec{\eta}_m,\vec{l}_m,z,\vec{r},\omega_1)\bar{E}^*(\vec{\eta}_m,\vec{l}_m,z,\vec{r},\omega_2)\rangle\bar{f}(\omega_1-\omega_2). \tag{2.70}$$

To express the equation more concisely, I note that the ensemble-averaged quantity does not depend on a particular electron, thus I write:

$$\Gamma_\omega(z,\vec{r}_1,\vec{r}_2,\omega_1,\omega_2) = N_e\bar{f}(\omega_1-\omega_2)\langle\bar{E}(\vec{\eta},\vec{l},z,\vec{r},\omega_1)\bar{E}^*(\vec{\eta},\vec{l},z,\vec{r},\omega_2)\rangle. \tag{2.71}$$

Also, following the ensemble averaging definition, I can express it as a double integral:

$$\Gamma_\omega(z,\vec{r}_1,\vec{r}_2,\omega_1,\omega_2) = N_e\bar{f}(\omega_1-\omega_2)\iint_{-\infty}^{\infty} f_l(\vec{l})f_\eta(\vec{\eta})\bar{E}(\vec{\eta},\vec{l},z,\vec{r},\omega_1)\bar{E}^*(\vec{\eta},\vec{l},z,\vec{r},\omega_2)d\vec{l}d\vec{\eta}. \tag{2.72}$$

or explicitly as a sum according for the alternative definition of ensemble averaging:

$$\Gamma_\omega(z,\vec{r}_1,\vec{r}_2,\omega_1,\omega_2) = N_e\bar{f}(\omega_1-\omega_2)\sum_{k=1}^{N}\bar{E}(\vec{\eta}_k,\vec{l}_k,z,\vec{r},\omega_1)\bar{E}^*(\vec{\eta}_k,\vec{l}_k,z,\vec{r},\omega_2), \tag{2.73}$$

where N is an integer and sufficiently large. As one can see here, the radiation from different electrons is correlated only with itself. This is a consequence of dropping the term with $\bar{f}(\omega_1)\bar{f}(-\omega_2)$. Thus, the calculation of $\Gamma_\omega(z,\vec{r}_1,\vec{r}_2,\omega_1,\omega_2)$ requires knowledge of the electron beam phase space distribution $f_l(\vec{l})f_\eta(\vec{\eta})$ and the radiation from a single electron, $\bar{E}(\vec{\eta},\vec{l},z,\vec{r},\omega)$, accounting for an arbitrary tilt and shift of the electron.

In the last equation, the variation of $\bar{E}$ with respect to ω is slow enough on the scale of $\bar{f}$, so ω_1 can be used in $\bar{E}^*(\vec{\eta},\vec{l},z,\vec{r},\omega_1)$ instead of ω_2. To justify this, one should look at the width scales: the width of $\bar{f}$ is proportional to $1/\sigma_T$, and the undulator resonance width amounts to ω_r/N_w, where ω_r is the resonance frequency. Considering a real-case example for X-rays, the wavelength is 0.1 nm, the number of undulator periods $N_w = 10^2$, and the duration of the electron beam $\sigma_T = 5$ ps, as in the PETRA IV conceptual design report [19]. Here, $\omega_r/N_w \sim 2\times10^{17}$, and $1/\sigma_T \sim 2\times10^{11}$, so $\omega_r/N_w \gg 1/\sigma_T$. As a result, the following expression for the correlation function in the frequency domain is obtained:

$$\Gamma_\omega(z,\vec{r}_1,\vec{r}_2,\omega_1,\omega_2) = N_e\bar{f}(\omega_1-\omega_2)G(z,\vec{r}_1,\vec{r}_2,\omega_1), \tag{2.74}$$

where $G(z,\vec{r}_1,\vec{r}_2,\omega)$:

$$G(z,\vec{r}_1,\vec{r}_2,\omega) = \langle\bar{E}(\vec{\eta},\vec{l},z,\vec{r}_1,\omega)\bar{E}^*(\vec{\eta},\vec{l},z,\vec{r}_2,\omega)\rangle, \tag{2.75}$$

and one can result in the expression for the intensity distribution:

$$\bar{I}_\omega(z,\vec{r},\omega) = \langle|\bar{E}(\vec{\eta},\vec{l},z,\vec{r},\omega)|^2\rangle. \tag{2.76}$$

Both Eqs. 2.75 and 2.76 can be used for numerically efficient calculations of synchrotron radiation. This requires calculating N fields from single electrons and then averaging over them. As one can see, for calculating the intensity distribution $\bar{I}_\omega(z,\vec{r},\omega)$ in Eq. 2.76, *one*

needs to sum up intensities and not the fields as in Eq. 2.64, which saves a lot of computational resources. This method of summing intensities, which I refer to in this thesis as the Intensity Addition Method (IAM), was first implemented in `SRW`. I considered the difference between the approach of summing up fields (FAM) vs. intensities (IAM) more closely in **Paper II**.

It is worth mentioning that the coherence features in the spatial and frequency domains are now factorized, which is in accordance with the theory presented in Section 2.2. To develop this observation further, usually, synchrotron radiation is seen through an monochromator with a transfer function $T(\omega)$, so one needs to rewrite Eq. 2.74:

$$\Gamma_\omega(z,\vec{r}_1,\vec{r}_2,\omega_1,\omega_2) = N_e\bar{f}(\omega_1-\omega_2)G(z,\vec{r}_1,\vec{r}_2,\omega_1)T(\omega_1)T^*(\omega_2) \tag{2.77}$$

I notice here that in this expression, spatial and frequency coherence features are separated. In the next section, I will show that the relationship between the frequency and time domains correlation functions follows a similar relation as the generalized Wiener–Khinchin theorem in Eq. 2.33.

2.4.2. Consistency of quasi-stationary approximation and Wiener–Khinchin theorem for synchrotron radiation

To show that Eq. 2.77 describes a source with the same properties as the one under Eq. 2.33, one needs to perform a Fourier transform to the time domain:

$$\Gamma_t(z,\vec{r}_1,\vec{r}_2,t_1,t_2) = \frac{1}{(2\pi)^2}\iint_{-\infty}^{\infty}\Gamma_\omega(z,\vec{r}_1,\vec{r}_2,\omega_1,\omega_2)e^{-i\omega_1 t_1}e^{i\omega_2 t_2}d\omega_1 d\omega_2 =$$

$$\frac{N_e}{(2\pi)^2}\iint_{-\infty}^{\infty}\bar{f}(\omega_1-\omega_2)G(z,\vec{r}_1,\vec{r}_2,\omega_1)T(\omega_1)T^*(\omega_2)e^{-i\omega_1 t_1}e^{i\omega_2 t_2}d\omega_1 d\omega_2 \tag{2.78}$$

This radiation is seen through a monochromator that has the bandwidth $\Delta\omega_m$ around the frequency ω_0. In the case when the monochromator bandwidth $\Delta\omega_m$ is much larger than the typical scale of the width of $\bar{f}$, $\Delta\omega_m \gg 1/\sigma_T$, I can conclude that T does not vary much on the scale of $\bar{f}$, and then I can write that $T(\omega_1)T(\omega_2) = |T(\bar{\omega})|^2$, which leads me to the following expression:

$$\Gamma_t(z,\vec{r}_1,\vec{r}_2,t_1,t_2) = \frac{N_e}{(2\pi)^2}\int_{-\infty}^{\infty}\bar{f}(\Delta\omega)e^{-i\Delta\omega\bar{t}}d\Delta\omega\int_{-\infty}^{\infty}G(z,\vec{r}_1,\vec{r}_2,\bar{\omega})|T(\bar{\omega})|^2e^{i\bar{\omega}\Delta t}d\bar{\omega} =$$

$$g_t(\vec{r}_1,\vec{r}_2,\Delta t)f(\bar{t}). \tag{2.79}$$

In this expression, I separated two integrals. One can see that this result is a recurrence of the generalized Wiener-Khinchin theorem from Eq. 2.33 but written here in the inverse form.

2.4.3. Quasi-homogeneity approximation for synchrotron radiation

As one can see, synchrotron radiation behaves as a quasi-stationary source in many practical cases, especially in the X-ray range. To describe radiation transverse coherence properties,

one writes the cross-spectral density function in the standard form used in statistical optics, $G(z, \vec{r}_1, \vec{r}_2, \bar{\omega})$. Recalling the definition of quasi-homogeneity from Eq. 2.43, i.e. $G(0, \vec{r}_1, \vec{r}_2, \omega) = g(0, \Delta\vec{r}, \omega)\bar{I}(0, \vec{\bar{r}}, \omega)$, it is reasonable to assume that synchrotron radiation follows this definition. In other words, the width of $g(0, \Delta\vec{r}, \omega)$ remains constant across the radiation intensity distribution. A proof for this can be found in the previously cited paper [70] for third-generation light sources. However, in the general case, one can rely on the following qualitative reasoning.

The dimension of the radiation coherence spot at the source is determined by the diffraction-limited source size from a single electron. To observe varying radiation coherence spots across the source intensity distribution, electrons at different positions would need to have different diffraction sizes. This can only occur in the following scenarios: if the electron beam energy varies significantly transversely and/or longitudinally, if the magnetic field of an undulator is nonuniform at the scale of the electron beam dimensions, or if there is an angular tilt of the electron beam while Courant–Snyder parameters vary along the electron beam[5]. Typically, the electron beam at a synchrotron radiation source is adjusted in such a way that these sophisticated effects are largely suppressed. Therefore, with a reasonable degree of confidence, one can conclude that $g(0, \Delta\vec{r}, \omega)$ does not vary significantly across the radiation intensity distribution at the source location. However, electron beams at linear accelerators may undergo these sophisticated effects and result in a non-homogeneous distribution of the cross-spectral density function, which should be studied in future works.

2.5. SERVAL: stochastic emission rapid evaluator

Quasi-homogeneity and quasi-stationarity approximations, coupled with the Gaussian statistics of synchrotron radiation, provide highly useful prerequisites for modelling this radiation. It is possible to generate a single statistical realisation of the process by utilising only a priori knowledge of correlation functions and intensities. In this section, I will present novel, numerically efficient algorithms, which I refer to as `SERVAL` algorithms, for simulating partially coherent fields. These algorithms build upon previously developed theory but utilise conceptually different principles compared to conventional Monte Carlo-like approaches or mode decomposition methods. A statistical realisation of a field is shaped by starting from a complex white Gaussian noise distribution, which is then constrained by appropriate mathematical supports in the direct and/or reciprocal domains.

I subsequently present `SERVAL` algorithms, each illustrated by a corresponding **Paper**: **I**, **II** and in Section 2.5.4. The description of the algorithms is preceded by heuristic considerations, developed to show the consistency of the constructed fields' intensity and cross-spectral density function distributions with the real fields. In the corresponding papers, I illustrate the application of the algorithms to use cases: bending magnet radiation, undulator radiation, and SASE FEL, accompanied by more detailed explanations and additional cross-checks. This chapter is concluded by **Paper III** in which I present an experimental result for obtaining subfemtosecond pulses at the SASE3 beamline of the European XFEL using a method we referred to as attoseconds-at-harmonics. This experiment was replicated numerically

[5] As an example of the last case: if the larger "head" of the electron beam shines to the left and a finer "tail" to the right, then in the far zone one expects to observe different widths of spikes across the intensity distribution. This potential scenario may occur at linear accelerator-based facilities.

with `Genesis 1.3 v.2` code. The paper is the showcase of the `SERVAL` application limits, as the statistics of resulting pulses is non-Gaussian due to non-linear transformation of attoseconds-at-harmonics process.

2.5.1. Heuristic approach I: homogeneous/stationary sources. Paper I.

Although the first `SERVAL` algorithm was initially developed for quasi-homogeneous/quasi-stationary sources, introducing it first for an incoherent source allows me to demonstrate its different use cases and versatility. A fully incoherent source has an intensity distribution $\bar{I}(\vec{r},\omega)$ at frequency component ω and a correlation function at the source that is expressed by the Dirac delta function $\delta(\vec{r}_2-\vec{r}_1)$. Naively reasoning, one might assume that a single statistical realisation of radiation at the source location can be expressed as complex Gaussian white noise $\mathcal{N}(\vec{r})$, which is then multiplied by the square root of the source intensity distribution $\bar{I}(\vec{r},\omega)$. I denote the polarisation component of this modelled field as $\bar{\phi}(\vec{r},\omega)$ and write the expression for the field:

$$\bar{\phi}(\vec{r},\omega)=\sqrt{\bar{I}(\vec{r},\omega)}\mathcal{N}(\vec{r}), \tag{2.80}$$

where the real and imaginary component of the noise $\mathcal{N}(\vec{r})$ have the zero mean and the variance of unity, the same as in Fig. 2.1, and follows the main property: $\langle\mathcal{N}(\vec{r}_1)\mathcal{N}^*(\vec{r}_2)\rangle=\delta(\vec{r}_2-\vec{r}_1)$. Then, upon the ensemble averaging Eq. 2.80, it is easy to find that:

$$\langle\bar{\phi}(\vec{r},\omega)\bar{\phi}^*(\vec{r},\omega)\rangle=\bar{I}(\vec{r},\omega), \tag{2.81}$$

showing that the statistical average returns the expected intensity distribution of the real source. Moreover, by calculating the correlation of $\bar{\phi}(\vec{r},\omega)$, I find that:

$$G_{\bar{\phi}}(\vec{r}_1,\vec{r}_2,\omega)=\langle\bar{\phi}(\vec{r}_1)\bar{\phi}^*(\vec{r}_2)\rangle=\sqrt{\bar{I}(\vec{r}_1,\omega)\bar{I}(\vec{r}_2,\omega)}\delta(\vec{r}_2-\vec{r}_1), \tag{2.82}$$

and if I normalise this quantity:

$$g_{\bar{\phi}}(\vec{r}_1,\vec{r}_2,\omega)=\frac{G_{\bar{\phi}}(\vec{r}_1,\vec{r}_2,\omega)}{\sqrt{\bar{I}(\vec{r}_1,\omega)\bar{I}(\vec{r}_2,\omega)}}=\delta(\vec{r}_2-\vec{r}_1), \tag{2.83}$$

I find that the correlation function for the constructed field $\bar{\phi}$ corresponds to the correlation function of a fully incoherent source, a result one would expect from the form of Eq. 2.80.

It is also not surprising that the field $\bar{\phi}$ naturally reproduces the van Cittert-Zernike theorem. I perform the Fourier transform of $\bar{\phi}$ to the inverse space:

$$\hat{\bar{\phi}}(\vec{k},\omega)=\int_{-\infty}^{\infty}\sqrt{\bar{I}(\vec{r},\omega)}\mathcal{N}(\vec{r})e^{i\vec{r}\vec{k}}d\vec{r}, \tag{2.84}$$

then by auto-correlating this field, I obtains:

$$\begin{aligned}\langle\hat{\bar{\phi}}(\vec{k}_1,\omega)\hat{\bar{\phi}}^*(\vec{k}_2,\omega)\rangle&=\left\langle\iint_{-\infty}^{\infty}\sqrt{\bar{I}(\vec{r}_1,\omega)\bar{I}(\vec{r}_2,\omega)}\mathcal{N}(\vec{r}_1)\mathcal{N}^*(\vec{r}_2)e^{i(\vec{r}_1\vec{k}_1-\vec{r}_2\vec{k}_2)}d\vec{r}_1d\vec{r}_2\right\rangle=\\&=\iint_{-\infty}^{\infty}\sqrt{\bar{I}(\vec{r}_1,\omega)\bar{I}(\vec{r}_2,\omega)}\delta(\vec{r}_1-\vec{r}_2)e^{i(\vec{r}_1\vec{k}_1-\vec{r}_2\vec{k}_2)}d\vec{r}_1d\vec{r}_2=\int_{-\infty}^{\infty}\bar{I}(\vec{r}',\omega)e^{i\vec{r}'(\vec{k}_1-\vec{k}_2)}d\vec{r}'.\end{aligned} \tag{2.85}$$

As mentioned, the field shaped in Eq. 2.80 describes a fully incoherent source. As seen from Eq. 2.83, this type of a source radiates in all directions: the smallest feature of the source is its correlation function, $\delta(\vec{r}_2 - \vec{r}_1)$, which transforms in the far field into an unbounded distribution with a fine, spiky structure, whose typical width is determined by the spatial Fourier transform of the source intensity distribution.

One can implement Eq. 2.80 in a highly numerically efficient computational algorithm for simulating the field from fully incoherent sources. This requires only the generation the samples of complex Gaussian white noise and one multiplication operation by the square root of the source intensity distribution. The field is then ready for further propagation operations.

It is worth noting that the field in Eq. 2.80 is represented at the source position; one can invert the variables and simulate the source as seen from the observation position for numerical convenience. The field intensity should then be expressed in angular size as seen from the observation position and simulated in inverse space, with real space corresponding to the observation position, e.g., at the entrance to an optical system. Since every optical system has a finite size, this method of simulation is practical, as the numerical grid in real space can be adjusted to match the size of the entrance aperture. This approach avoids the need to numerically propagate the field from the source position to the entrance of the optical system, which is virtually impossible to achieve numerically, as the field seen from the source is unbounded in inverse space.

Thomas Young's experiment

Having this, I present here a numerical replication of the original Young's experiment, as reported in the Bakerian Lecture read on November 24, 1803 [71] (*Exper. 1.*). Here I provide the quote from the lecture to describe his experimental setup:

> *"I made a small hole in a window-shutter, and covered it with a piece of thick paper, which I perforated with a fine needle. For greater convenience of observation, I placed a small looking glass without the window-shutter, in such a position as to reflect the sun's light, in a direction nearly horizontal, upon the opposite wall, and to cause the cone of diverging light to pass over a table, on which were several little screens of card-paper. I brought into the sunbeam a slip of card, about one-thirtieth of an inch in breadth, and observed its shadow, either on the wall, or on other cards held at different distances. Besides the fringes of colours on each side of the shadow, the shadow itself was divided by similar parallel fringes, of smaller dimensions, differing in number, according to the distance at which the shadow was observed, but leaving the middle of the shadow always white."*

As I mentioned in the previous section, I simulate solar radiation as it is seen from observation position – Earth. I depict a single monochromatic realisation of the angular size of the Sun and the corresponding fluctuating distribution of the field in Fig. 2.4. A semi-transparent mask in the right subfigure of Fig. 2.4 represents the portion of radiation that did not pass through a paper sheet with a hole made by a fine needle. As one can see, this aperture was used to extract the coherent portion of radiation.

To simulate the original experiment, I divided the visible spectrum into ten colours. Then, I simulated the free space propagation of each colour from the perforated sheet, their

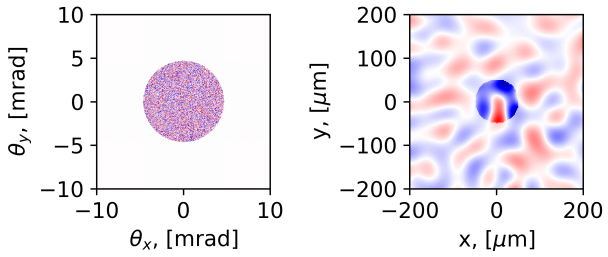

Figure 2.4: (a) Sun intensity distribution at a given wavelength (500 nm) as seen from Earth. (b) Visible solar radiation distribution at the observation position. The hole made by a needle (100 μm) is represented as a mask over the subplot in (b) to illustrate the setup of Young's experiment.

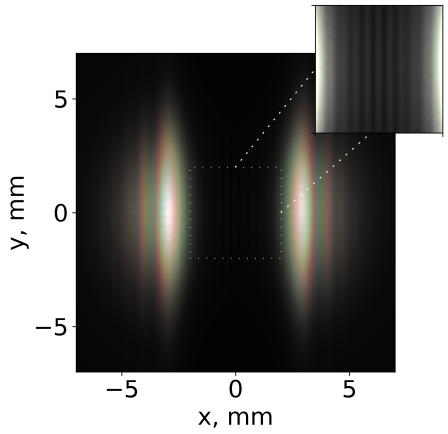

Figure 2.5: Result of Young's original interference experiment using a slip of card. Color fringes and the shadow cast by the obstacle are visible, separated by white parallel lines (highlighted in the callout). To enhance visibility, the callout colormap has been adjusted to be ten times more sensitive than in the main image.

diffraction on a "one-thirtieth-inch" obstacle, and the final free space propagation down to the observation screen. I assumed that the distance from the paper sheet to the obstacle (a slip of card) is 0.2 m, and from the obstacle to the screen is 1 m. A numerical replica of this experiment is shown in Fig. 2.5. In this image, I converted the resulting intensities into a red-green-blue representation and adjusted its colour appearance in a graphics editor (white balance corrections, slight contrast adjustments, and saturation enhancement) to realistically represent what the human eye would see.

This experiment differs significantly from the typical Young's double-slit experiment presented in university optics courses, where strict monochromaticity and a plane wavefront of radiation are assumed. This simulation demonstrates the flexibility of the proposed numerical approach for simulating radiation from a fully incoherent source. I present two additional demonstrations. The first, shown in Appendix E, visually illustrates the "spikes" of Sirius radiation overlaid with the image of the stellar interferometer [72]. The second use case for the algorithm is presented in the following paper.

Paper I

In the **Paper I**: A. Trebushinin, G. Geloni, S. Serkez, R. Khubbutdinov, and E. Saldin, 'Pinhole camera for electron beam size diagnostic at storage ring with an ultralow emittance', Phys. Rev. Accel. Beams, vol. 27, no. 3, p. 032802, Mar. 2024, doi: 10.1103/PhysRevAccelBeams.27.032802, my co-authors and I used the proposed algorithm to simulate a pinhole camera system for measuring ultra-small electron beam transverse sizes at synchrotron radiation facilities using bending magnet radiation at high photon energies, specifically 200–300 keV. We determined that this radiation can be approximated as fully incoherent, allowing us to apply the proposed algorithm. We demonstrated the image formation properties of a pinhole camera on a shot-to-shot basis and verified its point spread function. The results obtained in **Paper I** showcase one of the possible applications of the proposed algorithm for calculating optical systems.

Pinhole camera for electron beam size diagnostic at storage ring with an ultralow emittance

Andrei Trebushinin,* Gianluca Geloni, and Svitozar Serkez
European XFEL, 4, Holzkoppel Street, 22869 Schenefeld, Germany

Ruslan Khubbutdinov and Evgeny Saldin
Deutsches Elektronen-Synchrotron, Notkestraße 85, 22607 Hamburg, Germany

(Received 27 December 2023; accepted 22 February 2024; published 8 March 2024)

In this work, we propose to use a pinhole camera at high photon energies, specifically 200–300 keV, to measure ultra-small electron beam size by means of bending magnet radiation. We show that there is a sufficient photon flux at the detector position. Our theoretical analysis includes an examination of the applicability of the van Cittert-Zernike theorem for the bending magnet radiation generated by an ultralow emittance electron beam and a detailed analysis of the imaging properties of rectangular pinhole cameras. This led us to practical, universal formulas. We identify the optimal aperture size and resolution of the camera in the given geometry. The theoretical findings are further substantiated by wavefront propagation numerical simulations of partially coherent radiation. This study serves both as a practical guide for optical engineering and an educational resource for explaining the imaging properties of pinhole cameras.

DOI: 10.1103/PhysRevAccelBeams.27.032802

I. INTRODUCTION

Advancements in the magnetic lattice design for storage rings [1], along with the rapid design and construction of next-generation synchrotron radiation (SR) light sources [2,3], and cited within [4], have significantly reduced the transverse electron beam size with respect to third-generation light sources. This leads to a clear benefit in terms of (spectral) brightness and coherence properties [5,6] for users' applications [7,8] but imposes tight requirements on electron beam diagnostic techniques based on synchrotron radiation, in particular, those that utilize pinhole cameras.

The imaging properties of pinhole cameras have been known since ancient times and are now routinely used to visualize the objects at different wavelengths. In the case of x rays, they have served as robust and effective tools for electron beam size measurements throughout the development years of SR sources, with recent applications [9–11]; a review table can be found in [12], numerical analyses of the spatial resolution of x-ray pinholes were conducted in [9,11] with SRW code [13,14] and with comparisons to measurements presented in [15]. Incoherent imaging of objects as small as the transverse size of the electron beam in the modern diffraction-limited storage rings (with low emittance on the order of 20 pm rad) requires the use of shorter wavelengths compared to previously proposed setups to achieve sufficient resolution. The reason being the width of the point-spread function is proportional to the square root of the radiation wavelength [16], Eq. 319.

Incoherent imaging enables the direct measurement of the source size distribution without being influenced by the radiation distribution from a single electron emitter. In the case presented here, the setups necessitate the installation of a dedicated radiation source, for example, a three-pole magnetic chicane with a high magnetic field. In contrast, techniques that rely on the partially coherent properties of radiation, wherein the correlation function retains information about the electron beam size, usually do not require the installation of a separate radiation source. However, data interpretation and the retrieval of electron beam size may be more complex. An overview of SR-based diagnostics for measuring the transverse size of the electron beam can be found in [12,17]. Furthermore, there exist more subtle techniques that leverage both imaging and partially coherent properties of radiation to determine the electron beam size, as demonstrated in [18,19].

In this paper, we propose a pinhole camera setup using higher than usual photon energies, up to 200–300 keV, generated by a central magnet of a magnetic chicane, so it can be considered as the bending magnet radiation. Our research focuses on optimizing the resolution capabilities of this setup. For this, we studied the imaging characteristics of a rectangular pinhole camera with wave optics

*andrei.trebushinin@xfel.eu

approaches based on [16]. This study is augmented by examining the applicability of the van Cittert-Zernike theorem in the case of bending magnet radiation. As a result, we present analytical design formulas and an expression for the point spread function of a rectangular pinhole camera and compare these results with numerical simulations. We validate these theoretical derivations with wavefront propagation simulations in the OCELOT toolkit [20,21] using the Gaussian random fields approach [22] for simulating partially coherent radiation. We conclude our paper with the calculation of photon flux to demonstrate that it is sufficient for electron beam diagnostics purposes.

II. THEORY

In this section, we first provide proof of the applicability of the van Cittert-Zernike theorem within the parameter space of our problem, with a quantitative estimation presented in Sec. II A. Then we outline the requirements for an aperture to function as a pinhole and to form an image. We conclude this discussion by presenting calculations for the optimal parameters of a pinhole camera to achieve the best possible resolution. Our findings include simple design formulas and universal plots that can be employed in the optical engineering of pinhole cameras. These results are further supplemented by wavefront propagation simulations of pinhole optics.

A. Applicability of the van Cittert-Zernike theorem

Let us consider the applicability of the van Cittert-Zernike theorem to bending magnet radiation at a frequency much higher than its critical frequency. The theorem connects the radiation distribution of the source with the coherence properties in the far zone. It can be stated as follows: The modulus of the spectral degree of coherence between two points in the far field of an incoherent source is equivalent to the two-dimensional Fourier transform of the source intensity distribution. The validity of this theorem forms the basis for applying incoherent imaging theory in the case of a pinhole camera.

Within statistical optics, SR is described as a Gaussian random process. An important consequence of this is that the higher-order correlation functions of the process can be expressed in terms of the first-order correlation function (G) with the help of the moment theorem. As a result, knowing the second-order correlation function in the space-frequency domain is all one needs to completely characterize the signal from a statistical viewpoint.

The following definition holds:

$$G(\vec{r}_1, \vec{r}_2, \omega_1, \omega_2) = \langle E(\vec{r}_1, \omega_1) E^*(\vec{r}_2, \omega_2) \rangle, \tag{1}$$

where brackets indicate ensemble averaging, E is the electric field (considered as a scalar, i.e., limiting ourselves to a given polarization component), $\vec{r}$ is the transverse coordinate, and ω is the radiation frequency. By ensemble averaging in the case of SR, we mean averaging of radiation samples from different electron bunches that are considered to share the same phase-space distribution.

Since SR radiation constitutes an ensemble of pulses of finite duration, it is an intrinsically nonstationary statistical process. However, in most practical cases, the electron beam defines the duration of the radiation pulses (σ_t), which is the order of several picoseconds (corresponding to a few millimeters length), while the coherence time is related to the formation length of the radiation (L_f). For example, for bending magnet radiation at the critical wavelength $\lambda\!\!\!^{-}_c$, coherence time is given simply by $(\tau_c \approx L_f(1 - v/c) \sim \lambda\!\!\!^{-}_c/c)$, where $\gamma = 1/\sqrt{1 - v^2/c^2}$ is the Lorentz factor. It is evident that for x-ray sources, $\tau_c \ll \sigma_t$, resulting in a very large number of spikes, classifying this type of source as quasistationary and granting applicability of the Wiener–Khinchin theorem. In this case, $\langle E(\vec{r}, \omega) \rangle$ varies negligibly at the spike width scale $\sim 1/\sigma_t$. Hence, we can simplify the correlation function to

$$G(\vec{r}_1, \vec{r}_2, \omega) = \langle E(\vec{r}_1, \omega) E^*(\vec{r}_2, \omega) \rangle. \tag{2}$$

This function is known as cross-spectral density.

Before continuing, we introduce the notion of spectral degree of coherence $g(\vec{r}_1, \vec{r}_2)$, as

$$g(\vec{r}_1, \vec{r}_2) = \frac{G(\vec{r}_1, \vec{r}_2)}{[G(\vec{r}_1, \vec{r}_1) G(\vec{r}_2, \vec{r}_2)]^{1/2}}, \tag{3}$$

where, for the notation simplicity, we omitted the dependence on ω. The function $g(\vec{r}_1, \vec{r}_2)$ is normalized to unity by definition.

The concept of quasistationarity in the time domain is the temporal analogy of quasihomogeneity in the spatial domain. A quasihomogeneous source obeys the assumption that $\langle |E(\vec{r})|^2 \rangle$ varies slowly on the scale of the transverse coherence length, which is the effective width of the spectral degree of coherence $g(\Delta\vec{r})$. Because of this, for quasihomogeneous sources, the following approximation holds

$$G(\vec{r}, \Delta\vec{r}) = I(\vec{r}) g(\Delta\vec{r}), \tag{4}$$

where now $I(\vec{r})$ is proportional to the radiation intensity distribution at the source and where $\Delta\vec{r} = \vec{r}_2 - \vec{r}_2$.

A significant special case follows from Eq. (4) when $g(\Delta\vec{r})$ has a spatial width comparable to the radiation wavelength. In practical calculations, it is possible to approximate $g(\Delta\vec{r})$ with a two-dimensional Dirac delta function $\delta(\Delta\vec{r})$ even when the optical system has much poorer resolution than the wavelength [23]. Thus the expression for the cross-spectral density can be approximated by

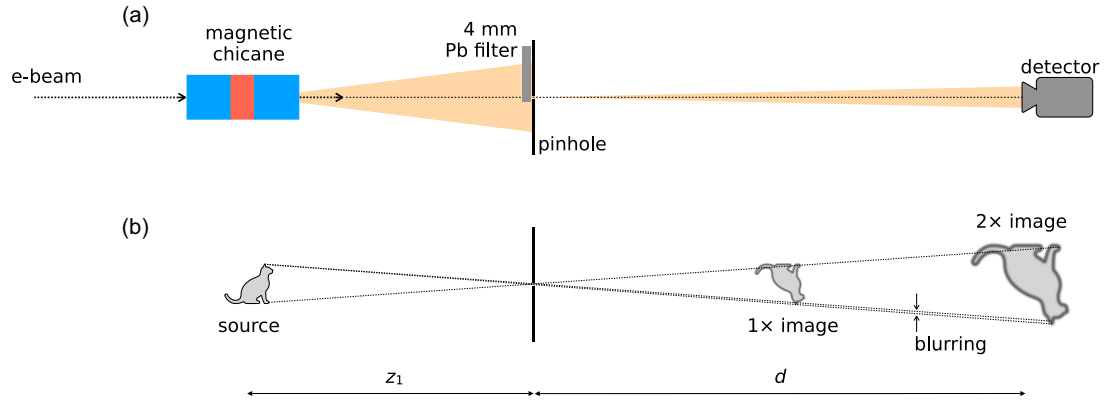

FIG. 1. Pinhole camera imaging setup: (a) outline of the proposed setup and (b) a visual explanation of the imaging properties of a pinhole in the ray-tracing approximation. Image blurring represents the actual blurring.

$$G(\vec{r}, \Delta\vec{r}) = I(\vec{r})\delta(\Delta\vec{r}), \tag{5}$$

This kind of source is transversely incoherent. Both types of sources: Eqs. (4) and (5) follow the van Cittert-Zernike theorem. The original theorem was formulated for incoherent sources in [24,25], followed by the generalized version that was presented in [26,27].

Here we provide a quantitative estimate of the applicability of the theorem in the case of bending magnet radiation. We can always express the diffraction-limited size and the divergence of the radiation through SR formation length (L_f) as $\sigma_{r'} \sim \sqrt{\lambda/L_f}$ and $\sigma_r \sim \sqrt{\lambda L_f}$. This always guarantees that

$$\sigma_r \sigma_{r'} \sim \lambda. \tag{6}$$

In our case of small wavelengths, we consider the asymptotic limit with a large $y = \lambda_{\mathrm{ph}_c}/\lambda_{\mathrm{ph}}$ and obtain $\sigma_{r'} \sim 1/(\sqrt{y}\gamma)$, where $\lambda_{\mathrm{ph}_c} \sim R/\gamma^3$ [28]. Using the relation in Eq. (6), we obtain that $L_f \sim R/\gamma$. Substituting this into the expression for the diffraction-limited radiation size results in $\sigma_r \sim R/(\sqrt{y}\gamma^2)$. To estimate the beam size, we use $R \approx 10$ m, $y \approx 10$, and $\gamma = 12000$. This yields $\sigma_r \sim 20$ nm. We see that this size is much smaller than the size of the electron beam, and thus we are in the quasihomogeneous asymptotic regime and can safely apply the van Cittert-Zernike theorem.

B. Rectangular pinhole camera

In the following analysis, we consider the behavior of x-ray pulses impinging on a rectangular pinhole, although our results are applicable to any wavelength. Upon applying similarity techniques, only one dimensionless parameter determines the characteristics of the pinhole camera: the Fresnel number.

First, we define a pinhole camera as an optical element that is typically associated with the following requirements: (i) The pinhole must be situated in the far zone from the source. This condition is necessary for relating the cross-spectral density function of the imaged object in the far zone to the source's intensity distribution. This requirement stems from the van Cittert-Zernike theorem. (ii) The pinhole size must be larger than the radiation coherence length, ensuring the aperture does not alter the cross-spectral density function. (iii) The source size must be larger than the aperture size to achieve adequate resolution.

These three conditions are general requirements for an aperture to function as a pinhole and to form an image of the source. We present the outline of the pinhole imaging setup in Fig. 1. In Figs. 2 and 3, we present snapshots of the radiation as seen from a perfect monochromator at a specific frequency ω. This representation remains general because, in the frequency domain, different spikes in the spectrum are statistically independent and can be analyzed separately.

After propagating to the far zone, the radiation from the source undergoes spatial filtering by the pinhole. The pinhole ensures that the coherence properties of the

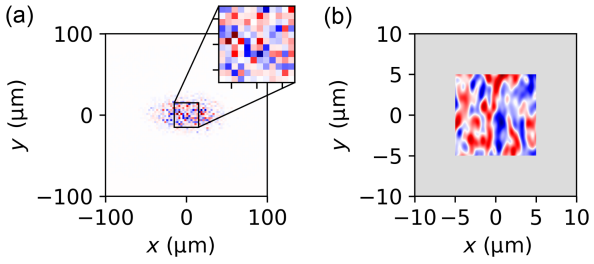

FIG. 2. (a) A single statistical realization of the monochromatized radiation field at the source, characterized by a Gaussian distribution with a standard deviation of the transverse size of 20×10 μm^2. This realization includes a noise structure that models the source's incoherence. (b) A single statistical realization after propagation through a 10×10 μm^2 aperture. In these images, false colors represented by red and blue indicate the positive and negative amplitudes of the slowly varying envelope of the electric field.

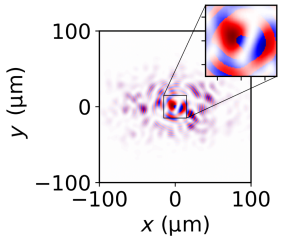

FIG. 3. A single shot image taken after the pinhole in the far zone. The spiky structure indicates the acquired coherence of the radiation that occurred upon free space propagation. Note quadratic phase front curvature, visible as rings of alternating false color.

radiation are preserved while it significantly alters the spatial frequency distribution (k_x, k_y), or equivalently, the angular distribution. This effectively creates a secondary source, preserving the coherence length in the far zone along with all information about the source size. Consequently, an image of the source forms in the far zone beyond the pinhole. In the following section, we will detail the optimal parameters for the pinhole camera and elaborate on the first and second conditions previously discussed.

C. Optimal parameters for a rectangular pinhole

We observe that the pinhole point spread function can be factorized and may be presented as multiplication of two one-dimensional line spread functions for each direction: $l_{\mathrm{ps}} = l_{\mathrm{ps}_x} \cdot l_{\mathrm{ps}_y}$, where line spread functions are written as [16], Eq. 313

$$l_{\mathrm{ps}_{x,y}}(\Omega, y') = \int_{-1}^{1} \mathrm{d}\xi \frac{\sin\left[2(\xi\Omega + y'\sqrt{\Omega})(1-|\xi|)\right]}{\xi\Omega + y'\sqrt{\Omega}}, \quad (7)$$

where ξ is the transverse coordinate normalized by the aperture size. The point spread function is determined solely by the dimensionless parameter $\Omega = a^2/(\lambda\!\!\!^{-} z_{\mathrm{eff}})$, where $z_{\mathrm{eff}} = z_1 d/(z_1 + d)$, z_1 is the distance from the source to the pinhole, d is the distance from the pinhole to the image plane, and a is the half-width of the aperture.

To optimize pinhole imaging performance and achieve higher resolution, one should minimize the width of the distribution given by Eq. (7) with respect to the Ω parameter. Figure 4 presents a scan of the line spread function as a function of Ω. Due to the presence of sinc-function side lobes, the shape of the line spread function is nontrivial. Given that its full width at half maximum may not clearly indicate the best performance, selecting the optimum Ω parameter is a subjective matter. We chose $\Omega = 4.5$. This choice ultimately leads to the following formula for the optimal pinhole camera aperture size:

$$a^2 \approx 4.5\lambda\!\!\!^{-} z_{\mathrm{eff}}. \quad (8)$$

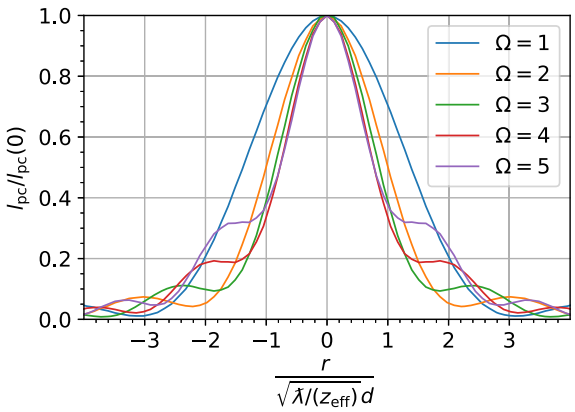

FIG. 4. Line spread functions for various Ω. We may choose the optimum as $\Omega = 4.5$, while other choices can be equally valid as in the region $2 < \Omega < 5$ we have almost the same width of the main peak and slightly different "wings." Here we found an optimum between defocusing aberration and diffraction effects.

This corresponds to an optimum between defocusing aberrations and diffraction effects. For a detailed explanation of the limits of large and small Ω, we refer the reader to [16].

We analyzed the imaging problem numerically using the OCELOT toolkit [21], employing a model where a point source propagates through an optical system. This simulation yields a point spread function at the pinhole when the aperture is set to its optimal size. The results are presented in Fig. 5.

We also studied the evolution of the point spread function downstream of the aperture, as illustrated in Fig. 6(a). After normalizing the spatial units, as depicted in Fig. 6(b), the relative resolution stabilizes to its minimum, approximately 0.3 times the diffraction length ($\lambda\!\!\!^{-} z/a^2$), from the slit, as also noted in [9]. We provide an expression for the full width at the half maximum of the line spread function:

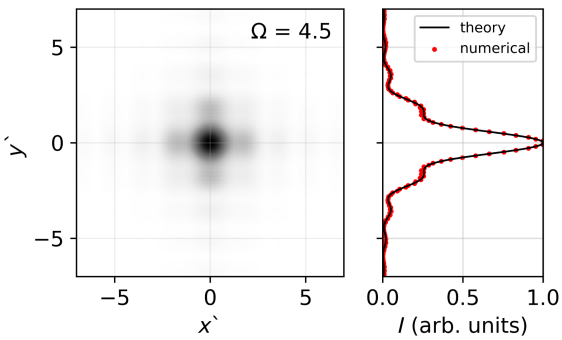

FIG. 5. Comparison of the analytical point spread function with numerical calculations for $\Omega = 4.5$.

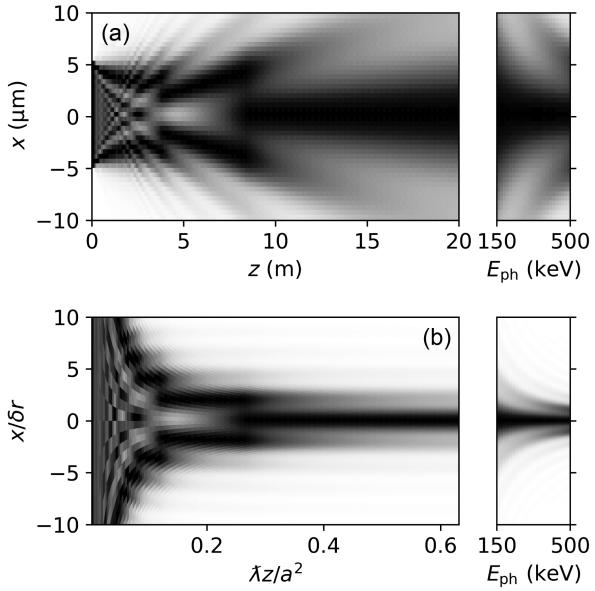

FIG. 6. Line spread function evolution after the pinhole with the optimal size of $\Omega = 4.5$ or 10×10 μm^2 at 250 keV. In (a), the axes are presented in physical units, while in (b), the axes are in dimensionless units. The horizontal axis is in units of the diffraction length, where 0.63 corresponds to the image location at 20 m. The vertical axis is expressed in units of relative resolution, as derived from the expression in Eq. (9). The right-hand side of (a) and (b) illustrates the variation of the line spread function with respect to energy. Interestingly, the distribution undergoes a series of abrupt transitions before reaching the far zone, indicating that the transition from the near zone to the far zone is not smooth but rather abrupt.

$$\delta r \simeq 1.5\sqrt{\frac{\lambda}{z_{\mathrm{eff}}}}d. \tag{9}$$

As evident from the preceding discussion, rectangular geometry serves as a demonstrative approach for teaching the optics of a pinhole camera. Explaining the concept with a rectangular aperture helps to demonstrate the properties of the diffracted field, eliminating the need for complex derivations.

D. Numerical simulations

Wavefront simulations based on the propagation of partially coherent fields were investigated in [22]. We used this technique to model the bending magnet radiation. We generated numerous (10^4) statistical realizations of the radiation field, as illustrated in Figs. 2(a) and 3, and ensemble-averaged them to obtain an experimentally observable distribution, as would be observed on a beamline equipped with a conventional monochromator. In Figs. 7 and 8, we illustrated how the size of the point spread function compares to the size of the image. We utilized the parameters listed in Table I.

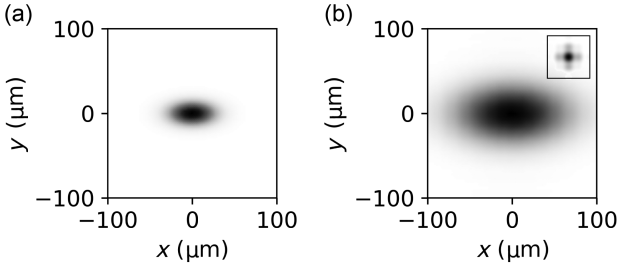

FIG. 7. (a) Source distributions and (b) its twofold magnified image, convolved with the point spread function (provided to scale in an embedded inset).

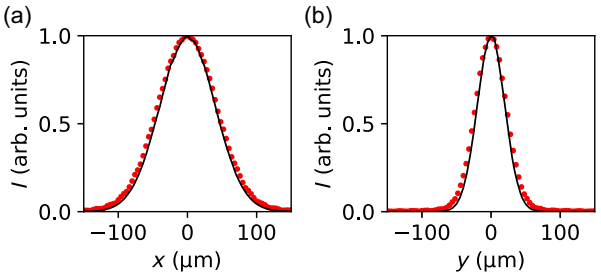

FIG. 8. Image (dashed line) and the source distribution (solid line), which is 2 times magnified for comparison. Slice over $x = 0$ and $y = 0$ from Fig. 7 for each direction correspondingly.

We roughly estimated the expected blurring of the size of the image beam size using an approximate formula

$$\sigma_i = \sqrt{4\sigma_e^2 + \sigma_{\mathrm{psf}}^2}. \tag{10}$$

This formula underestimates the actual resulting size because it assumes that widths sum up quadratically, which is only true for Gaussian distributions. However, in this case, we are dealing with a non-Gaussian distribution of the point spread function, as observed in Fig. 4. The factor of 4 originates from the specific geometry of the pinhole camera. Based on a Gaussian fit, σ_{psf} is estimated to be

TABLE I. Simulation parameters.

Parameter	Value
Natural emittance ($\epsilon_{0_x} \times \epsilon_{0_y}$)	20×5 (pm rad)^2
Beta function ($\beta_{x,y}$)	20 m
Beam size ($\sigma_x \times \sigma_y$)	20×10 μm^2
Beam energy (E_{beam})	6 GeV
Photon energy (E_{ph})	250 keV
Source to pinhole (z_1)	10 m
Pinhole to image (d)	20 m
Pinhole size (a)	5 μm
Point spread function:	
FWHM	10.3 μm
σ_{psf}	6.7 μm

TABLE II. Image sizes.

	σ_i, μm [(Eq. (10)]	σ_i, μm (simulation)
$\sigma_x = 20$ μm	40.6	42.3
$\sigma_y = 10$ μm	21.1	22.3

6.7 μm from the simulation. We present a comparison of this estimation with the simulation results in Table II.

III. PROPOSED SETUP

In this section, we propose the conceptual design of a setup to diagnose the electron beam size. We suggest a three-pole, 1-m-long magnetic chicane, schematically depicted in Figs. 1 and 9, to serve as a synchrotron radiation source. The device features a single yoke with coils powered by a single power supply. The magnetic field in the outer compensatory coils is three times lower than that in the central coil. The design's advantages include its compactness and low cost. The SR background from the outer magnets of the chicane and other storage ring bending magnets is negligibly small, as we operate at large values of $y = \lambda_{\mathrm{ph}_c}/\lambda_{\mathrm{ph}}$. This kind of device should be installed in a zero-dispersion section of the storage ring. This placement is crucial to prevent an increase in beam emittance.

In the hard x-ray range, a rectangular pinhole can be easily formed using a combination of two perpendicular conventional slits. It is important to note that the slits should be sufficiently thick to block 300-keV-order hard x-ray light.

The SR emitted by the central pole is filtered through a 4-mm-thick lead filter to narrow down the radiation bandwidth. We need this filtration to mitigate the effects of dispersion at the lower end of photon energies. The exponentially decaying tail of the SR spectrum, combined with the transmission characteristic of the filter, effectively creates a bell-shaped spectrum with a 150 keV bandwidth and 250 keV central energy, as seen in Fig. 11. The filter thickness is optimized for sufficient photon flux at the detector and acceptable resolution based on the radiation bandwidth. We estimate the photon flux to be around 8×10^7 photons/s for a 4-mm-thick Pb filter, chicane magnetic field of 1.7 T, and 100 mA electron beam.

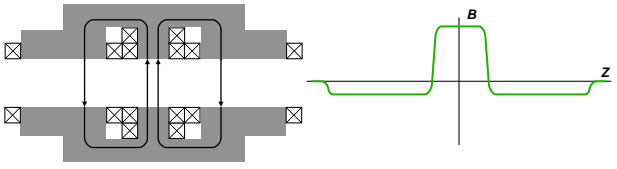

FIG. 9. Magnetic chicane for the proposed x-ray pinhole camera. The magnetic field of the central pole is about 1.7 T. The overall length of the device is 1 m.

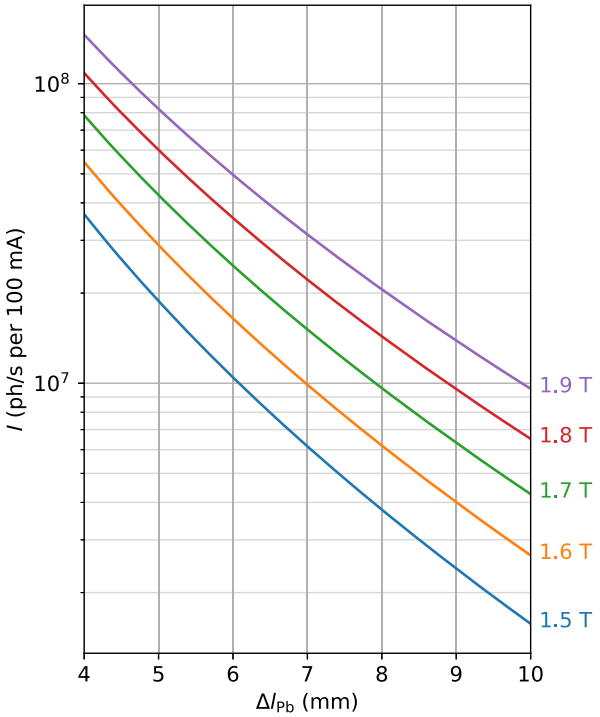

FIG. 10. Estimation of the photon flux through the pinhole from a 6 GeV electron beam as a function of the thickness of the Pb filter, plotted for different amplitudes of the magnetic field of the central magnet of the chicane.

Figure 10 provides an estimation of the photon flux for magnetic fields ranging from 1.5 to 1.9 T.

IV. DISCUSSION

In this section, we address important considerations for implementing the pinhole camera in a real facility, which were not covered in the main body of this paper. First, one needs to consider that to obtain accurate results from the

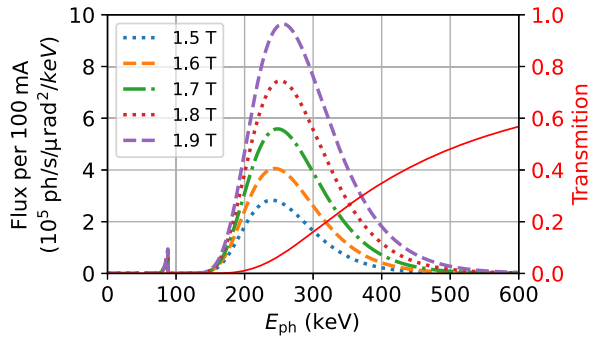

FIG. 11. On-axis spectrum of synchrotron radiation upon spectral filtering with 4 mm lead plate. We provide the distribution for different magnetic field strengths of the central pole, assuming a 6 GeV electron beam and with the red line the transmission characteristic of 4 mm of Pb. Calculations are made with SPECTRA code [30].

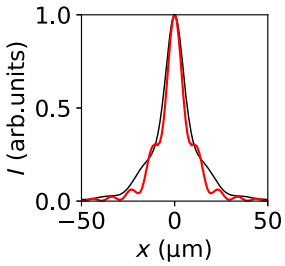

FIG. 12. Comparison of the line spread functions for monochromatic light (red line) and averaged over the whole energy range (black line) presented in Fig. 11 with green line.

measured images, one must perform a deconvolution operation. This operation uses the point spread function described earlier in this paper. Moreover, it is crucial to consider the broad spectrum of radiation passing through the pinhole, as illustrated in Fig. 11. To address this, one must calculate a weighted average of the point spread over the spectrum and perform a deconvolution operation using this average. We present this in comparison to the line spread functions for 250 keV in Fig. 12. The variation of the line spread functions within this energy range is depicted in the right subplot of Fig. 6. The FWHM of the spectrum-averaged line spread function increases from 10.3 μm for monochromatic radiation to 13.7 μm. The subsequent step in data analysis involves deconvolution using the point spread function of the x-ray camera employed in the experiment, as discussed in [9].

Another important question to address is the design of an appropriate detector for the proposed setup. Given these stringent requirements, one may use indirect detectors that convert x-ray photons to the visible range using a scintillator. For high conversion efficiency of the scintillator, materials with a high atomic number (Z) are preferred, such as lutetium compounds, such as Lu_2O_3:Eu, as suggested in [31]. A scintillator made from such materials will generate a sufficient number of photons to be detected by a standard industrial camera and associated optics, as noted by [31]. The photon flux for a specific detector can be readily calculated using data from Fig. 11.

V. CONCLUSION

In this paper, we discussed the applicability of the van Cittert-Zernike theorem to the imaging of incoherent synchrotron radiation with a pinhole. As a result of our analysis, we have provided an exact expression for the point spread function, which can be factorized as the product of two one-dimensional line spread functions. Using simple analytical expressions, we derived design formulas for a rectangular pinhole camera and calculated its resolution. As a practical application, we proposed a diagnostic beamline based on a magnetic chicane to measure the transverse electron beam size at ultralow-emittance machines with a pinhole camera. Operating at high photon energies (∼200–300 keV) and applying spectral filtering with a 4-mm-thick lead plate allows one to maximize spatial resolution, resulting in a point spread function width of approximately 13.7 μm. We conclude our paper with estimates of the photon flux and demonstrate sufficient photon flux for effective imaging using the pinhole camera.

ACKNOWLEDGMENTS

We thank Serguei Molodtsov and Kai Bagschik for their interest in this work. We thank Andreas Koch for the discussion on possible detector design.

[1] D. Einfeld, J. Schaper, and M. Plesko, Design of a diffraction limited light source (DIFL), in *Proceedings of the Particle Accelerator Conference, Dallas, TX, 1995* (IEEE, New York, 1995), pp. 177–179.

[2] C. G. Schroer, R. Roehlsberger, E. Weckert, R. Wanzenberg, I. Agapov, R. Brinkmann, and W. Leemans, PETRA IV: Upgrade of PETRA III to the ultimate 3D x-ray microscope, Conceptual Design Report, Deutsches Elektronen-Synchrotron DESY, Hamburg, Report No. PUBDB-2019-03613, 2019, https://dx.doi.org/10.3204/PUBDB-2019-03613.

[3] C. Abraham *et al.*, Diamond-II Conceptual Design Report (2019), https://www.diamond.ac.uk/dam/jcr:ec67b7e1-fb91-4a65-b1ce-f646490b564d/Diamond-IIConceptualDesignReport.pdf.

[4] P. Raimondi *et al.*, The extremely brilliant source storage ring of the European Synchrotron Radiation Facility, Commun. Phys. **6**, 82 (2023).

[5] R. Khubbutdinov, A. P. Menushenkov, and I. A. Vartanyants, Coherence properties of the high-energy fourth-generation x-ray synchrotron sources, J. Synchrotron Radiat. **26**, 1851 (2019).

[6] G. Geloni, S. Serkez, R. Khubbutdinov, V. Kocharyan, and E. Saldin, Effects of energy spread on brightness and coherence of undulator sources, J. Synchrotron Radiat. **25**, 1335 (2018).

[7] P. Li, M. Allain, T. A. Grünewald, M. Rommel, A. Campos, D. Carbone, and V. Chamard, 4th generation synchrotron source boosts crystalline imaging at the nanoscale, Light Sci. Appl. **11**, 73 (2022).

[8] H. N. Chapman, Fourth-generation light sources, Int. Union Crystallogr. **10**, 246 (2023).

[9] C. Thomas, G. Rehm, I. Martin, and R. Bartolini, X-ray pinhole camera resolution and emittance measurement, Phys. Rev. ST Accel. Beams **13**, 022805 (2010).

[10] P. Elleaume, C. Fortgang, C. Penel, and E. Tarazona, Measuring beam sizes and ultra-small electron emittances using an x-ray pinhole camera, J. Synchrotron Radiat. **2**, 209 (1995).

[11] M. Tordeux, L. Cassinari, O. Chubar, J.-C. Denard, D. Pédeau, and B. Pottin, Ultimate resolution of soleil x-ray pinhole camera, in *Proceedings of the 8th European Workshop on Beam Diagnostics and Instrumentation for Particle Accelerators, DIPAC 2007, Venice, Italy* (CERN, Geneva, Switzerland, 2007).

[12] S. Takano, Beam diagnostics with synchrotron radiation in light sources, in *Proceedings of the International Particle Accelerator Conference, IPAC 2010, Kyoto, Japan* (ICR, Kyoto, 2010).

[13] O. Chubar and P. Elleaume, Accurate and efficient computation of synchrotron radiation in the near field region—INSPIRE, in *Proceedings of the 6th European Particle Accelerator Conference, EPAC 1998, Stockholm* (IOP, London, 1998).

[14] O. V. Chubar, Precise computation of electron-beam radiation in nonuniform magnetic fields as a tool for beam diagnostics, Rev. Sci. Instrum. **66**, 1872 (1995).

[15] S. Kongtawong, O. Chubar, and T. Shaftan, Simulation of synchrotron radiation from electron beams affected by vibrations and drifts, Phys. Rev. Accel. Beams **25**, 024601 (2022).

[16] G. Geloni, E. Saldin, E. Schneidmiller, and M. Yurkov, Statistical optics approach to the design of beamlines for synchrotron radiation, arXiv:physics/0603269.

[17] G. Kube, Review of synchrotron radiation-based diagnostics for transverse profile measurements, in *Proceedings of the 8th European Workshop on Beam Diagnostics and Instrumentation for Particle Accelerators, DIPAC 2007, Venice, Italy* (CERN, Geneva, Switzerland, 2007).

[18] M. Labat, O. Chubar, J. Breunlin, N. Hubert, and A. Andersson, Bending magnet synchrotron radiation imaging with large orbital collection angles, Phys. Rev. Lett. **131**, 185001 (2023).

[19] M. Siano, B. Paroli, M. Potenza, L. Teruzzi, U. Iriso, A. Nosych, E. Solano, L. Torino, D. Butti, A. Goetz, T. Lefevre, S. Mazzoni, and G. Trad, Two-dimensional electron beam size measurements with x-ray heterodyne near field speckles, Phys. Rev. Accel. Beams **25**, 052801 (2022).

[20] S. Serkez, Design and optimization of the grating monochromator for soft x-ray self-seeding FELs, Ph.D. thesis, Verlag Deutsches Elektronen-Synchrotron, 2015, No. PUBDB-2015-04348.

[21] I. Agapov, G. Geloni, S. Tomin, and I. Zagorodnov, OCELOT: A software framework for synchrotron light source and FEL studies, Nucl. Instrum. Methods Phys. Res., Sect. A **768**, 151 (2014).

[22] A. Trebushinin, G. Geloni, Y. Rakshun, and S. Serkez, Gaussian random field generator for simulating partially coherent undulator radiation, Optica **9**, 842 (2022).

[23] J. W. Goodman, *Statistical Optics*, 2nd ed. (Wiley, Hoboken, NJ, 2000).

[24] P. H. van Cittert, Die Wahrscheinliche Schwingungsverteilung in Einer von Einer Lichtquelle Direkt Oder Mittels Einer Linse Beleuchteten Ebene, Physica (Utrecht) **1**, 201 (1934).

[25] F. Zernike, The concept of degree of coherence and its application to optical problems, Physica (Utrecht) **5**, 785 (1938).

[26] J. Goodman, Some effects of target-induced scintillation on optical radar performance, Proc. IEEE **53**, 1688 (1965).

[27] W. H. Carter and E. Wolf, Coherence and radiometry with quasihomogeneous planar sources, J. Opt. Soc. Am. **67**, 785 (1977).

[28] Here we looked at the argument ξ of Eq. 5.44 in [29] and estimated at which angle the intensity drops to half its value, which gives $y(\frac{3}{2}(\gamma\psi)^2) = 0.7$, resulting in an exact value of $\sigma_{r'} = 0.22/\gamma$, see Fig. 6.12 in [29].

[29] P. J. Duke, *Synchrotron Radiation: Production and Properties*, Oxford Series on Synchrotron Radiation Vol. 3 (Oxford University Press, Oxford, 2000).

[30] T. Tanaka and H. Kitamura, SPECTRA: A synchrotron radiation calculation code, J. Synchrotron Radiat. **8**, 1221 (2001).

[31] A. Koch, Discussion on the possible design of the detector (personal communication).

2.5.2. Heuristic approach II: quasi- homogeneous/stationary sources. Paper II.

In this section, I extend the algorithm presented in previous Section 2.5.1 to account for a finite coherence spot size at the source. I will shape the field $\bar{\phi}(\vec{r},\omega)$ using mathematical supports that represent not only the source intensity distribution $\bar{I}(\vec{r},\omega) = \langle \bar{E}(\vec{r},\omega)\bar{E}^*(\vec{r},\omega)\rangle$, but also its angular distribution $\hat{I}(\vec{k},\omega) = \langle \hat{E}(\vec{k},\omega)\hat{E}^*(\vec{k},\omega)\rangle$. Then this field will have a proper correlation function at the source. First, I take the spatial Fourier transform of Eq. 2.80:

$$\hat{\phi}(\vec{k},\omega) = \mathcal{F}\left[\sqrt{\bar{I}(\vec{r},\omega)}\mathcal{N}(\vec{r})\right](\vec{k}) \tag{2.86}$$

where the Fourier transform is denoted as $\mathcal{F}\left[\dots\right](\vec{k})$ operator, and *modify* this field by multiplying it by the effective radiation divergence $\hat{I}(\vec{k},\omega)$ at the source location:

$$\hat{\phi}(\vec{k},\omega) = \sqrt{\hat{I}(\vec{k},\omega)}\mathcal{F}\left[\sqrt{\bar{I}(\vec{r},\omega)}\mathcal{N}(\vec{r})\right](\vec{k}). \tag{2.87}$$

and take the inverse Fourier transform to obtain the field back in real space:

$$\bar{\phi}(\vec{r},\omega) = \mathcal{F}^{-1}\left[\sqrt{\hat{I}(\vec{k},\omega)}\mathcal{F}\left[\sqrt{\bar{I}(\vec{r}',\omega)}\mathcal{N}(\vec{r}',\omega)\right](\vec{k})\right](\vec{r}), \tag{2.88}$$

where $\vec{r}'$ is the internal variable for the Fourier transform. This is the initial formulation of the SERVAL algorithm, which with co-authors we provided in **Paper II**[6].

Now, the field should be checked to ensure it follows the correlation function embedded in the intensity distributions $\bar{I}(\vec{r},\omega)$ and $\hat{I}(\vec{k},\omega)$. To verify this, I auto-correlate the obtained field in Eq. 2.88 and explicitly write the integrals of the direct Fourier transform:

$$\begin{aligned}\langle \bar{\phi}(\vec{r}_1,\omega)\bar{\phi}^*(\vec{r}_2,\omega)\rangle = \Bigg\langle \mathcal{F}\mathcal{F}^{-1}\Bigg[\sqrt{\hat{I}(\vec{k}_1,\omega)\hat{I}(\vec{k}_2,\omega)}\times \\ \times \iint_{-\infty}^{\infty} \sqrt{\bar{I}(\vec{r}_1',\omega)\bar{I}(\vec{r}_1',\omega)}\mathcal{N}(\vec{r}_1')\mathcal{N}^*(\vec{r}_2')e^{i(\vec{r}_1'\vec{k}_1-\vec{r}_2'\vec{k}_2)}d\vec{r}_1'd\vec{r}_2'\Bigg](\vec{r}_1,\vec{r}_2)\Bigg\rangle,\end{aligned} \tag{2.89}$$

where $\mathcal{F}\mathcal{F}^{-1}[\dots]$ denotes two consecutive Fourier transforms. Then bringing the averaging operation under the integral sign and accounting for the noise property $\langle \mathcal{N}(\vec{r}_1)\mathcal{N}^*(\vec{r}_2)\rangle =$

[6] In this paper, we referred to SERVAL as **S**pontaneous **E**mission **R**apid e**VAL**uator. While writing this thesis, I decided to change the transcription to **S**tochastic **E**mission **R**apid e**VAL**uator. SERVAL is actually a backronym, meaning that we initially chose the name "SERVAL" and only then came up the transcription. We aimed to name the algorithm in the manner similar to the OCELOT toolkit [73]–[75]. Serval is a type of predatory wild cat native to Africa, similar to the ocelot, although from a different continent. Ultimately, the SERVAL algorithm acts as rapid as its eponymous wild cat.

SERVAL algorithm was proposed as an "eureka" solution by **S. Serkez** in response to my question about the problem of simulating the partial coherence of synchrotron radiation sources. At the time, S. Serkez had developed the "SASE estimator & imitator," implemented in the OCELOT toolkit, utilizing this same algorithm for simulating the longitudinal domain of SASE FEL radiation.

$\delta(\vec{r}_2 - \vec{r}_1)$ I obtain the following expression:

$$\langle \bar{\phi}(\vec{r}_1,\omega)\bar{\phi}^*(\vec{r}_2,\omega)\rangle = \mathcal{F}\mathcal{F}^{-1}\left[\sqrt{\hat{I}(\vec{k}_1,\omega)\hat{I}(\vec{k}_2,\omega)}\times \right.$$
$$\left. \times \iint_{-\infty}^{\infty} \sqrt{\bar{I}(\vec{r}_1',\omega)\bar{I}(\vec{r}_1',\omega)}\delta(\vec{r}_1' - \vec{r}_2')e^{i(\vec{r}_1'\vec{k}_1 - \vec{r}_2'\vec{k}_2)}d\vec{r}_1' d\vec{r}_2'\right](\vec{r}_1,\vec{r}_2). \quad (2.90)$$

After this, I integrate over $d\vec{r}_1$ accounting for the filtering property of Dirac delta function:

$$\langle \bar{\phi}(\vec{r}_1,\omega)\bar{\phi}^*(\vec{r}_2,\omega)\rangle = \mathcal{F}\mathcal{F}^{-1}\left[\sqrt{\hat{I}(\vec{k}_1,\omega)\hat{I}(\vec{k}_2,\omega)}\int_{-\infty}^{\infty}\bar{I}(\vec{r}',\omega)e^{i\vec{r}'(\vec{k}_1-\vec{k}_2)}d\vec{r}'\right](\vec{r}_1,\vec{r}_2). \quad (2.91)$$

This expression contains an integral that resembles one from the generalized van Cittert-Zernike theorem for a quasi-homogeneous source, or more specifically, its formulation for the cross-spectral density function Fourier transform in Eq. 2.58, where one relates the Fourier integral of the source intensity distribution with $\hat{g}(\Delta\vec{k},\omega)$:

$$\langle \bar{\phi}(\vec{r}_1,\omega)\bar{\phi}^*(\vec{r}_2,\omega)\rangle = \iint_{-\infty}^{\infty}\sqrt{\hat{I}(\vec{k}_1,\omega)\hat{I}(\vec{k}_2,\omega)}\hat{g}(\Delta\vec{k},\omega)e^{-i(\vec{r}_1\vec{k}_1-\vec{r}_2\vec{k}_2)}d\vec{k}_1 d\vec{k}_2. \quad (2.92)$$

Then, following the general definition of quasi-homogeneity from Eq. 2.44: $\langle \hat{E}(\vec{k}_1,\omega)\hat{E}^*(\vec{k}_2,\omega)\rangle = \sqrt{\hat{I}(\vec{k}_1,\omega)\hat{I}(\vec{k}_2,\omega)}\hat{g}(\Delta\vec{k},\omega)$, I result in the expressions:

$$\begin{aligned}
\langle \bar{\phi}(\vec{r}_1,\omega)\bar{\phi}^*(\vec{r}_2,\omega)\rangle &= \\
= \iint_{-\infty}^{\infty}\langle \hat{E}(\vec{k}_1,\omega)\hat{E}^*(\vec{k}_2,\omega)\rangle e^{-i(\vec{r}_1\vec{k}_1-\vec{r}_2\vec{k}_2)}d\vec{k}_1 d\vec{k}_2 &= \\
= \left\langle \int_{-\infty}^{\infty}\hat{E}(\vec{k}_1,\omega)e^{-i\vec{r}_1\vec{k}_1}d\vec{k}_1 \int_{-\infty}^{\infty}\hat{E}^*(\vec{k}_2,\omega)e^{i\vec{r}_2\vec{k}_2}d\vec{k}_2\right\rangle &= \\
= \langle \bar{E}(\vec{r}_1,\omega)\bar{E}^*(\vec{r}_2,\omega)\rangle. &
\end{aligned} \quad (2.93)$$

This shows that the field $\bar{\phi}(\vec{r},\omega)$ follows the same correlation function as the field $\bar{E}(\vec{r},\omega)$. Since I describe complex Gaussian random processes, higher-order correlation functions can be expressed in terms of the first-order correlation function.

In addition to the analytical derivation presented here I also verify the preservation of the Gaussian

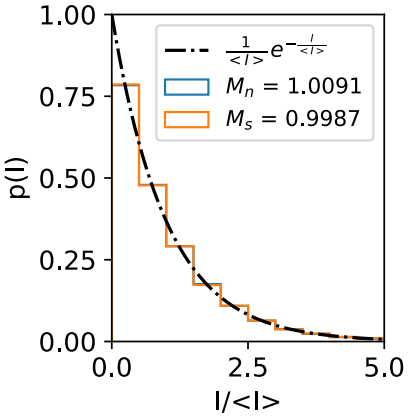

Figure 2.6: Instantaneous intensity probability distribution: The black line represents the theoretical expectation—negative exponential distribution. The blue histogram shows the distribution of the initial Gaussian white noise (50001 statistical realizations), and the orange histogram represents the distribution for the resulting field. $\bar{\phi}(\vec{r},\omega)$.

statistics. I cross-check that after shaping the field $\tilde{\phi}(\vec{r}, \omega)$, its instantaneous intensity probability distribution follows a negative exponent law, as seen in Fig. 2.6. This serves as final proof that the constructed field follows the desired statistical properties.

The formulation of the algorithms for the spatial domain is not unique in the sense of domain interchangeability. As demonstrated, the Wiener-Khinchin theorem is a mathematical twin of the van Cittert–Zernike theorem, written for the cross-spectral density of the inverse spatial domain following Eq. 2.58. Therefore, one can easily adapt the expression in Eq. 2.88 for the longitudinal domain. The algorithm itself has been "in the air" in different domains of science and adapted for various applications (as cited in **Papers II**), particularly for the FEL physics [73], [76][7]. However, it has never been applied to the simulation of the transverse domain of synchrotron radiation, that I present in **Papers II**.

[7] In [76], a different noise distribution was chosen, which I discuss in Appendix C.

OPTICA

Gaussian random field generator for simulating partially coherent undulator radiation

Andrei Trebushinin,[1,*] Gianluca Geloni,[1] Yakov Rakshun,[2] and Svitozar Serkez[1,3]

[1]European XFEL, 4, Holzkoppel Street, 22869 Schenefeld, Germany
[2]Budker Institute of Nuclear Physics, 11, Lavrentieva Avenue, 630090 Novosibirsk, Russia
[3]e-mail: svitozar.serkez@xfel.eu
*Corresponding author: andrei.trebushinin@xfel.eu

Received 11 April 2022; revised 3 June 2022; accepted 15 June 2022; published 22 July 2022

Wavefront propagation codes play pivotal roles in the design of optics at synchrotron radiation sources. However, they usually do not account for the stochastic behavior of the radiation field originating from shot noise in the electron beam. We propose a computationally efficient algorithm to calculate a single statistical realization of partially coherent synchrotron radiation fields at a given frequency. This field can be consequently propagated from the source position downstream through an optical beamline to the sample position. The proposed algorithm relies on a method for simulating Gaussian random fields. We initially generate the radiation field as Gaussian white noise and then restrict it in both real and inverse space domains for a given radiation size and divergence. We exploit the assumption of quasi-homogeneity of the source. However, we show that the method is applicable with reasonable accuracy outside of this assumption. The proposed algorithm is consistent with other well-established approaches, and, in addition, it possesses an advantage in terms of computational efficiency. It can be extended to other types of sources that follow Gaussian statistics. Finally, the demonstration of the algorithm is well suited for educational purposes.

https://doi.org/10.1364/OPTICA.460902

1. INTRODUCTION

Advance in the design of storage-ring-based synchrotron radiation sources [1,2] led to a reduction in electron beam emittance down to the diffraction limit for a wide range of photon wavelengths λ such that

$$\epsilon_{x,y} < \sigma_{r'}\sigma_r = \frac{\lambda}{4\pi}, \tag{1}$$

where $\sigma_{r'}$ and σ_r are the natural divergence and size of radiation at the source emitted by a filament, respectively, i.e., with zero transverse size. electron beam. Radiation from diffraction-limited light sources possesses full transverse coherence. However, even brand new fourth-generation light sources are only partially coherent at high enough photon energies.

The process of designing beamlines for modern synchrotron radiation sources involves simulations of partially coherent radiation and its propagation through an optical system. Ray-tracing codes, such as in [3–5] and references within [6], have often served this aim. However, these codes assume poor spatial coherence, while already at third-generation light sources, the radiation in vertical direction is diffraction limited at photon energies of the order of 1 keV. In this case, the usefulness of ray-tracing becomes limited. One needs to accurately account for diffraction effects using wave optics approaches or, alternatively, come up with a solution to adapt ray-tracing for this purpose, such as a hybrid approach [6].

The wave optics approach allows to straightforwardly account for the effects related to fully coherent radiation. Nevertheless, the case of partially coherent radiation remains a sophisticated problem. Various authors have covered the theoretical basis of the statistical properties of synchrotron radiation in many publications [7–13]. In [7], a statistical optics approach is applied to the case of third-generation synchrotron radiation sources. The characteristics of synchrotron radiation heavily depend on the presence of shot noise in an electron beam. Because of this, amplitudes and phases of the radiation exhibit stochastic fluctuations. In other words, radiation field distributions change from realization to realization, and to obtain statistically meaningful intensities and correlation functions, one needs to average over a statistical ensemble so that the framework of statistical optics [14] becomes quite natural. Here we consider undulator sources that are mostly widespread. Approaches for simulating partially coherent undulator radiation are proposed in several codes and in plenty of publications. Based on the framework of statistical optics, one can consider propagating the cross-spectral density function of the electric field by exploiting coherent mode decomposition methods; see [15–19]. This method requires significant computational resources, as discussed in [20]. Nevertheless, the authors of [21] report improved CPU efficiency of the coherent mode decomposition method.

An alternative type of method is based on Monte-Carlo-like simulations. If one is interested in radiation field intensity

Corrected 2 September 2022

at a given frequency, one can calculate radiation from separate electrons. Then, one can simply sum up intensities from these individual electrons: this procedure is valid when the length of an electron beam is long compared to the radiation wavelength, which is always the case for conventional use of synchrotrons. One of the most well-known wave optics simulation toolkits, Synchrotron Radiation Workshop (SRW) [22–24], uses a Monte-Carlo-like approach for treating partially coherent radiation in simulations [25–31]. We discuss this approach in Section 3.B.

When computational resources allow for it, one can also use a Monte-Carlo-like approach where the electric fields from particles—not the intensities—are summed up to form a single realization of the synchrotron radiation field. We discuss the field addition method (FAM) in Section 3.A with the aim to facilitate understanding of the theory, Section 2. In this approach, instead of dealing with ensemble-averaged quantities, one considers separate realizations of a stochastic process, similar to what is done, for example, in free electron laser (FEL) simulations [32].

The algorithm we propose here follows a similar way for simulating partially coherent synchrotron radiation. It relies on the generation of instances of the stochastic process, instead of dealing with ensemble-averaged quantities such as correlation functions or averaged intensities. The method we propose is based on a Gaussian random field (GRF) generator. In practice, we restrict complex Gaussian noise by the effective size and divergence of the radiation field. Introducing Gaussian noise, we effectively emulate the contribution of shot noise accounting for all electrons at once. As a result, the algorithm provides the complex amplitude of a multimode field of undulator radiation, suitable for propagation through a beamline. We call this method the synchrotron emission rapid evaluator (SERVAL) and present its description along with a comparative analysis with Monte-Carlo-like approaches. Also, we demonstrate the application of SERVAL in the case of a simple focusing system with an exit pupil. SERVAL is part of the Ocelot [33] toolkit, which was developed for start-to-end simulations of FEL and synchrotron light sources.

2. THEORETICAL BACKGROUND ON UNDULATOR RADIATION STATISTICAL PROPERTIES

A. Qualitative Reasoning

Undulator radiation has an intrinsic stochastic structure caused by random distribution of electrons in a volume of 6D phase space. This distribution follows shot noise statistics, as the number of electrons located in the finite volume of the electron beam phase space is *discrete* and *random*. This shot noise is imprinted in the radiation structure. It manifests itself as longitudinal and transverse spikes in the radiation pulse as illustrated in Figs. 1 and 2. By its nature, those fields follow the same statistics as *thermal light*: both are described in terms of Gaussian random processes [14].

The duration of a temporal spike of undulator radiation field in the t domain is coherence time at a given harmonic. The transverse spiky structure may be explored with a monochromator that is capable of resolving a single spike in the radiation spectrum. For example, in [34,35], $\Delta E/E = 8 \times 10^{-9}$ relative resolution was reached at energy 14.41 keV, which is $\Delta\omega_m \sim 2 \times 10^{11}$ Hz in absolute units. This allowed to resolve a single spike in the spectrum with absolute width of $2\pi/\sigma_T \sim 2 \times 10^{11}$ Hz. In the case of an ideal setup (perfect monochromator and detector), a two-dimensional detector will show a transverse spiky structure in the radiation pulse, as illustrated in Figs. 1 and 2. Note that resolving one spike in the frequency domain is mathematically equivalent to studying the emission at a specific frequency ω.

In contrast with thermal sources, which are fully incoherent and whose coherent spot size at the source is about the radiation wavelength, undulator sources are partially coherent, and they exhibit a coherent spot size equal to the single-electron diffraction size. For the case of thermal light, the relation of the spiky structure in the far zone with the source size is described by Van Cittert–Zernike theorem [36,37]. This theorem relates the cross-spectral density in the far zone with the intensity distribution at the source via Fourier transform. For undulator radiation, this theorem is applied only to the special case of quasi-homogeneous sources. To assess the coherence properties of the source, one should compare the natural size and divergence of the radiation from a single electron with the size and divergence of the electron beam. Applicability of Van Cittert–Zernike theorem to undulator radiation was thoroughly reviewed in [7] and discussed in the following sections of this paper. For further use, here we introduce two dimensionless parameters to describe the radiation size and divergence of the single electron with respect to those of the electron beam:

$$D_{x,y} = \frac{\sigma^2_{x',y'}}{\lambda/(2\pi L_w)}, \quad N_{x,y} = \frac{\sigma^2_{x,y}}{\lambda L_w/(2\pi)}, \tag{2}$$

where $\sigma_{x',y'}$ and $\sigma_{x,y}$ are the electron beam divergence and size in each direction, respectively. The source has a large number of spikes if $N \gg 1$ and $D \gg 1$ in both planes. In the case of single electron radiation, N and D become vanishingly small, resulting in a single spike.

B. Mathematical Description

The radiation field from an undulator generated by an electron beam with N_e electrons can be written as the sum of the fields (our mathematical notation coincides with that in [7]) from each individual electron. We represent the field of undulator radiation in the $\omega\vec{r}$ domain by a function $\tilde{E}(z, \vec{r}, \omega)$, where the radiation field is considered at a given frequency ω. $\tilde{E}(z, \vec{r}, \omega)$ is related with the field $E(z, \vec{r}, t)$ in the $t\vec{r}$ domain by inverse Fourier transform. The radiation from the whole electron beam is written as

$$\tilde{E}_b(z, \vec{r}, \omega) = \sum_{k=1}^{N_e} \tilde{E}(\vec{\eta}_k, \vec{l}_k, z, \vec{r}, \omega) e^{i\omega t_k}, \tag{3}$$

where z is the distance from the undulator center to the observation plane, and $\vec{r}$ is transverse coordinates in the observation plane. Here we consider a mono-energetic electron beam. With Monte-Carlo-like approaches, this can be easily accounted in Eq. (3) by just adding into the formulas the Lorentz factor of the kth electron, γ_k.

The kth electron has its transverse offset $\vec{l}_k$ and deflection angle $\vec{\eta}_k$ from the reference trajectory inside an undulator, and an arrival time t_k with respect to the reference electron. In the $\omega\vec{r}$ domain, the arrival time contributes to the expression of the electric field as an additional phase factor $\exp(i\omega t_k)$. Quantities $\vec{\eta}_k$, $\vec{l}_k$ are assumed to follow Gaussian distributions $f_\eta(\vec{\eta})$ and $f_l(\vec{l})$, with zero mean values and variances $\sigma_{x',y'}$, $\sigma_{x,y}$. Approximation of the beams with transverse Gaussian shapes is very applicable for storage rings.

Having Eq. (3), one may check that $\tilde{E}_b$ is a circular complex Gaussian random variable, [7], (for fixed z, $\vec{r}$, and ω), which is a

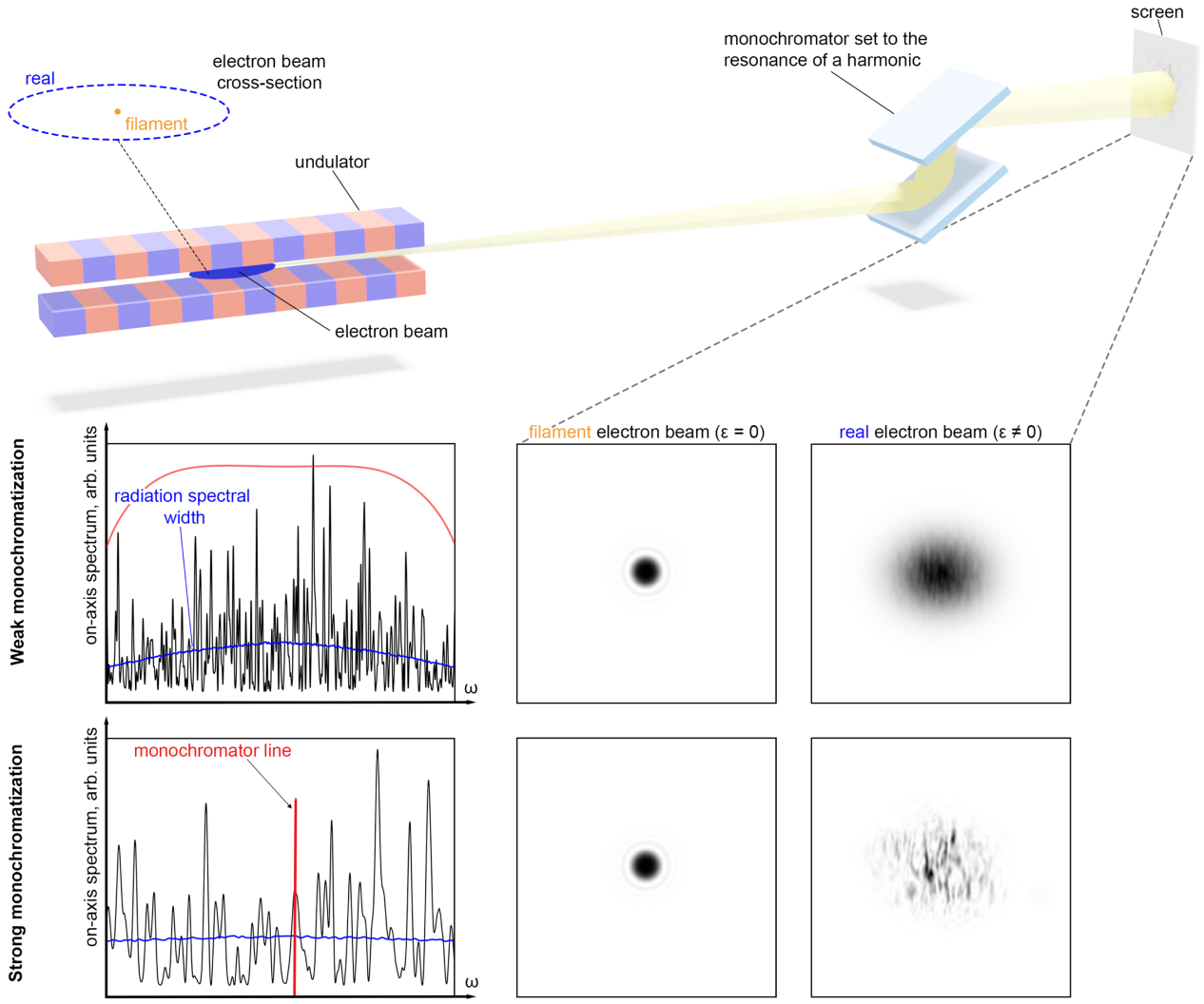

Fig. 1. Spiky structure of synchrotron radiation. We compare radiation from a filament electron beam and from an electron beam with non-zero emittance. Figures on the left contain a single realization of spectrum (black lines) and ensemble-averaged spectrum (blue lines). Red lines represent the resolving power of monochromators. The plot on the top row illustrates a typical monochromatization incapable of resolving spectral spikes. To obtain the intensity observed at a detector (after single passage of the electron beam), one needs to average over these frequencies/realizations. This is justified, as the different spikes in the spectrum are not correlated in the time or, correspondingly, frequency domain. The bottom plot represents the resolving power of a monochromator that allows to resolve a single spectral spike of undulator radiation revealing its transverse spiky structure. The four figures on the right represent transverse intensity distribution upon monochromatization.

fundamental property of thermal sources as well as synchrotron radiation. This fact will be used in the proposed algorithm.

Returning to the longitudinal direction, an electron arrival time t_k also follows Gaussian distribution $f_t(t_k)$ with standard deviation σ_T for most cases. Here σ_T is the duration of the electron beam. The electron beam length $c\sigma_T$ is almost always much larger than the radiation wavelength ($\omega\sigma_T \gg 1$). Here we do not consider coherent synchrotron radiation (CSR) *effect*. This fact implies that the phase ωt_k in Eq. (3) is uniformly distributed over the interval $(0, 2\pi)$. Also, radiation fields from individual electrons are not correlated with each other.

In general, synchrotron radiation is a non-stationary process. However, in a realistic case, the natural spectral width of undulator radiation at fundamental harmonic resonance is of order ω_r/N_w, where ω_r is the resonance frequency, and N_w is the number of undulator periods. The relation $\omega_r\sigma_T/N_w \gg 1$ still holds {see the parameters estimation in [7], paragraph after Eq. (10)}. This relation means that the longitudinal width of the spikes is much smaller than the radiation bandwidth. Having this, one can conclude that the source is quasi-stationary and derive a relation {Eq. (19) in [7]} that is an analogous to Wiener–Khinchin theorem. Quasi-stationary approximately means that the number of spikes in the longitudinal direction is large and they have the same width across the spectrum. We refer to this case as a "long" electron beam approximation.

1. Cross-Spectral Density Function

As remarked before, at conventional synchrotrons, a "long" electron beam approximation applies, and under this assumption, we can express the spatial coherence separately from the longitudinal correlation, via the *cross-spectral density function* G at fixed frequency ω {see, e.g., Eq. (12) in [7]}:

$$G(z, \vec{r}_1, \vec{r}_2, \omega) \equiv \langle \bar{E}(\vec{\eta}, \vec{l}, z, \vec{r}_1, \omega) \bar{E}^*(\vec{\eta}, \vec{l}, z, \vec{r}_2, \omega) \rangle, \quad (4)$$

where $\langle ... \rangle$ denotes averaging over the ensemble of fields $\bar{E}(\vec{\eta}_k, \vec{l}_k, z, \vec{r}, \omega)$ emitted by electrons with the deflections $\vec{\eta}_{1,...,N_e}$ and offset $\vec{l}_{1,...,N_e}$ at fixed frequency ω. Then, it is customary to define a normalized version of G, the *spectral degree of coherence* $g(z, \vec{r}_1, \vec{r}_2)$, as

$$g(z, \vec{r}_1, \vec{r}_2) = \frac{G(z, \vec{r}_1, \vec{r}_2)}{\sqrt{\langle |\bar{E}(\vec{\eta}, \vec{l}, z, \vec{r}_1)|^2 \rangle \langle |\bar{E}(\vec{\eta}, \vec{l}, z, \vec{r}_2)|^2 \rangle}}. \quad (5)$$

Starting from here, we will omit ω in the equations for brevity of the notation.

2. Quasi-Homogeneous Sources

Quasi-homogeneity is the transverse equivalent of quasi-stationarity. It means that at different transverse positions across the radiation beam intensity $\bar{I}(z, \vec{\bar{r}})$ transverse spikes have the same "shape." It allows us to factorize cross-spectral density of the virtual source (located at $z = 0$):

$$G(0, \vec{\bar{r}}, \Delta\vec{r}) = \bar{I}(0, \vec{\bar{r}}) g(0, \Delta\vec{r}), \quad (6)$$

where we introduced two new variables: $\vec{\bar{r}} = (\vec{r}_1 + \vec{r}_2)/2$ and $\Delta\vec{r} = (\vec{r}_1 - \vec{r}_2)$.

Quasi-homogeneous sources are characterized by a special relation that is strictly related to the van Cittert–Zernike theorem [36,37] between source-intensity distribution $\bar{I}(0, \vec{\bar{r}})$ and spectral degree of coherence in the far zone $g(z_0, \Delta\theta)$, where z_0 denotes the position in the far zone. Despite the word "spectral," this degree of coherence determines coherence properties in *real* or *inverse* space domain at given frequency ω, which is implied. Namely, these two quantities form a Fourier pair. Note that the factorization presented in Eq. (6) is possible if

(i) intensity of the radiation at the source varies slowly at the scale of coherence length (i.e., large number of transverse spikes);
(ii) transverse coherence length does not depend on the transverse position (i.e., similar shape of transverse spikes).

3. SIMULATING UNDULATOR RADIATION BY AN ELECTRON BEAM DIRECTLY

We introduce two different approaches to simulate radiation field from an undulator at a given frequency emitted by an electron beam with finite emittance.

The first one—*FAM*—is to sum up radiation fields (amplitudes and phases) of all individual electrons in the beam, as suggested in Eq. (3). This would allow one to construct a single realization of the field at given radiation frequency. Conventional monochromator resolution effectively sums up intensities from neighboring spectral spikes, as can be deduced from Fig. 1. Looking at single-shot pulses downstream, a conventional monochromator is equivalent to averaging over numerous realizations.

In the second approach—*intensity addition method* (IAM)—radiation fields from each electron are propagated to a sample location, and afterwards, one sums up their intensity distributions. This method relies on the assumption of a long electron beam, discussed in Section 2, and is easily applicable to wavelengths below visible light.

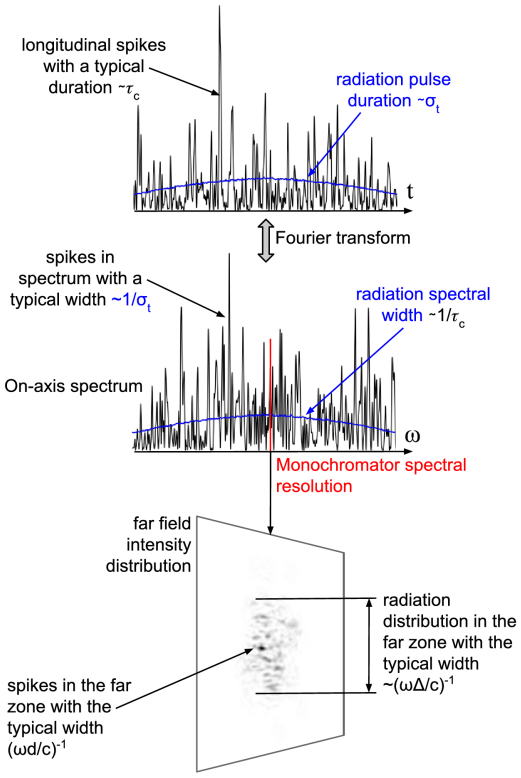

Fig. 2. Illustration of the spiky structure of a specific harmonic of undulator radiation. The red line indicates a resolving power of the monochromator. Black line represents an on-axis radiation spectrum and its time domain, and blue line shows the ensemble-averaged values. The bottom figure represents the transverse spiky structure of undulator radiation upon strong monochromatization (red line). Here we tacitly imply the quasi-homogeneity and quasi-stationarity of the source. d and Δ represent source size and typical spike size at the source, respectively, τ_c is the coherence length, σ_t is the typical radiation pulse duration, ω denotes radiation carrier frequency, and c is speed of light.

Of course, in both approaches, summing up over all electrons in the beam is not computationally feasible; however, electrons can be modeled with a smaller number of macroparticles with proportionally larger charges.

As mentioned, the IAM using macroparticles is implemented in well-known code SRW.

A. Field Addition Method

Summing up fields of N_e electrons according to Eq. (3) will result in a single statistical realization of monochromatized undulator radiation with transverse spiky structure as illustrated in Fig. 1.

The observed intensity upon averaging over realizations (with an ideal monochromator) is

$$I_\omega = \left\langle \left| \sum_{k=1}^{N_e} \bar{E}(\vec{\eta}_k, \vec{l}_k, z, \vec{r}) \exp(i\omega t_k) \right|^2 \right\rangle, \quad (7)$$

where the transverse ensemble-averaged intensity distribution converges and becomes "smooth." This approach is illustrated in Fig. 3 and provides the most straightforward solution to the problem of simulating partially coherent synchrotron radiation.

Also with this method, one can simulate *coherent synchrotron radiation* (CSR) by summing all fields emitted by the electrons

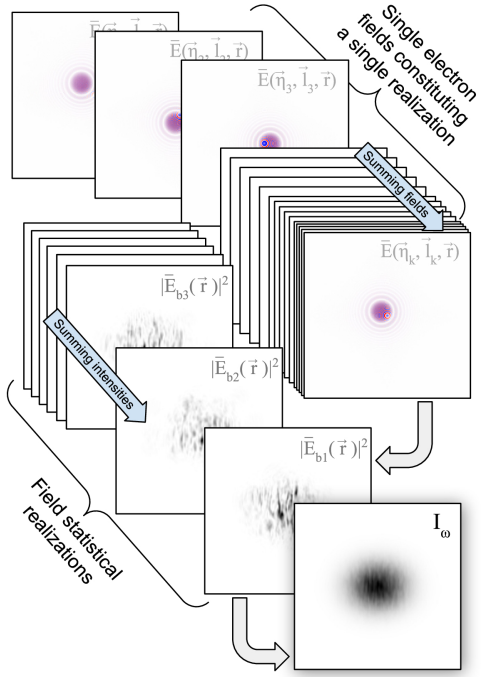

Fig. 3. Scheme of the field addition method. Radiation from macroparticles $\bar{E}(\vec{\eta}_k, \vec{l}_k, \vec{r})$ is summed up to compose a single field realization $\bar{E}_{1b}(\vec{r})$. Each $\bar{E}(\vec{\eta}_k, \vec{l}_k, \vec{r})$ is displayed with false color (positive values with red and negative with blue) to show the amplitude and phase of the radiation. After averaging over different field realizations $\bar{E}_b(\vec{r})$, one obtains the resulting intensity.

in phase ωt_k (pancake beam approximation) or any other phase distribution allowing to account for the sizes of the electron beam comparable to the radiation wavelength, e.g,. THz radiation.

We note that both numbers—number of bunches N_b and number of electrons N_e—have a direct physical meaning. However, the number of electrons in a beam is immense. To deal with this in simulations, one needs to exploit a concept of macroparticles N_p. This number is relatively low, of order of hundreds, but sufficient for obtaining statistically meaningful intensities and correlations. Depending on the degree of coherence, this number may vary: a poorer degree of coherence requires a higher number of realizations for obtaining statistically meaningful results, i.e., one macroparticle is enough to simulate a zero-emittance beam. The optimal amount of macroparticles should be found empirically when increasing the quantity leads to a diminishing change in the simulation results.

The time needed for such calculations can be estimated as the time required to calculate N_e instances of the fields (for each electron), and afterward averaging over N_b field realizations $\bar{E}_b$. To sum up, if τ_{calc} is the time needed for calculating the field from a single electron, then the time needed for the resulting ensemble-averaged intensity is $T_{calc} = \tau_{calc} \cdot N_e \cdot N_b$.

B. Intensity Addition Method

In the case of a long electron beam, the calculation time can be shortened by knowing that the electron arrival times t_k are not correlated with each other. Because of this, radiation from different electrons is also not correlated. This means that when we rewrite the ensemble-averaged intensity in Eq. (7) as

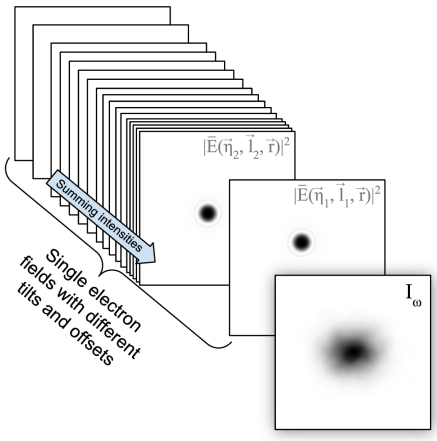

Fig. 4. Scheme of the intensity addition method. Having a "long" electron beam, one sums up intensities to obtain the resulting intensity distribution after propagating radiation from each macroparticle through a beamline. Computationally, fields from single electrons are saved in cache memory as different slices of an array (as schematically depicted). These slices then are used to perform beam propagation simulations.

$$I_\omega = \left\langle \sum_{k=1}^{N_e} \bar{E}(\vec{\eta}_k, \vec{l}_k, z, \vec{r}) \bar{E}^*(\vec{\eta}_k, \vec{l}_k, z, \vec{r}) \right\rangle + \left\langle \sum_{k=1}^{N_e} \sum_{\substack{n=1 \\ k \neq n}}^{N_e} \bar{E}(\vec{\eta}_k, \vec{l}_k, z, \vec{r}) \bar{E}^*(\vec{\eta}_n, \vec{l}_n, z, \vec{r}) \times \exp[i\omega(t_k - t_n)] \right\rangle, \tag{8}$$

the second term vanishes after averaging over the statistical ensemble. The sum over N_e electrons in the first term in Eq. (8) is equal to an integral over the transverse electron beam phase space (smooth) distribution functions of offsets $f_l(\vec{l})$ and deflections $f_\eta(\vec{\eta})$:

$$I_\omega = \left\langle \sum_{k=1}^{N_e} |\bar{E}(\vec{\eta}_k, \vec{l}_k, z, \vec{r})|^2 \right\rangle = N_e \iint_{\mathbb{R}^4} f_l(\vec{l}) f_\eta(\vec{\eta}) |\bar{E}(\vec{\eta}, \vec{l}, z, \vec{r})|^2 \mathrm{d}\vec{l}\mathrm{d}\vec{\eta}, \tag{9}$$

which gives us the radiation distribution. Averaging over the ensemble reduces to a sum of N_e single electrons, which provides a way to evaluate the integral:

$$I_\omega \propto \sum_{k=1}^{N_e} |\bar{E}(\vec{\eta}_k, \vec{l}_k, z, \vec{r})|^2. \tag{10}$$

Moreover, one can calculate the cross-spectral density according to Eq. (4). This approach, based on Eq. (10), grants a powerful and time-efficient method for calculating partially coherent synchrotron radiation.

The time needed for calculation becomes just $T_{calc} = \tau_{calc} \cdot N_e$. We call this approach, for simplicity, IAM. We depict the scheme of this method in Fig. 4.

4. SERVAL ALGORITHM

In this section, we will show that it is possible to obtain results of the FAM described in Section 3.A within a convenient computational

time and under the assumption of quasi-homogeneity of the source using an alternative approach. This algorithm—SERVAL—simulates the stochastic properties of synchrotron radiation that are imprinted in each pulse due to the shot noise in the electron beam. It requires the electron beam to be long, which is actually a non-restrictive assumption in most cases at synchrotrons. We will present this algorithm analytically, showing its strict validity in the case of quasi-homogeneous sources. We also discuss deviations from this approximation and present the application of SERVAL for simulating a beamline.

A. Algorithm Description

We shape the transverse distribution of the field from an undulator as a GRF in a manner similar to those mathematically described in [38], explained in simple words in [39], and exploited in imitating spectra and power distributions of FEL in the linear regime in [33,40].

The SERVAL field at the center of an undulator ($z = 0$) can be written in the following form:

$$\phi(\vec{r}) = \mathcal{F}^{-1}\left\{\sqrt{\hat{I}(\vec{\theta})}\mathcal{F}\left\{\sqrt{\bar{I}(\vec{r}')}\mathcal{W}(\vec{r}')\right\}(\vec{\theta})\right\}(\vec{r}), \tag{11}$$

where $\mathcal{F}\{\cdot\}(\vec{\theta})$ and $\mathcal{F}^{-1}\{\cdot\}(\vec{r})$ are direct and inverse Fourier transforms, respectively, and $\mathcal{W}(\vec{r}) = X(\vec{r}) + iY(\vec{r})$ is complex Gaussian white noise, where $X(\vec{r})$, $Y(\vec{r})$ follow the normal distribution with a mean equal to zero and variance equal to unity. Finally,

$$\bar{I}(\vec{r}) = |\bar{E}_b(0,\vec{r})|^2 = \int_{\mathbb{R}^2} f_l(\vec{l})|\bar{E}(\vec{\eta},\vec{l},0,\vec{r})|^2 \mathrm{d}\vec{l}, \tag{12}$$

$$\hat{I}(\vec{\theta}) = |\hat{E}_b(0,\vec{\theta})|^2 = \int_{\mathbb{R}^2} f_\eta(\vec{\eta})|\hat{E}(\vec{\eta},\vec{l},0,\vec{\theta})|^2 \mathrm{d}\vec{\eta} \tag{13}$$

are the intensity distributions of the radiation from the whole electron beam in $\vec{r}$ domain and inverse-spatial $\vec{\theta}$ domain, correspondingly. The fields $\bar{E}(\vec{\eta},\vec{l},0,\vec{r})$ and $\hat{E}(\vec{\eta},\vec{l},0,\vec{\theta})$ are calculated with a help of Eq. (39) and Eq. (40) from [41]. The physical idea behind Eq. (11) is that the resulting field $\phi(\vec{r})$ should follow Gaussian statistics and obey the correct first order cross-spectral density function $g(0,\vec{r}_1,\vec{r}_2)$ under the quasi-homogeneous approximation, as we show in Appendix A. Following Eq. (11), the proposed algorithm consists of four steps: (i) creating complex Gaussian white noise, (ii) constraining it by radiation distribution in the spatial domain at the source location, (iii) Fourier transform to inverse-spatial domain, and (iv) constraining the resulting field in the inverse-spatial domain. $\vec{r}$ and $\vec{\theta}$ are assumed to be uncorrelated. We discuss these steps in more detail below:

(i) Creating complex Gaussian white noise $\mathcal{W}(\vec{r}_n) = X(\vec{r}_n) + iY(\vec{r}_n)$ in spatial domain.
(ii) Constraining the complex Gaussian white noise by multiplication of the effective distribution of the radiation at the source expressed by Eq. (12). The result of this step is depicted in Fig. 5(b).
(iii) Fourier transforming to the inverse-spatial domain [Fig. 6(a)]. At this stage, we have a fully incoherent light source bounded in space akin to a *thermal light source*.

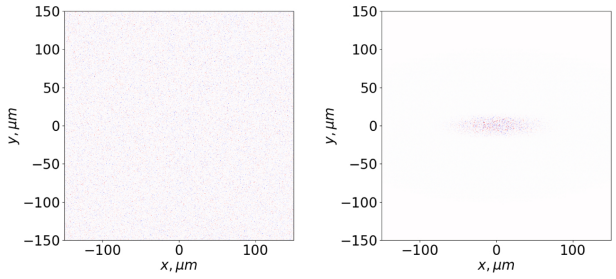

Fig. 5. Intensity of complex Gaussian white noise in spatial domain before (a) and after (b) constraining by the effective field size.

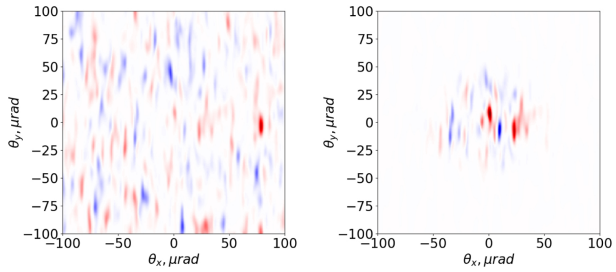

Fig. 6. Angular intensity distribution of the field before (a) and after (b) applying radiation divergence constraints.

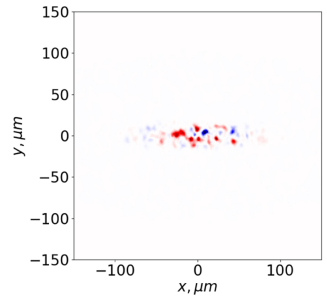

Fig. 7. Radiation distribution at the source in real space.

(iv) Constraining the inverse-spatial distribution in Fig. 6(a) by multiplication with the effective radiation divergence following Eq. (13). This field is ready for propagation through free space, as the free-space propagator works in the inverse-space domain.

After an inverse Fourier transform of the field in Fig. 6(b) back to real space, one obtains the intensity distribution at the source, presented in Fig. 7.

As a result, Figs. 7 and 6(b) depict a single realization of undulator radiation distribution at the source (in the center of the undulator cell), seen through a monochromator capable of resolving beyond the width of a single spike in the frequency domain.

SERVAL yields a radiation field at a given frequency (similar to what other codes do: SRW, mode decomposition algorithm, etc.). Nevertheless, if one needs to simulate transverse radiation distribution downstream a typical monochromator (encompassing numerous spikes), one simply generates single realizations at

slightly different frequencies within the monochromator bandwidth as illustrated in Fig. 1. To obtain the intensity observed at a detector, one needs to average over these frequencies/realizations. This is justified, as the different modes in the spectrum are not correlated (in either t or, correspondingly, ω domain). The computational efficiency of the proposed algorithm may be estimated considering the steps involved: generate $N_x \cdot N_y$ realizations of $\mathcal{W}(r_n)$, and carry out two multiplications by constraints and two Fourier transforms. We present a speed test where we compare SERVAL with direct simulation approaches in Appendix B. As we found, using a common laptop, SERVAL performs two orders of magnitude faster compared to the FAM and two times faster than the IAM. However, this result may vary depending on the hardware and programming environment used.

B. Underlining Assumptions and Approximations

As anticipated in Section 2, and demonstrated in Appendix A, SERVAL is mathematically well-founded for quasi-homogeneous sources, where the cross-spectral density at the source factorizes [Eq. (6)]. This is a strong restriction. In Appendix A, we show to which extent we can apply SERVAL when quasi-homogeneity (large number of spikes) does not hold. We found that our method is satisfactorily applicable if a source is not strictly quasi-homogeneous.

When using SERVAL, we consider single-cell undulators: the single source must have only one waist. This basically implies no quadrupoles, phase shifters, etc., in the magnetic structure of the insertion device. For a magnetic structure with imperfections, one can calculate the intensity distributions from a filament beam [Eqs. (12) and (13)] numerically for a given magnetic structure and then convolve them with the electron beam phase space. If we simulate radiation with SERVAL, the effects of the electron beam emittance (along with energy spread) are accounted for in $\bar{I}(\vec{r})$ and $\hat{I}(\vec{\theta})$ [Eq. (11)].

Under these assumptions, SERVAL accurately calculates synchrotron radiation pulses with computational advantages over direct methods. The SERVAL algorithm is not exclusively restricted to undulator sources, as $\bar{I}(\vec{r})$ and $\hat{I}(\vec{\theta})$ do not impose any additional restrictions except quasi-homogeneity. Thus, this GRF generator can be used to simulate the stochastic properties of other types of radiation sources.

5. APPLICATION OF THE SERVAL ALGORITHM FOR WAVEFRONT PROPAGATION SIMULATIONS

In this section, we present an application of SERVAL for simulating the electromagnetic field emitted by an undulator and its propagation through a beamline using the Ocelot toolkit. To illustrate SERVAL performance outside of its applicability region, we set the electron beam parameters such that they, strictly speaking,

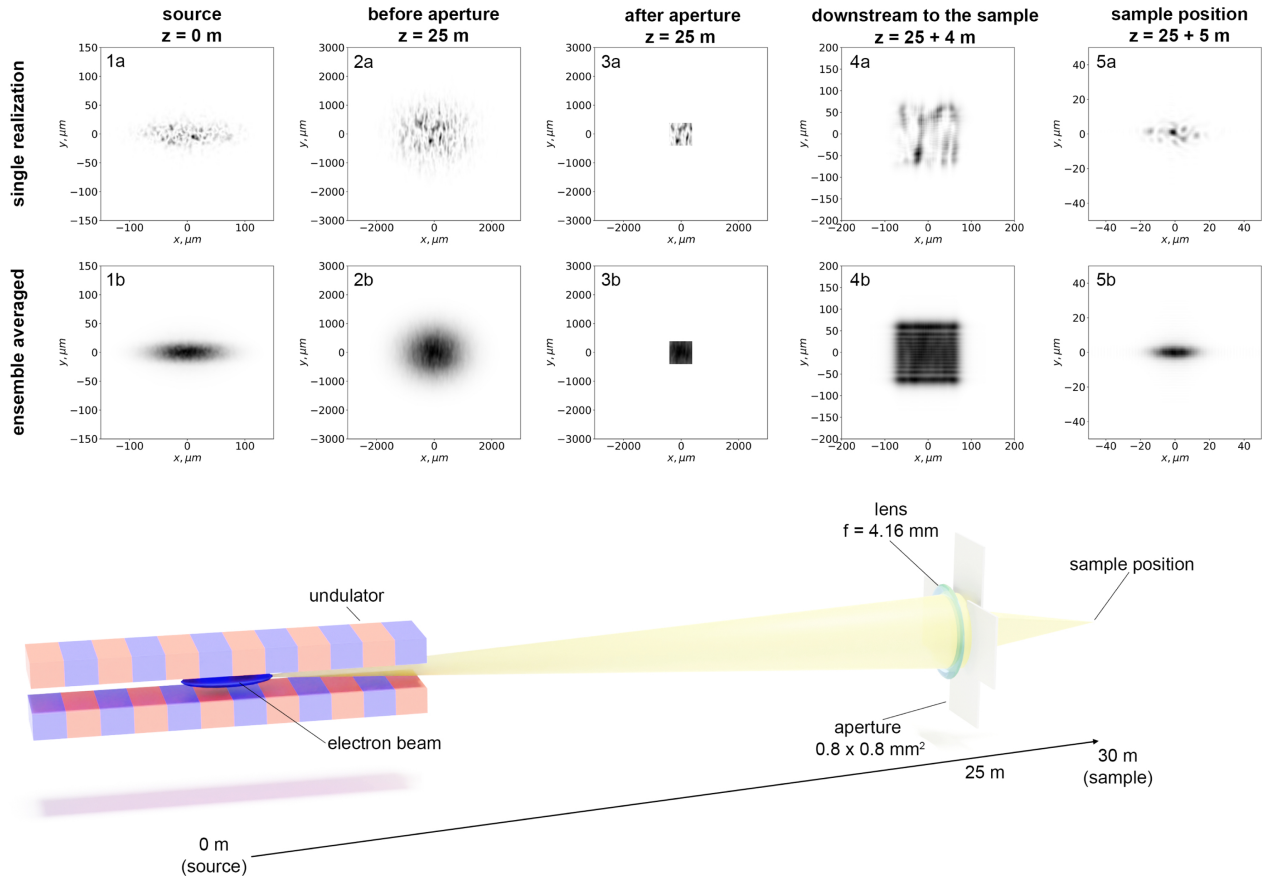

Fig. 8. Optical scheme assumed for simulation. Here we propagate radiation at the given frequency, which is why *no monochromator* is presented in the beamline scheme. Left to right: undulator, thin lens with focal distance 4.16 m combined with 0.8 × 0.8 mm^2 aperture, both located at 25 m downstream from the center of the undulator. The lens re-images the radiation at the sample, located 5 m downstream. (1a)–(5a) and (1b)–(5b) illustrate simulated evolution of radiation distribution. In the top row, we depict single realization shots, and in the bottom row, averaged intensity distributions.

Table 1. Assumed Undulator Parameters

E_{ph}, [eV]	λ_w, [mm]	Periods
2167	18.	200

Table 2. Assumed Electron Beam Parameters

E, [GeV]	σ_x, [μm]	σ_y, [μm]	$\sigma_{x'}$, [μrad]	$\sigma_{y'}$, [μrad]
3	38	4.7	25	20

do not follow the approximation of quasi-homogeneity. In the presented simulation, the resulting number of spatial radiation spikes is relatively small. The applicability of SERVAL is discussed in detail in Appendix A.

We consider a simple optical system consisting of a radiation source (undulator), an aperture, and a focusing element (see Fig. 8). The undulator and the electron beam parameters are presented in Tables 1 and 2.

These electron beam parameters correspond to $N_x = 4.4$, $N_y = 0.07$ and $D_x = 24.7$, $D_y = 15.8$ according to the definition in Eq. (2).

In Fig. 8, we present radiation intensity distributions of SERVAL-generated field at different positions upon propagation through the simple optical scheme. In this simulation, we propagate *monochromatic realization* of the radiation field, which is why we do not depict the monochromator in the figure. We show both single realization and ensemble-averaged distributions. In this simulation, we used a transverse mesh of 601×601 pixels^2 and averaged over 401 statistical realizations of the field, which converges towards routinely observable smooth distributions. We calculate the intensity distribution at the source and present it in Figs. 8(1a) and 8(1b), then propagate this radiation downstream the beamline using a free-space propagator over 25 m [Figs. 8(2a) and 8(2b)]. Afterwards, we cut this radiation with a 0.8×0.8 mm^2 aperture [Figs. 8(3a) and 8(3b)] and, using a thin lens with focal distance $f = 4.16$ m, focus the radiation down to the sample. To show the diffraction effect that takes place after aperturing, we present the intensity distribution after 4 m of free-space propagation downstream the lens in Figs. 4(a) and 4(b). Upon aperturing at the sample position, we observe a reduction in the number of spikes in the radiation structure. Note that due to higher coherence in the vertical direction, the diffraction pattern is much more pronounced. We present the demagnified image of the source in [Figs. 8(5a) and 8(5b)].

Here we note that averaging over statistical realizations is equivalent to observing the intensity distributions through a conventional monochromator. This can be explained by the fact that common monochromator resolution is still much broader than spike width. One may find further reasoning on this in [7].

We note that considering the electron beam size, we observe more spikes in the horizontal direction than in the vertical one. The typical spike size corresponds to the transverse coherence length. Results of propagating radiation modeled with SERVAL reveals the main aspects of partially coherent radiation and its propagation. Generation of each realization and its propagation in Ocelot took a couple of seconds using a laptop. Of course, such a radiation field can be propagated with other numerical codes such as SRW involving more complex optical elements, however with a benefit of processing multimode fields.

6. CONCLUSION

In this paper, we propose a novel computationally efficient algorithm, SERVAL, for simulating partially coherent synchrotron radiation emitted by an undulator at a specific harmonic. The proposed method is based on generating a GRF followed by application of constraints in real and inverse space domains. The result exhibits multimode structure that qualitatively corresponds to a radiation "slice" along the radiation pulse or that could be observed experimentally upon extreme monochromatization.

The algorithm yields a radiation field at the source position, which is usually in the middle of the undulator. One can propagate this field through an optical beamline to the sample location by conventional methods and codes for coherent radiation propagation. The proposed algorithm may be exploited for educational purposes when explaining the basics of coherence.

APPENDIX A: SERVAL REGION OF APPLICABILITY

1. Analytical Treatment

In this appendix, we show explicitly that under the assumption of quasi-homogeneity, the SERVAL algorithm can be used to simulate undulator radiation. First, we will show that the SERVAL field cross-spectral density function coincides with that of the electric field originated from the undulator.

The SERVAL field produced by the GRF generator is written as

$$\phi(\vec{r}) = \mathcal{F}^{-1}\left\{\sqrt{\hat{I}(\vec{\theta})}\mathcal{F}\left\{\sqrt{\bar{I}(\vec{r}')}\mathcal{W}(\vec{r}')\right\}(\vec{\theta})\right\}(\vec{r}). \tag{A1}$$

Then the cross-spectral density function is the following:

$$\begin{aligned}\langle\phi(\vec{r}_1)\phi^*(\vec{r}_2)\rangle = \Bigg\langle &\iint_{\mathbb{R}^4} e^{-2\pi i\{(\vec{r}_1\cdot\vec{\theta}_1)-(\vec{r}_2\cdot\vec{\theta}_2)\}}\sqrt{\hat{I}(\vec{\theta}_1)\hat{I}(\vec{\theta}_2)} \\ &\times \iint_{\mathbb{R}^4} e^{2\pi i\{(\vec{r}'_1\cdot\vec{\theta}_1)-(\vec{r}'_2\cdot\vec{\theta}_2)\}}\sqrt{\bar{I}(\vec{r}'_1)\bar{I}(\vec{r}'_2)} \\ &\times \mathcal{W}(\vec{r}'_1)\mathcal{W}^*(\vec{r}'_2)\mathrm{d}\vec{r}'_1\mathrm{d}\vec{r}'_2\mathrm{d}\vec{\theta}_1\mathrm{d}\vec{\theta}_2\Bigg\rangle,\end{aligned} \tag{A2}$$

where $(\cdot)$ denotes a dot product. The field $\phi(\vec{r})$ is taken at the source position, i.e., center of the undulator. We bring averaging over an ensemble $\langle\ldots\rangle$ inside the integral and take the integral over $\vec{r}'_1$, where we account for the relation $\langle\mathcal{W}(\vec{r}'_1)\mathcal{W}^*(\vec{r}'_2)\rangle = \delta(\vec{r}'_1 - \vec{r}'_2)$:

$$\begin{aligned}\langle\phi(\vec{r}_1)\phi^*(\vec{r}_2)\rangle = &\iint_{\mathbb{R}^4} e^{-2\pi i\{(\vec{r}_1\cdot\vec{\theta}_1)-(\vec{r}_2\cdot\vec{\theta}_2)\}}\sqrt{\hat{I}(\vec{\theta}_1)\hat{I}(\vec{\theta}_2)} \\ &\times \int_{\mathbb{R}^2} e^{2\pi i\{((\vec{\theta}_1-\vec{\theta}_2)\cdot\vec{r}'_2)\}}\bar{I}(\vec{r}'_2)\mathrm{d}\vec{r}'_2\mathrm{d}\vec{\theta}_1\mathrm{d}\vec{\theta}_2.\end{aligned} \tag{A3}$$

Under the assumption of quasi-homogeneity, we can apply van Cittert–Zernike theorem, which relates the intensity distribution at the source $\bar{I}(\vec{r}'_2)$ with the cross-spectral density function in the far zone $g(\Delta\vec{\theta})$ via Fourier transform; here we imply that $\Delta\vec{\theta} = \vec{\theta}_2 - \vec{\theta}_1$:

$$\langle\phi(\vec{r}_1)\phi^*(\vec{r}_2)\rangle = \iint_{\mathbb{R}^4} e^{-2\pi i\{(\vec{r}_1\cdot\vec{\theta}_1)-(\vec{r}_2\cdot\vec{\theta}_2)\}}\sqrt{\hat{I}(\vec{\theta}_1)\hat{I}(\vec{\theta}_2)}g(\Delta\vec{\theta})\mathrm{d}\vec{\theta}_1\mathrm{d}\vec{\theta}_2. \tag{A4}$$

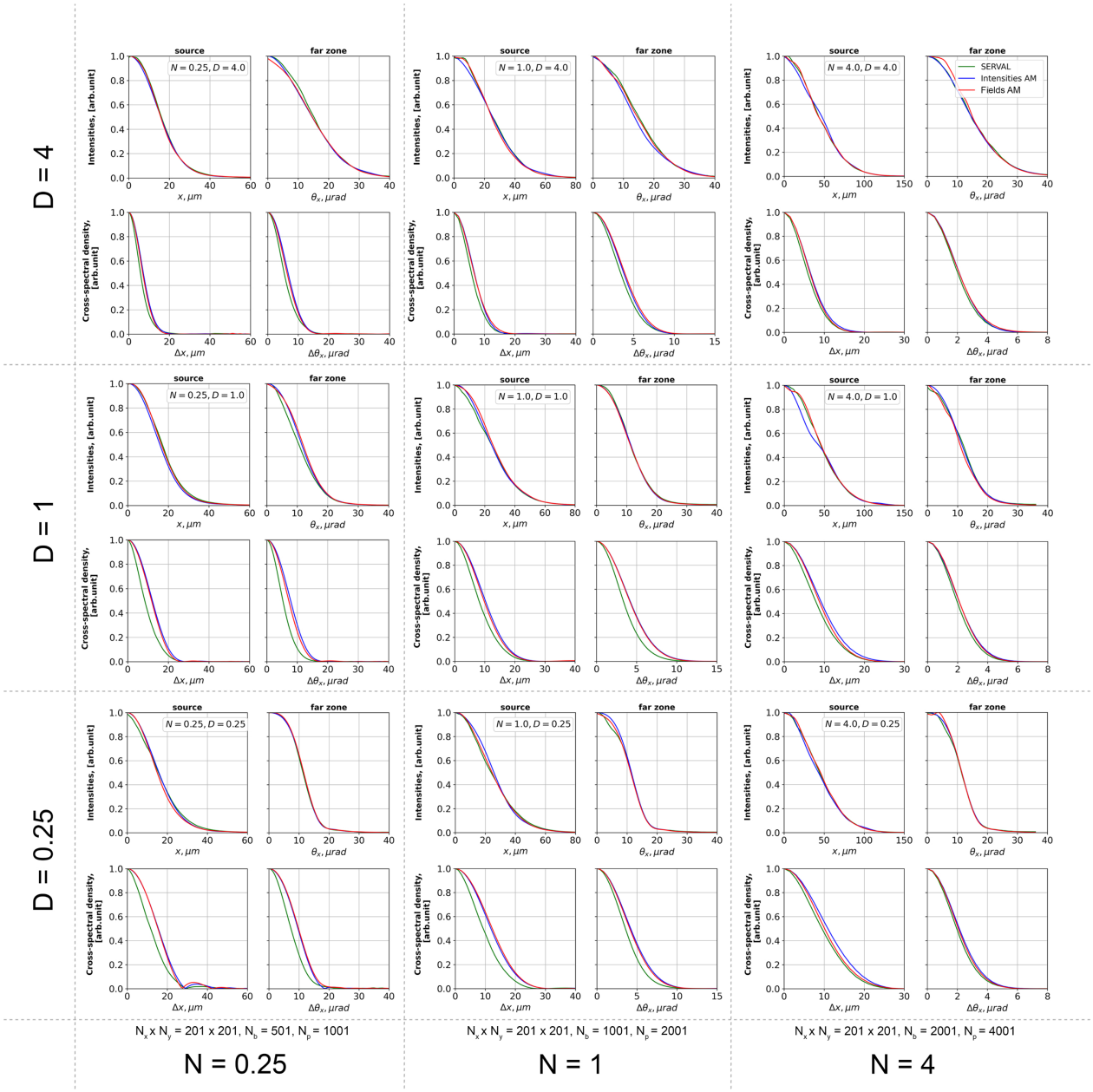

Fig. 9. Simulation results with different combinations of N and D parameters. In turn, each combination contains results obtained with three methods: SERVAL algorithm (green line), intensity addition method (blue line), and field addition method (red line). For each N and D combination, the top rows show *intensity distributions*, bottom rows square moduli of *cross-spectral density functions* for radiation *at the source* location (left columns) and *in the far zone* (right columns). For each N parameter, we use different numbers of statistical realizations and macroparticles taken, which we mark at the bottom of each column.

Accounting for the relation $\sqrt{\hat{I}(\vec{\theta}_1)\hat{I}(\vec{\theta}_2)}g(\Delta\vec{\theta}) = \langle \hat{E}(\vec{\eta}, \vec{l}, 0, \vec{\theta}_1)\hat{E}^*(\vec{\eta}, \vec{l}, 0, \vec{\theta}_2)\rangle$ and putting $\langle ... \rangle$ outside of the integral, we obtain

$$\begin{aligned}\langle \phi(\vec{r}_1)\phi^*(\vec{r}_2)\rangle &= \left\langle \int_{\mathbb{R}^2} \hat{E}\left(\vec{\eta}, \vec{l}, 0, \vec{\theta}_1\right) e^{-2\pi i(\vec{r}_1\cdot\vec{\theta}_1)} \mathrm{d}\vec{\theta}_1 \right. \\ &\quad \left. \times \left(\int_{\mathbb{R}^2} \hat{E}\left(\vec{\eta}, \vec{l}, 0, \vec{\theta}_2\right) e^{-2\pi i(\vec{r}_2\cdot\vec{\theta}_2)} \mathrm{d}\vec{\theta}_2 \right)^* \right\rangle \\ &= \left\langle \bar{E}\left(\vec{\eta}, \vec{l}, 0, \vec{r}_1\right) \bar{E}^*\left(\vec{\eta}, \vec{l}, 0, \vec{r}_2\right) \right\rangle. \end{aligned} \tag{A5}$$

As a result, under the assumption of quasi-homogeneity, SERVAL fixes the correct first order correlation function for the field. Since synchrotron radiation is a Gaussian random process, this is sufficient to fix correlation functions at any order, and therefore to fully define the process.

We now show that the same relation also holds for intensity distributions. Setting $\vec{r}_1 = \vec{r}_2 = \vec{r}$ in the previous equation, we obtain an expression for intensity distributions at the source in $(\vec{r})$ domain:

$$\left\langle \phi(\vec{r})\phi^*(\vec{r}) \right\rangle = \left\langle \bar{E}(\vec{\eta}, \vec{l}, 0, \vec{r})\bar{E}^*(\vec{\eta}, \vec{l}, 0, \vec{r}) \right\rangle = \bar{I}(\vec{r}), \tag{A6}$$

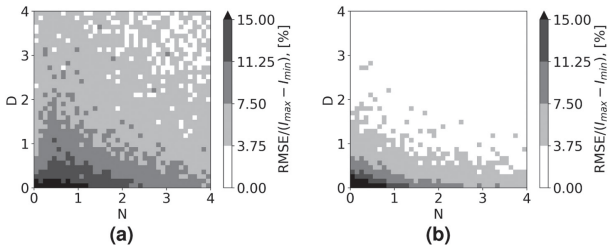

Fig. 10. RMSE of cross-spectral density functions of SERVAL and IAM for different sized N and divergence D of the electron beam. (a) Cross-spectral density function discrepancy *at the source*. (b) Cross-spectral density function discrepancy *in the far zone*.

and in the same manner, one can show equality for the inverse space domain, i.e.,

$$\left\langle \hat{\phi}(\vec{\theta}_1)\hat{\phi}^*(\vec{\theta}_2)\right\rangle = \left\langle \hat{E}(\vec{\eta},\vec{l},0,\vec{\theta}_1)\hat{E}^*(\vec{\eta},\vec{l},0,\vec{\theta}_2)\right\rangle, \tag{A7}$$

and when $\vec{\theta}_1 = \vec{\theta}_2 = \vec{\theta}$,

$$\left\langle \hat{\phi}(\vec{\theta})\hat{\phi}^*(\vec{\theta})\right\rangle = \hat{I}(\vec{\theta}). \tag{A8}$$

2. Simulations

Here we demonstrate the accuracy of the SERVAL algorithm beyond its strict region of applicability of quasi-homogeneous approximation. This approximation applies when $N \gg 1$, $D \gg 1$. Using SERVAL, IAM, and FAM, we calculate intensity distributions and plot them as well as cross-spectral density functions at both the source and in the far zone. We present results for a combination of N, $D = 0.25, 1, 4$ in Fig. 9. For the speed test calculation, we use Eq. (33) from [41] for the field in the far zone. As one can see, SERVAL provides correct intensity and cross-spectral density distributions already with $N = 4$ and $D = 4$. Fluctuation of the intensity distributions is caused by a finite number of statistical realizations and macroparticles generated in this simulation.

To illustrate the discrepancy trends, we present a parameter scan of root mean square error (RMSE) between SERVAL and IAM over different combinations of N and D parameters. In Fig. 10, each pixel is valued as RMSE, normalized to the factor $1/(I_{\max} - I_{\min})$ and expressed in percent, where $I_{\max}$ and $I_{\min}$ are the maximum and minimum intensities for the IAM result within the simulation window. To facilitate the comparison, the figures are plotted with the same color scale.

These figures show the main trend for the correlation functions: higher N and D values provide higher similarity of SERVAL with the intensity addition method results. The intensity distributions coincide exceedingly well for all N and D parameters (Fig. 9). As one can see from Fig. 10(a), SERVAL is less applicable for a focused beam. However, the presence of apertures in a focusing system reduces the discrepancy of the cross-spectral density in focus between SERVAL and IAM.

APPENDIX B: COMPUTATIONAL EFFICIENCY

We compared computational efficiency of the discussed algorithms. Computational time to generate a single statistical realization differs drastically for FAM (~**670** ms/realization with 400 macroparticles) and SERVAL (~**4.2** ms/realization) on a usual laptop using Python programming language. Here the transverse mesh consisted of 201 × 201 pixels, with $N = 4$, $D = 4$.

IAM does not exploit the concept of statistical realizations. For this method, we performed a test based on a comparison of the time needed to generate an ensemble-averaged (i.e., "weakly monochromatized") field. We measured the time needed to generate the field presented in Fig. 9 ($N = 4$, $D = 4$) using SERVAL and IAM. The main criterion for the comparison is that fields should have a sufficient level of convergence with the reasonable number of macroparticles taken: ($N_p = 4001$) for IAM and number of realizations ($N_b = 2001$) for SERVAL. This test showed that SERVAL calculates this field for **11 s** and IAM for **27.6 s**. For memory-saving calculations, one can simulate and propagate each realization or radiation from a macroparticle separately or by chunks (10, 100, ... realizations) and store the rest of them on the hard-drive memory, but surely this may significantly slow down a simulation. We note that all three methods are very well suited for parallel computing.

A single SERVAL realization may contain a large amount of spikes. Since each realization is propagatable through the beamline to the sample, one would expect faster convergence at large N and D, compared with IAM, which implies propagating a single spike—radiation from each macroparticle—individually.

Comparing SERVAL with the mode decomposition method presented in [20], one can find that with SERVAL, calculation of the N_b realizations of the field with the mesh grid $N_g = N_x \times N_y$ starting from noise takes only $N_b(\mathcal{O}(N_g log(N_g)) + 2N_g)$ *arithmetic operations*, where $\mathcal{O}(\cdot)$ is the big O notation. For the mode decomposition method, calculations require taking $N_g^2 + N_m$ *two-dimensional integrals* with the "matrix method", where N_m is the number of modes calculated, and with the "two steps method", it takes $2N_m N_g(2 + N_m)$ integrations.

APPENDIX C: DOUBLE-SLIT EXPERIMENT SIMULATION

Here we present the results of a double-slit experiment simulated with SERVAL as well as with the IAM. We exploit parameters similar to those used in the simulation depicted in Fig. 9, $N = 4$

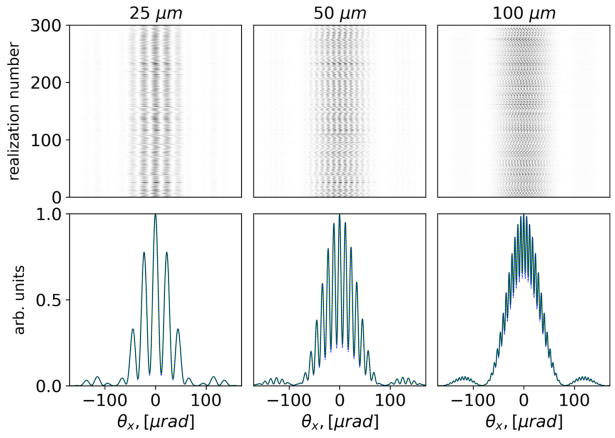

Fig. 11. Interference pattern in the far zone after diffraction at the double slits. Two vertical 8 μm slits are located 25 m from the source. Slit separation is indicated at the top. SERVAL algorithm, green line; intensity addition method, blue line. The top row represents fringe distribution depending on the realization number for the vertical axis and a transverse distribution obtained with SERVAL for horizontal axis. After averaging over the ensemble, this results in the distributions presented in the bottom row. The approaches show excellent agreement.

and $D = 4$. In Fig. 11, we present the simulation result for vertical orientation of the slits.

With SERVAL, we simulate single realizations of partially coherent radiation. Visibility $\mathcal{V} = (I_{\max} - I_{\min})/(I_{\max} + I_{\min})$ of the diffraction fringes from each realization is equal to unity, which can be seen corresponding to fully coherent radiation. However, this is because each statistical realization is fully deterministic. In other words, it is represented by one given electric field function. To describe a partially coherent source, one needs to collect an ensemble of these statistical realizations to result in statistically meaningful intensities and correlations. By itself, a single realization does not represent the coherence properties of the source.

Acknowledgment. We thank Evgeny Saldin for the initial discussions on the realization of the proposed method and his guiding support. We thank Serguei Molodtsov for his interest in this work.

Disclosures. The authors declare no conflicts of interest.

Data availability. Data presented in this paper are generated with the Ocelot toolkit [33]; the algorithm code described in the paper is publicly available at the dev_gen development branch of Ocelot and located in ocelot/ocelot/optics/wave.py.

REFERENCES

1. R. Bartolini, "Challenges in the design and construction of diffraction limited synchrotron light sources," presented at DESY Photon Science Users' Meeting (28 January2021).
2. R. Hettel, "Challenges in the design of diffraction-limited storage rings," in *5th International Particle Accelerator Conference (IPAC)*, JACoW, Geneva, Switzerland, 2014, p. 5.
3. F. Cerrina, "Ray tracing of recent VUV monochromator designs," Proc. SPIE **0503**, 68–77 (1984).
4. A. Erko, *Modern Developments in X-Ray and Neutron Optics*, Springer Series in Optical Sciences (Springer, 2008), Vol. **137**.
5. M. S. del Rio, N. Canestrari, F. Jiang, and F. Cerrina, "SHADOW3: a new version of the synchrotron x-ray optics modelling package," J. Synchrotron Radiat. **18**, 708–716 (2011).
6. X. Shi, R. Reininger, M. S. del Rio, and L. Assoufid, "A hybrid method for x-ray optics simulation: combining geometric ray-tracing and wavefront propagation," J. Synchrotron Radiat. **21**, 669–678 (2014).
7. G. Geloni, E. Saldin, E. Schneidmiller, and M. Yurkov, "Transverse coherence properties of x-ray beams in third-generation synchrotron radiation sources," Nucl. Instrum. Methods Phys. Res. A **588**, 463–493 (2008).
8. Y. Takayama, N. Takaya, T. Miyahara, S. Kamada, W. Okamoto, T. Hatano, R. Tai, and Y. Kagoshima, "Spatial coherence of undulator radiation beyond the van Cittert–Zernike theorem," Nucl. Instrum. Methods Phys. Res. A **441**, 565–576 (2000).
9. S. Marchesini and R. Coisson, "Spatial coherence of synchrotron radiation," Recent Research Developments in Optics UCRL-JRNL-200688 (Lawrence Livermore National Laboratory (LLNL), 2003).
10. R. Coïsson and S. Marchesini, "Gauss–Schell sources as models for synchrotron radiation," J. Synchrotron Radiat. **4**, 263–266 (1997).
11. R. Coïsson, "Spatial coherence of synchrotron radiation," Appl. Opt. **34**, 904–908 (1995).
12. K.-J. Kim, "Brightness, coherence and propagation characteristics of synchrotron radiation," Nucl. Instrum. Methods Phys. Res. A **246**, 71–76 (1986).
13. K.-J. Kim, "A new formulation of synchrotron radiation optics using the Wigner distribution," Proc. SPIE **0582**, 2–9 (1986).
14. J. Goodman, *Statistical Optics*, Wiley Series in Pure and Applied Optics (Wiley, 2015).
15. R. Khubbutdinov, A. P. Menushenkov, and I. A. Vartanyants, "Coherence properties of the high-energy fourth-generation x-ray synchrotron sources," J. Synchrotron Radiat. **26**, 1851–1862 (2019).
16. A. Singer, "Coherence properties of third and fourth generation x-ray sources. Theory and experiment," Technical Report DESY-THESIS–2013-023 (Deutsches Elektronen-Synchrotron (DESY), 2013).
17. W.-Q. Hua, F.-G. Bian, L. Song, X.-H. Li, and J. Wang, "Hard x-ray optics simulation using the coherent mode decomposition of the Gaussian Schell model," Chin. Phys. C **37**, 068001 (2013).
18. W. Q. Hua, F. G. Bian, L. Song, Y. Wang, and J. Wang, "Application of Gaussian Schell-model and its coherent mode decomposition on hard x-ray synchrotron radiation," in *Symposium on Photonics and Optoelectronics* (2012), pp. 1–6.
19. A. Singer and I. A. Vartanyants, "Modelling of partially coherent radiation based on the coherent mode decomposition," Proc. SPIE **8141**, 814106 (2011).
20. M. Glass, "Statistical optics for synchrotron emission: numerical calculation of coherent modes," Ph.D. thesis (Université Grenoble Alpes, 2017).
21. R. Li and O. Chubar, "Memory and CPU efficient coherent mode decomposition of partially coherent synchrotron radiation with subtraction of common quadratic phase terms," Opt. Express **30**, 5896–5915 (2022).
22. O. Chubar, "Synchrotron radiation workshop," 2013, https://github.com/ochubar/SRW.
23. O. Chubar and P. Elleaume, "Accurate and efficient computation of synchrotron radiation in the near field region," in *European Particle Accelerator Conference* (1998), pp. 1177–1179.
24. O. Chubar, Y. S. Chu, K. Kaznatcheev, and H. Yan, "Application of partially coherent wavefront propagation calculations for design of coherence-preserving synchrotron radiation beamlines," Nucl. Instrum. Methods Phys. Res. A **649**, 118–122 (2011).
25. O. Chubar, L. Wiegart, A. Fluerasu, M. Rakitin, J. Condie, P. Moeller, and R. Nagler, "Simulations of coherent scattering experiments at storage ring synchrotron radiation sources in the hard x-ray range," Proc. SPIE **11493**, 1149310 (2020).
26. L. Wiegart, M. Rakitin, Y. Zhang, A. Fluerasu, and O. Chubar, "Towards the simulation of partially coherent x-ray scattering experiments," AIP Conf. Proc. **2054**, 060079 (2019).
27. O. Chubar, M. S. Rakitin, Y.-C. Chen-Wiegart, A. Fluerasu, and L. Wiegart, "Simulation of experiments with partially coherent x-rays using synchrotron radiation workshop," Proc. SPIE **10388**, 1038811 (2017).
28. L. Wiegart, A. Fluerasu, D. Bruhwiler, and O. Chubar, "Partially coherent wavefront propagation simulations: mirror and monochromator crystal quality assessment," AIP Conf. Proc. **1741**, 040013 (2016).
29. N. Canestrari, O. Chubar, and R. Reininger, "Partially coherent x-ray wavefront propagation simulations including grazing-incidence focusing optics," J. Synchrotron Radiat. **21**, 1110–1121 (2014).
30. O. Chubar, L. Berman, Y. S. Chu, A. Fluerasu, S. Hulbert, M. Idir, K. Kaznatcheev, D. Shapiro, Q. Shen, and J. Baltser, "Development of partially-coherent wavefront propagation simulation methods for 3rd and 4th generation synchrotron radiation sources," Proc. SPIE **8141**, 814107 (2011).
31. O. Chubar, "Simulation of emission and propagation of coherent synchrotron radiation wave fronts using the methods of wave optics," Infrared Phys. Technol. **49**, 96–103 (2006).
32. S. Reiche, "Numerical studies for a single pass high gain free-electron laser," DESY-THESIS–2000-012 (1999), p. 177.
33. "Ocelot," https://github.com/ocelot-collab/ocelot.
34. M. Yabashi, K. Tamasaku, and T. Ishikawa, "Characterization of the transverse coherence of hard synchrotron radiation by intensity interferometry," Phys. Rev. Lett. **87**, 140801 (2001).
35. M. Yabashi, K. Tamasaku, and T. Ishikawa, "Measurement of x-ray pulse widths by intensity interferometry," Phys. Rev. Lett. **88**, 244801 (2002).
36. P. H. van Cittert, "Die Wahrscheinliche Schwingungsverteilung in Einer von Einer Lichtquelle Direkt Oder Mittels Einer Linse Beleuchteten Ebene," Physica **1**, 201–210 (1934).
37. F. Zernike, "The concept of degree of coherence and its application to optical problems," Physica **5**, 785–795 (1938).
38. A. Lang, "Simulation of stochastic partial differential equations and stochastic active contours," Ph.D. Thesis (Universität Mannheim, 2007).
39. G. Goon, "Cosmic microwave background simulations," GitHub (2021), https://github.com/garrett361/cmbpy.
40. T. Pfeifer, Y. Jiang, S. Düsterer, R. Moshammer, and J. Ullrich, "Partial-coherence method to model experimental free-electron laser pulse statistics," Opt. Lett. **35**, 3441–3443 (2010).
41. G. Geloni, E. Saldin, E. Schneidmiller, and M. Yurkov, "Fourier treatment of near-field synchrotron radiation theory," Opt. Commun. **276**, 167–179 (2007).

2.5.3. Coherence properties of SASE FEL radiation

In this section, I will briefly discuss the coherence properties of SASE FEL. A comprehensive study on the statistical properties of SASE FEL can be found in the pioneering work [24] and in various textbooks on FEL physics, e.g., [77]–[79]. Here, I will outline the fundamental aspects needed for the further development of the `SERVAL` algorithm and extend it beyond the quasi-homogeneous/quasi-stationary approximations. I will focus on the longitudinal coherence properties of SASE radiation, assuming that the radiation is fully coherent transversely.

The theory previously outlined in this thesis explains the statistical properties of Gaussian processes and is applicable to different kinds of radiation sources, even as complex as SASE FEL, albeit with some limitations. SASE, despite its laser-like name, starts from usual synchrotron radiation and inherits the statistical properties for electron beam shot noise. This means that Gaussian statistics are preserved in the linear mode of operation as shown in [24] because the amplification process basically acts as a linear transformation of the input stochastic signal. Linear mode of operation refers to the phase of amplification where there is an exponential gain in the power of radiation. For illustration, I plot the evolution of the SASE process in Fig. 2.7. A more detailed explanation of the SASE process within this thesis can be found in **Paper III**, [80]. Only after reaching the saturation, the radiation statistics start to deviate from Gaussian, as noted in [24].

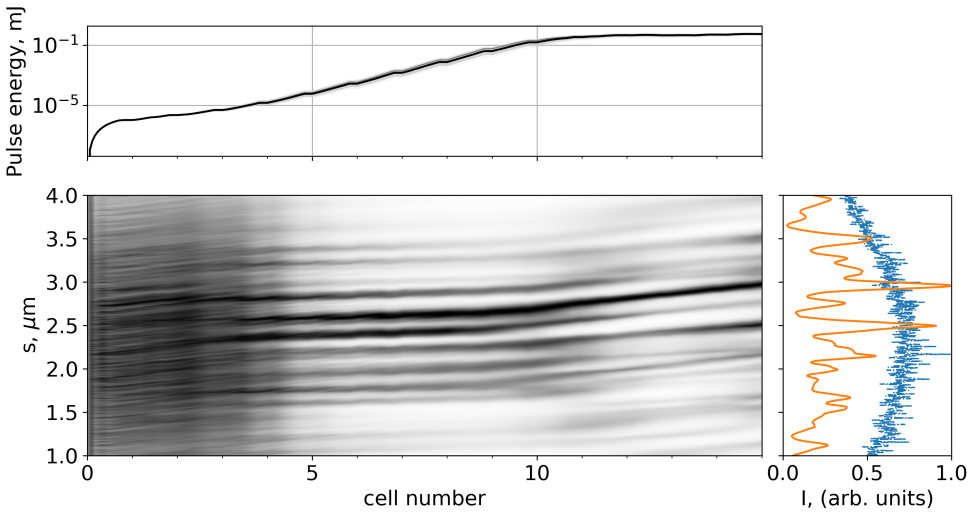

Figure 2.7: The SASE FEL process begins with spontaneous emission driven by shot noise in the electron beam. This emission is then exponentially amplified until saturation around cell 10. Beyond that point, the radiation power grows nearly linearly. The top subplot shows pulse energy along the undulator. The bottom color map displays the longitudinal radiation profile averaged over the transverse direction. The right subplot shows radiation power profiles along the pulse, after cell 1 (blue) and cell 15 (orange).

Transversely, radiation undergoes a mode selection process and rapidly acquires almost full transverse coherence, which is typically maintained with further FEL amplification and delivered to users, which I illustrate in Fig. 2.8.

From here on, I consider transversely coherent radiation from SASE FEL; therefore I focus on describing its longitudinal (time-frequency domains) coherence. Thanks to characteristic spiky structure of SASE radiation, understanding and modelling its temporal coherence is of

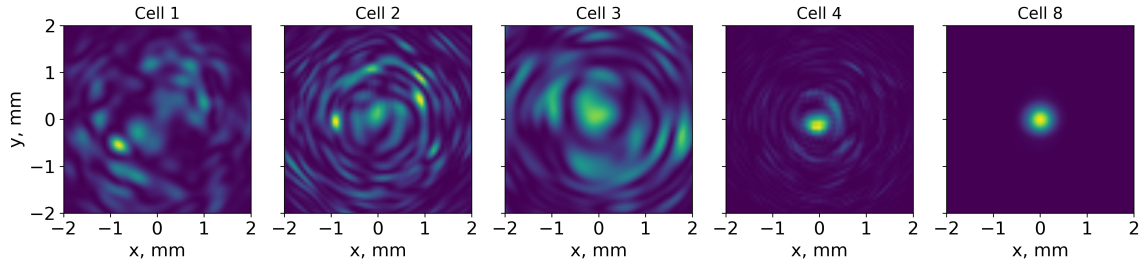

Figure 2.8: Monochromatic transverse intensity distribution of SASE in the far zone from the cell labelled at the top of the subfigures.

substantial practical interest.

Preservation of Gaussian statistics allows one to use SERVAL in application to the longitudinal domain of SASE radiation in the linear mode of operation. However, as one can see, SERVAL in its Eq. 2.88 formulation does not account for any chirps and has a factorised phase space distribution. Meanwhile, the SASE FEL may have a complex chirped-pulse structure. Frequency chirps of radiation heavily depend on the energy chirp in the electron beam. It can be shown with the undulator resonance condition that the energy chirp of the electron beam relates to the radiation instantaneous frequency as follows:

$$\omega(t) = \frac{2\gamma^2(t)k_w c}{1 + K^2/2}, \tag{2.94}$$

where $\gamma(t) = \gamma_0 + \gamma_n(t)$ is a function of time. Normally the value of energy deviation $\gamma_n(t)$ is much smaller (i.e. $\gamma_n(t)/\gamma_0 \ll 1$) that one can expand $\gamma^2(t)$ and obtain the following expression for the instantaneous frequency along the SASE FEL pulse:

$$\omega(t) = \frac{2\gamma_0^2 k_w c}{1 + K^2/2}\left(1 + \frac{2\gamma_n(t)}{\gamma_0}\right). \tag{2.95}$$

As one can see here, in the first approximation, the SASE instantaneous frequency replicates the energy chirp in the electron beam. Essentially, this dependence maps the phase space of the radiation.

One way to represent the radiation is through the Wigner function distribution, which can be thought, loosely speaking as "the phase space":

$$\mathcal{W}(\bar{t}, \bar{\omega}) = \int_{-\infty}^{\infty} \Gamma_\omega(\bar{\omega}, \Delta\omega) e^{-i\Delta\omega\bar{t}} d(\Delta\omega). \tag{2.96}$$

or, alternately, defined via $\Gamma_t(\bar{t}, \Delta t)$:

$$\mathcal{W}(\bar{t}, \bar{\omega}) = \frac{1}{2\pi}\int_{-\infty}^{\infty} \Gamma_t(\bar{t}, \Delta t) e^{i\bar{\omega}\Delta t} d(\Delta t). \tag{2.97}$$

Having this, one can calculate a time-frequency representation of a radiation pulse in time (the longitudinal coordinate along the beam) and frequency (photon energy) domains. Moreover, one can represent a single statistical realisation in terms of the Wigner function distribution. This can be done based on the fact that the averaging operation for $\Gamma_\omega(\bar{\omega}, \Delta\omega)$ can be taken out of the integral. In Fig. 2.9, I present a Wigner distribution calculated from a single realization of SASE pulse, emitted by a linearly chirped electron beam. This figure is adapted from [37]. In Fig. 2.10, authors of [37] introduced important concepts such as instantaneous bandwidth, instantaneous frequency, group delay, and group duration. In real experiments at facilities, such as the European XFEL, lasing windows of electron beams often exhibit nonlinear energy chirps [37]. A simulation of one such example is presented in Fig. 2.10. The next milestone for developing the SERVAL algorithm is to account for these kinds of frequency chirps or, more generally, arbitrary Wigner function distributions of the radiation.

2.5.4. Heuristic approach III: non- homogeneous/stationary sources.

One could notice that for a source that can be represented $\tilde{\Gamma}(\omega, \Delta\omega) = f_\omega(\Delta\omega)\bar{I}(\bar{\omega})$ it is possible to take the intensity out under the integral sign of the Wigner function definition in Eq. 2.96, so it can be written as the following:

$$\mathcal{W}(\bar{t}, \bar{\omega}) = \bar{I}(\bar{\omega}) \int_{-\infty}^{\infty} f_\omega(\Delta\omega) e^{-i\Delta\omega\bar{t}} d(\Delta\omega) = \\ = \bar{I}(\bar{\omega}) I(\bar{t}). \tag{2.98}$$

With this representation of the Wigner function, it is possible to see that the previous version of SERVAL in Eq. 2.88, implicitly implied the factorised Wigner function:

$$\phi(\bar{t}) = \mathcal{F}^{-1}\Big[\bar{I}(\bar{\omega})\mathcal{F}\left[I(\bar{t})\mathcal{N}(\bar{t})\right](\bar{\omega})\Big](\bar{t}) = \\ = \mathcal{F}^{-1}\Big[\mathcal{F}\left[\mathcal{W}(\bar{t}, \bar{\omega})\mathcal{N}(\bar{t})\right](\bar{\omega})\Big](\bar{t}), \tag{2.99}$$

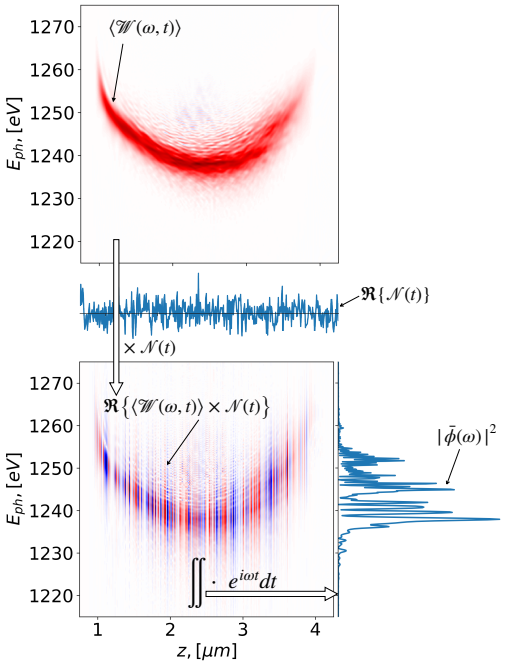

Figure 2.11: Visualisation of the Wigner-function-based algorithm. A known Wigner function is multiplied by complex white noise, followed by a Fourier-like integral. The result is a single realisation of the radiation spectrum.

where I adapted SERVAL from Eq. 2.88 for the longitudinal domain. This adaptation is possible because the proof of the correctness of the simulated SERVAL field relies on the generalised van Cittert–Zernike theorem (in its formulation for the inverse space domain, as shown in Eq. 2.58), which is the mathematical twin of the generalised Wiener-Khinchin theorem.

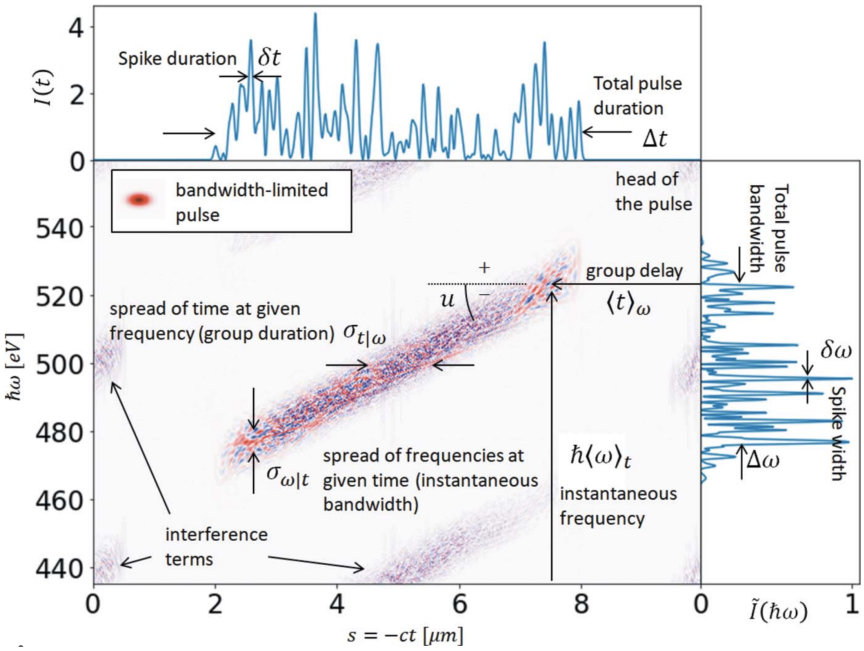

Figure 2.9: Adopted from **[37]**: "Time–frequency analysis terminology illustrated on a single-shot Wigner distribution of a modeled SASE pulse with negative frequency chirp u. The Wigner distribution for a bandwidth-limited pulse of Gaussian shape is provided in the inset."

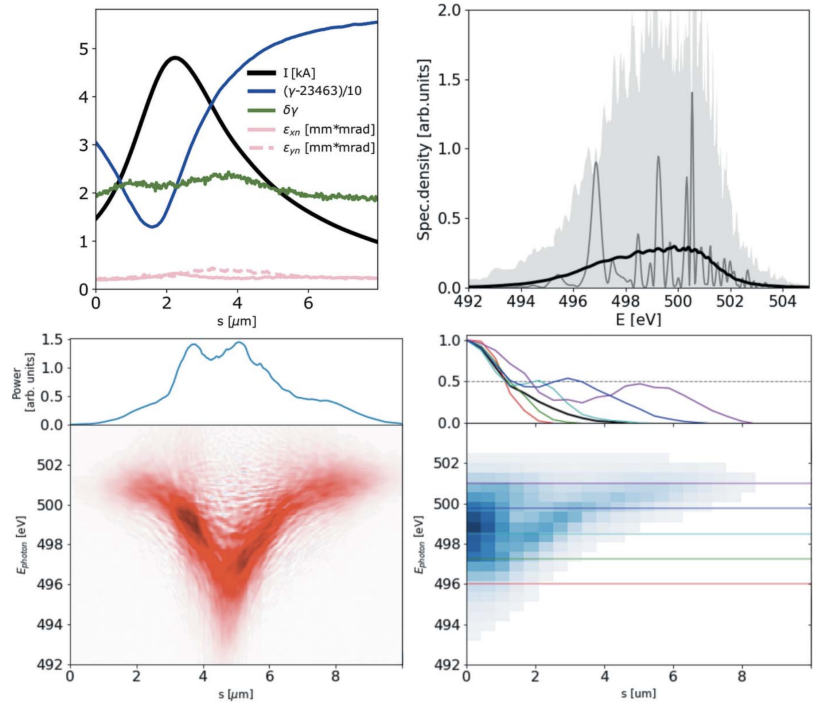

Figure 2.10: Adopted from **[37]**: "The European XFEL 100 pC electron beam with a non-linear energy chirp produces SASE radiation with different durations at different photon energies. Note the bifurcation in Wigner distribution above 499 eV. Analysis based on 1000 simulated SASE spectra."

Now, if I consider a non-factorisable Wigner function $\mathcal{W}(t,\omega)$ and write it as the integral:

$$\bar{\phi}(\omega) = \int_{-\infty}^{\infty} \sqrt{\mathcal{W}(t,\omega)}\mathcal{N}(t)e^{i\omega t}dt. \tag{2.100}$$

I present corresponding algorithm to Eq. 2.100 outline in Fig. 2.11. I hypothesize that with Eq. 2.100, one can model statistical realizations of a field with a desired Wigner function distribution, preserving the statistical properties of a process.

Analytical proof
As usual, to show that Eq. 2.100 follows correct correlation function of the field that is embed in the input Wigner function $\mathcal{W}(t,\omega)$, I do auto-correlation the field from Eq. 2.100:

$$\left\langle \bar{\phi}(\omega_1)\bar{\phi}^*(\omega_2)\right\rangle = \left\langle \iint_{-\infty}^{\infty} e^{i(\omega_1 t_1-\omega_2 t_2)}\sqrt{\mathcal{W}(\omega_1,t_1)\mathcal{W}(\omega_2,t_2)}\mathcal{N}(t_1)\mathcal{N}^*(t_2)dt_1dt_2\right\rangle. \tag{2.101}$$

where I impose the condition $\mathcal{W}(\omega,t)\geq 0$.

As previously, I utilize the shot noise property $\left\langle \mathcal{N}(t_1)\mathcal{N}^*(t_2)\right\rangle = \delta(t_1-t_2)$ and integrate over t_1:

$$\left\langle \bar{\phi}(\omega_1)\bar{\phi}^*(\omega_2)\right\rangle = \int_{-\infty}^{\infty} e^{it'(\omega_1-\omega_2)}\sqrt{\mathcal{W}(\omega_1,t')\mathcal{W}(\omega_2,t')}dt', \tag{2.102}$$

where I have formally replaced t_2 with t'. I now assume that the Wigner function distribution can be factorised as follows:

$$\mathcal{W}(\omega,t) \approx \sum_n \bar{I}^{(n)}(\omega)f^{(n)}(t), \tag{2.103}$$

where $f^{(n)}(t)$:

$$f^{(n)}(t) = \begin{cases} f(t), & \text{if } t_n \leq t < t_{n+1} \\ 0, & \text{otherwise,} \end{cases} \tag{2.104}$$

and $\bar{I}^{(n)}(\omega)$ is a function that approximates the cross-section over the interval $t_n \leq t < t_{n+1}$. Each interval is chosen such that the coherence length along a pulse remains approximately constant within it.

This representation of the Wigner function distribution dictates the form of the second-order correlation function. For the frequency domain, for example, I have:

$$\Gamma_\omega(\bar{\omega},\Delta\omega) = \int_{-\infty}^{\infty} \mathcal{W}(\bar{\omega},t')e^{i\Delta\omega t'}dt' \approx \int_{-\infty}^{\infty}\sum_n \bar{I}^{(n)}(\bar{\omega})f^{(n)}(t')e^{i\Delta\omega t'}dt'. \tag{2.105}$$

I then interchange the order of integration and summation and set the integration limits to the n-th time interval:

$$\Gamma_{\omega}(\bar{\omega}, \Delta\omega) \approx \sum_{n} \bar{I}^{(n)}(\bar{\omega}) \int_{t_n}^{t_{n+1}} f(t') e^{i\Delta\omega t'} dt'. \tag{2.106}$$

I expect to find that $\left\langle \bar{\phi}(\bar{\omega}_1)\bar{\phi}^*(\bar{\omega}_2) \right\rangle$ matches the representation of $\Gamma_{\omega}(\bar{\omega}, \Delta\omega)$ expressed in Eq. 2.106.

Substituting Eq. 2.103 in Eq. 2.102, I obtain:

$$\left\langle \bar{\phi}(\omega_1)\bar{\phi}^*(\omega_2) \right\rangle \approx \int_{-\infty}^{\infty} \sqrt{\sum_{m,n} \bar{I}^{(n)}(\omega_1) f^{(n)}(t') \bar{I}^{(m)}(\omega_2) f^{(m)}(t')} e^{it'(\omega_1 - \omega_2)} dt'. \tag{2.107}$$

Next, I observe that the double summation reduces to a single summation, as only terms where the product $f^{(n)}(t')f^{(m)}(t')$ has the same n and m indices yield non-zero products:

$$\left\langle \bar{\phi}(\omega_1)\bar{\phi}^*(\omega_2) \right\rangle \approx \int_{-\infty}^{\infty} \sqrt{\sum_{n} (f^{(n)}(t'))^2 \bar{I}^{(n)}(\omega_1) \bar{I}^{(n)}(\omega_2)} e^{it'(\omega_1 - \omega_2)} dt'. \tag{2.108}$$

Since $f^{(n)}(t)$ vanishes outside the specified time interval, only the n-th term contributes to the integral at the time interval in Eq. 2.108, allowing me to rewrite it as a sum of integrals:

$$\left\langle \bar{\phi}(\omega_1)\bar{\phi}^*(\omega_2) \right\rangle \approx \sum_{n} \sqrt{\bar{I}^{(n)}(\omega_1) \bar{I}^{(n)}(\omega_2)} \int_{t_n}^{t_{n+1}} f(t') e^{it'(\omega_1 - \omega_2)} dt', \tag{2.109}$$

where $f^{(n)}(t)$ has been replaced by the original $f(t)$, a substitution valid within the integration limits, and the square root expression has been taken outside the integral since it does not depend on the integration variable. This expression resembles a generalised "quasi" source representation. I can further simplify Eq. 2.109 by assuming that the spectral correlation width at given frequency is much narrower than that of the overall pulse spectral distribution $\bar{I}^{n}(\omega)$ for the given n-th interval, allowing me to write:

$$\left\langle \bar{\phi}(\omega_1)\bar{\phi}^*(\omega_2) \right\rangle \approx \sum_{n} \bar{I}^{(n)}\left(\frac{\omega_1 + \omega_2}{2}\right) \int_{t_n}^{t_{n+1}} f(t') e^{it'(\omega_1 - \omega_2)} dt'. \tag{2.110}$$

From this expression, I observe that it coincides with the expected form given in Eq. 2.106. Following this analytical proof I will present several numerical examples showing validity of the Eq. 2.100 in emulating partially coherent fields.

Numerical examples

I simulate a chirped pulse of SASE radiation in the linear regime using the `Genesis 1.3 v2` code [65]. During the amplification process I remain the radiation in the linear regime because, when saturation is reached, SASE radiation begins to deviate from Gaussian statistics [77], [81], whereas Eq. 2.100 strictly assumes a Gaussian process.

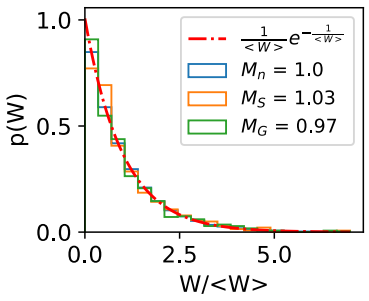

Figure 2.12: Histogram of the instantaneous intensity distribution. The red dot-dashed line represents a fit to the Gaussian noise distribution, shown by the blue histogram. The histogram for the `SERVAL` field is shown in orange, while the distribution for the `Genesis 1.3 v2` output is displayed in green.

I use the ensemble-averaged Wigner function output from the `Genesis 1.3 v2` simulation as input to the algorithm based on Eq. 2.100 to generate an entirely new ensemble of statistical realisations. The expectation is that the ensemble-averaged Wigner function resulting from this emulation will match the input, thereby ensuring the correct statistical representation of each single instance of the simulated field. The relevant comparison is shown in Fig. 2.13. Additionally, I verify the preservation of the statistical properties of the resulting field and confirm that the instantaneous intensity follows a negative exponential distribution, as expected for a Gaussian random process, what I demonstrate in Fig. 2.12.

To demonstrate the algorithm's ability to replicate various phase space distributions, I slightly modified the input Wigner function by adding two successive radiation pulses with an offset energy, in addition to the quadratically chirped pulse presented in Fig. 2.13. The results of this modification are presented in Fig. 2.14.

Upon exploring other complex distributions, such as donut shapes or more intricate quadratic chirp distributions, as presented in Fig. 4 of [37], I conclude that the emulated fields consistently follow the imprinted Wigner function distribution.

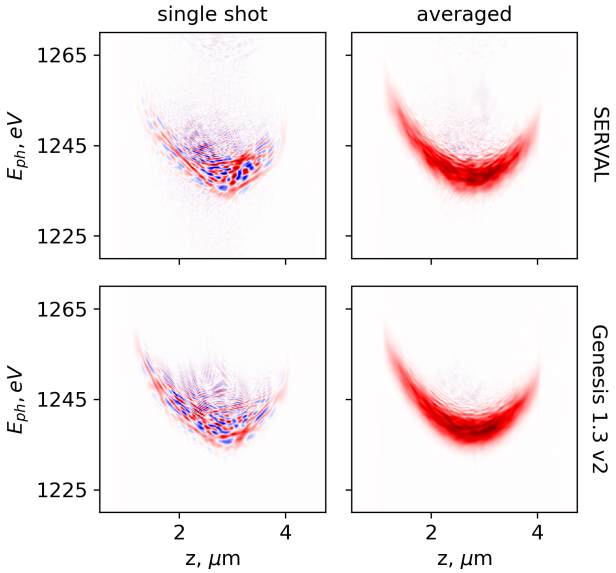

Figure 2.13: The first row presents the results of the `Genesis 1.3 v2` simulation, showing Wigner function distributions for both a single-shot event and an ensemble average over 1000 events. The second row shows the emulated field, generated according to Eq. 2.100 from the averaged Wigner function distribution.

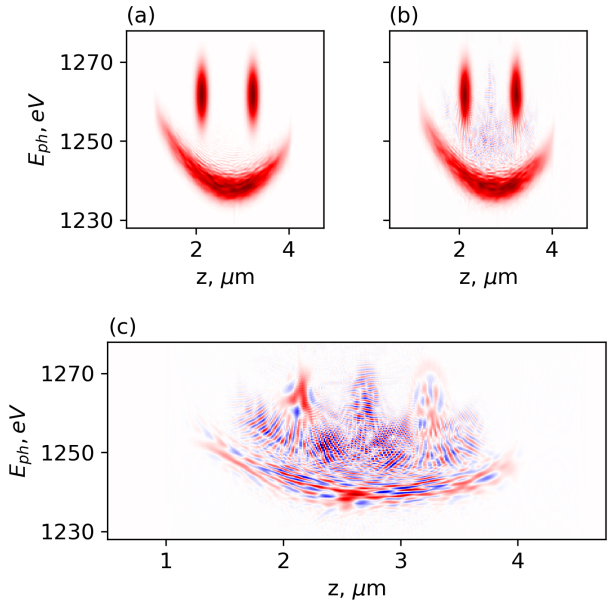

Figure 2.14: The modified Wigner distribution is shown in (a), while (b) presents the averaged Wigner distribution reproduced using Eq. 2.100. Panel (c) displays one statistical realisation of the Wigner distribution obtained with the algorithm.

2.5.5. Attosecond-at-Harmonic: limits of SERVAL applicability. Paper III.

In **Paper III**, I present a special mode of SASE FEL operation, demonstrating that the resulting radiation does not adhere to Gaussian statistics. In this paper, my co-authors and I introduce a method for obtaining subfemtosecond X-ray pulses at the European XFEL. This method leverages the natural bunching properties at harmonics and does not necessitate any special hardware. For the numerical replication of the pulses described in this paper, I utilised the `Genesis 1.3 v2` code. Thus, I illustrate through this paper that the application of `SERVAL` should always be conducted thoughtfully, based on the specific case under study. In this particular case, it was not feasible to use `SERVAL` due to the non-linear nature of the harmonics amplification, where Gaussian statistics are not preserved. Therefore, first-principle codes should be employed.

photonics

MDPI

Communication

Experimental Demonstration of Attoseconds-at-Harmonics at the SASE3 Undulator of the European XFEL

Andrei Trebushinin [1,*], Gianluca Geloni [1], Svitozar Serkez [1], Giuseppe Mercurio [1], Natalia Gerasimova [1], Theophilos Maltezopoulos [1], Marc Guetg [2] and Evgeny Schneidmiller [2]

[1] European XFEL, Holzkoppel 4, 22869 Schenefeld, Germany;
[2] Deutsches Elektronen-Synchrotron, Notkestrasse 85, 22607 Hamburg, Germany
* Correspondence: andrei.trebushinin@xfel.eu

Abstract: We report on observations of single spike spectra (3–13% of events) upon employing a previously proposed method for single spike generation via harmonic conversion. The method was tested at the soft X-ray SASE3 undulator of the European XFEL. The first part of the undulator allows one to amplify bunching at the fundamental as well as the higher harmonics. The downstream undulator is tuned to a harmonic, the fourth in our case, to amplify pulses with a shorter duration. We estimate the generated pulse duration within such a subset of short pulses at a level of 650 as. Considering the demonstrated probability of single spike events, this method is attractive for high repetition-rate free electron lasers.

Keywords: FEL; attoseconds; harmonic

Citation: Trebushinin, A.; Geloni, G.; Serkez, S.; Mercurio, G.; Gerasimova, N.; Maltezopoulos, T.; Guetg, M.; Schneidmiller, E. Experimental Demonstration of Attoseconds-at-Harmonics at the SASE3 Undulator of the European XFEL. *Photonics* **2023**, *10*, 131. https://doi.org/10.3390/photonics10020131

Received: 29 December 2022
Revised: 18 January 2023
Accepted: 20 January 2023
Published: 27 January 2023

1. Introduction

Bunching at harmonics driven by amplification of the fundamental has drawn the attention of researchers in the past and has been described in numerous publications, e.g., [1–4]. The authors of [4] proposed to use this effect for generating single spike sub-femtosecond pulses at free-electron laser facilities. The proposed setup requires minimal hardware manipulations and only the availability of variable gap undulator cells. In our contribution, we present an experimental demonstration of obtaining these nearly single-mode radiation pulses at the SASE3 undulator of the European XFEL with a two stage setup. For brevity, we shall call this the "attoseconds-at-harmonics" method.

During the amplification process in free-electron lasers (FELs), see Figure 1, the longitudinal phase space of the electron beam evolves along the undulator: in the linear regime it gradually undergoes sinusoidal energy and density modulations at the wavelength of the fundamental harmonics, as the electrons "rotate" in an FEL bucket; see the upper panels in Figure 2. At the onset of saturation, these modulations become non-linear and deviate from the sinusoidal shape. This leads to the growth of a rich harmonic content, shown in Figure 1A. The growth of bunching at harmonics is rapid and non-linear, which is characterized by a power law dependence with respect to the fundamental ($b_n(t) \sim b_1^n(t)$), see Figure 1B, where b_n denotes the bunching at the corresponding n-th harmonic.

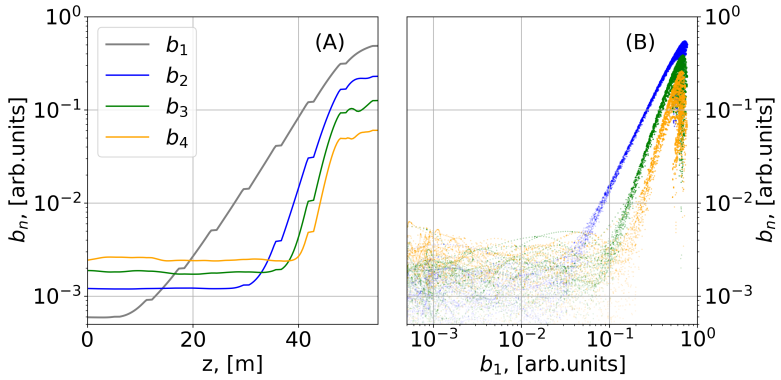

Figure 1. Simulation of the harmonics bunching growth with the GENESIS 1.3 code [5]. (**A**): Evolution of the bunching factor for the fundamental (1st), 2nd, 3rd, and 4th harmonic. The maximum value of bunching along electron beam is presented. (**B**) The dependence of the harmonics bunching on the bunching at the fundamental. The initially negligible level of the higher harmonics content is followed by a linear dependence with different slopes. Afterwards, this is followed by a hook-like dependence representing saturation.

We illustrate the amplification process with snapshots of the electron beam and radiation properties in the bottom panels of Figure 2, which show the radiation power dependence, bunching factors, and radiation spectra. Up to the 6th undulator cell, before reaching saturation, we observe growth at the fundamental harmonic while the bunching at the 4th harmonic remains at the noise level. This corresponds to a long plateau in Figure 1B, where each mapped point corresponds to the bunching factor calculated at a given position along the electron beam. At the 8th cell, we see a rapid harmonic growth. This corresponds to the linear part of the graph on the right panel of Figure 1B, which confirms (actually, this relation $b_n(t) \sim b_1^n(t)$ strictly holds in steady state regime, while for the time-dependent simulation results, Figure 1, the slope for the 4th harmonic deviates from 4, although this is still the power law dependence) the power law dependence of the higher harmonic bunching with respect to the fundamental. A deviation from this linear dependence indicates saturation.

Upon reaching saturation at 42 m, shown in Figure 2, the bunching at the 4th harmonic is proportional to that at the fundamental raised to the power of 4. Afterwards, the beam radiates in the downstream radiator tuned to the given harmonic, as depicted at Figure 2d. The power law dependence leads to effective suppression of spikes with low values of bunching and to an increase in the relative height of the dominant spikes which results in the reduction of the width of the spike and total pulse duration.

The authors of [4] proposed to use this effect for generating sub-femtosecond pulses with two or *multi*-stage undulator schemes. In the first stage, one creates bunching at the harmonic of the fundamental λ. The following stages are successively tuned to the wavelengths that correspond to the harmonics of the previous stages (λ/n). These can be sequences, for example, 1→2→4, 1→4, 1→3, etc. In this way, lasing at the harmonics starts from a substantial level of bunching created at the previous stages.

The idea behind this scheme is to generate the events with a minimum number of spikes in the first stage and to reduce their effective number and width further by exploiting prominent bunching at the harmonics in the following stages. This way, pre- and post-spikes are greatly mitigated, as we show in Figure 2c. This allows for the generation of single spike sub-femtosecond pulses on a statistical basis, at the level of several percent of the total number of pulses [4]. This method is attractive for high repetition rate machines, since one can post-select the ensemble of events with desired pulse duration and other properties using non-invasive spectral or temporal diagnostics.

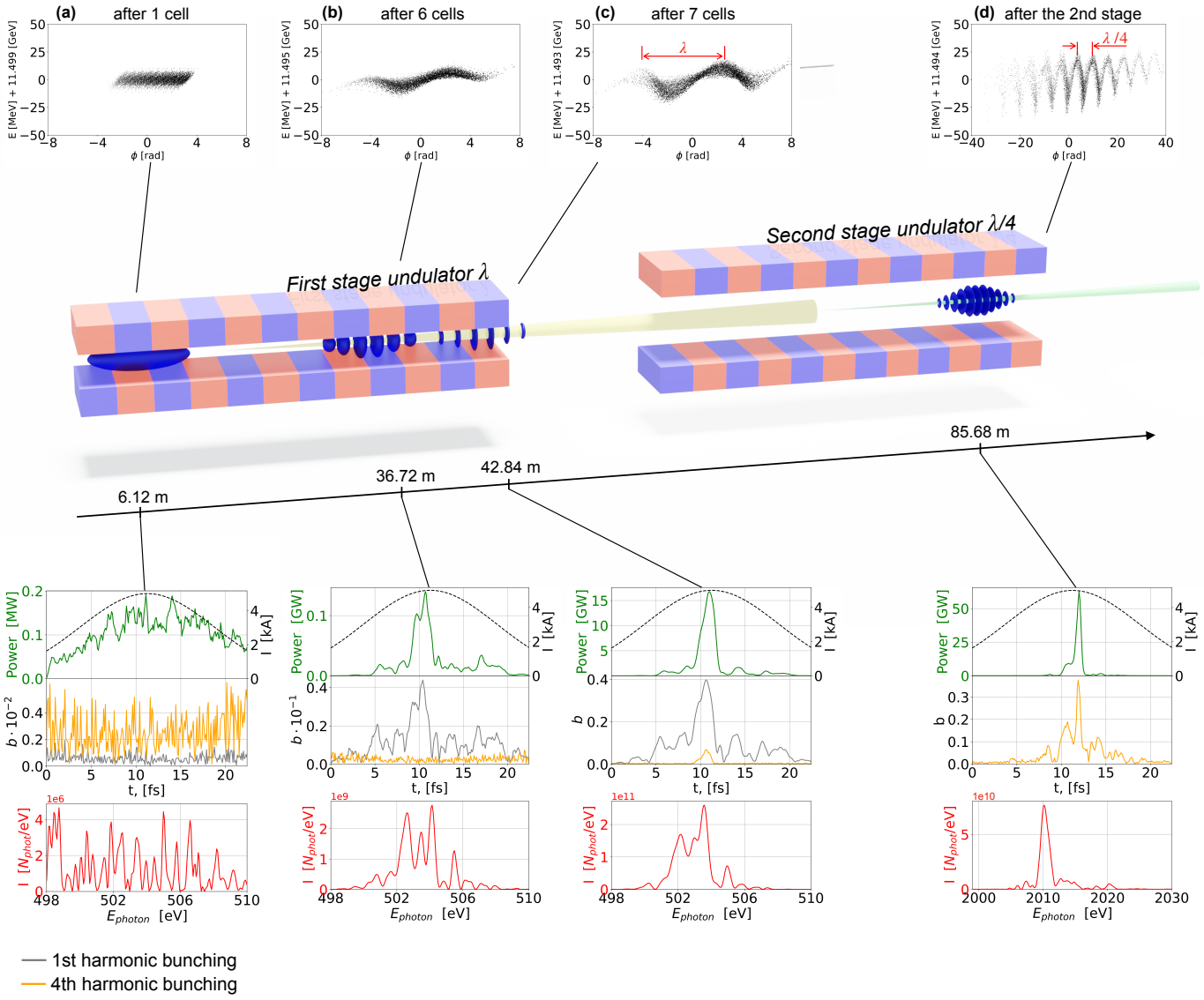

Figure 2. The attoseconds-at-harmonics setup, the four top and bottom sub-figures (**a**–**d**) illustrate the amplification process along the undulator. At the top, we present FEL buckets and at the bottom the radiation and electron beam parameters: power dependence in time domain (green line), bunching factors (gray and yellow lines), and the spectra (red line). (**a**–**c**) The lasing process at the first stage and (**d**) the resulting radiation and the electron beam parameters after the second stage.

2. Experiment at SASE3 Undulator at the European XFEL

We performed two separate experiments using the two stage setup at the SASE3 undulator of the European XFEL. The second stage was set to the 4th harmonic of the first one. In Table 1, we present the experimental parameters.

Table 1. Experimental parameters.

Experiment	E_{ebeam} (GeV)	E_{1h} (eV)	Cells_{1h}	XGM_{1h} (μJ)	E_{4h} (eV)	Cells_{4h}
675h4 (#1 and #2)	14	675	10	18	2700	1
503h4 (#1 and #2)	11.5	503	9	52	2012	$6 \rightarrow 8$

During the first experiment (October 2020), we used a compressed 100 pC electron beam to minimize the amount of SASE spikes in the first stage tuned to the fundamental

photon energy of 675 eV, the spectrometer resolution was 0.13 eV [6]. The pulse energy downstream from 10 active undulator cells was at the level of 18 μJ. We recorded spectra of the fundamental, finding their relative bandwidth at a level of 0.5 %, see Figure A1a. To optimize the performance of the high harmonic bunching, we stopped FEL amplification at the fundamental at the beginning of the nonlinear regime. The second stage was set to 4×675 eV $= 2700$ eV with one undulator closed. The spectrometer resolution at this photon energy was 0.7 eV. We aimed at seeing only the effect of coherent radiation at the harmonic without further amplification. In the recorded spectra, as expected, we observed sporadic events with spikes dominant over their satellites, Figure 3a. The data from this experiment are represented by the run identifier 675h4#1 in the present article (notation like 675h4#1 encodes the main parameters of an experimental run; the first number stands for the energy at the fundamental harmonic, h4 represents which particular harmonic is considered, and #1 is the number of the run). The results were reproducible after optimization attempts, run 675h4#2.

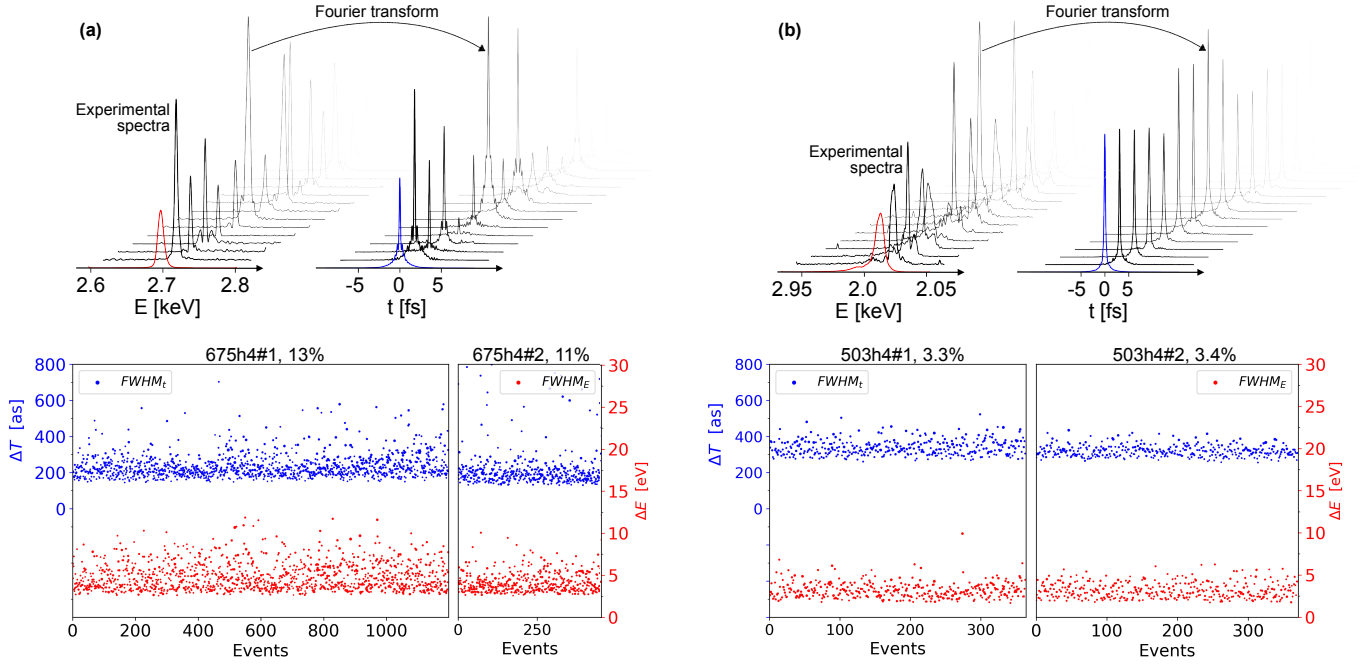

Figure 3. Results of data analysis. The filtered experimental data from experiment 675h1 are presented in (**a**) and those from experiment 503h1 are shown in (**b**). We present the filtered spectra in the top right panels of the sub-figures and the corresponding time domain distributions obtained by Fourier transformation in the top left panels. In the bottom panels, we show the width of the peaks: blue and red dots correspond to time and spectrum characteristics.

One of the challenges of the experiment was the diagnostics of the pulse energy. It was measured with an X-ray Gas Monitor (XGM) [7]. In two pulse operation, this device is sensitive not only to the fundamental but also at its harmonics.

During the second experiment (September 2021), we tuned nine undulator cells to the fundamental photon energy of 503 eV with a spectrometer resolution of 0.2 eV. Similarly, we optimized the electron beam compression to minimize the number of spectral spikes and acquired spectra, run 503h4#1, Figure 3b. We tuned the second stage to the fourth harmonic, and recorded radiation spectra again, with a resolution of 1.2 eV at 2012 eV. In run 503h4#2, we used *six* closed cells; after closing *two* more cells, we observed a minor increase in pulse energy from 57 μJ by 11 μJ.

Data Analysis

During the experiments, we collected raw spectra from the SASE3 soft X-ray spectrometer [6]. We filtered this set of spectra for single spike events only. We relied on the fact that, on a statistical basis, a single spike event in a spectrum corresponds to a single spike event in the time domain.

At first, we extracted raw data from the SASE3 spectrometer, see Figure 4a, subtracted the background, and proceeded with the application of a noise reduction algorithm, see Figure 4b. The last step was needed to facilitate the finding of peaks in the spectra, see Figure 4c. The number of single spike events was at the level of 11–13 % for the first experiment and 3% for the second experiment. The filtered events and the corresponding values for the minimal pulse duration are presented in Figure 3.

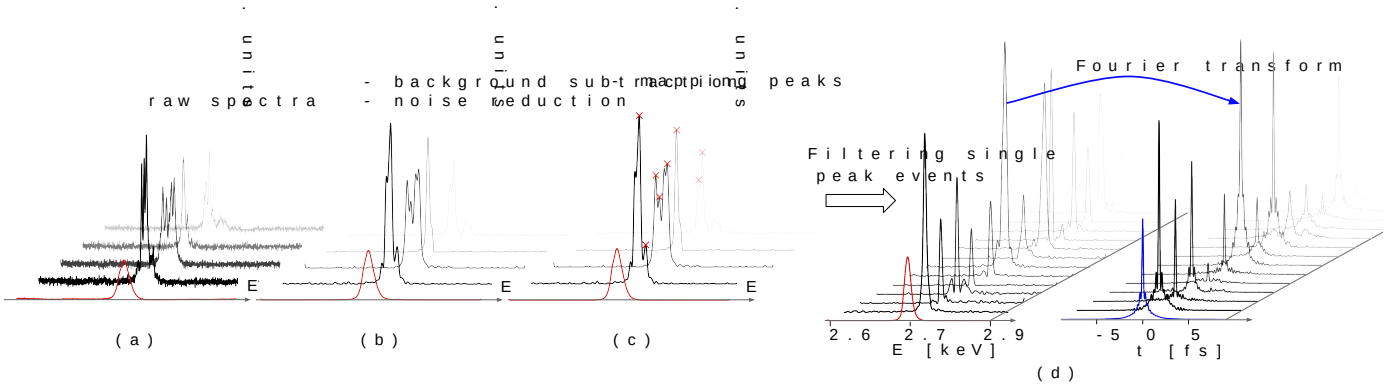

Figure 4. Data analysis procedure: (**a**) raw spectra extracted from the SASE3 spectrometer; (**b**) background subtracted, noise reduced; (**c**) spectrum peaks mapped; (**d**) single peak events chosen, Fourier transform performed to estimate *minimal possible* pulse duration. The red/blue line in front of the black lines represents averaged spectrum; the black line shows single shot events. Horizontal axes of (**a**–**c**) represent the energy span.

We refer to minimal pulse duration because the actual time domain power distribution is unknown in these experiments; in fact, we plan to conduct measurements with the angular streaking technique [8] to measure the actual temporal duration. At the moment, we lack direct temporal diagnostics for the attoseconds-at-harmonics experiments, and we can only provide the lower estimate of the pulse duration under the assumption of Fourier limit. We performed a Fourier transform of the spectral amplitude, in other words, we assumed a flat phase across the spectrum. Therefore, we only obtained the *minimal possible* pulse duration. Results are presented in Table 2 with the spread expressed with median absolute deviation; we also report here our estimate of the real pulse duration $(\Delta t_e)_{FWHM}$ based on the reasoning in Appendix B.

Table 2. Experimental results.

	675h4#1 (as)	**675h4#2 (as)**	**503h4#1 (as)**	**503h4#2 (as)**
$(\Delta t_{eFT})_{FWHM}$	234 ± 29	234 ± 27	338 ± 27	319 ± 18
$(\Delta t_e)_{FWHM}$	650 ± 140			

3. Discussion

As we indicated before, the attoseconds-at-harmonics method will be particularly suitable for high repetition-rate machines. For example, the European XFEL allows generating up to 27,000 photon pulses per second (2700 per train of electron bunched, trains go at 10 Hz repetition rate) [9]. Such a high repetition rate is a unique feature of superconducting FEL drivers. In this case, the attoseconds-at-harmonic method can potentially provide from 80 up to 350 single spike events per train, ten times per second.

The numbers in Table 2 provide only a rough estimation for the pulse duration. In these results, we evaluated both the minimal possible $(\Delta t_{eFT})_{FWHM}$ and the actually expected pulse duration $(\Delta t_e)_{FWHM}$. The estimations on the minimal possible pulse duration are based on a Fourier transform of the spectral amplitude and on the measure of the spread of the resulting distributions. The estimation for the actually expected pulse duration is more intricate and is explained in detail in Appendix B.

We expect to conduct further experiments: firstly, we aim to provide an absolute measurement of the harmonic pulse energy with the XGM diagnostic and, secondly, to perform angular streaking experiments to reveal the time domain of such pulses. The latter will give us a clear indication of the real pulse duration and validate the analysis of the present paper. Additionally, further theoretical analysis on statistical properties of such pulses may be possible.

Finally, we should place the attoseconds-at-harmonic method in the context of the many techniques for obtaining sub-fs level single spike pulses that have been proposed and/or tested at different facilities. A comprehensive overview of these methods is given in [10]. Given the statistical nature of the attoseconds-at-harmonics method, it should be clear that this technique might not be useful for every user's experiment, as it is based on a "post-selection" of short pulses out of an ensemble. Nevertheless, one of the benefits of the attoseconds-at-harmonics method is that it is free to implement and does not require any additional hardware to be installed, except for the availability of variable gap undulators.

4. Conclusions

In this paper, we show experimental results on the generation of quasi-single spike FEL pulses by applying the attoseconds-at-harmonics method. We estimate that a fraction (3–13%) of such pulses can be as short as several hundred attoseconds (650 as). We expect that this work will be followed up, in the future, by direct time-domain measurements with the angular streaking technique at the European XFEL.

Author Contributions: Conceptualization: authors contributed equally; Methodology, A.T., G.G., S.S., G.M. and E.S.; Software, A.T.; Validation, G.G., G.M., T.M., M.G. and E.S.; Formal analysis, A.T. and G.M.; Investigation, A.T., G.M., N.G., T.M., M.G. and E.S.; Resources, G.M., N.G. and T.M.; Data curation, N.G. and T.M.; Writing – original draft, A.T.; Writing – review & editing, authors contributed equally; Visualization, A.T. and S.S.; Supervision, G.G., S.S. and E.S.; Project administration, G.G. and E.S. All authors have read and agreed to the published version of the manuscript.

Funding: The cost of the article was covered by the journal using one of the author's voucher discounts (100%). This research received no extra funding.

Institutional Review Board Statement: Not applicable.

Informed Consent Statement: Not applicable.

Data Availability Statement: The data presented in this study are available on request from the corresponding author. The data are not publicly available due to requirements of internal authorization with the European XFEL account.

Acknowledgments: We thank Serguei Molodtsov for his interest in this work.

Conflicts of Interest: The authors declare no conflict of interest.

Appendix A. Fundamental Harmonic in the Experiments

Before setting up lasing at the 4th harmonic we collected spectra at the fundamental from the first stage undulator and analyzed their statistical properties, which we show in Figure A1. We assume Gaussian statistics even if we are not in the linear regime to provide a crude estimate of the radiation statistical properties. Under this assumption, we can estimate its group duration (Group duration is the radiation duration at a given frequency. This should not be confused with the total pulse duration if the time-frequency chirp is present [11]. The strict mathematical definition is given in Equation (34) and Figure 10 in the referred article.).

Due to the lack of longitudinal electron beam phase space diagnostics we cannot directly measure energy chirps. However as the calculated group duration weakly depends on the photon energy across the SASE spectra, the higher orders of the electron- and photon beam energy chirp can be neglected and chirps are predominantly linear. As in both experiments the radiation spectral bandwidths are approximately 1.5 times larger than the expected SASE bandwidths, we deduce that the pulse durations is about two times larger than the average group durations, resulting in *average* duration of about 7.5 and 5 fs for first stage radiation during the experiments at 675 eV and 503 eV respectively.

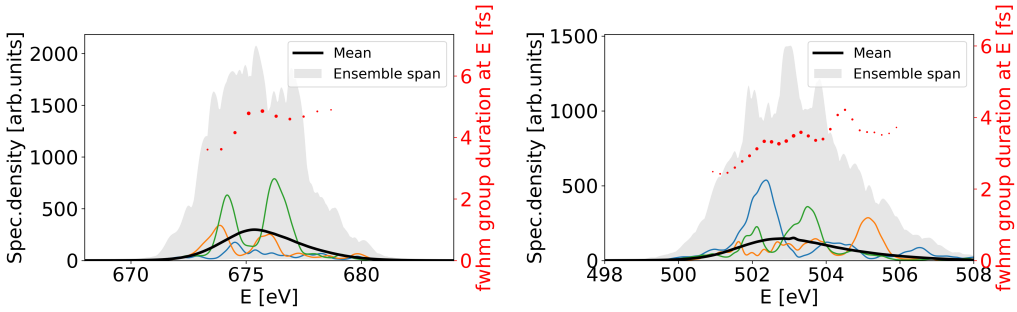

(**a**) Experiment 675h1 (**b**) Experiment 503h1

Figure A1. SASE spectra at the fundamental harmonic obtained during the experiments. We depict group duration at the given photon energy with red dots, the ensemble-averaged spectrum is marked with the black line and with the blue, orange and green colors we show single events. The pale grey region corresponds to a zone between maximum and minimum spectral values in the ensemble.

Appendix B. Results of Numerical Simulations

We numerically replicated the experimental results from experiment 675h1 with the Genesis 1.3 v4 FEL simulation code [5]. In this simulation we generated 1000 events, showing good agreement with first, Figure A2a, and second stage experimental spectra, Figure A2b. We deduced the electron beam compression parameters, unknown to us, by the simulations tuned in such a way as to replicate the performance and SASE spectra from the first stage undulator, Figure A2a. The 4th harmonic bunching of the electron beam was amplified in the second stage undulator what we present in Figure A2b in comparison with experimental spectra 675h1 run.

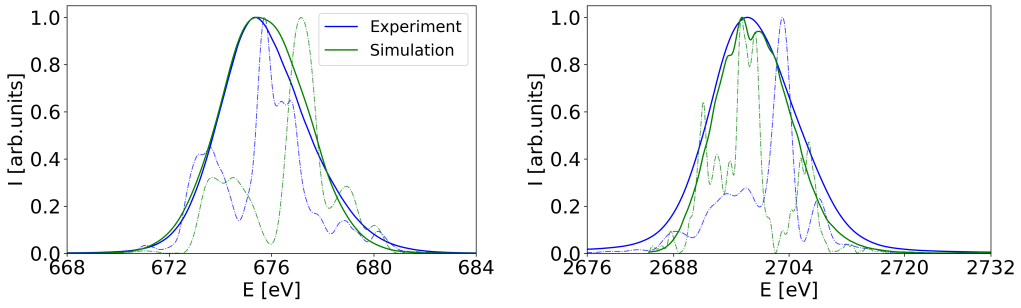

(**a**) Fundamental (**b**) 4th harmonic

Figure A2. Simulation results in comparison to the experiment 675h1. Solid saturated lines denote ensemble average spectrum, dash-dotted pale lines represent single shot events.

Out of 1000 simulated events from the second undulator stage 58 contain a single pronounced spike (i.e., 5.8%) with minor satellites in the spectrum. We present a typical spectrum in Figure A3.

Simulations provide full information on both time and frequency domains of the FEL radiation and allows us to empirically find the ratio of the actual pulse duration $(\Delta t_s)_{FWHM}$

and the Fourier limited one $(\Delta t_{sFT})_{FWHM}$. The ratio is equal to $N = \left\langle \frac{(\Delta t_s)_{FWHM}}{(\Delta t_{sFT})_{FWHM}} \right\rangle = 2.8 \pm 0.5$, where $\langle ... \rangle$ denotes averaging over an ensemble. In other words, we expect the actual pulse in the time domain to be 2.8 times longer than the Fourier limited estimate. Applying this coefficient to our experimental results, we obtain an estimate of average pulse duration at a level of $(\Delta t_e)_{FWHM} = N \times (\Delta t_{eFT})_{FWHM} = 650 \pm 140$ as.

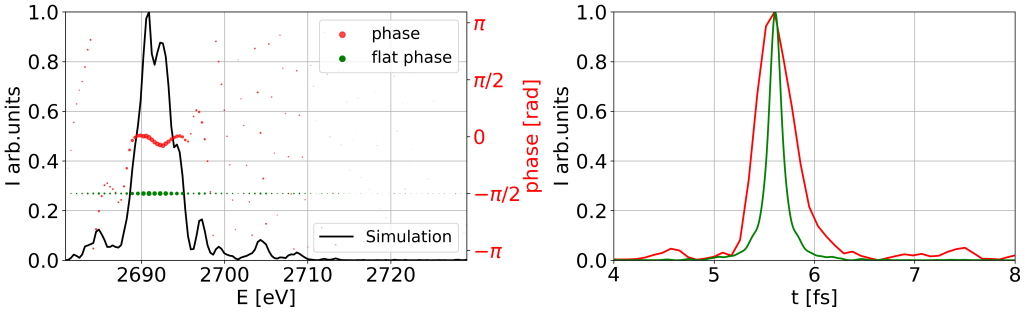

Figure A3. Simulated single spike event. The radiation spectrum with a single spike is presented on the left (black line). The actual phase is presented with red dots, the corresponding time distribution is presented with the red line on the right. The green dots on the left sub-figure represent the suggested assumption of the Fourier limited pulse (a flat phase across the spectrum). The Fourier limited pulse is shown by the green line on the right.

References

1. Bonifacio, R.; De Salvo, L.; Pierini, P. Large Harmonic Bunching in a High-Gain Free-Electron Laser. Nuclear Instruments and Methods in Physics Research Section A: Accelerators. *Spectrometers Detect. Assoc. Equip.* **1990**, *293*, 627–629. https://doi.org/10.1016/0168-9002(90)90334-3.
2. Huang, Z.; Kim, K.-J. Three-Dimensional Analysis of Harmonic Generation in High-Gain Free-Electron Lasers. *Phys. Rev. E* **2000**, *62*, 7295–7308. https://doi.org/10.1103/PhysRevE.62.7295.
3. Huang, Z.; Kim, K.-J. Nonlinear Harmonic Generation of Coherent Amplification and Self-Amplified Spontaneous Emission. Nuclear Instruments and Methods in Physics Research Section A: Accelerators. *Spectrometers Detect. Assoc. Equip.* **2001**, *475*, 112–117. https://doi.org/10.1016/S0168-9002(01)01553-4.
4. Saldin, E.L.; Schneidmiller, E.A.; Yurkov, M.V. Scheme for Attophysics Experiments at a X-Ray SASE FEL. *Opt. Commun.* **2002**, *212*, 377–390.
5. Reiche, S. Numerical Studies for a Single Pass High Gain Free Electron Laser. Ph.D. Thesis, Universität Hamburg, Hamburg, Germany, 2000.
6. Gerasimova, N.; La Civita, D.; Samoylova, L.; Vannoni, M.; Villanueva, R.; Hickin, D.; Carley, R.; Gort, R.; Van Kuiken, B.E.; Miedema, P.; et al. The soft X-ray monochromator at the SASE3 beamline of the European XFEL: From design to operation. *J. Synchrotron Rad.* **2022**, *29*, 1299–1308. https://doi.org/10.1107/S1600577522007627
7. Maltezopoulos, T.; Dietrich, F.; Freund, W.; Jastrow, U.F.; Koch, A.; Laksman, J.; Liu, J.; Planas, M.; Sorokin, A.A.; Tiedtke, K.; et al. Operation of X-Ray Gas Monitors at the European XFEL. *J. Synchrotron Rad.* **2019**, *26*, 1045–1051. https://doi.org/10.1107/S1600577519003795.
8. Hartmann, N.; Hartmann, G.; Heider, R.; Wagner, M.S.; Ilchen, M.; Buck, J.; Lindahl, A.O.; Benko, C.; Grünert, J.; Krzywinski, J.; et al. Attosecond Time–Energy Structure of X-Ray Free-Electron Laser Pulses. *Nat. Photon* **2018**, *12*, 215–220. https://doi.org/10.1038/s41566-018-0107-6.
9. Decking, W.; Abeghyan, S.; Abramian, P.; Abramsky, A.; Aguirre, A.; Albrecht, C.; Alou, P.; Altarelli, M.; Altmann, P.; Amyan, K.; et al. A MHz-Repetition-Rate Hard X-Ray Free-Electron Laser Driven by a Superconducting Linear Accelerator. *Nat. Photonics* **2020**, *14*, 6. https://doi.org/10.1038/s41566-020-0607-z
10. Serkez, S.; Geloni, G.; Tomin, S.; Feng, G.; Gryzlova, E.V.; Grum-Grzhimailo, A.N.; Meyer, M. Overview of Options for Generating High-Brightness Attosecond x-Ray Pulses at Free-Electron Lasers and Applications at the European XFEL. *J. Opt.* **2018**, *14*, 024005. https://doi.org/10.1088/2040-8986/aa9f4f
11. Serkez, S.; Gorobtsov, O.; Rivas, D.E.; Meyer, M.; Sobko, B.; Gerasimova, N.; Kujala, N.; Geloni, G. Wigner Distribution of Self-Amplified Spontaneous Emission Free-Electron Laser Pulses and Extracting Its Autocorrelation. *J. Synchrotron Rad.* **2021**, *28*, 3–17. https://doi.org/10.1107/S160057752001382X.

2.6. Conclusion

The content of this chapter is intended to enhance the results of the presented papers and vice versa. The chapter is supported by the necessary theoretical background, including an introduction to types of random processes and a discussion of important classes of sources such as stationary and ergodic sources. I then introduced the concept of Gaussian statistics for random processes, which significantly simplifies the analysis of random processes by linking higher-order correlation functions with the first-order one. Following this, I explored concepts such as quasi-stationarity and quasi-homogeneity, highlighting their mathematical similarities. Concluding the theoretical part, I outlined coherence theory for synchrotron radiation sources and free-electron lasers.

The goal of this chapter is to present three algorithms for simulating fully incoherent fields, partially coherent fields, and partially coherent fields with arbitrary Wigner function distributions. These algorithms replicate random fields by generating complex Gaussian white noise and then constraining this noise with appropriate mathematical supports. For fully incoherent sources, the support is simply the ensemble-averaged intensity distribution of the random source. For partially coherent sources, this support is supplemented by the source's effective divergence in the inverse space domain (also ensemble-averaged). These approaches assume that the radiation Wigner function distributions are factorised. However, I extend the algorithm to simulate fields with arbitrary Wigner function distributions.

All three algorithms have practical applications, such as simulating bending magnet radiation (**Paper I**), undulator radiation (**Paper II**), and SASE FEL radiation in the linear regime (Section 2.5.4). Additionally, I provided an example of simulating the original Young's double slit experiment, which is presented in Section 2.5.1, using one of the versions of the code. I have endeavoured to explain not only the practical advancements of these algorithms but also their limitations, which are crucial to consider when simulating complex systems as one described in **Paper III**. I mentioned a method that extends the applicability of these algorithms to non-Gaussian statistics, which could be a subject for further study beyond the scope of this thesis.

In conclusion, I hope that the algorithms presented here will serve as valuable tools for optical simulations. In the next chapter, I will present the results of the experiments for measuring electron beam size at hard X-ray beamlines of the European XFEL, where `SERVAL` played a very important role at the stage of numerical simulations.

Chapter 3

Direct observation of spike structure of synchrotron radiation for transverse electron beam size measurement

In this chapter, I present the results of the first observation of the spiky transverse structure of synchrotron radiation and the corresponding measurements of the electron beam size at the European XFEL. During the measurements, I directly observed synchrotron radiation upon monochromatization at the photon energy of 5.5 keV with a Bragg crystal monochromator. By calculating the transverse intensity correlation from the collected events, I determined the electron beam size at the undulator cell where this radiation was emitted. This technique was tested at the hard X-ray SASE1 beamline of the European XFEL. The findings demonstrate the feasibility of using direct measurements of transverse synchrotron radiation spiky structure to determine the electron beam size with existing diagnostics tools at European XFEL. This provides a valuable tool for optimizing electron beam parameters and enhancing the performance of advanced FEL schemes.

3.1. Introduction

By definition, all stochastic sources exhibit randomly fluctuating field distributions, with the typical size of these fluctuations being related to the coherence length and coherence time of the radiation. However, directly demonstrating these fluctuations is challenging, for example for a thermal source in the visible wavelength range, due to the extremely short coherence time [82]. In such cases, it is virtually impossible to set a camera shutter speed short enough to capture these field variations in real time.

Currently, there is a lively scientific discussion on coherence measurements of sunlight, in particular [82]: "While solar spectroscopy has long been studied, comprehensive experimental studies on the temporal coherence properties of sunlight are surprisingly hard to find in the literature." Interestingly, even the spatial coherence of direct sunlight on Earth was not measured until modern times, which is now demonstrated in [83]. The authors of [83] present direct measurements of the mutual coherence function of solar radiation in visible range. They also provided a photograph of a speckle image of direct sunlight radiation (taken from [84]), which serves as indirect evidence of the fluctuating field of the thermal sources. Concluding this brief literature review on sunlight, I must admit my surprise that even the coherence properties of sunlight radiation are somewhat understudied and remain an ongoing area of research.

Another example of stochastic radiation is SASE FEL. It was first shown theoretically [24], [85]–[87] and then experimentally [88]–[93] that SASE consist of fluctuating "spikes" on shot-to-shot basis, clearly indicating the randomness of the process. Similar fluctuations takes

place in time domain along the single pulse. The naming "spikes" should be distinguished from another commonly used term – "speckles". Speckles refer to the stationary characteristic diffraction pattern being a result of interference of coherent light reflected from or transmitted through a static granulated object. Whereas spikes refer to the inherent rapidly changing structure of the radiation source. In case of the synchrotron radiation and SASE FEL, these fluctuations is inherited from the shot noise in the electron beam and its dimensions.

FEL radiation originates from shot noise, leading to spontaneous emission that is subsequently amplified, resulting in SASE. As was discussed, SASE radiation exhibits a spiky structure in the longitudinal domain, so one would expect to observe spikes in the structure of synchrotron radiation as well but both in the time and spatial domains.

This can be qualitatively understood by noting that synchrotron radiation is confined in both space–time domains and their reciprocal counterparts. Constraining stochastic radiation within a limited bandwidth inevitably leads to a finite coherence volume, which manifests as a spiky radiation distribution. The typical size of these spikes corresponds to the coherence length and time of the radiation. Unlike SASE FEL, synchrotron radiation replicates electron beam dimensions in real space. Thus, by measuring the coherence length in the far zone or spectral coherence in the frequency domain, one can retrieve the transverse size and electron beam duration correspondingly[1]. The goal of this study is to directly reveal the transverse spikes of synchrotron radiation, proving it is a fluctuating field in the transverse domain, and, following the van Cittert-Zernike theorem, retrieve the transverse electron beam size.

Although it is possible to measure the transverse correlation function of the radiation using interferometric techniques, to my best knowledge the spikes in the synchrotron radiation structure have never been observed directly. The authors of [94] conducted a remarkable experiments using a monochromator with unprecedented resolving power at the Spring-8 facility to resolve synchrotron radiation longitudinal spikes (modes) and measure pulse duration. But at the time of publishing, the transverse distribution of monochromatized single-shot events was not feasible to observe due to detection systems limitations. This experiment was later complemented with measurements of the transverse coherence length [95] of synchrotron radiation using a setup similar to the Hanbury Brown and Twiss experiment, through which the authors retrieved the electron beam size.

In this contribution, I present the measurements of the transversely spiky structure of synchrotron radiation using a so-called K-monochromator [46] and a spontaneous radiation imager [47] available at the European XFEL. While the spikes can, in principle, be observed in the measured single-shot monochromatized pulse distributions, the high noise level makes their direct visual identification challenging. Therefore, I performed a cross-correlation analysis to recover their typical size from the recorded images. By determining the typical size of these spikes, i.e., the transverse coherence length, I retrieved the electron beam size following the van Cittert-Zernike theorem. I also modeled the expected images with numerous detrimental effects and demonstrated agreement with the experimental findings.

I also discuss the practical use of this method for optimizing the FODO lattice and subsequently the nominal SASE performance, which is increasingly important when tuning advanced schemes such as self-seeding [96]–[99] (especially in the hard X-rays range [100]), 2-color generation [101], and others. Recent advancements in generating (sub)-femtosecond-

[1] However, at modern synchrotron radiation sources, at some photon energies, single electron radiation size dominates over the size of the electron beam in transverse domain, so this method is not applicable in this case.

order pulses [27]–[31], at FELs (or even shorter) necessitate electron beam diagnostic tools to accurately characterise the electron beams, while manipulating their phase space. This becomes particularly crucial when dealing with transversely tilted beams or those exhibiting substantial energy chirp [37]. Under such circumstances, a comprehensive understanding of the transverse electron beam characteristics along the entire FEL undulator line becomes essential for optimizing the SASE performance.

This chapter is organized as follows: first, I estimate the numerical parameters needed to spatially and spectrally resolve the transverse spikes of synchrotron radiation at the European XFEL. Then, I present the numerical method I used to perform the correlation analysis of the noisy data. Subsequently, I show the simulation results that replicated the expected radiation behavior. In the real experiment, the signal was so low that the signal-to-noise ratio in most cases fall below unity. Therefore, I upgraded the correlation analysis accounting for quasi-homogeneity of the radiation and I conducted averaging over auto-correlation function to effectively increase statistics. Finally, I present the experimental results for measuring the auto-correlation function exhibiting a prominent signal. Based on the analysed width of the measured correlation distributions I retrieved the electron beam size. I conclude the chapter with a discussion on the possible implementation of the method in the control room of the European XFEL and future extensions for electron beam size diagnostics.

3.2. Underlying theory

3.2.1. Qualitative estimations

As noted in the introduction, synchrotron radiation exhibits limited coherence, meaning that its intensity profile contains spikes that vary stochastically from shot to shot in both the longitudinal and transverse domains. Additionally, these spikes are statistically independent of one another. Consequently, when observing radiation emitted by a single passage of the electron beam using a conventional monochromator with a bandwidth much larger than the spectral correlation width, the detected spatial distribution will appear smooth, with all transverse spikes effectively averaged out.

For instance, at a conventional synchrotron radiation source based on a storage ring, one typically observes a smoothed transverse radiation distribution after monochromatization. This smoothing occurs because of the relatively long electron beam duration – on the order of several picoseconds – which also determines the radiation pulse duration. Given that the longitudinal coherence length is much shorter than the pulse duration, a large number of spikes are expected in the longitudinal temporal profile. By applying the generalized Wiener–Khinchin theorem, it can be estimated that even after conventional monochromatization, such as with Si (111), the number of spikes remains significant. This is why the authors of [94], [95] developed a specialized monochromator to be able to resolve spikes in the frequency domain for coherence measurements.

The situation is drastically different at linear accelerator facilities such as the European XFEL. Here, the electron beam duration is on the order of tens of femtoseconds. When generating synchrotron radiation with a single undulator cell, approximately a hundred periods long, there will be significantly fewer longitudinal spikes after monochromatization, even when using a conventional crystal monochromator based on the Si (111) reflection, as shown in Fig. 3.1. On an imager, this would result in the averaging of the spike distribution

within the monochromator bandwidth. Averaging over several tens of longitudinal spikes will produce a low-contrast transverse distribution that still retains the imprint of the spikes, as illustrated by the blue-colored distribution in Fig. 3.1.

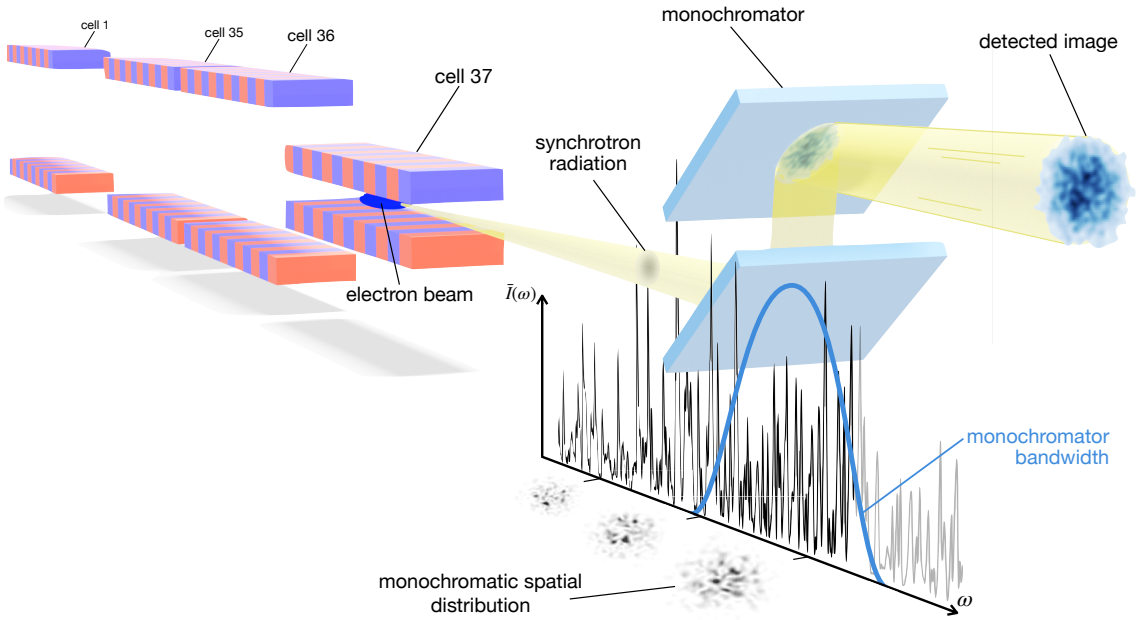

Figure 3.1: Schematic representation of the experimental setup. Radiation is emitted from cell 37 at SASE1. The blue distribution after the monochromator represents the averaged transverse profile of different longitudinal spikes after monochromatisation. The black-and-white spatial distribution near the spectrum shows the monochromatic intensity distribution from individual spikes.

This result is achievable only with an ideal, noiseless imager; in practice, the signal captured by the imager will likely be dominated by noise. Typically, the coherence properties of radiation are described using the auto-correlation function, which helps mitigate the impact of noise. Before analyzing the image properties using the auto-correlation function, I will provide a more quantitative estimate of the number of spikes that pass through the monochromator and the required spatial resolution of the detector.

3.2.2. Quantitative estimations

Longitudinal amount of spikes

The number of spikes falling within its bandwidth can be calculated as follows [94]:

$$M_L = \sqrt{1 + \frac{\Delta\tau^2}{\tau_c^2}}, \tag{3.1}$$

where $\Delta\tau$ is the FWHM of the electron beam duration, $\hbar$ is the Plank's constant, the coherence length τ_c can be expressed via ΔE, which is the FWHM of the monochromator bandwidth.

$$\tau_c = \frac{4\hbar \ln 2}{\Delta E}. \tag{3.2}$$

Fig. 3.2 illustrates the dependence of the number of spikes with respect to the electron beam duration and the undulator radiation resonance energy for a specified monochromator reflection. Fig. 3.2 demonstrates the unique parameter space for synchrotron radiation at linear

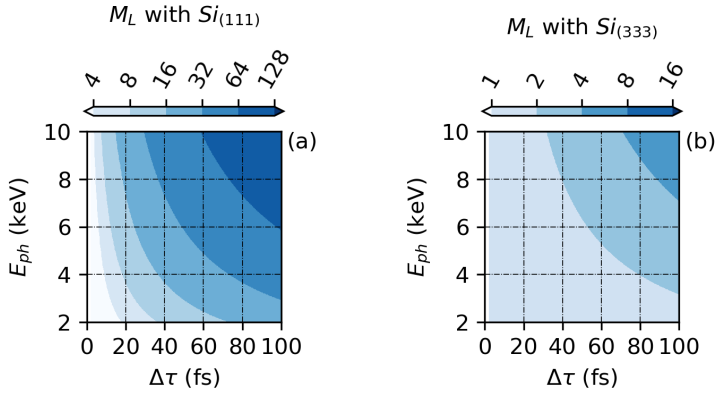

Figure 3.2: The colormap shows the number of longitudinal spikes after passage through the monochromator, for each crystal reflection indicated at the top of the corresponding subplot.

accelerator facilities. The measured pulse duration with CRISP [102] in the conducted experiments was approximately 37 fs (FWHM). Given the relative resolution of the monochromator of 2×10^{-4}, this results in around 22 longitudinal spikes after monochromatization.

Transverse coherence length
The transverse dimension of the spikes is related to the electron beam size as:

$$\sigma_{c_x,c_y} = \frac{z\lambda}{2\pi\sigma_{x,y}}, \tag{3.3}$$

which is basically derived from the van Cittert–Zernike theorem. With this equation one can estimate the resolution of the imaging system needed to resolve the spikes. I plot the distributions based on Eq. 3.3 in Figs. 3.3a, 3.3b, and 3.3c where I depict the resulting width of the correlation function versus electron beam transverse size and photon energy (with an undulator cell set to the first harmonic resonance). The parameters here correspond to the SASE1 beamline of the European XFEL. The distance from the cell 37 to the SR imager is 176 m. The length of each cell is 5 m and intersections between the cells are 1.1 m long.

These estimations clearly indicate that spikes in the transverse dimension are likely to be observed upon monochromatization at the European XFEL. In the next section, I will present a simulation of the experiment conducted at the European XFEL. Additionally, I will demonstrate a method for retrieving a correlation function in the presence of high noise levels.

3.3. Simulation

In order to analyse the expected experimental performance, I first simulated the experimental setup, which is schematically depicted in Fig. 3.1. It consists of undulator cell 37 (the last one) of the SASE1 undulator at the European XFEL, a K-monochromator [46], and an SR

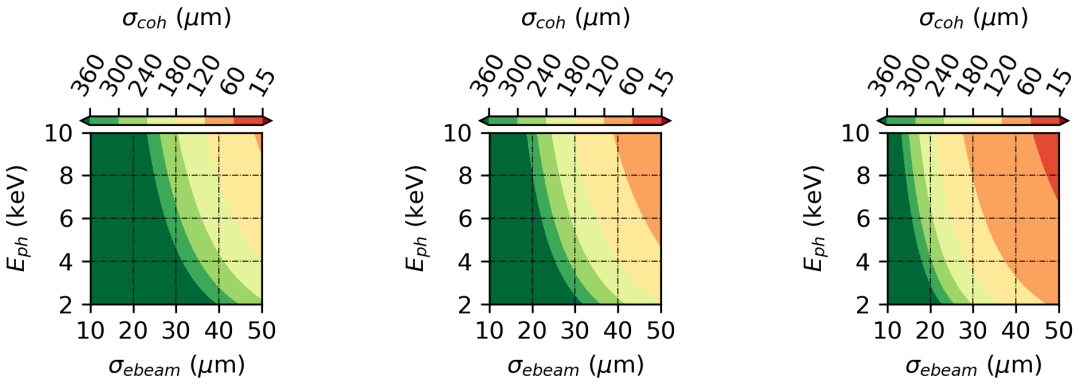

(a) cell 1 **(b)** cell 18 **(c)** cell 37

Figure 3.3: Colormap of the coherence length (rms) of the radiation from the corresponding cell of the SASE1 beamline, shown as a function of transverse electron beam size (rms) and photon energy.

imager [47]. The relative resolution of the K-monochromator using the Si (111) reflection is $\Delta E/E = 2 \cdot 10^{-4}$, as reported in [46]. The SR imager consists of a YAG scintillator and an imaging system, which is used to detect the visible light produced by the impinging X-rays. The undulator cell has 128 periods, with a period length of 4 cm.

To accurately simulate the pulses of synchrotron radiation observed through the monochromator, the first step is to simulate the transverse distribution of each longitudinal spike as a statistically independent realisation of a random process. The intensity-averaged collection of these realisations forms a single image (event) that would be recorded by the SR imager in practice. A sufficiently large number of these events must be simulated to conduct the correlation analysis. The SERVAL algorithm for simulating undulator radiation [103] is particularly well-suited for this task, as it delivers prompt and accurate results.

In Fig. 3.4, the radiation distribution of a single event recorded by the imager is shown, assuming that 22 longitudinal spikes passed through the monochromator for each pulse and anticipating the data analysis, in the experiment, I averaged over 13 electron beams for each recorded event to achieve a reasonable observed intensity. Consequently, in the simulation, I modeled 22×13 instances of the field, which, after averaging, constitute a single detected event. I then assembled the complete ensemble of these events, totaling 1000 simulated occurrences for the demonstration here.

I calculated the normalized auto-correlation function from the collected events:

$$g^{(2)}(z, \vec{r}_1, \vec{r}_2, \omega) = \frac{\langle I(z, \vec{r}_1, \omega) I(z, \vec{r}_2, \omega) \rangle}{\langle I(z, \vec{r}_1, \omega) \rangle \langle I(z, \vec{r}_2, \omega) \rangle}, \tag{3.4}$$

here $\langle \ldots \rangle$, as usual, denotes ensemble averaging, and the superscript indicates the order of the correlation function. The second-order (intensity) autocorrelation function is related to

the first-order (field) following Siegert relation[2]:

$$g^{(2)}(z, \vec{r}_1, \vec{r}_2, \omega) = 1 + |g^{(1)}(z, \vec{r}_1, \vec{r}_2, \omega)|^2. \tag{3.5}$$

The calculated auto-correlation function for these events are shown in Fig. 3.4(b), where the auto-correlation function for the variables x_1 and x_2 is plotted, with y_1 and y_2 held fixed. By taking a slice along the negative slope diagonal of the plot, one obtains $g^{(2)}(\bar{x}, \Delta x)$, which can be related with the electron beam size following Eq. 3.3.

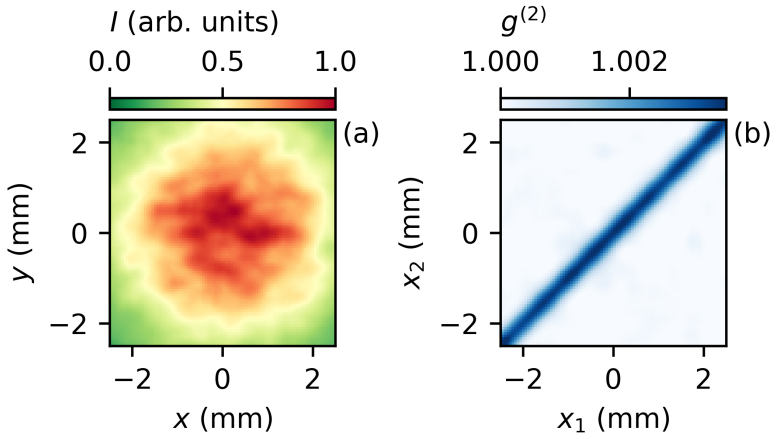

Figure 3.4: Simulated signal averaged over $M_L = 22 \times 13$ transverse modes and the corresponding autocorrelation function. The intensity distribution in panel (a) is normalised to its maximum value. The peak value of the autocorrelation function is $1 + 1/M_L$, reflecting a reduction in contrast due to averaging over M_L successive longitudinal spikes.

In practice, this signal is significantly impacted by pixel noise from the detector, owing to the inherently low intensity of synchrotron radiation. Such a weak signal is expected, as it is observed after passage of few electron beam passes through the undulator and undergoes monochromatization. I replicated the experimental conditions, where the signal-to-noise ratio (S/N) is extremely low – 0.9. Under these circumstances, the image quality is generally considered too poor for straightforward analysis. This effect and its impact on the correlation function are illustrated in Fig. 3.5.

Nevertheless, the correlation function can still be reconstructed from highly noisy data. By assuming quasi-homogeneity of synchrotron radiation [69], one can perform averaging over the positive slope diagonal, as illustrated in Fig. 3.5(b). This approach effectively measures the average correlation over the pixels containing signal, thereby increasing the collected statistics and suppressing the effects of noise. This concept is further demonstrated in Fig. 3.6, where the upper row shows a comparison between clean (Fig. 3.6(a)) and noisy signals (Fig. 3.6(b)). The comparison of the retrieved correlation function is presented in Fig. 3.6(c).

[2]Due to longitudinal averaging over many modes, the intensity autocorrelation function decreases by a factor inversely proportional to the number of modes. This contrast reduction does not affect the shape or width of the $g^{(2)}$ distribution; rather, it appears as a prefactor $1/M_L$ in front of $|g^{(1)}|^2$ in Eq. 3.5. Alternatively, this factor can be expressed in terms of experimental parameters such as the monochromator bandwidth and the electron beam pulse duration, as derived in my subsequent publications.

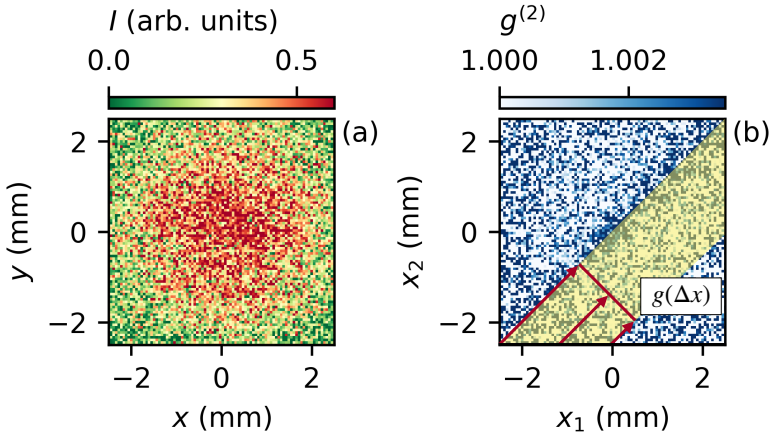

Figure 3.5: The same figure arrangement as Fig. 3.4, but for a noisy signal with a signal-to-noise ratio of 0.9.

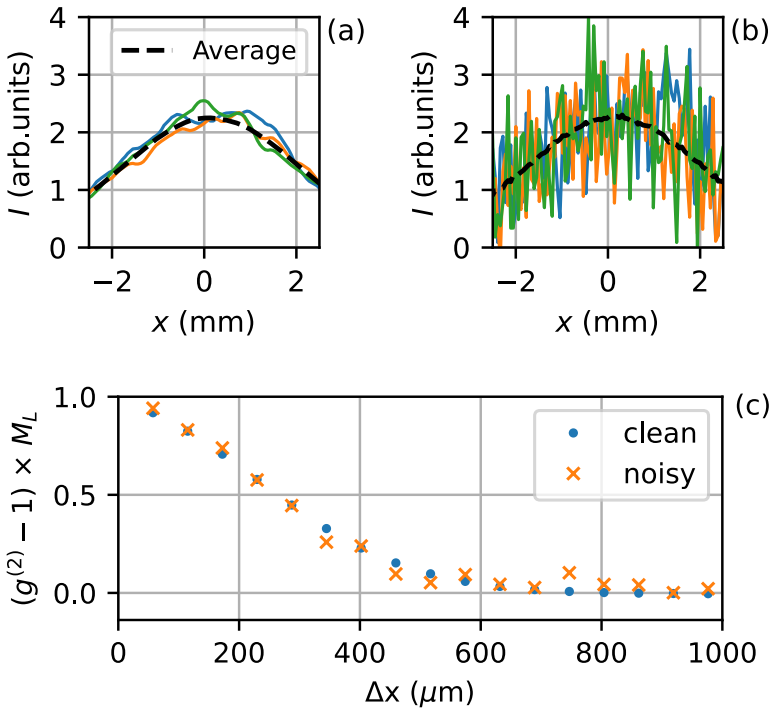

Figure 3.6: Data analysis procedure. (a, b): Comparison of the simulated signal detected with an ideal detector (a) and the simulated signal with added noise after background subtraction (b). (c): Comparison of the reconstructed autocorrelation functions from the ideal and noisy signals. The corresponding $(g^{(2)} - 1)M_L$ function is shown below, where M_L denotes the total number of longitudinal modes.

It is evident that, except for the first point, the noise is effectively suppressed. The first point in the correlation function should be ignored in this analysis, as it represents the correlation of the pixel noise. I assumed the pixel noise auto-correlation function to be expressed as a Dirac delta-function. This point is well beyond the range of the vertical axis

scale shown in Fig. 3.6. In the next section, I will present the experimental results, which are analysed based on this data retrieval procedure.

3.4. Experimental results

The experiments were conducted at the SASE1 beamline of the European XFEL. Four experiments were performed in total under slightly different conditions, primarily differing in the electron beam energy, which determined the minimum possible photon energy for tuning the undulator resonance. All four experiments utilized the Si (111) reflection of the K-mono to monochromatize the radiation with a relative resolution of 2×10^{-4}. There were two options available for the type of screen used in the SR-imager: a $Gd_2O_2S{:}Pr$-based scintillator (GOS) and a YAG screen differing in a trade-off between sensitivity and resolution. In the first experiment, I used the GOS scintillator. Despite GOS having a sensitivity advantage – 6.3 lsb/ph compared to YAG's 0.54 lsb/ph – its resolution of 61 μm (FWHM) was not sufficient for accurate correlation analysis. Subsequent experiments employed a YAG scintillator with a finer spatial resolution of 31 μm (FWHM).

I abandoned the idea of using the Si (333) reflection, which has a bandwidth one order of magnitude narrower (1×10^{-5} in relative units) than Si (111). This would have resulted in an order of magnitude lower impinging photon flux on the SR-imager, compounded by the less sensitive YAG screen. A more sensitive camera, or a specialized camera, should be installed to take advantage of the narrower bandwidth and consequently more contrast-rich resulting images.

In Fig. 3.7, I present typical detected distributions: the ensemble-averaged distribution in Fig. 3.7(a) and a single-shot event in Fig. 3.7(b). The signal spot is barely discernible to the naked eye. However, one can notice intensity fluctuations in Fig. 3.7(b). The typical size of these fluctuations becomes apparent when looking at successive event distributions. Once the autocorrelation function is calculated and it is confirmed that the signal originates from the statistics of synchrotron radiation, I can claim that this is an image where synchrotron radiation spikes are detected.

For this particular experiment, I recorded statistics of around 3500 events for each measurement. This number of events is sufficient for a reliable data analysis. The result of the calculated auto-correlation function, Fig. 3.8a, represents the size of the electron beam under "matched" conditions, meaning that the Courant-Snyder parameters (also somehow known as "Twiss parameters" in [104][3]) are nominal, and the size of the electron beam along SASE1 undulator is sufficiently uniform. In this case, the beta function is assumed to be approximately $\beta_{x,y} \approx 30$ m. This value was calculated theoretically based on the actual readouts from the quadrupoles.

To verify that the observed signal is actually conditioned by the electron beam size, I intentionally changed the assumed matching conditions of the FODO lattice. I adjusted the current in one of the matching quadrupoles upstream the SASE1 undulator from 33.7 A ("matched" condition) to 43.8 A (mismatched condition). This led to a clear change in the

[3]Citation from [105]: "Wilson's constant referral to the Courant–Snyder matrix and the Courant–Snyder beta function as the Twiss parameters and Twiss matrix is an incorrect attribution that permeates the field. Some years ago Frank Cole contacted Richard Twiss, who didn't understand why the parameters were named for him." Richard Q. Twiss was a British astronomer. He is known for his work on the stellar inteferometer [72], [106] with Robert Hanbury Brown.

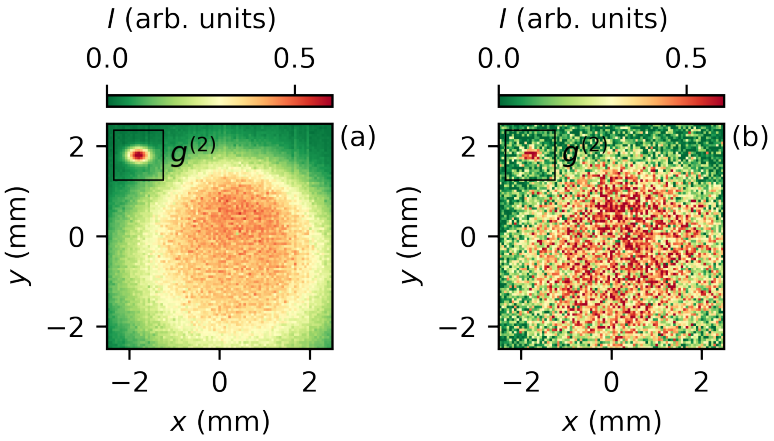

Figure 3.7: Typical image recorded during the experiment. Panel (a) shows the ensemble-averaged distribution, while panel (b) displays single-shot events. The autocorrelation function is shown in the upper left corner of each image, enclosed in a square frame.

observed correlation signal. I present two pairs of measurements conducted for cell 29 in Fig. 3.8 and cell 37 in Fig. 3.9 for "matched" and mismatched conditions on Subfigures (a) and (b) respectively. The measurement results are summarized in Tables 3.1 and 3.2. One can see the measured electron beam size always follows the expected change in the beta function.

Condition	Beta function (m)	$\sigma_x \times \sigma_y$ (μm^2)
Matched	$\beta_{x,y} \approx 30$	22×23
Mismatched	$\beta_x \times \beta_y \approx 80 \times 20$	33×21

Table 3.1: Calculated beta function and measured transverse electron beam size for cell 29

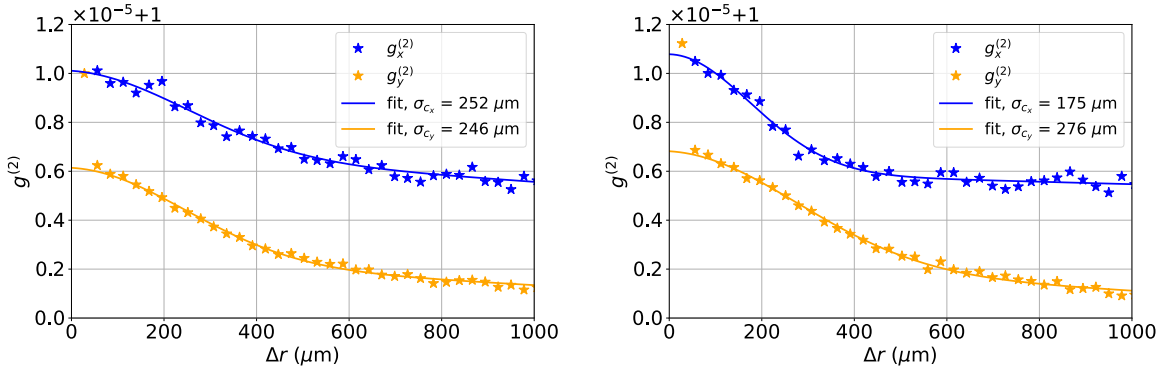

(a) Matched electron beam. Retrieved transverse electron beam size: $\sigma_x \times \sigma_y = 22 \times 23\ \mu m^2$

(b) Missmatched electron beam. Retrieved transverse electron beam size: $\sigma_x \times \sigma_y = 33 \times 21\ \mu m^2$

Figure 3.8: Results of the autocorrelation analysis of radiation from **cell 29**.

The results for the "matched" condition are not the same in both cells, which may indicate a deviation of the actual electron optics from the calculated configuration under nominal

Condition	Beta function (m)	$\sigma_x \times \sigma_y$ (μm^2)
"Matched"	$\beta_{x,y} \approx 30$	31×23
Mismatched	$\beta_x \times \beta_y \approx 20 \times 45$	18×27

Table 3.2: Calculated beta function and measured transverse electron beam size for cell 37

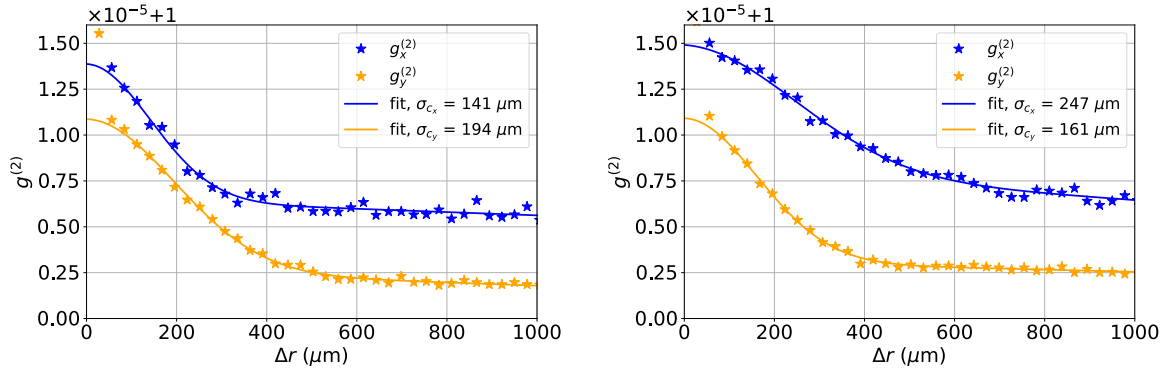

(a) "Matched" electron beam. Retrieved transverse electron beam size: $\sigma_x \times \sigma_y = 31 \times 23\ \mu\text{m}^2$

(b) Missmatched electron beam. Retrieved transverse electron beam size: $\sigma_x \times \sigma_y = 18 \times 27\ \mu\text{m}^2$.

Figure 3.9: Results of the autocorrelation analysis of radiation from **cell 37**

beamline conditions. This observation is further supported by other recorded runs from different undulator cells, which also show inconsistencies under nominal settings. Additional evidence comes from experiments measuring transverse electron beam parameters, such as dispersion, where non-zero values are commonly observed even under nominal conditions.

In total, I recorded more than 20 experimental runs with different configurations of undulator cells and mismatch conditions that still need to be analyzed. Other experiments at 8 keV photon beam energy showed the same results, including the test for matched-mismatched FODO conditions, where I clearly observed a change in the width of the correlation function when changing the magnetic field of the same quadrupole. These observations confirm that spikes of synchrotron radiation are detected.

There are no alternative methods for measuring the electron beam size at the European XFEL to cross-validate the results obtained here. The existing wire scanners are installed at a different location from the SASE1 undulator, making them unsuitable for cross-validation.

3.5. Outlook and discussion

In this study, I presented an experimental method for measuring the transverse size of an electron beam in an undulator. To enhance the effectiveness and versatility of this method, one could consider installing a more sensitive camera to increase the signal-to-noise ratio and enable the use of the Si (333) reflection. The monochromator bandwidth is inversely proportional to the effective time window over which the transverse size is averaged along the electron beam. A narrower bandwidth corresponds to a larger time window and vice versa, as depicted in Fig. 3.10. Thus, when using Si (111), the average slice size of the electron beam is measured due to the lower monochromator resolution. In contrast, the Si (333) reflection would correspond to a time window that encompasses the entire beam duration, as

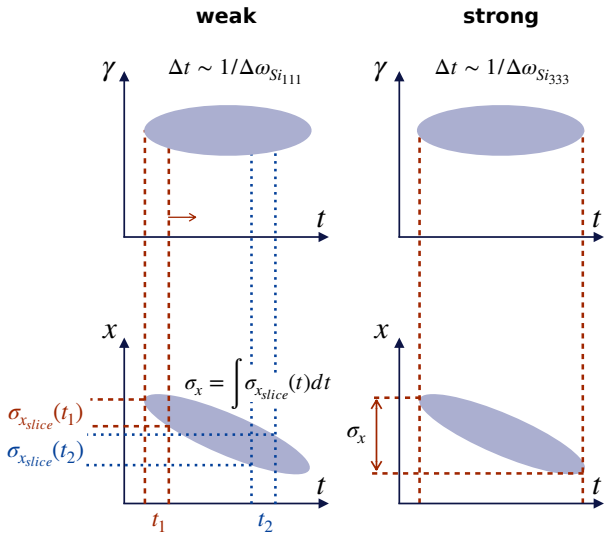

Figure 3.10: Schematic depiction of the electron beam phase space for the t-γ and t-x parameter pairs. The figures illustrate the effect of different levels of monochromatisation on the effectively measured electron beam size.

the Si (333) bandwidth can resolve a single spike in the frequency domain.

In practical terms, the ability to adjust the level of monochromatization allows for the measurement of two transverse sizes: the *projected size* of the entire electron beam with stronger monochromatization (e.g., Si (333)), and the average *slice size* with weaker monochromatization (e.g., Si (111)), as illustrated in Fig. 3.10. While the projected size can be measured using other techniques, such as wire-scanners [107], slice size diagnostics offer a novel and valuable tool for optimizing the FODO lattice and ensuring uniform electron beam size along the FEL undulator line.

Another activity beyond the scope of this thesis is the implementation of this method for measuring electron beam size as a routine procedure in the control room of the European XFEL. Consequently, this would improve SASE performance and facilitate tuning to obtain advanced pulse characteristics.

3.6. Conclusion

In this chapter, I experimentally demonstrated that synchrotron radiation exhibits spikes in the transverse dimension, a feature that naturally arises due to shot noise in the electron beam. The experiment was performed using only the available diagnostics infrastructure—specifically, the spontaneous radiation imager and the K-monochromator—without any hardware upgrades. The detected signal showed a very high level of pixel noise, caused by the low intensity of synchrotron radiation and the limited sensitivity of the detection system, which was not designed for such low photon flux. As a result, the spike structure could not be visually resolved. To overcome this issue, I carried out an autocorrelation analysis of the recorded image ensembles to extract the typical spike distribution. I proposed a data analysis procedure based on diagonal averaging, which improves effective statistics and allows for

reliable reconstruction of the autocorrelation function even in the presence of significant noise. Importantly, the width of the obtained autocorrelation function is directly related to the transverse electron beam size. Therefore, this approach enabled the measurement of the beam size using only the synchrotron radiation and existing beamline diagnostics.

Chapter 4

Peculiarities of undulator virtual source distribution

4.1. Introduction

Undulator radiation has been extensively studied and utilized for decades. The first proposal to use the transverse movement of relativistic electrons for electromagnetic radiation generation traces back to 1947 in theoretical works by V. L. Ginzburg [108][1]. In 1951, H. Motz considered the movement of relativistic electrons in a periodically alternating magnetic field [109], which he called an "undulator". This device was installed at a linear accelerator at Stanford University, and the first light was generated in 1952 [110]. Then, the first proposal to incorporate an undulator into storage rings was in 1958 by K.W. Robinson [111]. Although not for obtaining synchrotron radiation, but for the redistribution of damping of betatron and synchrotron oscillations. Since then, undulator radiation has been described in great detail both theoretically and experimentally as presented in [112]–[114] and citations within. However, only recently has an analytical expression for the virtual source distribution of undulator radiation in resonance from a single electron been derived [51], [69]. The authors of [51] theoretically described the undulator radiation virtual source distribution, which is located in the middle of the undulator. This distribution has a direct physical meaning and can be reproduced with a 1:1 focusing system. They also pointed out the mathematical singularities appearing at both ends of the source distribution for frequencies around the undulator resonance at the odd harmonics, which seemingly have not been described in more detail.

This suggests that there is a more complex undulator virtual source structure and suggests further studies. This is particularly relevant in light of the development of modern synchrotrons employing multi-bend achromat (MBA) magnetic structures [115]. At these radiation sources the electron beam size and divergence is smaller than those of radiation from a single electron in the broad X-ray wavelength range. Thus, more detailed aspects of the source may be directly observed. Moreover, understanding the properties of this distribution is crucial for examining the transverse coherence properties of undulator radiation, as the cross-spectral density function for undulator radiation depends on the single-electron radiation distribution at the virtual source location [70].

In this chapter, I aim to study the undulator radiation virtual source in greater detail than has previously been reported. I will start with a general expression for synchrotron radiation, beginning with the inhomogeneous electromagnetic wave equation in free space,

[1] I could not find the original work in Russian in the electronic format in the internet. Fortunately, the CIA kindly provided a declassified document of those years, which contains a translation of the mentioned article. It can be reached following the link: `https://www.cia.gov/readingroom/docs/CIA-RDP80-00809A000600340656-6.pdf`.

which means that one considers an electromagnetic field in the unbounded space with no medium. Assuming that a particle emitting the radiation is ultra-relativistic, I will derive here a paraxial wave equation, which is commonly used to characterize synchrotron radiation. Subsequently, I will provide an analytical solution for undulator radiation under the resonance approximation at any given position along an optical line. This expression assumes three approximations: the slowly varying envelope approximation (SVEA), the paraxial approximation, and the resonance approximation specific to the undulator case. In this chapter, I use two closely related terms: the *resonance approximation* and radiation *in resonance* or *resonance condition*. The first term refers to the derivation of the analytical expression for the undulator radiation in far zone, implying a large number of undulator periods, an observation angle confined to the central cone of undulator radiation, and a radiation frequency around the *resonance condition*. The *resonance condition* indicates that undulator radiation is considered at its resonance frequency of odd harmonics.

Further on, I will analyze the undulator radiation virtual source distribution in detail using numerical methods [73]–[75]. This analysis will highlight the transverse distribution peculiarities, or "features" that appear at both ends of the undulator's virtual source. The apparent width of these features reveals a finer structure of undulator radiation than is typically associated with the usual diffraction limited size given by $\sqrt{L_w \lambda}$, where L_w is the undulator length. I empirically find that the finer size is related to the period length λ_w as $\sqrt{\lambda_w \lambda}$. To investigate this, I examine the source behavior by reducing the number of undulator periods, thus reducing the resonance effect of the undulator. This results in appearance of a transverse "wiggling" effect of the source, replicating the actual electron path in the undulator. To verify the width of these features, I study the source distribution outside the resonance frequency, where similar wiggling can be observed and confirm that width is related to period length as $\sqrt{\lambda_w \lambda}$. As a result, this chapter will provide an overview of the nature of these peculiarities and suggest possible routes to study them further.

4.2. Synchrotron radiation from a single electron in free space

In this section, I derive the paraxial wave equation for calculating synchrotron radiation from a single electron. The derivations in this section are based on [116].

4.2.1. Helmholtz equation

I consider electric field $\vec{E}(\vec{r}, t)$, that is a real-valued function, which is distributed in time t and space $\vec{r} = x\vec{e_x} + y\vec{e_y} + z\vec{e_z}$. Here $\vec{e}_{x,y,z}$ are the unit vectors in three dimensional space setting some orthogonal reference frame and x, y, z are the coordinates. This electric field satisfies Maxwell's equations in vacuum:

$$\vec{\nabla} \cdot \vec{E} = 4\pi\rho \quad \text{Gauss's law} \tag{4.1}$$

$$\vec{\nabla} \cdot \vec{B} = 0 \quad \text{Gauss's law for magnetism} \tag{4.2}$$

$$\vec{\nabla} \times \vec{E} = -\frac{1}{c}\frac{\partial \vec{B}}{\partial t} \quad \text{Faraday's law of induction} \tag{4.3}$$

$$\vec{\nabla} \times \vec{B} = \frac{4\pi}{c}\vec{j} + \frac{1}{c}\frac{\partial \vec{E}}{\partial t} \quad \text{Ampère's circuital law (with Maxwell's addition),} \tag{4.4}$$

where $\rho(\vec{r},t)$ is charge density, $\vec{j}(\vec{r},t)$ is current density, and $\vec{B}(\vec{r},t)$ is the magnetic field. The equations are presented in *cgs* system.

To obtain the wave equation I substitute the forth equation into the third one:

$$c^2\vec{\nabla}\times(\vec{\nabla}\times\vec{E}) = -\frac{\partial^2\vec{E}}{\partial t^2} - 4\pi\frac{\partial\vec{j}}{\partial t}, \tag{4.5}$$

knowing $\vec{\nabla}\times(\vec{\nabla}\times\vec{E}) = \vec{\nabla}(\vec{\nabla}\cdot\vec{E}) - \nabla^2\vec{E}$ and using Gauss's law I obtain:

$$c^2\nabla^2\vec{E} - \frac{\partial^2\vec{E}}{\partial t^2} = -4\pi c^2\vec{\nabla}\rho + 4\pi\frac{\partial\vec{j}}{\partial t}, \tag{4.6}$$

which is partial differential equation of *hyperbolic* type. Writing this equation for the electric field in frequency domain one obtains the well-known Helmholtz equation:

$$c^2\nabla^2\vec{\tilde{E}} + \omega^2\vec{\tilde{E}} = 4\pi c^2\vec{\nabla}\tilde{\rho} - 4\pi i\omega\vec{\tilde{j}}, \tag{4.7}$$

which is *elliptic*. Here $\tilde{\rho}$ and $\vec{\tilde{j}}$ are Fourier transforms of charge and current densities in frequency domain.

Introducing a fixed Cartesian reference system $(\vec{e}_x,\vec{e}_y,\vec{e}_z)$, where z is the optical axis, one can always write:

$$\vec{\tilde{E}} = \vec{\tilde{E}}e^{i\omega z/c}. \tag{4.8}$$

This factorization is very helpful when $\vec{\tilde{E}}$ varies slowly on the scale of the wavelength $\lambda = 2\pi c/\omega$ (in SVEA) and allows to further simplify Eq. 4.7:

$$c^2e^{i\omega z/c}\left(\nabla^2 + \frac{2i\omega}{c}\frac{\partial}{\partial z}\right)\vec{\tilde{E}} = 4\pi c^2\vec{\nabla}\tilde{\rho} - 4\pi i\omega\vec{\tilde{j}}. \tag{4.9}$$

Next, I write this equation for a specific source: a single electron moving along a curvilinear abscissa s in a magnetic field. The latter means that its velocity $v = |\vec{v}(t)|$ is constant. Thus, the curvilinear abscissa can be expressed as $s = vt$.

The charge and current densities can be expressed mathematically with delta functions:

$$\rho(\vec{r},t) = -e\delta\big(\vec{r} - \vec{r}'(t)\big) \tag{4.10}$$

and

$$\vec{j}(\vec{r},t) = -e\vec{v}(t)\delta\big(\vec{r} - \vec{r}'(t)\big), \tag{4.11}$$

where $\vec{r}'(t)$ and $\vec{v}(t)$ are the electron's position and velocity in the given reference frame. The particle trajectory in the magnetic field should be determined separately.

I rewrite $\delta\big(\vec{r} - \vec{r}'(t)\big)$ as $\delta\big(\vec{r} - \vec{r}'(t)\big) = \delta\big(\vec{r}_\perp - \vec{r}'_\perp(t)\big)\delta\big(z - z'(t)\big)$ separating longitudinal and transverse dimensions and rewrite Dirac delta function for z direction as the following:

$$\delta\big(z - z'(t)\big) = \frac{1}{v_z(z)}\delta\big(t - t(z)\big), \tag{4.12}$$

here I used the well-known property of Dirac delta function:

$$\delta\big(f(x)\big) = \sum_i \frac{\delta(x - x_i)}{f'(x_i)}, \tag{4.13}$$

where x_i are the zeros of some function $f(x)$. There is only one zero for the function $z - z'(t)$ at t value that is indicated by $t(z)$. Also $|f'(t(z))| = v_z(z(t))$. Remembering that $s(z) = ut(z)$ I rewrite ρ and $\vec{j}$ from Eqs. 4.10 and 4.11 as the following:

$$\rho(\vec{r}_\perp, z, t) = -\frac{e}{v_z(z)}\big(\vec{r}_\perp - \vec{r}'_\perp(t)\big)\delta\left(\frac{s(z)}{v} - t\right) \tag{4.14}$$

and

$$\vec{j}(\vec{r}_\perp, z, t) = -\frac{e}{v_z(z)}\vec{v}(z)\delta\big(\vec{r}_\perp - \vec{r}'_\perp(t)\big)\delta\left(\frac{s(z)}{v} - t\right). \tag{4.15}$$

Then performing Fourier transform I obtain:

$$\bar{\rho}(\vec{r}_\perp, z, \omega) = -\frac{e}{v_z(z)}\delta\big(\vec{r}_\perp - \vec{r}'_\perp(z)\big)e^{i\omega s(z)/v} \tag{4.16}$$

and

$$\bar{\vec{j}}(\vec{r}_\perp, z, \omega) = -\frac{e}{v_z(z)}\vec{v}(z)\delta\big(\vec{r}_\perp - \vec{r}'_\perp(z)\big)e^{i\omega s(z)/v}. \tag{4.17}$$

Now I rewrite Eq. 4.9 substituting Eqs. 4.16 and 4.17 in it and obtain:

$$\left(\nabla^2 + \frac{2i\omega}{c}\frac{\partial}{\partial z}\right)\tilde{\vec{E}} = \frac{4\pi e}{v_z(z)}\exp\left[i\omega\left(\frac{s(z)}{v} - \frac{z}{c}\right)\right]\left[i\frac{\omega}{c^2}\vec{v}(z) - \vec{\nabla}\right]\delta\big(\vec{r}_\perp - \vec{r}'_\perp(z)\big). \tag{4.18}$$

As mentioned, $\tilde{\vec{E}}$ does not vary much along the propagation axis z on the scale of λ, which can be mathematically expressed as $|\partial_z \tilde{E}_{x,y}| \ll (\omega/c)|\tilde{E}_{x,y}|$. Therefore, the second derivative with respect to z will be much smaller than the first derivative present in the expression and can be neglected. This allows me to apply the paraxial approximation for Eq. 4.18:

$$\left(\nabla_\perp^2 + \frac{2i\omega}{c}\frac{\partial}{\partial z}\right)\tilde{\vec{E}}_\perp(z, \vec{r}_\perp) = \frac{4\pi e}{c}\exp\left[i\omega\left(\frac{s(z)}{v} - \frac{z}{c}\right)\right]\left[i\frac{\omega}{c^2}\vec{v}_\perp(z) - \vec{\nabla}\right]\delta\big(\vec{r}_\perp - \vec{r}'_\perp(z)\big), \tag{4.19}$$

where I denoted the gradient operator over transverse coordinates as $\nabla_\perp$. In Eq. 4.19, I wrote only the transverse components and substituted c instead of $v_z(z)$ as one considers the ultra relativistic particle. Note that Eq. 4.18 has been transformed to the *parabolic* type.

In this thesis, I consider the case of ultra-relativistic particles, i.e., $\gamma^2 \gg 1$. In practice, this means that almost the entire power of the emitted radiation will be concentrated in a cone of angular size about $1/\gamma$, which is a result of the Lorentz boost. This observation is valuable as such small angles automatically ensure that the paraxial approximation is fulfilled and mathematically justified.

For brevity of notation in further derivation I denote differential operator and right hand side of the Eq. 4.19 in the following form:

$$\mathcal{D}\left[\tilde{\vec{E}}_\perp(z, \vec{r}_\perp)\right] = \vec{f}(z, \vec{r}_\perp), \tag{4.20}$$

where $\mathcal{D}$ is differential operator of the left hand side of Eq. 4.19 and $\vec{f}(z, \vec{r}_\perp)$ contains the right hand side terms of this equation.

4.2.2. Solution of the paraxial approximation of the Helmholtz equation

The solution for Eq. 4.20 is relatively easy to find using the Green's function method. A Green's function should satisfy the following equation:

$$\mathcal{D}\left[G(z_0 - z; \vec{r}_{\perp 0} - \vec{r}_\perp)\right] = \delta(\vec{r}_{\perp 0} - \vec{r}_\perp)\delta(z_0 - z), \tag{4.21}$$

that effectively describes radiation from a point source. In the case of unbounded space with no medium – free space – the solution for this equation is well-known and can be written as:

$$G(z_0 - z'; \vec{r}_{\perp 0} - \vec{r}'_\perp) = -\frac{1}{4\pi(z_0 - z')} \exp\left[i\omega \frac{|\vec{r}_{\perp 0} - \vec{r}'_\perp|^2}{2c(z_0 - z')}\right]. \tag{4.22}$$

where, as usual, coordinates with primes correspond to the source location and those with subscript $_0$ refer to the observer location.

One can express the solution of the non-homogeneous Eq. 4.20 at the point $\vec{r}_{\perp_0}$ using Green's function from Eq. 4.22 as an integral over z' and $\vec{r}'$ in the following form:

$$\vec{\tilde{E}}(\vec{r}_{\perp 0}, z_0) = \iint_{-\infty}^{\infty} G(z_0 - z', \vec{r}_{\perp 0} - \vec{r}'_\perp)\vec{f}(z', \vec{r}'_\perp) d\vec{r}'_\perp dz' \tag{4.23}$$

The form of Eqs. 4.21 and 4.23 is general for differential equation theory[2] and can be applied in various physical scenarios. For example, by extending the theory presented here, the calculation of synchrotron radiation in a waveguide can be written using the same integral as in Eq. 4.23, but with an appropriate Green's function. The Green's function should be found using Eq. 4.21 with the imposed boundary conditions of a waveguide. This problem will be considered in Chapter 5.

Now I can write Eq. 4.23 with $\vec{f}(z', \vec{r}'_\perp)$ and $G(z_0 - z', \vec{r}_{\perp 0} - \vec{r}'_\perp)$ substituted into the integral explicitly:

$$\begin{aligned}\vec{\tilde{E}}_\perp(\vec{r}_{\perp 0}, z_0, \omega) = -\frac{e}{c}\int_{-\infty}^{\infty} dz' \frac{1}{z_0 - z'} \int_{-\infty}^{\infty} d\vec{r}'_\perp \exp\left[i\omega\left(\frac{s(z')}{v} - \frac{z'}{c}\right)\right] \\ \left[i\frac{\omega}{c^2}\vec{v}_\perp(z') - \vec{\nabla}'_\perp\right]\delta\left(\vec{r}'_\perp - \vec{r}'_\perp(z')\right) \exp\left[i\omega\left(\frac{|\vec{r}_{\perp_0} - \vec{r}'_\perp|^2}{2c(z_0 - z')}\right)\right],\end{aligned} \tag{4.24}$$

and then taking the integral over the transverse direction I obtain:

$$\begin{aligned}\vec{\tilde{E}}_\perp(\vec{r}_{\perp 0}, z_0, \omega) = -\frac{i\omega e}{c^2}\int_{-\infty}^{\infty} dz' \frac{1}{z_0 - z'}\left[\left(\frac{v_x(z')}{c} - \frac{x_0 - x'(z')}{z_0 - z'}\right)\vec{e}_x + \left(\frac{v_y(z')}{c} - \frac{y_0 - y'(z')}{z_0 - z'}\right)\vec{e}_y\right]\times \\ \exp\left[i\omega\left(\frac{(x_0 - x'(z'))^2 + (y_0 - y'(z'))^2}{2c(z_0 - z')} + \frac{s(z')}{v} - \frac{z'}{c}\right)\right].\end{aligned} \tag{4.25}$$

[2]Surely, with proper notation adaptation.

Once the trajectory and velocity of the electron are known, this integral can be directly used in the calculations of synchrotron radiation.

One can also find a solution of the Helmholtz equation presented in Eq. 4.18 using the same approach with Green's functions and apply the paraxial approximation to the solution; there is no difference between applying the paraxial approximation at the stage of deriving the wave equation or at the stage of solving it. This was studied and presented in [116].

Another point to note is that traditionally, radiation from a charged particle is derived using the Liénard-Wiechert potential in the time domain. This is another way of approaching the problem, but it is equivalent to the approach presented here. This question is also extensively discussed in [116].

In some certain cases Eq. 4.25 can be simplified to obtain a final analytical expression for the field. One can notice the oscillatory behaviour of the exponential factor $\exp[i\omega(s(z')/v - z'/c)]$. As one integrates of over z' in Eq. 4.25 the term $\omega(s(z')/v - z'/c)$ will grow, which leads to oscillatory behaviour of the integrand. This means that the integrand will not effectively contribute to the integral. The range along the z direction within which the integrand still contributes to the final value of the integral can be estimated as $\omega(s(z')/v - z'/c) \sim 1$. The length at which this holds is referred to as the formation length (L_f) of radiation at the given frequency ω. If one considers the speed of the particle to be of the order of the speed of light but noticeably smaller, one can find that $L_f \sim \lambda$. However, in the ultra-relativistic case when v is very close to the speed of light ($\gamma^2 \gg 1$), $s(z)/v$ and z/c compensate each other, resulting in L_f being significantly larger than λ. The exact expression for L_f largely depends on the magnetic configuration considered. For example, in the case of a bending magnet, this length is estimated to be $\sim R/\gamma$ for the critical wavelength, where R is the bending radius. For the specific case of undulator radiation, the natural scale of the undulator is its period length λ_w, but the effective formation length is L_w – the length of the whole device! Such an increase in the formation length occurs due to the resonance effect, when radiation at each period constructively contributes to the electric field.

4.3. Undulator radiation virtual source

Studying the virtual source distribution analytically while accepting only two approximations – SVEA and paraxial – is challenging. Deriving the analytical expressions for undulator radiation inevitably requires accepting the resonance approximation. This implies that the number of undulator periods is large, $N_w \gg 1$, and radiation from the undulator is considered within the central cone $\theta_c \sim 1/(\sqrt{2N_w}\gamma_z)$, where $\gamma_z = \gamma/\sqrt{1 + K^2/2}$ and K is the undulator deflection parameter. The resonance approximation aids in deriving the well-known field distribution of the undulator in the far-field zone [117].

In this section, I will present numerical results that reveal a highly intriguing virtual source distribution. For this, I will utilize the `OCELOT` toolkit, where synchrotron radiation calculations are based on taking the integral derived from the Fourier transform of the Liénard-Wiechert potential. As mentioned, this approach is equivalent [51] to taking the integral presented in Eq. 4.25. Considering the undulator virtual source without accepting the resonance approximation numerically helps to study it in more detail than previously presented.

4.3.1. Analytical expression for the field of undulator radiation

I present here the well-known expression for the electric field distribution of undulator radiation for x-polarization component[3], as the results of the derivations from [116]:

$$\tilde{E}_{\perp}(\vec{r}_{\perp 0}, z_0, \omega) = -\frac{K\omega e L_w}{2c^2 z_0 \gamma} A_{JJ} \exp\left[\frac{i\omega z_0}{2c}\theta^2\right] \mathrm{sinc}\left[\frac{\omega L_w \theta^2}{4c} + \frac{C L_w}{2}\right], \tag{4.26}$$

where angle $\vec{\theta}$ is the observation angle in the far zone that is equal to $\vec{r}_{\perp_0}/z_0$. $L_w = \lambda_w N_w$ is the undulator length, N_w is the number of undulator periods and λ_w is the undulator period length, $C = \omega/(2\gamma_z^2 c) - k_w$ is the detuning parameter, where $k_w = 2\pi/\lambda_w$. $A_{JJ} = J_0(\zeta) - J_1(\zeta)$ where $\zeta = K^2/(4 + 2K^2)$ and J_n is the n-th order Bessel function of the first kind. $K = eB\lambda_w/2\pi m_e c$ is the undulator (deflection) parameter, where m_e is the electron mass and B is the y-component of the magnetic field in the undulator along the z-axis.

This expression describes the undulator field distribution in the far zone at the distance z_0 measured from the center of the undulator and at perfect resonance, i.e $C = 0$. Using the field propagator from [51] or the one derived in Appendix A[4], one can back propagate the field to the virtual source position $z_0 = 0$:

$$\tilde{E}_{\perp}(\vec{r}_{\perp 0}, 0, \omega) = i\frac{K\omega e}{2c^2\gamma} A_{JJ}\left[\pi - 2\mathrm{Si}\left(\frac{\omega \vec{r}_{\perp 0}}{L_w c}\right)\right] \tag{4.27}$$

Actually, it is quite natural to define the source location of the undulator radiation at the very centre of the undulator. This choice of location is logical from at least two perspectives: the symmetry of the radiation distribution at the virtual source and the plane phase front.

Knowing this field distribution, one can obtain the distribution at an arbitrary observation position z_0 outside the magnetic setup using the free space propagator, as was shown in [51], and write it as follows:

$$\tilde{E}_{\perp}(\vec{r}_{\perp 0}, z_0, \omega) = \frac{K\omega e A_{JJ}}{2c^2\gamma}\left[\mathrm{Ei}\left(\frac{i\omega r_{\perp 0}^2}{2z_0 c - L_w c}\right) - \mathrm{Ei}\left(\frac{i\omega r_{\perp 0}^2}{2z_0 c + L_w c}\right)\right], \tag{4.28}$$

where $\mathrm{Ei}(\cdot)$ denotes the exponential integral function. As was mentioned in [51], the field at the points $z_0 = L_w/2$ (at the end of the undulator) and $r_{\perp} = 0$ is singular. The appearance of this mathematical singularity is related to the use of the resonance approximation. To the best of my knowledge, this phenomenon has not received much attention, neither theoretically nor experimentally. In the following sections, I study this peculiarity in more detail using numerical methods.

4.3.2. Source peculiarities as a result of Wigner function propagation

The apparent singularity at the ends of the virtual source of single-electron undulator radiation can be studied numerically. In Fig. 4.1, I present the undulator source distribution along the device, which was obtained by back propagating the field distribution from the far zone to the source location using `OCELOT`. This distribution resembles a candy wrapper, with two

[3] For the undulator with the magnetic field distribution in y direction.

[4] They are equivalent in the paraxial approximation.

narrow virtual source features appearing at either end of the undulator. This are the traces of the peculiarities noted in [51]. It is evident that in reality, this feature should have a finite width, as depicted in Fig. 4.2, and the mathematical singularity appears as a result of the approximations taken in analytical calculations.

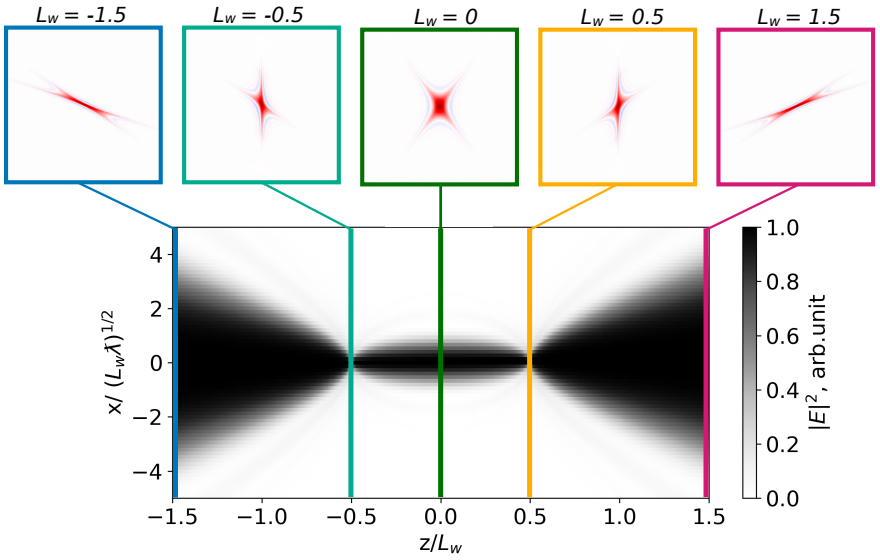

Figure 4.1: Candy-wrapper-like distribution of the undulator radiation virtual source. The source intensity distribution along the undulator versus the transverse x-dimension is shown. Both axes are normalised to the natural dimensions of the system: the undulator length and the diffraction size of undulator radiation. The intensity profile along the vertical-axis slice is normalised to its maximum value. Wigner function distributions at different positions along the device are shown at the top of the subplots.

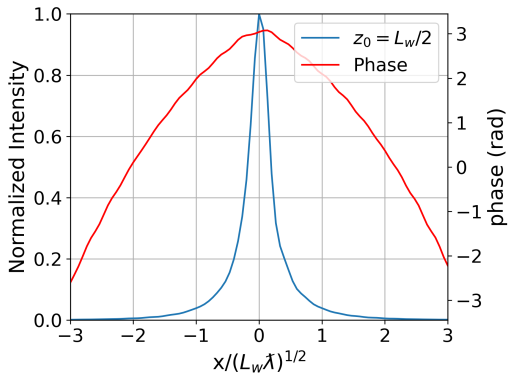

Figure 4.2: The virtual source distribution at the edge of the undulator at resonance. The distribution width is $FWHM_{z_0=L_w/2} = 0.38\sqrt{L_w\lambda}$. The radiation acquires a quadratic phase front as a result of propagation.

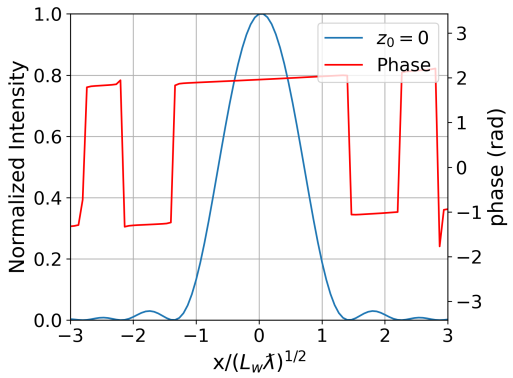

Figure 4.3: The virtual source distribution in the middle of the undulator at resonance. The distribution width is $FWHM_{z_0=0} = \mathbf{1.37}\sqrt{L_w\lambda}$. The phase tilt is due to a slight overall tilt in the electron velocity.

A qualitative explanation of this feature can be viewed from the perspective of a Wigner

function distribution in the transverse dimension. I depict the X-shaped Wigner function distribution at the center of the device in Fig. 4.4, which was presented also in [118]. The marginal distributions onto the horizontal (distance) and vertical (divergence) axes of the Wigner function will result in intensity distributions in the corresponding domains: real and inverse space, which, in this case, correspond to the spatial and angular distribution of the source.

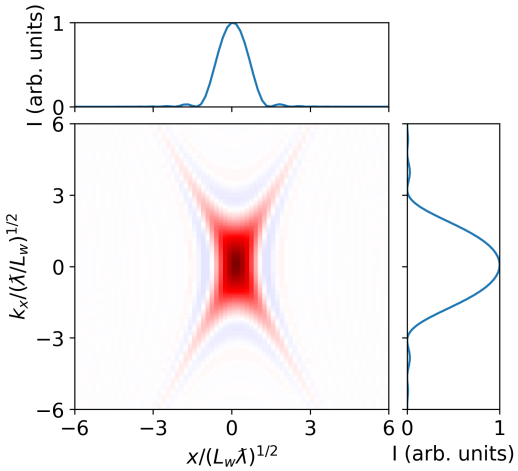

Figure 4.4: X-shaped Wigner function distribution at the centre of the undulator. The marginal distributions along the horizontal and vertical axes represent the spatial and angular profiles of the radiation, respectively.

Upon free-space propagation, the Wigner function distribution "shears" as described in [118], resulting in the types of distributions depicted in the subplots of Fig. 4.1 at both ends of the undulator. It can be observed that one axis of the "X" is now oriented parallel to the inverse space axis. A detailed calculation of the spatial distribution reveals that there is no singularity, however the distribution is noticeably narrower compared to the center of the device. For comparison, see Fig. 4.2 and Fig. 4.3.

The authors of [51] note that the far-field distribution and the distribution at the source are related via a Fourier transform (apart from the phase factor), implying that small features at the source correspond to large features in the far zone and vice versa. However, the resonance approximation restricts one to angles in the far zone that are comparable to the size of the central cone of the undulator radiation. For large angles, this approximation fails, and thus, the singularity is not truly singular but should have a finite width.

The reasoning presented above provides only a qualitative understanding of the nature of this feature. A reasonable question may arise: what is the characteristic distribution width of the observed features in Fig. 4.2 expressed in terms of an undulator parameters?

It is well known that the diffraction size of undulator radiation, given by $\sqrt{L_w\lambda}$, is directly related to the undulator length and also represents the formation length of the undulator radiation. This unique case, where the entire length of the device constitutes the formation length, is explained by the constructive summation of radiation from all periods. Thus, the resonant flux density scales proportionally to the square of the number of undulator periods. However, there is another typical scale in the undulator – its period length λ_w. Therefore, there should be features with typical size of $\sqrt{\lambda_w\lambda}$ in the structure of undulator radiation. This is a hypothesis. From this point on, I will refer to the diffraction size related to the overall

length of the undulator and corresponding contribution to the flux density as the *resonant* one, and conversely, the one related to the undulator period as the *non-resonant* one.

4.3.3. Undulator virtual source wiggling

First, I will present an analytical attempt to verify the dependency of the features on the period length. Following this, I will show numerical simulations that demonstrate the wiggling behaviour of the virtual source distribution along the undulators. I will then proceed with an empirical study with this numerical simulations to verify the size of the observed features and confirm the proposed hypothesis.

Analytical attempt

To demonstrate that the typical width of the undulator virtual source scales as $\sqrt{\lambda_w \bar{\lambda}}$, one can begin with the expression for the electric field in the far zone. Modifying Eq. 4.25: expanding $1/(z_0 - z')$ around z_0 and using the vector angle of observation $\vec{\theta}$ I write:

$$\vec{\tilde{E}}(\vec{\theta}, z_0, \omega) = -\frac{i\omega e}{c^2 z_0} \int_{-\infty}^{\infty} dz' \left(\frac{\vec{v}(z')}{c} - \vec{\theta} \right) \exp\left(i\omega \left[\frac{s(z')}{v} - \frac{z'}{c} \right] + \frac{i\omega}{2c} \left[z_0 \theta^2 - 2\vec{\theta} \cdot \vec{r}'(z') + z' \theta^2 \right] \right). \tag{4.29}$$

One can obtain the virtual source distribution by back-propagating this field to the source location ($z = z_s$), following Eq. 5 from [51]:

$$\vec{\tilde{E}}(\vec{r}, z_s, \omega) = \frac{i\omega z_0}{2\pi c} \int_{-\infty}^{\infty} d\vec{\theta} \exp\left[-\frac{i\omega\theta^2}{2c} (z_0 + z_s) \right] \vec{\tilde{E}}(\vec{\theta}, z_0, \omega) \exp\left[\frac{i\omega}{c} \vec{r} \cdot \vec{\theta} \right]. \tag{4.30}$$

Substituting Eq. 4.29 in the last equation one obtains:

$$\vec{\tilde{E}}(\vec{r}, z_s, \omega) = \frac{\omega^2 e}{2\pi c^3} \int_{-\infty}^{\infty} dz' \int_{-\infty}^{\infty} d\vec{\theta} \left(\frac{\vec{v}(z')}{c} - \vec{\theta} \right) \exp\left(i\omega \left[\frac{s(z')}{v} - \frac{z'}{c} \right] \right) \times$$
$$\times \exp\left(\frac{i\omega}{2c} \left[(z' - z_s)\theta^2 + 2\vec{\theta} \cdot (\vec{r} - \vec{r}'(z')) \right] \right). \tag{4.31}$$

The first exponent is oscillatory at the scales larger than the formation length L_f as one integrates along z'. Consequently, the integral limits can be set to $(-L_f, L_f)$ at least. This simplification remains general and does not depend on the type of source considered.

The second exponent contains a phase that is also oscillatory as one integrates over $\vec{\theta}$ with fixed integration limits for z'. Intuitively, within the range of z_s, which is around the "virtual source" $(-L_f, L_f)$, the integral effectively adds up for $\vec{r} \approx \vec{r}'(z_s)$. Considering the energy conservation law, whole energy in the pulse will be concentrated around this location at the source. Thus, assuming that z' varies insignificantly within undulator length $(-L_f, L_f)$, one estimates the integration range for angles to be $\theta_{x,y} < \sqrt{2c/(\omega(z' - z_s))}$. One observes large field values only within undulator $(-L_f, L_f)$ since the field diverges farther from the source. Therefore, at most $|z' - z_s| \sim L_f$, giving the estimation $\theta_{x,y} < \sqrt{2c/(\omega L_f)}$. Finally,

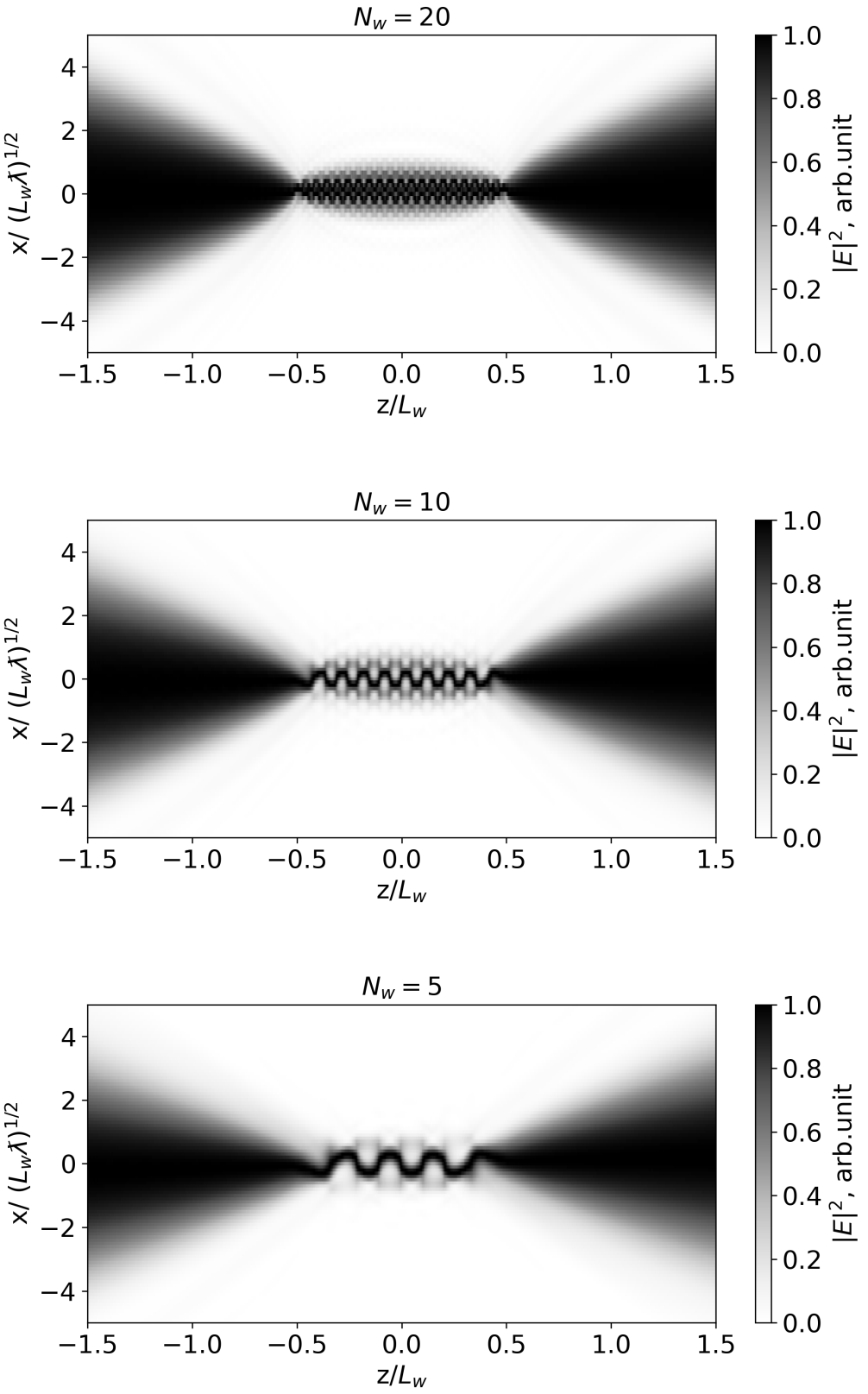

Figure 4.5: Candy-wrapper-like distribution of the undulator source. The "wiggling" of the source distribution is shown. From top to bottom, source distributions for 20-period, 10-period, and 5-period devices are presented. Each transverse slice is normalised to its maximum intensity.

the last term remains small only for deviations of $\vec{r}$ from the trajectory up to the order of $\delta r \sim c/\omega\sqrt{\omega L_f/c} \sim \sqrt{(cL_f)/\omega}$, which is the typical diffraction size. At this point, I have determined that the diffraction size of the radiation is $\delta r \sim \sqrt{(cL_f)/\omega}$, as expected. This does not contradict the hypothesis that there are two typical scales: one related to the undulator length and the other to its period length. The value of L_f can vary significantly depending on the chosen magnetic configuration. For undulator radiation, I seek evidence that the diffraction size differs from the resonant one determined by the undulator length, L_w. As seen, it is challenging to find an elegant mathematical confirmation of different formation lengths in an undulator. Therefore, another proofs should be sought using numerical approaches.

Numerical approach

To observe the features related to the non-resonant contribution, I employ two methods: decreasing the number of undulator periods and observing the radiation out of resonance. The first approach mitigates the resonance contribution of the device. By reducing the number of periods, one can observe more intrinsic details of the radiation at the source, which are not obscured by the resonance contribution. The second approach – setting the radiation out of resonance – removes strong resonance effects altogether, allowing for the observation of the pure non-resonant contribution.

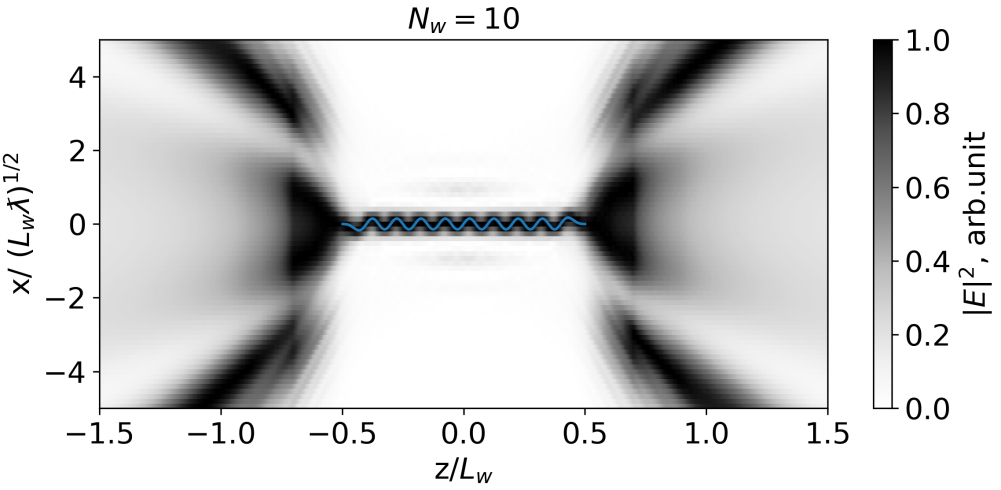

Figure 4.6: "Wiggling" of the undulator source distribution in the out-of-resonance case, with the frequency set between the first and second harmonics. Each transverse slice is normalised to its maximum intensity.

In both cases I expect to observe that the source size will differ significantly from the well-known resonant diffraction size: $\sqrt{L_w\lambda}$. I demonstrate this in Fig. 4.5, where a specific transverse shape of the undulator source emerges. One can see here the non-resonant structure (the "wiggling") of the undulator radiation superposed with the resonant one (the "candy wrapper") that decays when reducing number of periods. Judging only by this distribution it is difficult to extract the distribution width as both contributions being superposed: resonance and non-resonance.

To mitigate the resonance contribution I will examine the out-of-resonance case of the radiation from a ten-period device. I set the frequency detuning $C = 20$. One can observe

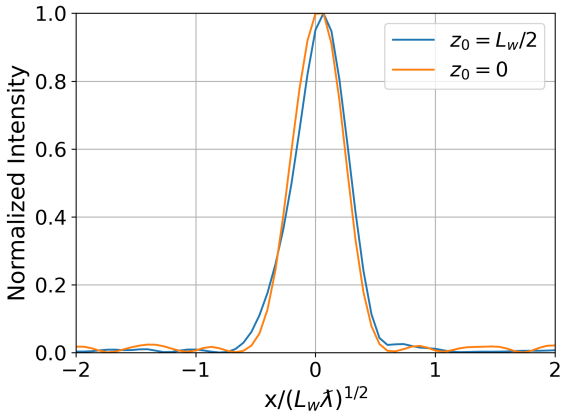

Figure 4.7: "Wiggling" of the undulator source distribution in the out-of-resonance case, shown for the intensity slices. The distribution width is given by $FWHM_{z_0=0} = 0.42\sqrt{L_w\bar{\lambda}}$.

the same wiggling of the source distribution in Fig. 4.6. I plot the intensity slices over specific locations in Fig. 4.7, where as usual $z_0 = 0$ is the centre of the device. Calculating $FWHM$ for both of these distributions in Fig. 4.6 yields $FWHM_{\bar{\lambda}} \approx 0.43\sqrt{L_w\bar{\lambda}}$. As I noted in Fig. 4.3, the diffraction limited size of the resonance case is $FWHM_{L_w} \approx 1.37\sqrt{L_w\bar{\lambda}}$. Assuming that the *non-resonance* source distribution has a similar bell-like shape to the *resonance* one, one expects to find that the ratio $FWHM_{L_w}/FWHM_{\lambda_w}$ is close to $\sqrt{10} = 3.16$ for a 10-period device. Calculating this width of the distribution in Fig. 4.7 for $z_0 = 0$, I obtain $FWHM_{L_w}/FWHM_{\lambda_w} = 3.19$. I tested this hypothesis for different numbers of periods in a device, and the results of these comparisons are presented in Table 4.1. As can be seen, the

N_w	$\frac{FWHM_{\lambda_w}}{\sqrt{L_w\bar{\lambda}}}$	$\frac{FWHM_{L_w}}{FWHM_{\lambda_w}}$	$\sqrt{N_w}$
5	0.60	≈ 2.28	≈ 2.24
10	0.43	≈ 3.19	≈ 3.16
20	0.30	≈ 4.57	≈ 4.47
30	0.25	≈ 5.48	≈ 5.48
40	0.21	≈ 6.52	≈ 6.32

Table 4.1: Table showing comparison of the ratio of $\frac{FWHM_{L_w}}{FWHM_{\lambda_w}}$ and $\sqrt{N_w}$ for different values of N_w.

ratio $FWHM_{L_w}/FWHM_{\lambda_w}$ and $\sqrt{N_w}$ coincide reasonably well, confirming the hypothesis that undulator radiation has a finer diffraction size amounting to $\sqrt{\bar{\lambda}\lambda_w}$.

4.4. Conclusion

In this Chapter, I presented numerical studies of the undulator radiation virtual source distribution. Initially, I explored the *in-resonance virtual source* peculiarities that appear at either end of the undulator, as was noted at first in [51]. I hypothesized that the finite size of these peculiarities should be related to the undulator period length. It is widely known that the diffraction size of the undulator radiation in resonance is determined by the undulator

length as $\sqrt{L_w \bar{\lambda}}$. The smaller features in the structure of the virtual source, which are related to the period length, are obscured by the "resonance" diffraction size. I confirmed this hypothesis by numerically examining the *out-of-resonance virtual source*. I observed a specific wiggling behavior along the undulator length, which reproduces the electron trajectory. I found that the width of this source distribution relates to the undulator period length as $\sqrt{\lambda_w \bar{\lambda}}$. I aim to work on this problem further to find convincing analytical and experimental confirmations of the findings presented here.

Chapter 5

Generation of synchrotron radiation within a waveguide

5.1. Introduction

Properties of synchrotron radiation are often deduced numerically. The conventional numerical codes typically assume that generation happens in space unbounded and free of any material. This leads to a natural boundary condition, where the field diminishes to zero at infinity. This assumption is a practical approximation since, in facilities radiation is generated and propagates within vacuum pipes with inner diameter much larger than the radiation waist size. The influence of these pipes on radiation across a broad range of wavelengths (from visible light to hard X-rays and beyond) is often negligible or undetectable. However, when dealing with highly divergent THz radiation, it becomes necessary to take into account the influence of pipe surface and other metallic components on the radiation, since the vacuum infrastructure starts to effectively act as an overmoded waveguide. In this chapter, I present a numerical code designed to calculate synchrotron radiation in the presence of boundary conditions imposed by the metallic walls.

The theoretical background for this problem was established in [119], which extends and complements prior works [51], [116]. In this chapter I aim to develop a code based on the derivations presented in [119], capable of accurately calculating synchrotron radiation in the waveguide. Such a tool is crucial for simulating and designing THz radiation beamlines at facilities, including those planned or under construction at SLAC [54], [57], [58] and the European XFEL [52], [120], as well as those already in operation, such one [121] at FLASH. The method I employed to program the code utilizes the Green's function method to solve the field equation. This approach offers considerable flexibility; once the Green's function for a given system is determined – which can usually be analytically derived for simple yet practical geometries – the solution is found by numerically evaluating a special integral.

In this chapter, I deduce the boundary conditions for the waveguide with an arbitrary cross-section, provide the expression for the Green's function for a circular waveguide based on [119], and present the general form of the integral to be evaluated. A significant part of this chapter is dedicated to cross-validating the developed code, which I call **S**ynchrotron **R**adiation in **W**ave**G**uide (`SRinWGuide`). The verification process begins with a straightforward scenario of free space using the corresponding paraxial Green's function for synchrotron radiation [116]. This step tests the accuracy of the integration process itself. I cross-check the results of `SRinWGuide` with one obtained using the Synchrotron Radiation Workshop (`SRW`) [38]. Subsequently, I validate the results obtained using the circular waveguide Green's function. I test whether the results obtained with this Green's function converge to the solution obtained using the free space Green's function in the paraxial approximation as the waveguide radius approaches infinity $R \to \infty$. Finally, I check a real-case scenario where

there is a strong influence of the metallic walls in a ten-period undulator device. I cross-check the results of the code with analytical expressions [119] derived under paraxial and resonance approximations.

The developed code has been uploaded to a GitHub repository [122], with plans for further development to meet the demands of accurate simulations of the THz radiation beamlines. The development and cross-checks of the code have revealed several challenges that necessitate further studies. For instance, the Green's function of the bounded system is an infinite sum of transverse modes, and identifying which of these modes effectively contribute to the integral beforehand is crucial. Contribution from some modes lead to highly oscillatory integrals, resulting in aliasing issues, while their contributions remain negligible. Additionally, the code's numerical efficiency can be further enhanced, along with addressing other programming-related issues in potential future work.

5.2. Boundary conditions and Green's function integral

In Chapter 4, I considered the solution of the wave equation for a single electron moving along an arbitrary trajectory in free space under the paraxial approximation. This treatment will now be extended to the case of a single electron moving in a magnetic field in the presence of metallic boundaries.

The derivation in this part of the thesis relies on those presented in [119]. Before starting it, I discuss the necessary underlying approximations. One considers an ultra-relativistic system, $1/\gamma^2 \ll 1$, which in turn means that radiation from this particle will be confined to relatively small angles, at the level of $1/\gamma$. This actually leads to the fact that the usual definition of the paraxial approximation is naturally fulfilled, $k_\perp^2 c^2/\omega^2 \ll 1$. For a waveguide, transverse modes lie in the discrete range of $k_\perp$ values, but the condition $k_\perp^2 c^2/\omega^2 \ll 1$ must still be fulfilled. A transverse dimension of the waveguide (here I consider a common example of a circular waveguide with radius R) defines the cutoff frequency $\omega_c \sim c/R$. Writing the transverse wavenumber as $k_c \sim 1/R$, one can see that the paraxial approximation is applicable when $\omega \gg \omega_c$. In this case, the waveguide is overmoded, i.e., $\lambda\!\!\!^{-} \ll R$, which I will assume to hold throughout this chapter. In this scenario, it is still possible to use the field in the same representation as in Chapter 4: the slowly varying envelope of the Fourier transform of the transverse electron field or simply the field $\tilde{\vec{E}}(z, \vec{r}_\perp)$.

The metallic walls boundary conditions mean that the electric field must be perpendicular to the surface (S):

$$\left(n_x \tilde{E}_y - n_y \tilde{E}_x\right)\Big|_S = \left(\vec{n} \times \tilde{\vec{E}}_\perp\right)\Big|_S = 0, \tag{5.1}$$

and

$$\left(\tilde{E}_z\right)\Big|_S = 0, \tag{5.2}$$

where $\vec{n}$ is normal vector to the surface S. Eq 5.2 is equivalent to:

$$\left[\left(\vec{\nabla} \times \tilde{\vec{H}}\right)_z\right]\Big|_S = 0, \tag{5.3}$$

which is a z component of Maxwell's equation for the curl of the magnetic field. Here $\vec{\tilde{H}}$ is the slowly varying envelope of the magnetic field written in the space-frequency domain.

I make use of the relation for the components magnetic field and electric: $\tilde{E}_x \simeq \tilde{H}_y$ and $\tilde{E}_y \simeq -\tilde{H}_x$, which hold in the paraxial approximation. Then, finally rewriting Eq. 5.3, I obtain:

$$\left(\frac{\partial \tilde{E}_x}{\partial x} + \frac{\partial \tilde{E}_y}{\partial y}\right)\Big|_S = \left(\vec{\nabla}_\perp \cdot \vec{\tilde{E}}_\perp\right)\Big|_S = 0 \tag{5.4}$$

So, writing together the wave equation and the boundary condition I obtain the following system:

$$\begin{cases} \mathcal{D}\left[\vec{\tilde{E}}_\perp(z,\vec{r}_\perp)\right] = \vec{f}(z,\vec{r}_\perp) \\ \left(\vec{n}\times\vec{\tilde{E}}_\perp\right)\Big|_S = 0 \\ \left(\vec{\nabla}_\perp \cdot \vec{\tilde{E}}_\perp\right)\Big|_S = 0\,, \end{cases} \tag{5.5}$$

where differential operator $\mathcal{D}$ and $\vec{f}(z,\vec{r}_\perp)$ were defined in Eq. 4.20.

This system should be solved for a given waveguide shape as shown in [119]. Once the Green's function is known, the solution can be written in a similar form as for Eq. 4.23, with the only assumption that the Green's function can now be a tensor G^α_β:

$$\tilde{E}^\alpha(\vec{r}_\perp, z) = \int_{-\infty}^{z} dz' \int d\vec{r'}_\perp \, G^\alpha_\beta(\vec{r}_\perp, \vec{r'}_\perp, z_0 - z') f^\beta(z', \vec{r'}_\perp), \tag{5.6}$$

Substituting explicitly $f^\beta(z', \vec{r'}_\perp)$ in this integral, where $\cdot^\beta$ denotes x and y components, and then integrating over $d\vec{r'}_\perp$ accounting for the filtering property of Dirac delta function, I obtain:

$$\tilde{E}^\alpha = \frac{4\pi e}{c}\int_{-\infty}^{z} dz' \left\{ \frac{i\omega}{c^2} \underbrace{v^\beta_\perp(z') G^\alpha_\beta\left(\vec{r}_\perp, \vec{r'}_\perp(z'), z - z'\right)}_{\text{velocity term}} + \underbrace{\partial'_\beta G^\alpha_\beta\left(\vec{r}_\perp, \vec{r'}_\perp(z'), z - z'\right)}_{\text{gradient term}} \right\} \times \exp\left[\frac{i\omega}{2c}\int_0^{z'} \frac{d\bar{z}}{\gamma_z^2(\bar{z})}\right], \tag{5.7}$$

where derivative ∂'_β is taken with respect to the variable $\vec{r'}_\perp(z')$ and the integration limits are assumed to be the same as in Eq. 4.25. Here I also used the relation from paper [119], which holds for a general trajectory $s(z)$:

$$\omega\left(\frac{s(z_A) - s(z_B)}{v} - \frac{z_2 - z_1}{c}\right) = \frac{\omega}{2c}\int_{z_A}^{z_B} \frac{d\bar{z}}{\gamma_z^2(\bar{z})}, \tag{5.8}$$

here z_A and z_B are two point at the trajectory along z axis.

Regarding the numerical implementation of the integral in Eq. 5.7, the problem is divided into two steps. First, one needs to derive or calculate a Green's function for a given system,

which is basically the solution to the eigenvalue problem for the operator $\mathcal{D}$, including the boundary conditions from the system in Eq. 5.5. Then, take the integral in Eq. 5.7 that is composed from the right-hand side of the wave equation in Eq. 5.5. The uniqueness of this approach is that any Green's function, once known, can be substituted as an input in the code, and the field distribution is calculated.

5.3. Numerical implementation

In this section, I provide details on the numerical techniques used for taking integral in Eq. 5.7. For its numerical evaluation $\tilde{E}^{\alpha}$ one needs to calculate the integrand expression of Eq. 5.7, which includes: taking the integral as in Eq. 5.8, calculating the velocity term, and estimating the gradient term. The main difficulty lies in the gradient term. Since the goal is to write a code that can accept an arbitrary Green's function, the derivative should be computed numerically following its definition:

$$\partial'_{\beta} G^{\alpha}_{\beta}\left(\vec{r}_{\perp}, \vec{r'}_{\perp}(z'), z - z'\right) = \lim_{h \to 0} \frac{G^{\alpha}_{\beta}\left(\vec{r}_{\perp}, \vec{r'}_{\perp}(z') + h\vec{e}_{\beta}, z - z'\right) - G^{\alpha}_{\beta}\left(\vec{r}_{\perp}, \vec{r'}_{\perp}(z'), z - z'\right)}{h} \tag{5.9}$$

where $\vec{e}_{\beta}$ is a unit vector along x or y axis. Taking this derivative numerically requires a careful choice of h. For this, I used an adaptive step size formula for the increment h: $h = \sqrt{\epsilon}|\vec{r'}_{\perp}(z') \cdot \vec{e}_{\beta}|$ for any value of $|\vec{r'}_{\perp}(z') \cdot \vec{e}_{\beta}|$ except when it returns zero, then $h = \sqrt{\epsilon}$, where ϵ is the machine epsilon. The choice of the increment h should be made carefully to mitigate both rounding errors in the case of small h and the errors of the differentiation formula itself. The accuracy of the formula can be estimated to be $O(h^1)$, where O is Big O notation or Bachmann–Landau notation.

Integration of both Eq. 5.7 and Eq. 5.8 can be performed trivially using a variety of integration rules: rectangle rule, trapezoidal rule, Simpson's rule, and more advanced Gauss–Legendre quadrature. These methods provide accuracies of $O(h^1)$, $O(h^2)$, $O(h^4)$, and $O(h^5)$ with respect to grid spacing. In the subsequent cross-checks, I utilized the trapezoidal rule, which is more accurate than the simple rectangle rule but faster to calculate than Simpson's rule and the Gauss–Legendre quadrature formula, where additional values of the integrand need to be evaluated. For the practical applications presented here, the accuracy level of the trapezoidal rule is sufficient. To sum up, the main concern should be about calculating the Eq. 5.9, as this expression may result in a loss of accuracy and even leads to numerical artifacts. As one will see in the following Section, the numerical implementation of Eq. 5.7 is fairly robust with respect to the above mentioned problems.

5.4. Code cross-checks

In this section, I first cross-check `SRinWGuide` for the free-space Green's function against the results provided by `SRW`, to ensure the correctness of the chosen numerical approach. It is also essential to examine the "gradient term" as the derivative is taken numerically. Next, I evaluate the code's performance for the circular waveguide Green's function, where I

cross-check it in the case of the free-space limit with the actual free-space Green's function. Subsequently, I compare the calculation results from the circular waveguide Green's function with the analytical expression from [119] for a realistic waveguide's radius for undulator radiation in resonance.

5.4.1. Free space Green's function

Codes for calculating synchrotron radiation [38], [123] employ an expression where the free-space Green's function is already substituted, and the derivative is taken analytically as in Eq. 4.25. This approach ensures a certain robustness compared to using Eq. 5.7 for calculations where the Green's function varies depending on the boundary conditions. In this section, I examine the limits of applicability of `SRinWGuide` compared to `SRW` using the free-space Green's function. Specifically, I cross-check four cases: radiation from two bending magnets, a three-pole device, an undulator, and a special case illustrating potential numerical issues.

Bending magnet radiation

Calculating radiation from a bending magnet can be non-trivial, even in seemingly simple arrangements like the one presented in Fig. 5.1a. Beyond presenting the cross-check here, it is important to highlight the various issues that may arise when simulating synchrotron radiation. These issues often have both numerical and physical aspects. In this section, I discuss possible solutions to mitigate their impact.

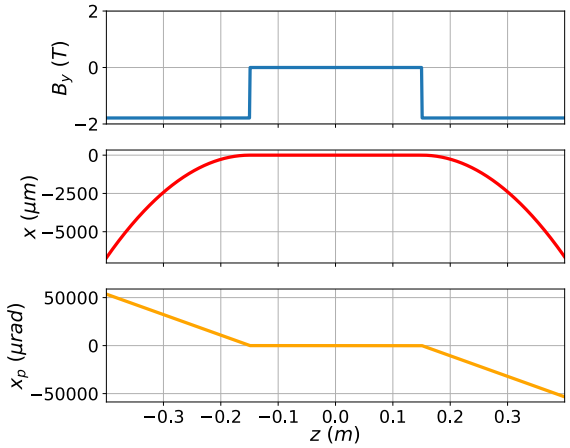

(a) The interspaced bending magnets. From top to bottom: the y component of the magnetic field, the x component of the trajectory and x_p is the angle of the electron's direction.

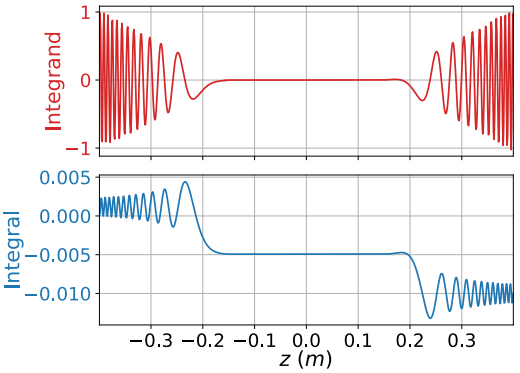

(b) Integrand as a function of z (top) and the corresponding integral value (bottom) for a pair of interspaced bending magnets.

Figure 5.1: The electron path is shown in panel (a), and the integrand and corresponding integral values from Eq. 5.7 are shown in panel (b), for a pair of interspaced bending magnets.

Firstly, it is observed that the integral exhibits highly oscillatory behavior, as depicted in Fig. 5.1b. In the case of free space, this characteristic can be discerned from the expression of

the integral in Eq. 4.24 that I rewrite here:

$$\vec{\tilde{E}}_{\perp}(\vec{r}_{\perp 0}, z_0, \omega) = -\frac{i\omega e}{c^2}\int_{-\infty}^{\infty} dz' \frac{1}{z_0 - z'}\left[\left(\frac{v_x(z')}{c} - \frac{x_0 - x'(z')}{z_0 - z'}\right)\vec{e}_x + \left(\frac{v_y(z')}{c} - \frac{y_0 - y'(z')}{z_0 - z'}\right)\vec{e}_y\right]\times \exp\left[i\omega\left(\frac{(x_0 - x'(z'))^2 + (y_0 - y'(z'))^2}{2c(z_0 - z')} + \frac{s(z')}{v} - \frac{z'}{c}\right)\right] \tag{5.10}$$

For example, for an observer located at the optical axis ($x_0, y_0 = 0$), the phase increases, and the integral begins to oscillate rapidly, as the electron diverges from the optical axis. This integral behaviour should be avoided in calculations, as the high oscillations may lead to aliasing problems and incorrect integral estimation. In reality, the contributions from these oscillating parts cancel each other out with each oscillation, resulting in net increments to the integral that are nearly zero. In this specific simulation, the oscillation frequency remains at a manageable level relative to the chosen mesh step size. For `SRinWGuide`, the appearance of the highly oscillatory integral cannot be avoided with the analytical method, as the integral is taken in the general form following Eq. 5.7 (with Green's function as the input), and one must always be aware of this problem.

Secondly, as one can see in Eq. 5.10 I indicated integration limits $(-\infty, \infty)$, while in numerical calculations one obviously has to set the finite limits (z_A, z_B), where A and B indicate the start and end of the numerically defined trajectory or its "edges". The interval (z_A, z_B) is assumed to contain all magnetic structures that effectively contribute to the radiation. However, it is important to recognize that defining only a part of the trajectory (z_A, z_B) is not entirely correct from a physical perspective. This represents a physical scenario where an electron suddenly appears at A, accelerates from 0 to β instantly, travels to point B through the given magnetic fields, then decelerates and disappears at B. This instant acceleration and deceleration of an electron contributes to radiation as *two additional sources*. I present the results of this cross-check in Fig. 5.2 where one can observe the effect from these two sources as oscillations in the intensity distribution. This actually indicates of the interference of the bending magnets' radiation with these two edges. This effect is not truly physical but is almost unavoidable when defining the trajectory in this way. For cross-checking, this aspect is not critical, as the primary goal is to verify the integration procedure itself, and this feature actually adds to its validity. I found an excellent agreement between `SRW` and `SRinWGuide`, which confirms the correct integration procedure.

One practical solution to this problem is to estimate the outer parts of the integral in Eq. 5.10 semi-analytically, which was done is `SRW`. This effectively corresponds to the case when, in the intervals $[-\infty, z_A]$ and $[z_B, +\infty]$, there is no magnetic field and the electron travels along a straight trajectory (see Fig. 5.3). Following the pioneering work on this topic [124], I rewrite the integral in Eq. 5.10 in the form:

$$\int_{-\infty}^{\infty} Ae^{i\Phi}dz = \int_{-\infty}^{z_A} Ae^{i\Phi}dz' + \int_{z_A}^{z_B} Ae^{i\Phi}dz' + \int_{z_B}^{\infty} Ae^{i\Phi}dz', \tag{5.11}$$

where Φ denotes the phase and A is the pre-exponential factor in Eq. 5.10. After performing an integration by parts of the outer integral up to the second order, one obtains the following

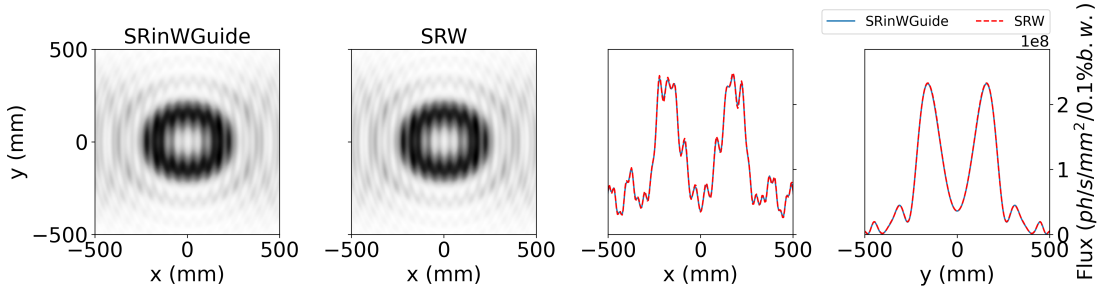

Figure 5.2: Comparison of computational results from `SRinWGuide` and `SRW` for the radiation from the interspaced bending magnets shown in Fig. 5.1. The intensity distributions include both polarisation components. The solid blue and dashed red lines in the line-out plots fully overlap.

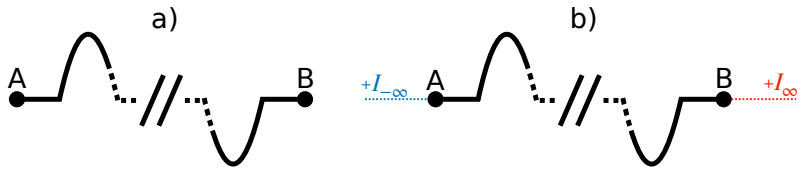

Figure 5.3: Schematic representation of the integration path over a magnetic structure. Panel (a) shows integration carried out solely within the region where the magnetic field is defined, i.e., from z_A to z_B. Panel (b) illustrates the case where the contribution from the outer regions $[-\infty, z_A]$ and $[z_B, +\infty]$ (terminating terms) is estimated semi-analytically.

expression:

$$\int_{-\infty}^{\infty} A e^{i\Phi} dz' \approx \int_{z_A}^{z_B} A e^{i\Phi} dz' + \left[\frac{A}{i\Phi'} + \frac{A'\Phi' - A\Phi''}{\Phi'^3} + \dots \right] e^{i\Phi} \Big|_{z_A}^{z_B}. \tag{5.12}$$

As I mentioned, this formula assumes that the electron travels along a straight trajectory in

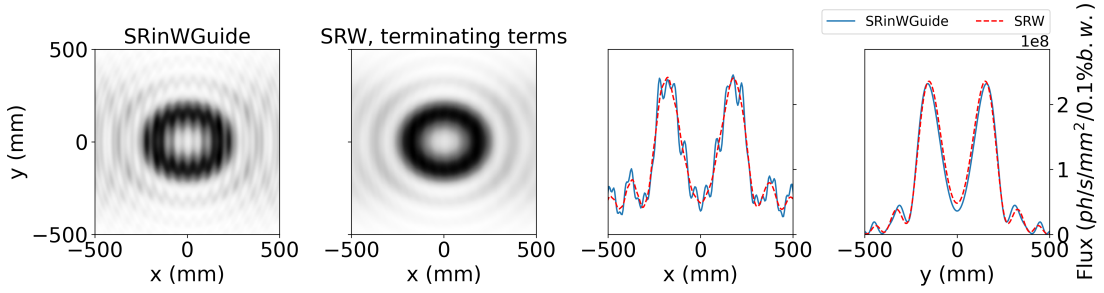

Figure 5.4: The same as Fig. 5.2, but now `SRW` performs the outer integral estimation (terminating terms).

the outer regions. However, in reality, there may be upstream and downstream magnetic devices that also contribute to the radiation and need to be accounted for. This semi-analytical estimation was implemented in `SRW` and can be turned "on" and "off", so I present the "off"-case in Fig. 5.2 and "on"-case in Fig. 5.4. However, it seems to be difficult to implement this in `SRinWGuide` due to the necessity of calculating both the first and the second order derivatives

in Eq. 5.12 numerically. Even if it is accounted for, this may lead to a loss of accuracy and possible numerical artifacts. This will be a subject for further study.

Three poles radiation
Another numerical example features a three-pole device, as shown in Fig. 5.5a. In this magnetic system, the first and the second magnetic field integrals are "closed", effectively returning the electron to $x, y = 0$ and $x_p, y_p = 0$. This causes the integrand to be zero by the end of the trajectory, as illustrated in Fig. 5.5a. Consequently, highly oscillatory behaviors are effectively suppressed, ensuring no aliasing problem. As previously described, there will be an influence from the edges, which is evident in the characteristic interference circles depicted in Fig. 5.6. Nevertheless, this is still a legitimate cross-check between `SRinWGuide` and `SRW`. Comparing the distribution in Fig. 5.6, I conclude that the second cross-check is also passed.

Undulator radiation
Another case that should be checked is undulator radiation (see Fig. 5.7a). In undulators, the integral value adds up "coherently" or better to say constructively at each period, which is seen in Fig. 5.7b. In this case, there is also no problem of highly oscillatory integrals. I present the resulting intensity distribution of the x-polarization component in Fig. 5.8. As one would expect, there should be a contribution from the edges of the trajectory, which cannot be seen for the x-polarization component plot. This can be explained by the fact that the radiation intensity from the device itself is much higher than that from the edges. However, it can be clearly seen for the y-polarization component, as depicted in Fig. 5.9. For this demonstration, I `turned off` the semi-analytical treatment of the trajectory edges in `SRW` and I found an excellent agreement between two codes. If I `turn on` the semi-analytical treatment in `SRW`, I obtain the the results with noticeable discrepancy, which I show in Appendix D

Straight section radiation
Continuing the discussion about the contribution from the edges of the trajectory, this can be pushed to the limit to become a paradox. I will demonstrate here radiation from a "straight section". In this case, the electron is created at point z_A, travels to z_B in space with no magnetic field, and then disappears at z_B. This case represents radiation from two point sources situated at A and B and is described by the expression from [125]:

$$\vec{\tilde{E}}_{AB} = \frac{i\omega eL}{c^2 z} \exp\left[\frac{i\omega\theta^2 z}{2c}\right] \vec{\theta}\, \mathrm{sinc}\left[\frac{\omega L}{4c}\left(\theta^2 + \frac{1}{\gamma^2}\right)\right], \tag{5.13}$$

where L is the length of this section. This radiation is solely contributed by the gradient term in the integral expression in Eq. 5.6. I depict the cross-check in Fig. 5.10 of this case with SRW and the analytical expression according to Eq. 5.13 and find an excellent agreement too.

Summary
To summarize, one always needs to consider the effects presented in these examples: highly oscillatory integrals and contributions from the edges of the trajectory. Disregarding these contributions may lead to confusing real radiation with numerical artifacts. As mentioned, it is challenging to treat these effects analytically in `SRinWGuide`, while both can be mitigated numerically. For the case of the highly oscillatory integral, one can decrease the mesh grid step size to some extent to manage the aliasing problem. Avoiding edge sources is more

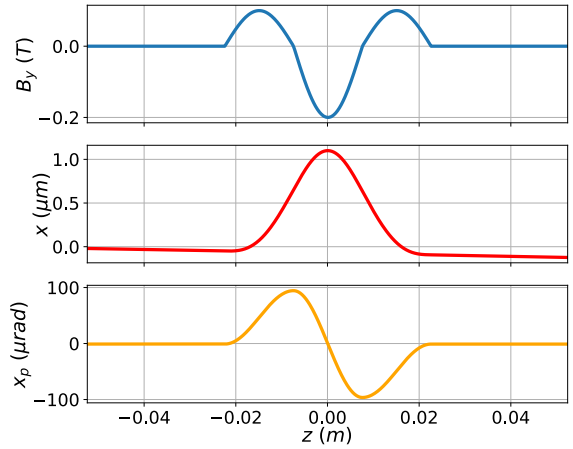

(a) Three poles. From top to bottom: the y component of the magnetic field, the x component of the trajectory and x_p is the angle of the electron's direction.

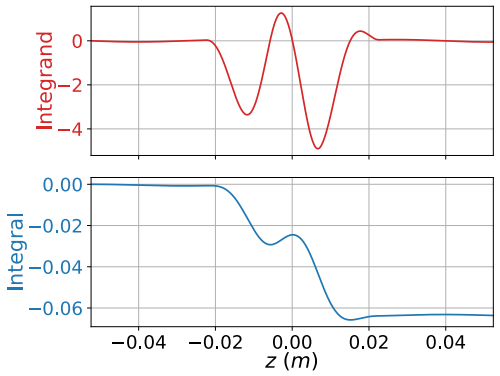

(b) Integrand as a function of z and the corresponding integral value (bottom) for the three-pole configuration.

Figure 5.5: Three poles.

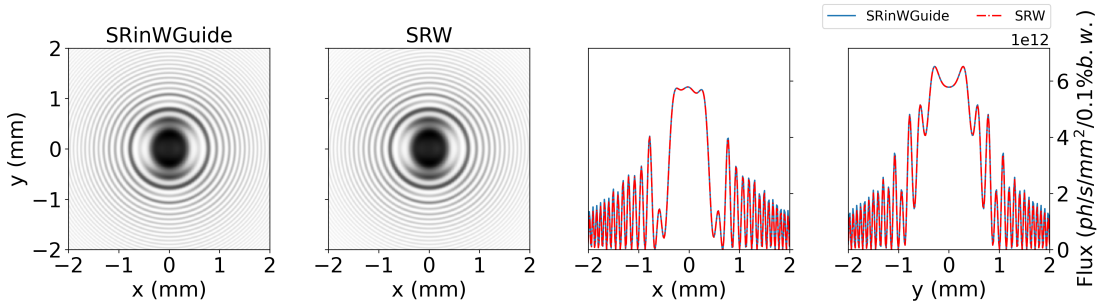

Figure 5.6: Comparison of computational results from `SRinWGuide` and `SRW` for the radiation from three poles (Fig. 5.6). The intensity distributions account for both polarization components.

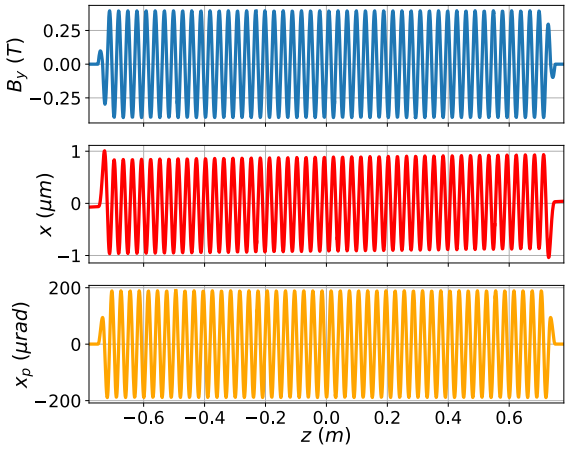

(a) Undulator. From top to bottom: the y component of the magnetic field, the x component of the trajectory and x_p is the angle of the electron's direction.

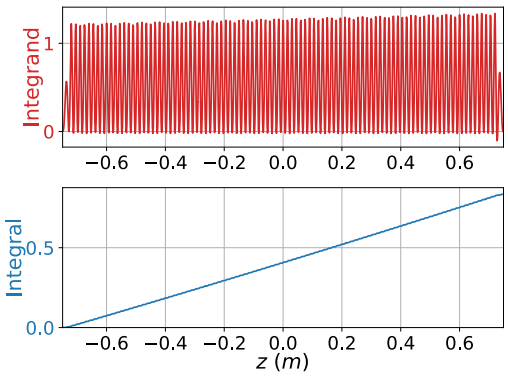

(b) Integrand value with respect to z on the top and the corresponding integral value on the bottom. The gradual increase in the integrand value is due to the change in distance from the observer.

Figure 5.7: Undulator.

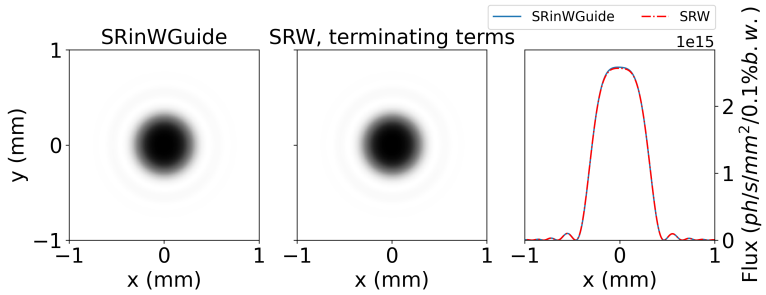

Figure 5.8: Comparison of computational result from `SRinWGuide` and `SRW` for the radiation from an undulator. Total flux is presented for both polarization components.

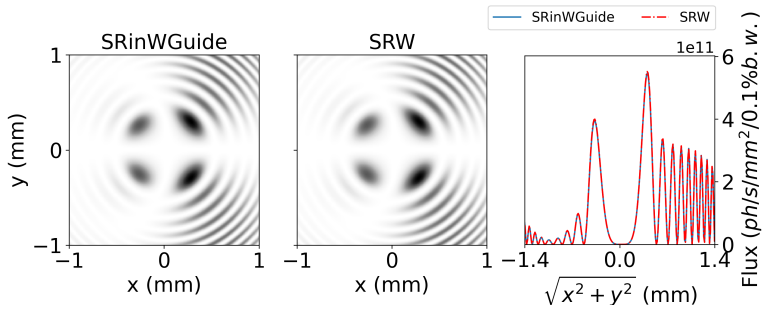

Figure 5.9: Same as 5.8, but with y-polarization component. The slice on the right subplot is presented for a diagonal cut.

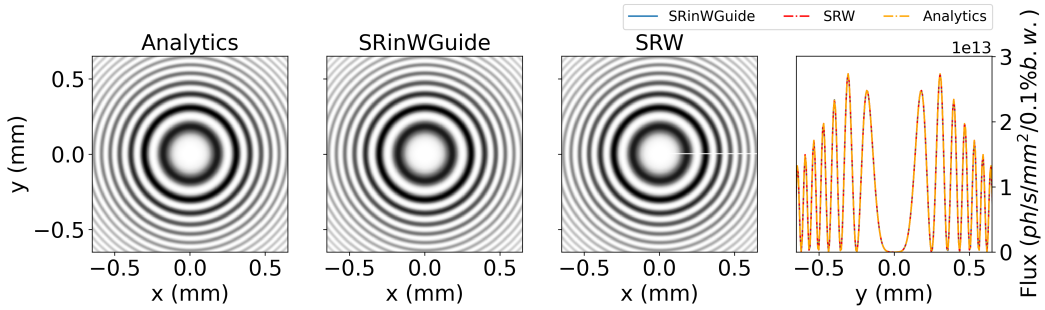

Figure 5.10: Radiation from the straight section. Comparison between the analytical result according to Eq. 5.13, `SRinWGuide`, and `SRW`. Total intensity from both polarisation components is presented.

difficult. The general strategy is to direct radiation from the edges outside of the simulation window by carefully manipulating the ends of the trajectory. Further efforts will be made to address these issues, hopefully with a more general analytical approach, as was done, for example, in `SRW` and `SPECTRA` codes.

5.4.2. Circular waveguide Green's function

In this section I present the result of the calculations using the circular waveguide Green's function and cross-check it with free space asymptotic and analytical expression.

The authors of [119] represent the Green's function for the circular waveguide in the following form:

$$
\begin{aligned}
G\left(\vec{r}_\perp, \vec{r'}_\perp, z-z'\right) = {} & \frac{c}{2i\omega}\sum_{m=0}^{\infty}\sum_{k=1}^{\infty}\left(A^{TE}_{mk}\right)^2\left(\frac{\mu_{mk}}{2R}\right)^2\exp\left[-\frac{ic(z-z')}{2\omega R^2}\mu^2_{mk}\right] \\
\times & \left\{\begin{bmatrix} J_{m-1}(\mu_{mk}r/R)\cos[(m-1)\phi] + J_{m+1}(\mu_{mk}r/R)\cos[(m+1)\phi] \\ -J_{m-1}(\mu_{mk}r/R)\sin[(m-1)\phi] + J_{m+1}(\mu_{mk}r/R)\sin[(m+1)\phi] \end{bmatrix}\right. \\
\otimes & \begin{bmatrix} J_{m-1}(\mu_{mk}r'/R)\cos[(m-1)\phi'] + J_{m+1}(\mu_{mk}r'/R)\cos[(m+1)\phi'] \\ -J_{m-1}(\mu_{mk}r'/R)\sin[(m-1)\phi'] + J_{m+1}(\mu_{mk}r'/R)\sin[(m+1)\phi'] \end{bmatrix} \\
+ & \begin{bmatrix} -J_{m-1}(\mu_{mk}r/R)\sin[(m-1)\phi] - J_{m+1}(\mu_{mk}r/R)\sin[(m+1)\phi] \\ -J_{m-1}(\mu_{mk}r/R)\cos[(m-1)\phi] + J_{m+1}(\mu_{mk}r/R)\cos[(m+1)\phi] \end{bmatrix} \\
\otimes & \left.\begin{bmatrix} -J_{m-1}(\mu_{mk}r'/R)\sin[(m-1)\phi'] - J_{m+1}(\mu_{mk}r'/R)\sin[(m+1)\phi'] \\ -J_{m-1}(\mu_{mk}r'/R)\cos[(m-1)\phi'] + J_{m+1}(\mu_{mk}r'/R)\cos[(m+1)\phi'] \end{bmatrix}\right\} \\
+ & \frac{c}{2i\omega}\sum_{m=0}^{\infty}\sum_{k=1}^{\infty}\left(A^{TM}_{mk}\right)^2\left(\frac{\nu_{mk}}{2R}\right)^2\exp\left[-\frac{ic(z-z')}{2\omega R^2}\nu^2_{mk}\right] \\
\times & \left\{\begin{bmatrix} J_{m-1}(\nu_{mk}r/R)\sin[(m-1)\phi] - J_{m+1}(\nu_{mk}r/R)\sin[(m+1)\phi] \\ J_{m-1}(\nu_{mk}r/R)\cos[(m-1)\phi] + J_{m+1}(\nu_{mk}r/R)\cos[(m+1)\phi] \end{bmatrix}\right. \\
\otimes & \begin{bmatrix} J_{m-1}(\nu_{mk}r'/R)\sin[(m-1)\phi'] - J_{m+1}(\nu_{mk}r'/R)\sin[(m+1)\phi'] \\ J_{m-1}(\nu_{mk}r'/R)\cos[(m-1)\phi'] + J_{m+1}(\nu_{mk}r'/R)\cos[(m+1)\phi'] \end{bmatrix} \\
+ & \begin{bmatrix} J_{m-1}(\nu_{mk}r/R)\cos[(m-1)\phi] - J_{m+1}(\nu_{mk}r/R)\cos[(m+1)\phi] \\ -J_{m-1}(\nu_{mk}r/R)\sin[(m-1)\phi] - J_{m+1}(\nu_{mk}r/R)\sin[(m+1)\phi] \end{bmatrix} \\
\otimes & \left.\begin{bmatrix} J_{m-1}(\nu_{mk}r'/R)\cos[(m-1)\phi'] - J_{m+1}(\nu_{mk}r'/R)\cos[(m+1)\phi'] \\ -J_{m-1}(\nu_{mk}r'/R)\sin[(m-1)\phi'] - J_{m+1}(\nu_{mk}r'/R)\sin[(m+1)\phi'] \end{bmatrix}\right\}, \qquad (5.14)
\end{aligned}
$$

where the radial distance $r = \sqrt{x^2 + y^2}$ and angle $\phi = \arctan(y/x)$ for the transverse polar coordinate $\vec{r}_\perp$ and defined in the similar way for the primed coordinate $\vec{r}'_\perp$. J_p indicates the Bessel function of the first kind of p-th order. μ_{mk} and ν_{mk} are the roots of the two following equations $J'_m(\mu_{mk})$ and $J_m(\nu_{mk})$ correspondingly. And finally:

$$A^{\mathrm{TE}}_{mk} = \sqrt{\frac{a_m}{\pi}} \frac{1}{\sqrt{\mu^2_{mk} - m^2}\, J_m(\mu_{mk})} \tag{5.15}$$

and

$$A^{\mathrm{TM}}_{mk} = \sqrt{\frac{a_m}{\pi}} \frac{1}{\nu_{mk}\, J_{m-1}(\nu_{mk})}, \tag{5.16}$$

where $a_0 = 1$ and $a_m = 2$ for $m \geq 1$. The first and most straightforward numerical cross-check is to increase the radius of the waveguide significantly and compare the result with the results obtained using the free space Green's function.

Free space limit

For this cross-check, I use a three poles device with a pole length of 0.45 m, the magnetic field of the central pole is 2 T, and the magnetic field of the side poles is 1 T. For the cross-check I calculated the on-axis spectral distribution where $m = 1$ and k-modes ranges from $0, 1, 2, \cdots, 1000$ and $0, 1, 2, \cdots, 1500$. The higher m-mode number results in zero value of radiation intensity on-axis. I present the comparison in Fig. 5.11.

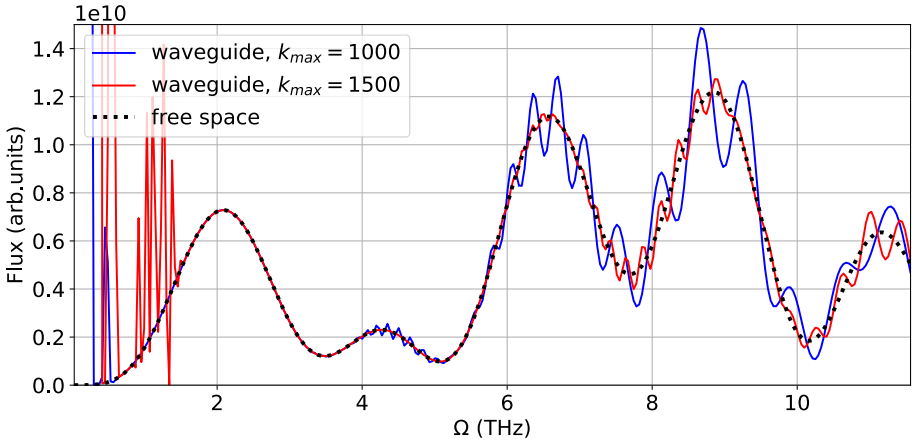

Figure 5.11: On-axis spectral flux from the three-pole device, calculated using the free-space Green's function (black dotted line) and the circular waveguide Green's function. The latter takes into account different numbers of k modes, when $m = 1$: the blue solid line corresponds to 1000 modes, and the red solid line corresponds to 1500 modes.

The presented distribution can be divided into three parts. At the lower end of the frequencies, there is a mismatch with the free-space case which is due to appearance of highly oscillatory integrals. As one integrates over the higher mode terms, the exponent's argument grows with μ_{mk} and ν_{mk}. Next, there is a region where the three lines coincide, which is the expected behavior. Finally, at the higher frequencies, an oscillatory behavior is observed,

indicating that more modes should be accounted for. This is evident when comparing the blue and red lines, where the oscillations for the red line appear at the higher frequencies than those for the blue line.

Spatial distribution
For this cross-check, I used a 10-period undulator with a period length of 0.9 m and the maximum magnetic field value of 2 T. The model magnetic field distribution does not have any end correction coils. This was done to ensure a fair comparison, as the analytically calculated field distribution [119] is calculated for an idealized sine-like field distribution. I compare the angular distribution of transverse radiation fields in Fig. 5.12 and their line-offs in Fig. 5.13.

In the cross-check, I show resulting distribution for $k = 1$ and $m = [-4, \cdots, 0, \cdots, 4]$. Accounting for higher m does not alter the resulting distribution. Summing up higher k-modes results in a more complex spatial distribution, which also coincide well with the analytical results. I believe that further studies are needed on the physical interpretation of these computational results, which should definitely be a subject for future work.

5.5. Conclusion

In this chapter, I demonstrated the feasibility of calculating synchrotron radiation generated within the constraints of a waveguide. The code, `SRinWGuide`, was developed using the paraxial approximation, which is naturally applicable in the case of synchrotron radiation. `SRinWGuide` accepts a Green's function for a given boundary condition as input. The code has demonstrated reliable simulation capabilities under various initial simulation parameters and boundary conditions, including free space and circular waveguide scenarios. I showed excellent numerical correspondence with the well-known code `SRW` for synchrotron radiation calculated in free space. Additionally, I conducted two cross-checks of the `SRinWGuide` output for the circular waveguide case, both of which also showed excellent agreement. The library is available for public use on GitHub, as referenced in [122]. The code will continue to be developed and enhanced with more numerical capabilities to accommodate the needs of numerical calculations for insertion devices designed for THz radiation generation.

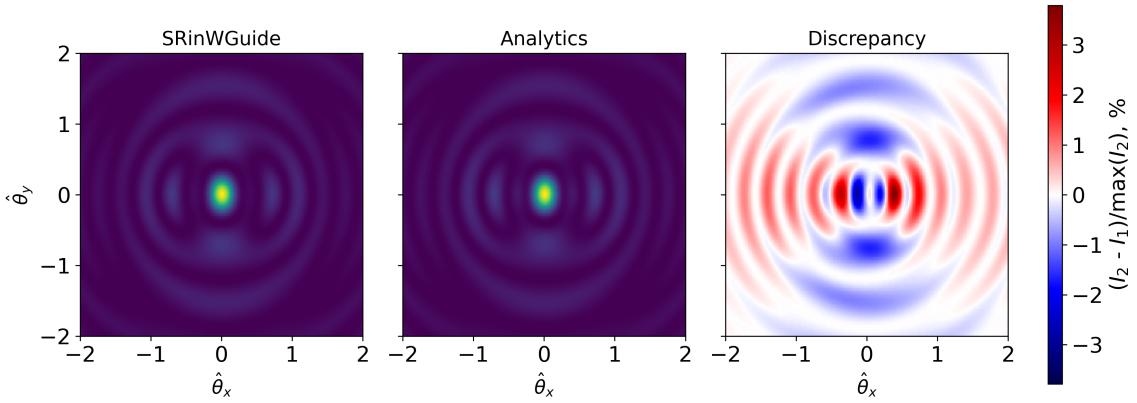

Figure 5.12: Spatial distribution of radiation in the far zone from a ten-period undulator inside a waveguide.

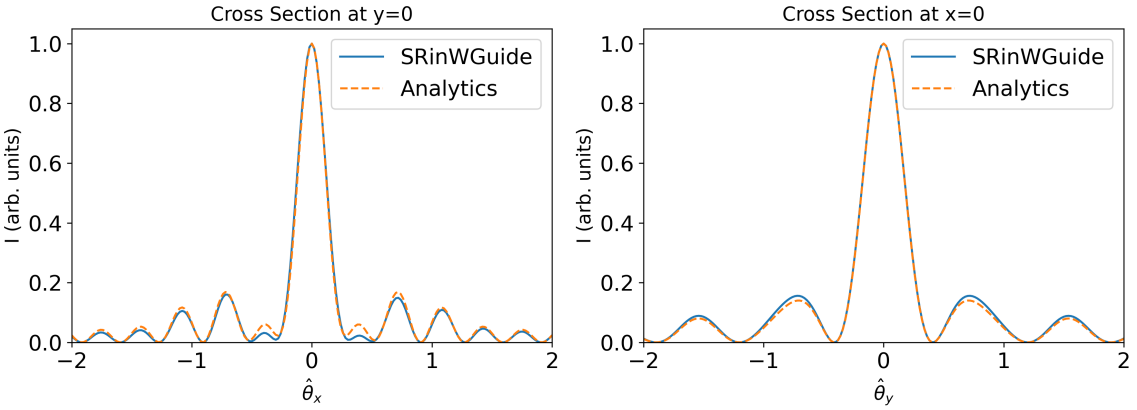

Figure 5.13: Cross sections of the spatial distributions shown in Fig. 5.12.

Chapter 6

Propagation of THz radiation in an iris waveguide

This chapter is a part of the conceptual design report for the STERN project. The results presented here are an outcome of ongoing collaboration within the FEL R&D group activity between DESY and European XFEL.

6.1. Introduction

THz radiation has drawn scientific attention over the past 20 years [52]. One application of THz radiation is in inducing atomic and molecular dynamics, and combining it with FEL X-rays for probing these samples, which would be of great practical interest as noted in [52]. One of the possible THz sources is accelerator-based sources. For example, one can consider building a dedicated THz SASE FEL facility [126] in close proximity to an X-ray FEL. Alternatively, there is the possibility of using the same spent[1] electron beam from an XFEL facility. For this purpose, there might be different kinds of accelerator-based THz sources: undulator-based [54], [127], coherent transition radiation [128], or Cherenkov waveguide [129]. Within the STERN project, it is considered to use Cherenkov waveguides to generate THz radiation.

Incorporating a THz source based on Cherenkov waveguides at the European XFEL facility, utilizing the spent electron beam of European XFEL, would necessitate propagating the THz radiation from the location of the beam dump at XHE4/XS4 to the experimental hall of the users' end stations in X-ray Headquarters (XHQ), a distance estimated to be 370 meters, as illustrated on the areal view of the European XFEL campus in Fig. 6.1. Propagation of THz radiation over such a long distance imposes significant challenges, especially if the transmission system is required to accept a broad range of frequencies, spanning from 3 THz up to 30 THz (even a broader bandwidth is considered down to 0.3 THz).

THz radiation is highly absorbed by media thus it is essential to minimise usage of any refractive optic elements, including filters and windows. To guide THz radiation one can consider using reflective optics or waveguides adjusted for the THz radiation range. The first approach, using reflective optics, is optimal for complex facilities geometries where one needs to guide radiation around corners. In contrast, waveguides are naturally suited for straight line facilities such as tunnels of European XFEL. At the THz radiation propagation beamline at the European XFEL, we plan to use both approaches: initial out-coupling from the electron beam axis occurs in XHE4/XS4, where radiation should be delivered to the XTD8 tunnel through a concrete radiation protection maze by means of a mirror-based system as illustrated in the call-out in Fig. 6.1. Afterwards we plan to propagate THz radiation through a 370-meter-long XTD8 tunnel using a waveguide.

[1] After SASE FEL X-ray undulators.

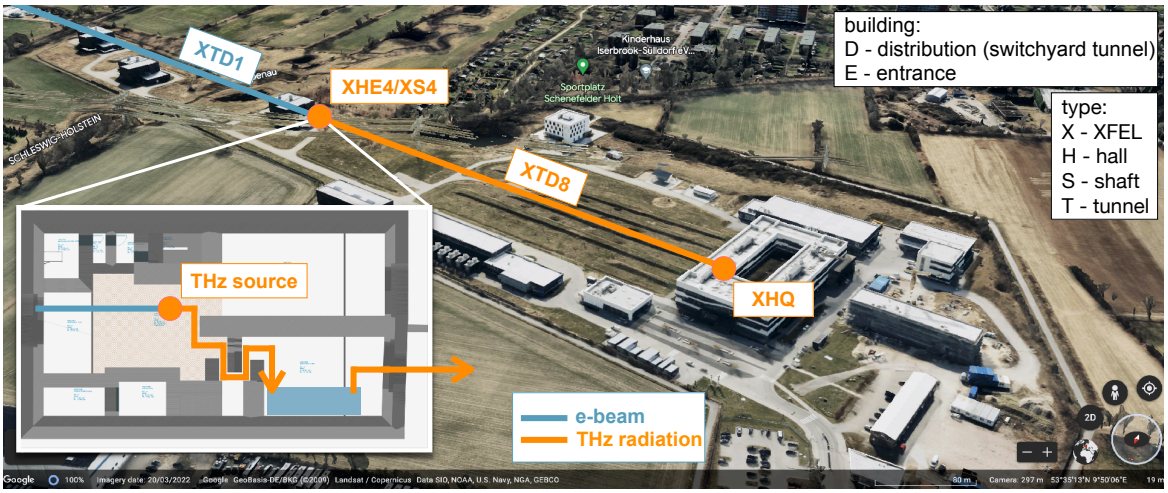

Figure 6.1: Aerial view of the European XFEL campus with the marked locations of XHE4/XS4 and the users' hall in XHQ; the distance between them is 370 m. In the call-out, a schematic of the XHE4/XS4 building at the UG2 level is shown, with the path of the THz radiation through the radiation protection maze outlined. The diagnostic table is marked with a cyan-blue rectangle.

In this Chapter, I provide an analysis of the *iris waveguide* performance for THz radiation propagation. I present two approaches to estimate its performance: one is based on numerical simulation and the second one is based on the analytical solution derived from complex boundary conditions. I calculate the propagation efficiency of the waveguide's fundamental mode and demonstrate the matching conditions for the incoming radiation. Additionally, I analyze the effects of imperfections on the iris waveguide's performance. Also, I present an outline of the *mirror-based propagation line* and describe a "matching" device that ensures efficient coupling of the radiation from the source and the initial mirror system to the iris line.

6.2. Iris line theory

A waveguide for THz radiation consists of metallic screens with concentric holes, as depicted in Fig.6.2 (a). The "virtual" surface created by the screen openings effectively acts as a waveguide. I refer to this device as an iris line or iris waveguide. The analysis of the electromagnetic field distribution such waveguide configuration was first conducted using a numerical approach by Fox and Li [130], followed by an analytical solution provided by Vainstein [131]. Vainstein introduced complex boundary conditions at this virtual surface of the screen openings and derived the explicit expression of the iris line eigenmodes. Later, it was proposed [55] to use an iris line in the present configuration in Fig.6.2 (a) for THz radiation transportation at FEL facilities [55]–[58]. The authors of [55] present a comparative theoretical analysis of the iris line based on the theories of Fox and Li, and Vainstein, in application to the design of the transportation line. In this chapter, I extend the numerical approach further using a simpler simulation technique that accounts for the iris line imperfections. I also cross-check the simulation results of the ideal iris line with the predictions given by Vainstein's theory and find excellent agreement.

Fox and Li's approach relies on the derivation of a radiation 'propagator' using physical optics. This implies that the iris line is essentially treated as a diffraction device, as depicted

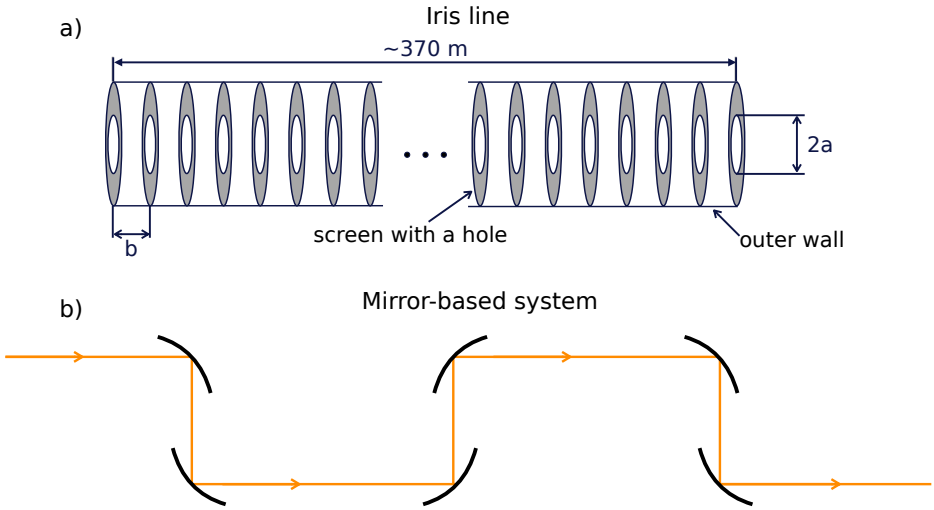

Figure 6.2: Outlines of the iris line and mirror system. The iris line has two main parameters: a is the radius of the hole and b is the spacing between screens.

in Fig. 6.3. The first observation is that radiation incident on each screen will be partially diffracted back inside the virtual waveguide and partially into the space between the screens. The latter portion of the radiation will be reflected several times and will eventually be lost between the two screens and does not affect the radiation propagated further. Therefore, Fox and Li made the primary approximation that the screen can be considered as fully absorbing.

The second observation is that the problem can indeed be converted to the problem of radiation diffraction at an aperture. In this case, the Fresnel number is the only dimensionless parameter needed to describe the problem: $N = a^2/(\lambda b)$, where a is the radius of the opening of the iris line screens, b is the spacing between screens, and λ is the radiation wavelength. Comparing the approaches of Fox and Li to that of Vainstein's, one can see that N describes the transmission efficiency T of the iris line, which I will show later in this section. For the simulations, I implemented the simplified Fox and Li approach. I propagate radiation in free space from the location of the n-th screen to the $(n+1)$-th screen and then apply a fully absorbing aperture, after which I repeat the propagation procedure for the next cell.

In constrast, Vainstein's approach addresses the problem by taking into account the boundary conditions of the metallic walls and screens of the iris line. The boundary condition on the surface can be expressed following [55] and written in the vector form:

$$\left[\vec{\tilde{E}} + (1+i)\beta_0\sqrt{cb/(4\omega)}\,(\vec{n}\cdot\vec{\nabla}_\perp)\vec{\tilde{E}}\right]_S = 0, \tag{6.1}$$

where S is the virtual surface formed by the openigns of the screens of the iris line, and $\vec{n}$ is the unit vector normal to S, $\beta_0 = 0.824$, c is the speed of light, ω is the radiation frequency and $\tilde{E}(r,\phi,z)$ is the slowly varying envelope of the electric field at position z along the iris line.

Continue following [55], I seek the solution for the field amplitude, $\tilde{E}(r,\phi,z)$, in the following form:

$$\tilde{E}(r,\phi,z) = u_{nj}(r)\exp[-in\phi - ik_z z]\,, \tag{6.2}$$

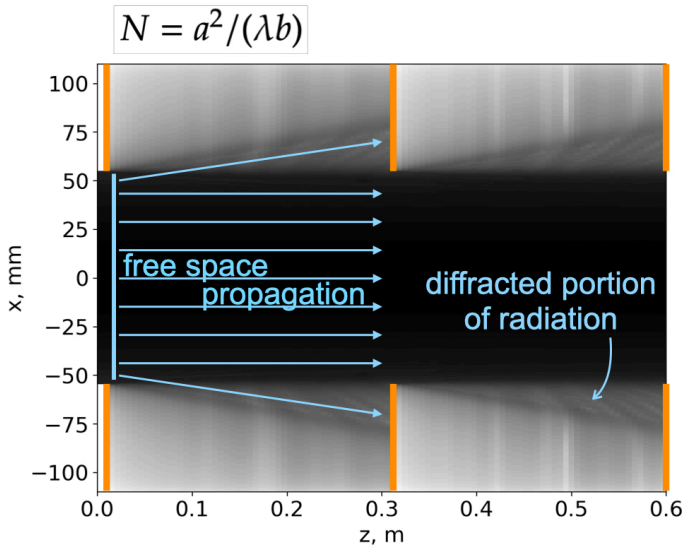

Figure 6.3: Illustration of wavefront propagation through the iris line.

where $n = 0, 1, 2, \ldots$. $u_{nj}(r)$ should be solution of the following homogeneous equation as I consider axially symmetric iris line:

$$r^2 u''_{nj} + r u'_{nj} + [(k_{nj})^2 - n^2)]u_{nj} = 0\,, \tag{6.3}$$

and after substituting $\tilde{E}(r, \phi, z)$ in Eq. 6.1 I obtain boundary condition on $u_{nk}(r)$ in the following form:

$$[u_{nj} + (1+i)\beta_0\sqrt{cb/(4\omega)}u'_{nj}]_{r=a} = 0. \tag{6.4}$$

assuming $N \gg 1$, I write the functions u_{nj} in the form:

$$u_{nj} = J_n(k_{nj}r), \tag{6.5}$$

where

$$k_{nj} = \frac{\nu_{nj}}{a}[1 - (1+i)\beta_0 M], \tag{6.6}$$

and ν_{nj} is the j-th root of the n-th order Bessel function of the first kind ($J_n(\nu_{nj}) = 0$), and $M = (8\pi N)^{-1/2}$. Substituting Eq. 6.6 into the dispersion relation:

$$k_z^2 + k_{nj}^2 = \frac{\omega^2}{c^2}, \tag{6.7}$$

I obtain:

$$k_z b = \frac{\omega b}{c} - 2\nu_{nj}^2 M^2 + 4\nu_{nj}^2 M^3(1+i)\beta_0. \tag{6.8}$$

taking the imaginary part from this I can find the radiation power losses per transit of one iris as:

$$2\mathrm{Im}(k_z b) = 8\nu_{nj}^2 M^3 \beta_0. \tag{6.9}$$

The relative loss after traveling the distance z of a given mode j of order n can be written in the following form:

$$\left(\frac{\Delta W}{W}\right)_{nj} = 1 - \exp\left(-\frac{\nu_{nj}^2 \beta_0}{(2\pi N)^{3/2}} \frac{z}{b}\right) = 1 - \exp\left(-\frac{\nu_{nj}^2 \beta_0 (\lambda b)^{3/2}}{(2\pi)^{3/2} a^3} \frac{z}{b}\right). \tag{6.10}$$

As one can see, lower-order modes tend to survive, showing weak dependency on the spacing between the irises, denoted by b, and much stronger dependence on λ and a. This result provides an analytical basis for cross-checks with the numerical approach.

6.3. Analysis of radiation propagation at 3 THz

In this section, I present the results of propagating 3 THz radiation through the iris line. Studying the iris line at the lowest radiation frequency is justified by the fact that with higher radiation frequency, the transmission performance of the iris line would only improve, as can be seen from Eq. 6.10. I examine the performance of the iris line using a numerical approach and cross-check both the level of radiation losses according to Eq. 6.10 and the spatial radiation distribution given by Eq. 6.5. I set the preliminary design parameters the same as in [55] of the iris line: $a = 0.055$ m and $b = 0.3$ m, that corresponds to $N = 101$.

I study the eigenmodes of the iris line by propagating a plane wave through it, as plane wave encompasses all possible modes. With this simulation one observes that predominantly the fundamental mode will remain upon sufficiently long propagation distance, as indicated by Eq. 6.10 or shown in Fig. 6.5. This way one can demonstrate the mode filtering mechanism happening in the iris line and the agreement between the numerical approach and the analytical expression given by Eq. 6.5. In Fig. 6.4 I show in the right upper subplot the resulting Bessel function intensity distribution that actually follows Eq. 6.5 as illustrated in Fig. 6.6.

The oscillating behavior in the relative losses per cell occurs because, even after 900 m of propagation, there is a mixture of higher modes, mainly the second mode, that is still present, as seen in Fig 6.5. Comparing the shape of the field distribution obtained from numerical simulations, there are minor differences relative to what is predicted by Vainstein's theory in Eq. 6.5. *The oscillating features suggest that the numerical approach accounts for all diffraction orders, while Vainstein's theory considers only the contributions from the zeroth-order diffraction.* The same result is presented in [55].

The fundamental mode, however, can be transported very efficiently, as illustrated in Fig. 6.7. The relative loss per iris cell remains constant at the level of 0.03%, which in a very good agreement (within 1% discrepancy) with Eq. 6.10. Additionally, the spatial distribution of the radiation is preserved along the iris line. Therefore, propagating through the iris line its fundamental mode is highly preferable, although it necessitates a careful solution to the mode matching problem during in-coupling.

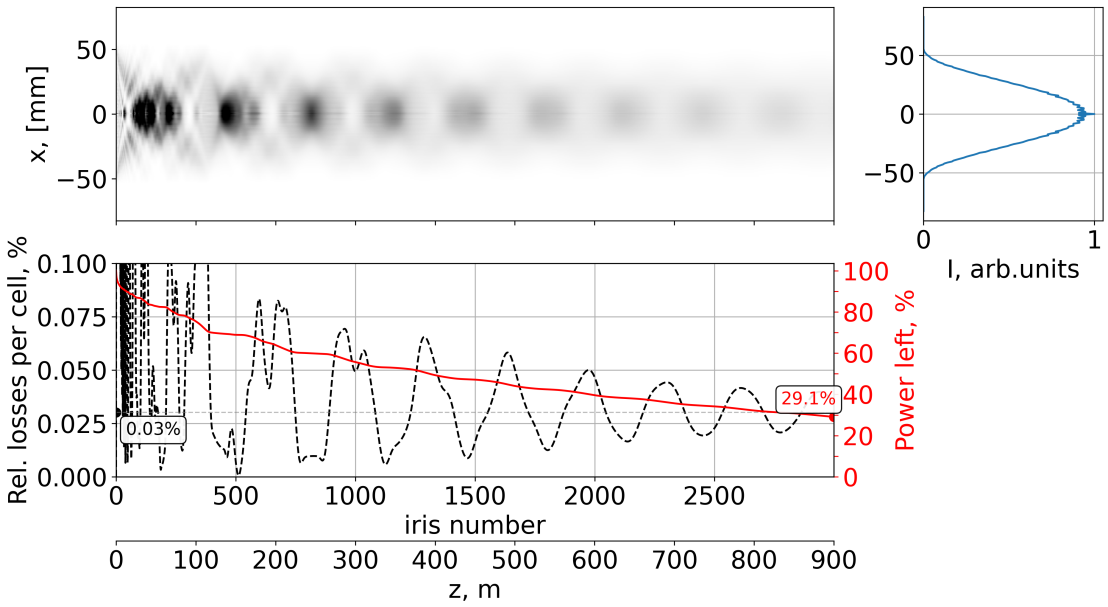

Figure 6.4: Result of plane wave propagation through an iris line. The upper right subplot shows the intensity distribution of the radiation at the exit of the iris line; each transverse slice is normalised to its maximum intensity. The bottom subplot represents radiation losses: the black dashed line indicates the relative loss per cell, and the red line shows the fraction of radiation remaining at a given distance from the entrance.

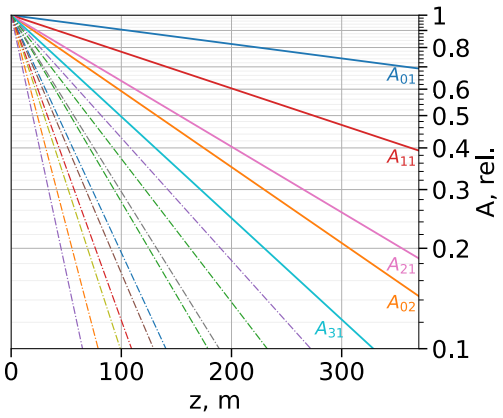

Figure 6.5: Analytical estimation of the radiation losses in the iris line. A_{nj} represents the relative amplitude of mode n and j after a given propagation distance.

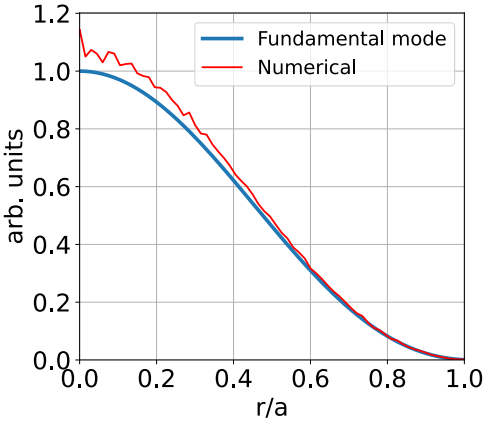

Figure 6.6: The radiation intensity distribution at the exit of the iris line shows a slight discrepancy, as Vanstein's approach accounts only for zeroth-order diffraction.

6.3.1. In-coupling condition

The geometry of the iris line imposes specific requirements on the incoming radiation: the iris line will geometrically filter out all radiation that arrives at the angles greater than $a/(bN)$. This effectively means that the incoming beam should be collimated. Another requirement for the radiation distribution is that it should closely approximate the fundamental mode distribution

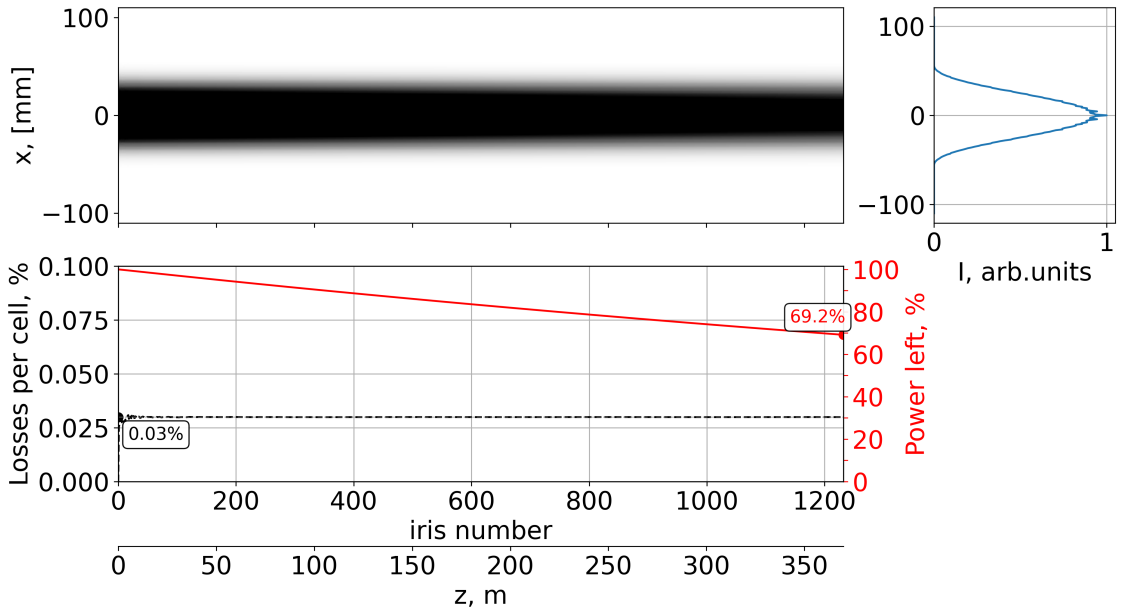

Figure 6.7: Notation of the figure is the same as in Fig. 6.4. Result of fundamental mode propagation through an iris line. Relative losses per cell are constant, and the spatial radiation distribution is perfectly preserved along the iris line.

given by Eq. 6.7. Achieving a perfect Bessel function distribution for the input radiation of the iris line is not always feasible. Therefore, it is essential to provide an approximation that closely fits this Bessel function distribution using a given bell-like distribution and then empirically adjust its width to achieve the highest possible output from the iris line. For instance, a model Gaussian distribution with an optimized width of $\sigma = a/2.85$ retains 67.8% of radiation power after 370 m of propagation, compared to 69.2% for the iris fundamental mode.

6.3.2. Wave packet enlargement

Until now, I have simulated the propagation of monochromatic spatial radiation distributions to study the effect of the iris line on the radiation distribution at a given wavelength. In reality, the entire non-monochromatic wave packet is propagated. In the presence of group delay dispersion one may end up with elongation of the pulse duration. I have examined this issue both analytically and numerically. Neither numerical simulations nor analytical methods have indicated any effect on either of the time and frequency domain distributions, aside for the expected attenuation that depends on the radiation wavelength.

6.3.3. Optimization of iris line dimensions for $0.3 - 30$ THz

Extending the frequency band from $3-30$ THz down to 0.3 THz will require adjustments to the dimensions of the iris line to maintain adequate efficiency at lower frequencies. Specifically, the radius a should be modified, while irises spacing – b – can remain unchanged. As indicated by Eq. 6.10, the radius significantly influences the transmission performance of

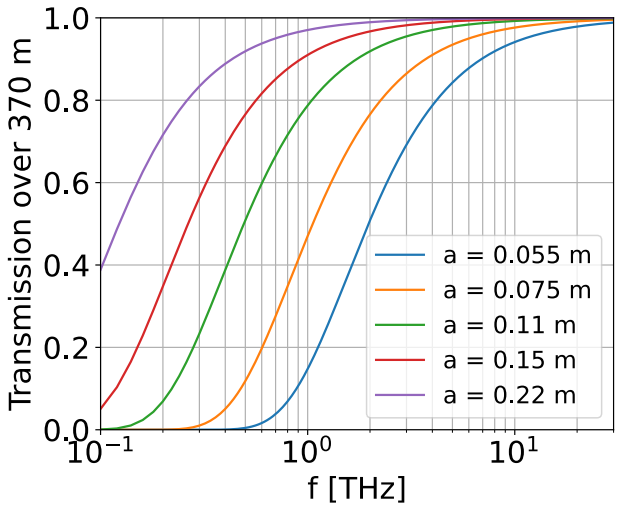

Figure 6.8: Transmission efficiency of different iris lines with iris openings of size a.

the iris line. Based on Eq. 6.10, I plot Fig. 6.8 where I illustrate the radiation transmission efficiency for 370 m of propagation for the entire 0.3 – 30 THz frequency band. The choice of an appropriate radius should be based on the technical feasibility of manufacturing such a long device within specified tolerances.

6.4. Estimation of tolerances

Building an iris line presents a significant technical challenge due to its length and the large number of iris apertures required. In this Section, I study the precision requirements for manufacturing and assembling each iris to maximize the transmission efficiency of the entire waveguide. As previously discussed, the iris line operates primarily on the principle of diffraction: each aperture acts as an obstacle, scattering half of the radiation back towards the axis of the waveguide and the other half - outward into the cavity between the apertures. This design minimizes Ohmic losses, which are inevitable when radiation encounters the metallic walls. The effect of the finite walls size was studied in [57]. In the idealised system where the walls are infinitesimally small the only losses occurring are due to the portion of radiation diffracted outward from the virtual waveguide. Most importantly, these losses are determined geometrically: any misalignment of the irises or diameter errors can result in "cutting" an additional portion of radiation compared to the ideally aligned case, thereby added losses.

I studied the transmission of an imperfect iris line by propagating the fundamental mode while introducing errors in the iris radius size δa_{size}, misalignments in the transverse plane (both in one direction and in both directions) – $\delta a_{x,y}$, and the influence of small, non-periodic displacements of the irises along the line – δb. I also simulated the combined effect of all the aforementioned imperfections.

Assuming that the amplitudes of errors follow a Gaussian distributions with some standard deviation (std), I simulated the propagation of the fundamental mode through 300 irises for each std value and then calculated the average relative loss per cell. The remaining

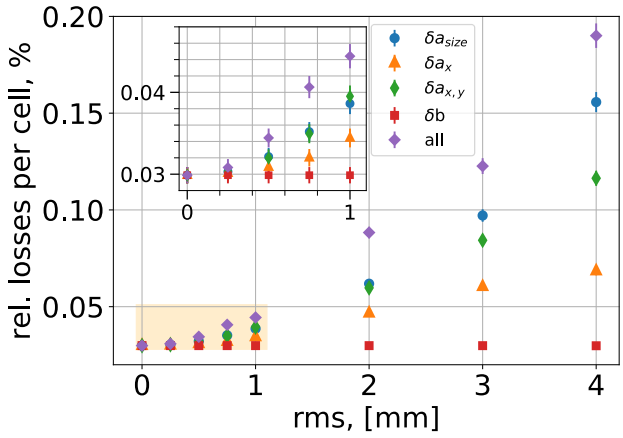

Figure 6.9: Effect of iris misalignments on relative losses per cell. Data points represent the resulting relative losses per cell for different standard deviation values of the errors. Blue circles correspond to errors in the iris radius, orange triangles indicate misplacement of the irises in the x direction only, and green diamonds show misplacement in both the x and y directions. Red squares correspond to uneven spacing between irises, while purple rhombuses represent the cumulative losses accounting for all effects, with corresponding misalignment values. The callout provides a close-up of the region with standard error values ranging from 0 to 1.

fraction of the radiation downstream 370 m of the waveguide can be estimated using the following expression: $T = e^{-\epsilon n}$, where ϵ is the relative loss per cell as shown in Fig. 6.9, and n is the number of screens. The results of this simulation are presented in Fig. 6.9, where I show the relative losses per cell with respect to the std value of the errors. I note the quadratic-like dependence, which is explainable since the losses in this model are solely due to diffraction and scale proportionally to the area blocked by the iris screen.

I defined an acceptable level of transmission coefficient deterioration to be within 10% with respect to the ideal case, which indicates that tolerances std should be at the level of 0.75 mm; this level of the errors gives transmission efficiency $T = 0.603$.

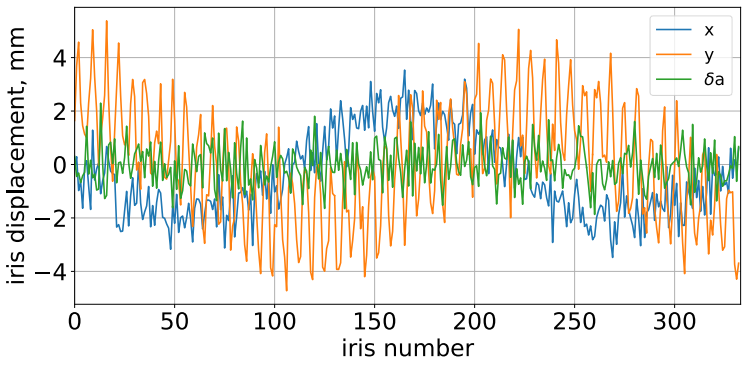

Figure 6.10: Modelled misalignments of the irises, accounting for the overall bends of the line over the full propagation distance of 370 m.

Then I simulated effects of smooth bends over the entire iris line[2]. In Fig. 6.10 I present

[2]akin to slope errors in the mirror surface, in contrast with "roughness"

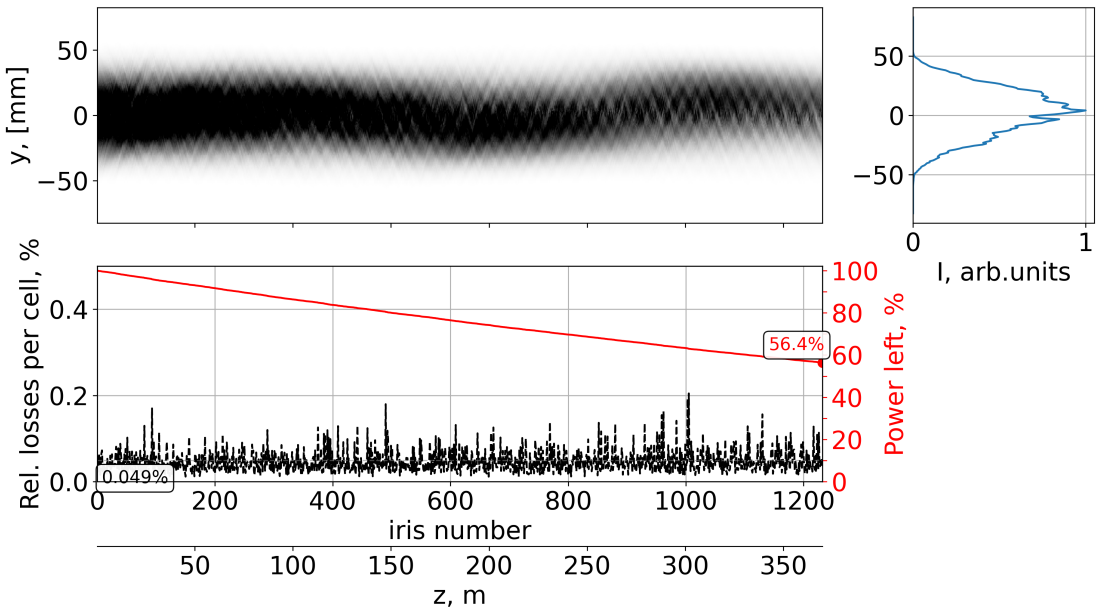

Figure 6.11: Notation of the figure is the same as in Fig. 6.4. Propagation of the fundamental mode through a non-ideal iris line, taking into account screen misalignments, the overall bend of the line, errors in the iris radius openings, and uneven spacing between the screens, as depicted in Fig. 6.10.

the misalignment of each individual iris overlaid with an adiabatic bend of the entire line, which I assumed to be nearly harmonic for this model example. I accounted for two types of bends: low and high frequency. One can see this in y direction in the Fig. 6.10. These higher oscillatory bends may occur between two stands that support the metallic tube of the iris line due to its own weight.

In principle, the amplitude of these bends should be within several std values of the misplacements of the irises to have almost no effect on the waveguide performance. I estimated that the tolerable amplitude of the bend is at the level of 2 mm when the other discussed misalignments have std value of 0.75 mm. I presented the results of the propagation of the fundamental mode in Fig. 6.11, which account for the effect of all misalignments and bends, resulting in nearly a 4% power drop in the output compared to the non-bended case with the same std level of the misplacement.

6.5. Out-coupling from the source and in-coupling into the iris line

6.5.1. Mirror-based propagation line

Before entering the iris line, the beam should be delivered through a concrete maze to the room where the diagnostic table will be located, as shown in Fig. 6.12. To address this, a mirror-based system can be used to propagate the radiation, where mirrors, placed at 45° angles, will facilitate guiding the radiation around corners.

We plan to use sections reminiscent of a Keplerian telescope, with equal focusing distances,

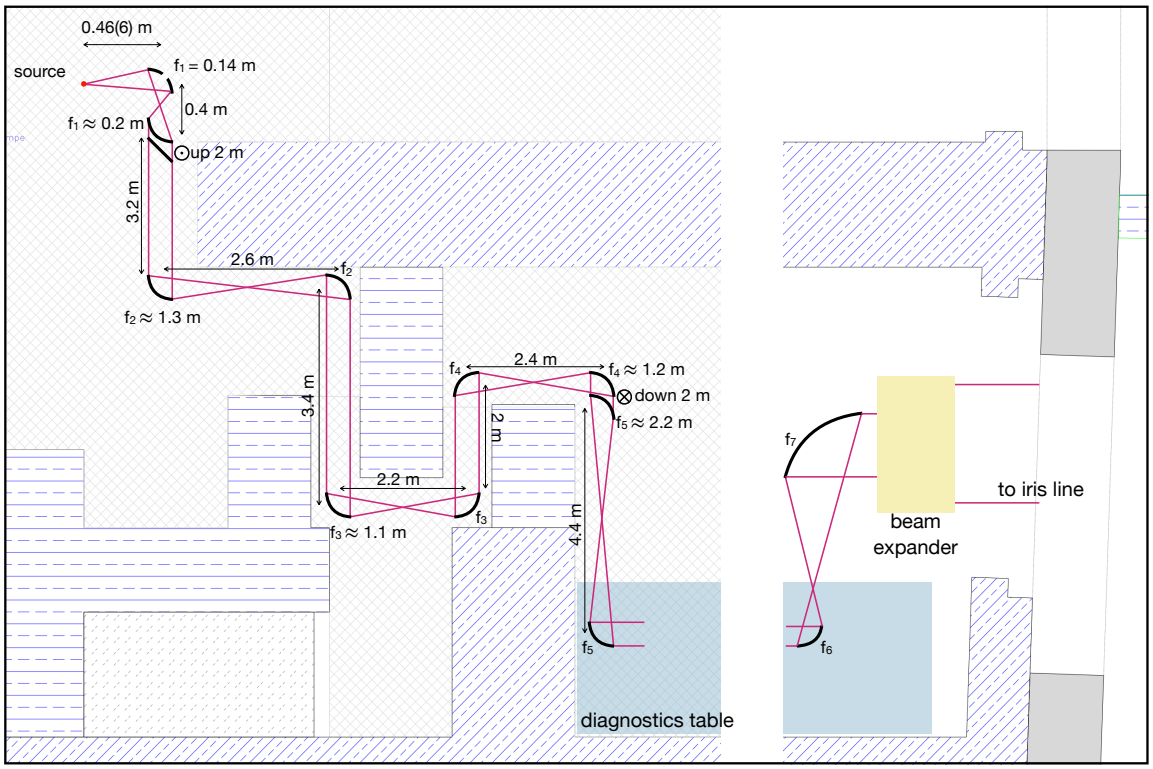

Figure 6.12: Scheme of the mirror delivery line to the diagnostic table in the XHE4/XS4 building. Focusing mirrors are represented by curved black lines, while circles with a dot and a cross inside indicate the periscope arrangement of the mirrors.

in combination with 'straight' sections, as depicted in Fig. 6.12. An alternative strategy could involve expanding the beam at the outset to achieve a large Rayleigh number, resulting in a highly collimated beam. However, this approach would necessitate more precise mirror alignment to steer the beam accurately. The system presented here mitigates this issue. Nevertheless, the optical system shows a potential for further optimization and modification. Additionally, the entire delivery line system should be mounted high enough to ensure that it does not obstruct personnel movement through the concrete maze, so the transmission line is elevated up to 2 meters, as marked in Fig. 6.12.

6.5.2. Design of a beam expander

The second part of the incoupling problem involves constructing a beam expander. This device would expand the beam transversely to match its size with the iris's opening, minimizing transmission losses in the waveguide as I described in the Sec. 6.3.3. This device also should be designed using reflective optics to avoid the excessive absorption of radiation that would inevitably occur with refractive lenses. The beam expander should be afocal, meaning that incoming and outcoming radiation is collimated. Also the system should allow magnification ensuring a constant output width of the radiation while the incoming width may vary. The principal design of such a device requires three functional optical elements composed of focusing and defocusing mirrors, as described in [132]. One of the possible solutions, referred

in [132] as the (+ − +) (focusing - defocusing - focusing elements) solution.

I outlined a mirror-based analogue of the beam expander, as presented in Fig. 6.13. The combination of focusing/defocusing mirrors and plane mirrors is arranged in three blocks: L_1, L_2, and L_3. These blocks should be movable to allow adjusting the distance between the optical elements D_1 and D_2 independently and accommodate the magnification function of the device. The third plane mirror, p_3, should be adjustable to align the optical axis of the

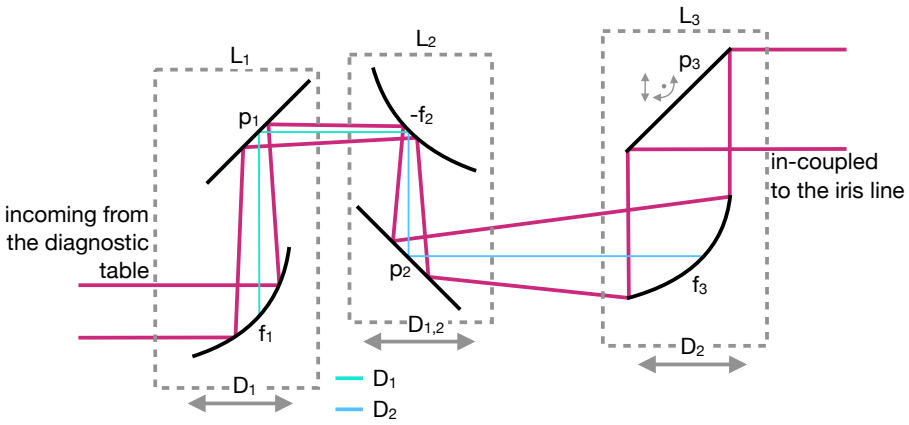

Figure 6.13: Conceptual design of a mirror-based beam expander. D_1 and D_2 denote the distances between the first and second functional optical elements, and between the second and third elements, respectively. The plane mirror p_3 should allow for pitch and roll adjustments, as well as movement in both the x and y directions with respect to the optical axis of the iris line.

beam expander with the iris line. This alignment can be achieved by adjusting the mirror's pitch and roll angles, as well as its Δx and Δy positions relative to the optical axis of the iris line.

6.6. Discussion and conclusion

In this section, I discussed the systems designed for the propagation of THz radiation generated with Cherenkov waveguides, aimed at delivering light pulses from XHE4/XS4 to the experimental hall of the European XFEL XHQ. The delivery system comprises three main components: the iris line, the mirror-based guiding line, and the afocal beam expander. The mirror-based guiding line facilitates the initial out-coupling of radiation from the source, guiding it to a diagnostic table. Following this, the afocal beam expander is used to match the outgoing radiation after the diagnostic table with the input requirements of the iris line, ensuring efficient transmission to the experimental hall. Finally, the iris line is responsible for transmitting radiation from XHE4/XS4 through a 370-meter-long XTD8 tunnel.

The beam expander must be afocal, ensuring that both the input and output radiation are collimated. The optical system should be designed to accommodate variations in the input waist size of the radiation without affecting the output size. Additionally, it should be

possible to adjust the output size in small increments to achieve optimal matching with the iris line for various radiation profiles.

The iris line is capable of transmitting a broad range of frequencies, and its efficiency can be optimised by adjusting the dimensionless parameter denoted as $N = a^2/(\lambda b)$. The transmission coefficient of the iris line is influenced by the radiation frequency and the structure of the line. For instance, an ideal iris line with $N = 101$ can achieve a transmission efficiency of 0.69 after 370 m of propagation when transporting the *fundamental* mode. However, imperfections such as errors in the aperture diameters, their centring misalignments (tolerance std 0.75 mm), as well as overall bends in the line (maximum amplitude 1.5 mm), reduce efficiency from 0.69 down to 0.56.

Chapter 7
Summary

I devoted this thesis to the study of the unique radiation pulse characteristics from synchrotrons and free-electron lasers. Among the various characteristics of radiation pulses, such as their duration, photon flux, etc., I placed particular emphasis on coherence, both in terms of simulations and experimental measurements. Furthermore, I refined the understanding of the virtual source structure of undulator radiation and focused on extending current simulation capabilities for synchrotron radiation to account for waveguide effects. This work was followed by studies on the propagation of THz radiation over long distances.

More specifically, in the first part of my thesis, I presented three versions of the numerical algorithm `SERVAL` for simulating single statistical instances of partially coherent radiation. The algorithm is based on the concept of confining a complex white noise distribution within specifically chosen mathematical supports to accurately shape the intensity distribution and correlation function of the resulting field. As a result, one obtains highly numerically efficient algorithms that rely solely on array-to-array multiplications and fast Fourier transforms.

The first version of the algorithm describes radiation from fully incoherent sources, such as thermal sources or radiation from a bending magnet at extremely high photon energies ($300 - 500$ keV), which I considered in **Paper I**. I then extended the algorithm to account for a finite divergence of the source, making it partially coherent. An example of this type of source is undulator radiation, which I discuss in **Paper II**. The final version of the algorithm accommodates an arbitrary Wigner function distribution of the emitted radiation. In Section 2.5.4, I summarize all three versions and suggest that they can be used in both spatial and temporal domains, being thus applicable not only to modelling optical processes but also, more broadly, Gaussian random fields. **Paper III** presents experimental results of a method for obtaining sub-fs pulses with free-electron lasers, which supplements the contents of the first part of the thesis. It serves as a showcase for the possible complexities of radiation sources in terms of statistical properties.

Continuing with coherence studies, I conducted measurements of the transverse coherence length of synchrotron radiation emitted by a single undulator cell of the SASE1 undulator at the European XFEL. I utilised direct observation of synchrotron radiation after monochromatization, which I refer to as a non-interferometric technique. Through this approach, I was able to directly observe the transversely spiky structure of synchrotron radiation. By measuring the transverse coherence length, it is possible to infer the transverse size of the electron beam that emitted this radiation, in accordance with the van Cittert-Zernike theorem. This provides a unique tool for electron beam size diagnostics along the long undulator beamlines of free-electron laser facilities.

I contributed to the research on undulator radiation by studying its virtual source structure from a single electron. I examined a peculiar source feature reported in [51] (a singularity appearing at both ends of the undulator) under the resonance approximation and investigated it beyond the resonance approximation using numerical wavefront propagation simulations. I

found that when the resonance approximation is dropped, the singularities disappear, giving rise to peculiar narrow structures instead. The size of these structures is related to the shorter formation length of the system, which corresponds to the undulator period length. Moreover, I observed an undulating structure in the backpropagated radiation inside the undulator, which is an imprint of the electron beam trajectory. I proposed two experiments to verify the undulator source peculiarities that I discovered.

Continuing my research on synchrotron radiation from a single electron, I developed a code that accounts for the waveguide effect on radiation generation. This influence becomes significant in the THz wavelength range, where the photon beam is strongly divergent. I proposed using the Green's function method for synchrotron radiation calculations. This approach allows for the generalization of the calculations for any given boundary conditions. I conducted thorough cross-checks of the developed code. First, I tested the free-space Green's function using the code Synchrotron Radiation Workshop. Then, I verified the free-space limit for a circular waveguide, ensuring that the calculations converged to the case of the free-space Green's function. Finally, I validated the code with a real-case scenario using the analytical expression for undulator radiation in a waveguide.

My research on THz radiation continued with the problem of its propagation over long distances, such as along the X-ray optics beamlines at free-electron laser facilities, which typically span several hundred meters. I considered two types of solutions: mirror-based systems and iris waveguides. I highlighted the key difference in the application of these two approaches, which lies in their geometry. The iris waveguide is suitable for straight paths, while the mirror system is better suited for complex, maze-like propagation geometries. I conducted numerical simulations to estimate the performance of the iris waveguide in terms of wavefront distribution and power transmission coefficient. The results indicate that the iris waveguide is expected to yield a transmission level of 56% over a distance of 370 m for a realistic setup. I also considered the in-coupling conditions for the iris waveguide and proposed a device for matching the radiation modes between the source and the iris waveguide to maximize transmission. Additionally, I explored the use of a mirror-based system to out-couple the radiation from the source and deliver it to the matching device.

In conclusion, synchrotrons and free-electron lasers serve as unique tools for studying matter and biological structures. Their operation and development represent the collective achievements of numerous scientists, engineers, and administrative staff, all contributing to humanity's ongoing quest to explore nature. Through this thesis, I hope to have advanced our understanding, even if only by a small increment.

Chapter 8
Publications

Publication directly related to this thesis

A. Trebushinin, G. Geloni, S. Serkez, R. Khubbutdinov, and E. Saldin, 'Pinhole camera for electron beam size diagnostic at storage ring with an ultralow emittance', Phys. Rev. Accel. Beams, vol. 27, no. 3, p. 032802, Mar. 2024, doi: 10.1103/PhysRevAccelBeams.27.032802.

A. Trebushinin, M. Siano, S. Serkez, and G. A. Geloni, 'Transverse coherence properties and propagation of x-ray radiation from spontaneous and free-electron laser sources', in Advances in Computational Methods for X-Ray Optics VI, SPIE, Oct. 2023, pp. 58–67. doi: 10.1117/12.2676700.

A. Trebushinin et al., 'Experimental Demonstration of Attoseconds-at-Harmonics at the SASE3 Undulator of the European XFEL', Photonics, vol. 10, no. 2, Art. no. 2, Feb. 2023, doi: 10.3390/photonics10020131.

A. Trebushinin, G. Geloni, Y. Rakshun, and S. Serkez, 'Gaussian random field generator for simulating partially coherent undulator radiation', Optica, vol. 9, no. 8, p. 842, Aug. 2022, doi: 10.1364/OPTICA.460902.

In preparation

A. Trebushinin, W. Freund, W. Qin, G. Perosa, A. Koch, J. Grünert, G. Geloni, and S. Serkez, 'Non-interferometric method for transverse electron beam size measurement with synchrotron radiation at a free-electron laser', in preparation

A. Trebushinin, W. Freund, W. Qin, G. Perosa, A. Koch, J. Grünert, G. Geloni, and S. Serkez, 'First observation of synchrotron radiation spikes for transverse electron beam size measurements at a free-electron laser', in preparation

A. Trebushinin, G. Geloni, and S. Serkez, 'Modeling instances of partially coherent field with an arbitrary Wigner function distribution'

Other publication

S. Liu et al., 'Cascaded hard X-ray self-seeded free-electron laser at megahertz repetition rate', Nat. Photon., vol. 17, no. 11, pp. 984–991, Nov. 2023, doi: 10.1038/s41566-023-01305-x.

V. A. Chernov et al., 'A concept of "materials" diffraction and imaging beamline for SKIF: Siberian circular photon source', Review of Scientific Instruments, vol. 94, no. 1, p. 013305, Jan. 2023, doi: 10.1063/5.0103481.

A. Trebushinin, S. Serkez, M. Veremchuk, Y. Rakshun, and G. Geloni, 'Spatial-frequency features of radiation produced by a step-wise tapered undulator', Journal of Synchrotron Radiation, vol. 28, no. 3, pp. 769–777, 2021.

B. Zakharov et al., 'A concept of 1-2 "structural diagnostics" diffraction beamline for "SKIF" synchrotron radiation facility', AIP Conference Proceedings, vol. 2299, no. 1, p. 060002, Nov. 2020, doi: 10.1063/5.0030401.

S. Serkez, A. Trebushinin, M. Veremchuk, and G. Geloni, 'Method for polarization shaping at free-electron lasers', Phys. Rev. Accel. Beams, vol. 22, no. 11, p. 110705, Nov. 2019, doi: 10.1103/PhysRevAccelBeams.22.110705.

S. Serkez et al., 'Super-X: Simulations for Extremely Hard X-Ray Generation With Short Period Superconducting Undulators for the European XFEL', Proceedings of the 39th Free Electron Laser Conference, vol. FEL2019, p. 4 pages, 0.771 MB, 2019, doi: 10.18429/JACOW-FEL2019-TUP061.

Appendix A

Free space propagation

In my thesis, I extensively utilised wavefront propagation techniques based on Fourier optics [133]. One of the most frequently used tools was the free-space propagator, which I applied in various parts of the thesis, including Chapter 2 and 3 for partially coherent radiation propagation, in Chapter 4 for studying virtual source of undulator radiation and Chapter 6 for modelling the iris waveguide for THz radiation propagation. I believe that the derivation of this propagator following [134], should be presented here, as the degree of its practical usefulness is equal to the ease with which it can be derived.

I write Helmholtz equation for the free space:

$$\nabla^2 \vec{E} + k_0^2 \vec{E} = 0, \tag{A.1}$$

where $k_0 = \omega/c$ and then I would like to write it in the inverse space domain. So, I define transverse domain Fourier transform:

$$\vec{\tilde{E}}(z, k_x, k_y, \omega) = \iint_{-\infty}^{\infty} \vec{E}(x, y, z, \omega) e^{i(k_x x + k_y y)} dx dy \tag{A.2}$$

and the corresponding inverse Fourier transform:

$$\vec{E}(x, y, z, \omega) = \frac{1}{4\pi^2} \iint_{-\infty}^{\infty} \vec{\tilde{E}}(z, k_x, k_y, \omega) e^{-i(k_x x + k_y y)} dk_x dk_y. \tag{A.3}$$

Substituting Eq. A.3 in Eq. A.1 I obtain:

$$\frac{d^2 \vec{\tilde{E}}}{dz^2} + k_0 \left(1 - \frac{k_x^2}{k_0^2} - \frac{k_y^2}{k_0^2}\right) \vec{\tilde{E}} = 0. \tag{A.4}$$

Once a field distribution $\vec{\tilde{E}}(\omega, k_x, k_y, 0)$ at $z = 0$ is known, one readily can write a solution for Eq. A.4 at an arbitrary position z:

$$\vec{\tilde{E}}(k_x, k_y, z, \omega) = \vec{\tilde{E}}(k_x, k_y, 0, \omega) \exp\left[ik_0 z \sqrt{1 - \frac{k_x^2}{k_0^2} - \frac{k_y^2}{k_0^2}}\right] \tag{A.5}$$

Then, the final field distribution is obtained by performing the Fourier transform back to real space. It is important to note that this equation is useful for both forward and backward propagation, which, for example, I utilised in studying the virtual source of undulator radiation. A numerical implementation of Eq. A.5 can be found in `OCELOT` toolkit [73], [74].

Appendix B

Brightness of undulator radiation

Slightly extending the results from Chapter 4, it is also valuable to examine the brightness of undulator radiation at the source location, defined as the maximum of the Wigner function distribution. Due to the revealed peculiarities in the undulator source structure, one would expect to observe an increase in brightness exactly at the end of the undulator compared to the middle position. This can be achieved by scanning positions along the undulator as a function of the detuning parameter C from the resonance, as shown in Fig. B.1a.

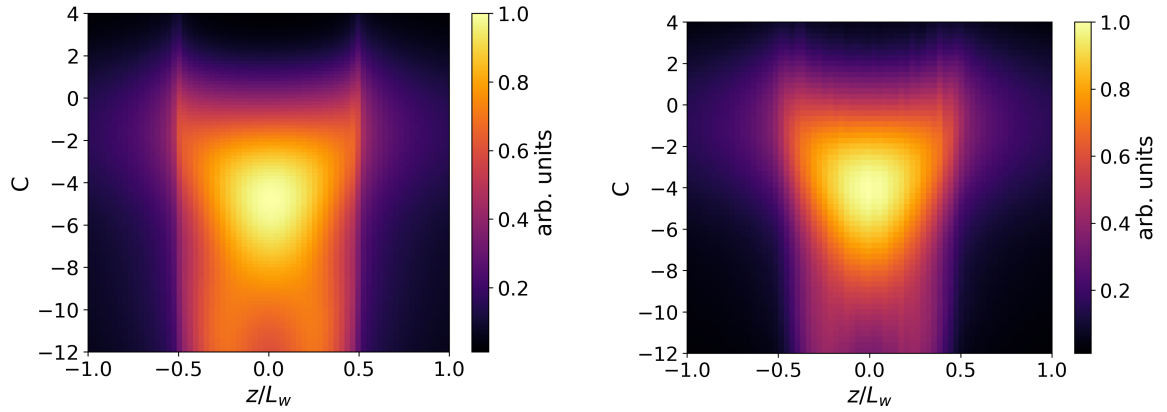

(a) 100-periods device

(b) 10-periods device

Figure B.1: "Batman" diagram. The colormap represents the value of the maximum Wigner function distribution for each combination of z/L_w and C. The overall colormap is normalised to the maximum value. The horizontal axis corresponds to the position along the undulator, and the vertical axis represents the detuning parameter C.

As one can see, the global maximum occurs around $C = -4$ and $z = 0$, which is consistent with the well-known fact that to maximise photon flux, one needs to introduce a slight detuning from the resonance. However, the maximum for the perfectly in-resonance case ($C = 0$) is not located in the middle of the undulator but rather at either end of the device. This effect could also be a subject for further study.

Appendix C

Choice of the noise for SERVAL algorithms

I utilised complex Gaussian white noise for SERVAL algorithms, which is justified by the fact that I simulated complex Gaussian random fields and the statistics should be preserved. However, one might observe that any noise $Z = X + iY$ would suffice for SERVAL when using Eq. 2.88. For example, one can define X and Y as follows:

$$X = -13\cos(t) + 5\cos(2t) + 2\cos(3t) + \cos(4t), \quad Y = 16\sin(t)^3, \tag{C.1}$$

and t is a random variable that is uniformly distributed within $[-\pi, \pi]$, e.g., Eq. C.1 describes the method to sample one instance of the noise Z. I illustrate the shape that the samples of Z form in the complex plane in Fig. C.1 (red dots and corresponding histograms).

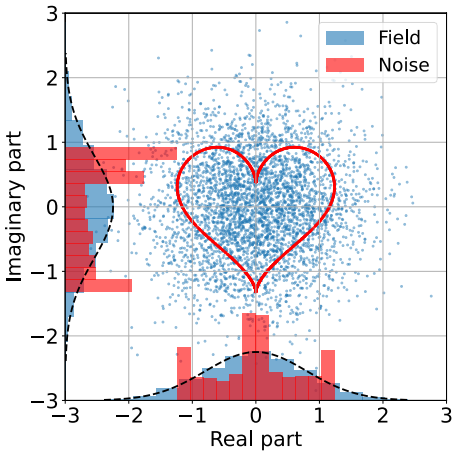

Figure C.1: Transformation of the 'heart' shape to a Gaussian distribution in the complex plane. Data is presented for a central pixel of the field distribution, consisting of a mesh of 31×31 points, with the field consisting of 4001 realisations. The data presented in red correspond to the initial noise Z generated with Eq. C.1, the blue-colored data represent samples of the resulting field using SERVAL. The sample was normalised to the mean value of the amplitudes of the corresponding signal for convenience.

After simulating a field with Eq. 2.88 using the noise defined here, one will observe that the statistics of the samples of the random variable $Z(\vec{r}_n)$ at any position $\vec{r}_n$ are transformed into complex Gaussian noise statistics, as illustrated in Fig. C.1 with blue dots and corresponding histograms. Furthermore, the instantaneous intensity of the resulting field will follow the expected negative exponential distribution, as shown in Fig. C.2.

This effect may be explained by the fact that, according to Eq. 2.88, Fourier transforms are performed. During the transform, the random variables along the given axis are summed. For a reasonably large mesh grid[1], the statistics of any initial noise Z will be transformed into Gaussian noise according to the central limit theorem.

However, SERVAL algorithm for the incoherent sources (Eq. 2.80) does not involve Fourier transforms. As a result, the resulting field distribution does not adhere to the correct statistics, and the mentioned statistical trick will not occur. Therefore, I always prefer to use complex Gaussian white noise at the start to ensure the accuracy of the final statistics of the simulated field and overall consistency.

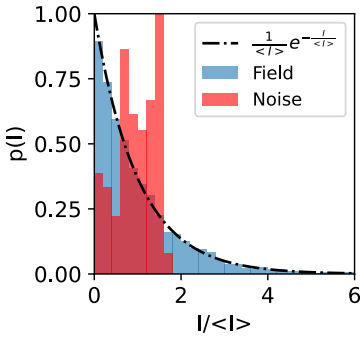

Figure C.2: Instantaneous intensity probability distribution: the red line represents the initial noise, and the blue line represents the final instantaneous intensity distribution after applying the SERVAL algorithm to the partially coherent source.

[1] although, in this case in Figs. C.1, C.2, there were only 31 points

Appendix D

Y-Polarisation Component of Undulator Radiation: SRW and SRinWGuide

I present the results of the cross-check between `SRinWGuide` and the `SRW` code for the y-polarisation component of undulator radiation, where the edge term discussed in Section 5.4 is accounted for semi-analytically in `SRW`. I found noticeable difference in the obtained results.

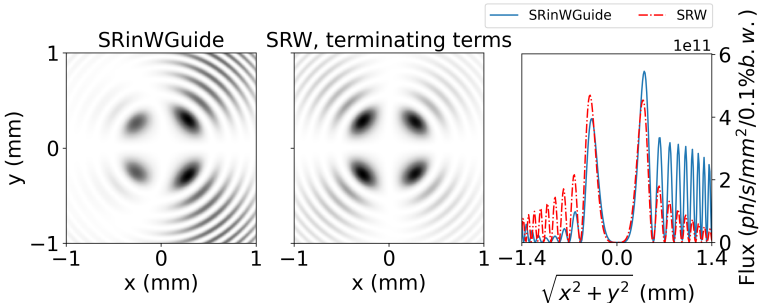

Figure D.1: Comparison of computational results from different codes for the y-polarisation component of the undulator radiation intensity. Semi-analytical treatment of the edge term is *turned on* in `SRW`. The slice in the right subplot represents a diagonal cut over the intensity distributions.

Appendix E

Stellar intensity interferometer photo overlaid with spiky distribution

In addition to Section 2.5.1 in Chapter 2, where I discuss an algorithm for simulating fully incoherent radiation, I present an image of the Narrabri Stellar Intensity Interferometer overlaid with a spiky field in Fig. E.1, representing intensity distribution of a single field realisation at a given moment in time.

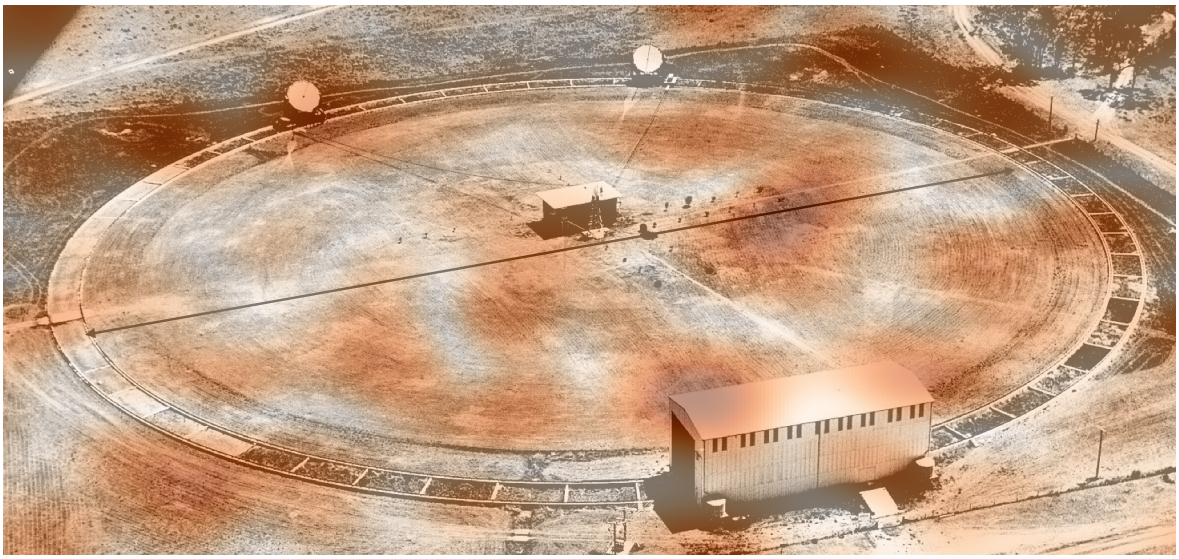

Figure E.1: The Narrabri Stellar Intensity Interferometer photo overlaid with spiky distribution. Photo is taken from [135].

List of Figures

2.1 Gaussian random process statistics. The upper left subplot represents the sum of random phasors, resulting in a sample of a Gaussian random process shown on the complex plane. The upper right subplot shows 10^4 samples plotted on the complex plane, with zero mean and unit variance; the red dot corresponds to the sample in the upper left. The lower left shows the resulting Rayleigh distribution, and the lower right shows the instantaneous intensity of the simulated samples. 10

2.2 Schematic representation of the geometry for Eq. 2.46. The parameter R_2 is represented in the same way. 17

2.3 Schematic representation of the geometry used for the generalized van Cittert–Zernike theorem. 19

2.4 (a) Sun intensity distribution at a given wavelength (500 nm) as seen from Earth. (b) Visible solar radiation distribution at the observation position. The hole made by a needle (100 μm) is represented as a mask over the subplot in (b) to illustrate the setup of Young's experiment. 28

2.5 Result of Young's original interference experiment using a slip of card. Color fringes and the shadow cast by the obstacle are visible, separated by white parallel lines (highlighted in the callout). To enhance visibility, the callout colormap has been adjusted to be ten times more sensitive than in the main image. 28

2.6 Instantaneous intensity probability distribution: The black line represents the theoretical expectation—negative exponential distribution. The blue histogram shows the distribution of the initial Gaussian white noise (50001 statistical realizations), and the orange histogram represents the distribution for the resulting field. $\bar{\phi}(\vec{r}, \omega)$. 39

2.7 The SASE FEL process begins with spontaneous emission driven by shot noise in the electron beam. This emission is then exponentially amplified until saturation around cell 10. Beyond that point, the radiation power grows nearly linearly. The top subplot shows pulse energy along the undulator. The bottom color map displays the longitudinal radiation profile averaged over the transverse direction. The right subplot shows radiation power profiles along the pulse, after cell 1 (blue) and cell 15 (orange). 52

2.8 Monochromatic transverse intensity distribution of SASE in the far zone from the cell labelled at the top of the subfigures. 53

2.11 Visualisation of the Wigner-function-based algorithm. A known Wigner function is multiplied by complex white noise, followed by a Fourier-like integral. The result is a single realisation of the radiation spectrum. 54

2.9 Adopted from **[37]**: "Time–frequency analysis terminology illustrated on a single-shot Wigner distribution of a modeled SASE pulse with negative frequency chirp u. The Wigner distribution for a bandwidth-limited pulse of Gaussian shape is provided in the inset." 55

2.10 Adopted from **[37]**: "The European XFEL 100 pC electron beam with a non-linear energy chirp produces SASE radiation with different durations at different photon energies. Note the bifurcation in Wigner distribution above 499 eV. Analysis based on 1000 simulated SASE spectra." 55

2.12 Histogram of the instantaneous intensity distribution. The red dot-dashed line represents a fit to the Gaussian noise distribution, shown by the blue histogram. The histogram for the `SERVAL` field is shown in orange, while the distribution for the `Genesis 1.3 v2` output is displayed in green. 58

2.13 The first row presents the results of the `Genesis 1.3 v2` simulation, showing Wigner function distributions for both a single-shot event and an ensemble average over 1000 events. The second row shows the emulated field, generated according to Eq. 2.100 from the averaged Wigner function distribution. 59

2.14 The modified Wigner distribution is shown in (a), while (b) presents the averaged Wigner distribution reproduced using Eq. 2.100. Panel (c) displays one statistical realisation of the Wigner distribution obtained with the algorithm. 59

3.1 Schematic representation of the experimental setup. Radiation is emitted from cell 37 at SASE1. The blue distribution after the monochromator represents the averaged transverse profile of different longitudinal spikes after monochromatisation. The black-and-white spatial distribution near the spectrum shows the monochromatic intensity distribution from individual spikes. 74

3.2 The colormap shows the number of longitudinal spikes after passage through the monochromator, for each crystal reflection indicated at the top of the corresponding subplot. 75

3.3 Colormap of the coherence length (rms) of the radiation from the corresponding cell of the SASE1 beamline, shown as a function of transverse electron beam size (rms) and photon energy. 76

3.4 Simulated signal averaged over $M_L = 22 \times 13$ transverse modes and the corresponding autocorrelation function. The intensity distribution in panel (a) is normalised to its maximum value. The peak value of the autocorrelation function is $1 + 1/M_L$, reflecting a reduction in contrast due to averaging over M_L successive longitudinal spikes. 77

3.5 The same figure arrangement as Fig. 3.4, but for a noisy signal with a signal-to-noise ratio of 0.9. 78

3.6 Data analysis procedure. (a, b): Comparison of the simulated signal detected with an ideal detector (a) and the simulated signal with added noise after background subtraction (b). (c): Comparison of the reconstructed autocorrelation functions from the ideal and noisy signals. The corresponding $(g^{(2)} - 1)M_L$ function is shown below, where M_L denotes the total number of longitudinal modes. 78

3.7 Typical image recorded during the experiment. Panel (a) shows the ensemble-averaged distribution, while panel (b) displays single-shot events. The autocorrelation function is shown in the upper left corner of each image, enclosed in a square frame. 80
3.8 Results of the autocorrelation analysis of radiation from **cell 29**. 80
3.9 Results of the autocorrelation analysis of radiation from **cell 37** 81
3.10 Schematic depiction of the electron beam phase space for the t-γ and t-x parameter pairs. The figures illustrate the effect of different levels of monochromatisation on the effectively measured electron beam size. 82

4.1 Candy-wrapper-like distribution of the undulator radiation virtual source. The source intensity distribution along the undulator versus the transverse x-dimension is shown. Both axes are normalised to the natural dimensions of the system: the undulator length and the diffraction size of undulator radiation. The intensity profile along the vertical-axis slice is normalised to its maximum value. Wigner function distributions at different positions along the device are shown at the top of the subplots. 92
4.2 The virtual source distribution at the edge of the undulator at resonance. The distribution width is $FWHM_{z_0=L_w/2} = 0.38\sqrt{L_w\bar{\lambda}}$. The radiation acquires a quadratic phase front as a result of propagation. 92
4.3 The virtual source distribution in the middle of the undulator at resonance. The distribution width is $FWHM_{z_0=0} = \mathbf{1.37}\sqrt{L_w\bar{\lambda}}$. The phase tilt is due to a slight overall tilt in the electron velocity. 92
4.4 X-shaped Wigner function distribution at the centre of the undulator. The marginal distributions along the horizontal and vertical axes represent the spatial and angular profiles of the radiation, respectively. 93
4.5 Candy-wrapper-like distribution of the undulator source. The "wiggling" of the source distribution is shown. From top to bottom, source distributions for 20-period, 10-period, and 5-period devices are presented. Each transverse slice is normalised to its maximum intensity. 95
4.6 "Wiggling" of the undulator source distribution in the out-of-resonance case, with the frequency set between the first and second harmonics. Each transverse slice is normalised to its maximum intensity. 96
4.7 "Wiggling" of the undulator source distribution in the out-of-resonance case, shown for the intensity slices. The distribution width is given by $FWHM_{z_0=0} = 0.42\sqrt{L_w\bar{\lambda}}$. 97

5.1 The electron path is shown in panel (a), and the integrand and corresponding integral values from Eq. 5.7 are shown in panel (b), for a pair of interspaced bending magnets. 103
5.2 Comparison of computational results from `SRinWGuide` and `SRW` for the radiation from the interspaced bending magnets shown in Fig. 5.1. The intensity distributions include both polarisation components. The solid blue and dashed red lines in the line-out plots fully overlap. 105

5.3 Schematic representation of the integration path over a magnetic structure. Panel (a) shows integration carried out solely within the region where the magnetic field is defined, i.e., from z_A to z_B. Panel (b) illustrates the case where the contribution from the outer regions $[-\infty, z_A]$ and $[z_B, +\infty]$ (terminating terms) is estimated semi-analytically. 105
5.4 The same as Fig. 5.2, but now `SRW` performs the outer integral estimation (terminating terms). 105
5.5 Three poles. 107
5.6 Comparison of computational results from `SRinWGuide` and `SRW` for the radiation from three poles (Fig. 5.6). The intensity distributions account for both polarization components. 107
5.7 Undulator. 108
5.8 Comparison of computational result from `SRinWGuide` and `SRW` for the radiation from an undulator. Total flux is presented for both polarization components. 108
5.9 Same as 5.8, but with y-polarization component. The slice on the right subplot is presented for a diagonal cut. 108
5.10 Radiation from the straight section. Comparison between the analytical result according to Eq. 5.13, `SRinWGuide`, and `SRW`. Total intensity from both polarisation components is presented. 109
5.11 On-axis spectral flux from the three-pole device, calculated using the free-space Green's function (black dotted line) and the circular waveguide Green's function. The latter takes into account different numbers of k modes, when $m = 1$: the blue solid line corresponds to 1000 modes, and the red solid line corresponds to 1500 modes. 110
5.12 Spatial distribution of radiation in the far zone from a ten-period undulator inside a waveguide. 112
5.13 Cross sections of the spatial distributions shown in Fig. 5.12. 112

6.1 Aerial view of the European XFEL campus with the marked locations of XHE4/XS4 and the users' hall in XHQ; the distance between them is 370 m. In the call-out, a schematic of the XHE4/XS4 building at the UG2 level is shown, with the path of the THz radiation through the radiation protection maze outlined. The diagnostic table is marked with a cyan-blue rectangle. 114
6.2 Outlines of the iris line and mirror system. The iris line has two main parameters: a is the radius of the hole and b is the spacing between screens. . 115
6.3 Illustration of wavefront propagation through the iris line. 116
6.4 Result of plane wave propagation through an iris line. The upper right subplot shows the intensity distribution of the radiation at the exit of the iris line; each transverse slice is normalised to its maximum intensity. The bottom subplot represents radiation losses: the black dashed line indicates the relative loss per cell, and the red line shows the fraction of radiation remaining at a given distance from the entrance. 118
6.5 Analytical estimation of the radiation losses in the iris line. A_{nj} represents the relative amplitude of mode n and j after a given propagation distance. 118
6.6 The radiation intensity distribution at the exit of the iris line shows a slight discrepancy, as Vanstein's approach accounts only for zeroth-order diffraction. 118

6.7 Notation of the figure is the same as in Fig. 6.4. Result of fundamental mode propagation through an iris line. Relative losses per cell are constant, and the spatial radiation distribution is perfectly preserved along the iris line. 119

6.8 Transmission efficiency of different iris lines with iris openings of size a. . . . 120

6.9 Effect of iris misalignments on relative losses per cell. Data points represent the resulting relative losses per cell for different standard deviation values of the errors. Blue circles correspond to errors in the iris radius, orange triangles indicate misplacement of the irises in the x direction only, and green diamonds show misplacement in both the x and y directions. Red squares correspond to uneven spacing between irises, while purple rhombuses represent the cumulative losses accounting for all effects, with corresponding misalignment values. The callout provides a close-up of the region with standard error values ranging from 0 to 1. 121

6.10 Modelled misalignments of the irises, accounting for the overall bends of the line over the full propagation distance of 370 m. 121

6.11 Notation of the figure is the same as in Fig. 6.4. Propagation of the fundamental mode through a non-ideal iris line, taking into account screen misalignments, the overall bend of the line, errors in the iris radius openings, and uneven spacing between the screens, as depicted in Fig. 6.10. 122

6.12 Scheme of the mirror delivery line to the diagnostic table in the XHE4/XS4 building. Focusing mirrors are represented by curved black lines, while circles with a dot and a cross inside indicate the periscope arrangement of the mirrors. 123

6.13 Conceptual design of a mirror-based beam expander. D_1 and D_2 denote the distances between the first and second functional optical elements, and between the second and third elements, respectively. The plane mirror p_3 should allow for pitch and roll adjustments, as well as movement in both the x and y directions with respect to the optical axis of the iris line. 124

B.1 "Batman" diagram. The colormap represents the value of the maximum Wigner function distribution for each combination of z/L_w and C. The overall colormap is normalised to the maximum value. The horizontal axis corresponds to the position along the undulator, and the vertical axis represents the detuning parameter C. 133

C.1 Transformation of the 'heart' shape to a Gaussian distribution in the complex plane. Data is presented for a central pixel of the field distribution, consisting of a mesh of 31×31 points, with the field consisting of 4001 realisations. The data presented in red correspond to the initial noise Z generated with Eq. C.1, the blue-colored data represent samples of the resulting field using `SERVAL`. The sample was normalised to the mean value of the amplitudes of the corresponding signal for convenience. 135

C.2 Instantaneous intensity probability distribution: the red line represents the initial noise, and the blue line represents the final instantaneous intensity distribution after applying the `SERVAL` algorithm to the partially coherent source. 136

D.1 Comparison of computational results from different codes for the y-polarisation component of the undulator radiation intensity. Semi-analytical treatment of the edge term is *turned on* in SRW. The slice in the right subplot represents a diagonal cut over the intensity distributions. 137

E.1 The Narrabri Stellar Intensity Interferometer photo overlaid with spiky distribution. Photo is taken from [135]. 139

References

[1] P. Willmott, *An introduction to synchrotron radiation: techniques and applications*, en, Second edition. Hoboken, New Jersey: Wiley, 2019, ISBN: 978-1-119-28045-3, [Online]. Available: https://onlinelibrary.wiley.com/doi/book/10.1002/9781119280453.

[2] A. M. Kondratenko and E. L. Saldin, "Generation of coherent radiation by a relativistic electron beam in an ondulator," English, *Part. Accel.; (United Kingdom)*, vol. 10:3-4, Aug. 1980, [Online]. Available: https://s3.cern.ch/inspire-prod-files-8/872da099a0e9c171a4dca19256f7ca0e.

[3] Y. S. Derbenev, A. M. Kondratenko, and E. L. Saldin, "On the possibility of using a free electron laser for polarization of electrons in storage rings," *Nuclear Instruments and Methods in Physics Research*, vol. 193, no. 3, pp. 415–421, Mar. 1982, ISSN: 0167-5087, DOI: 10.1016/0029-554X(82)90233-6.

[4] R. Bonifacio, C. Pellegrini, and L. M. Narducci, "Collective instabilities and high-gain regime in a free electron laser," *Optics Communications*, vol. 50, no. 6, pp. 373–378, Jul. 1984, ISSN: 0030-4018, DOI: 10.1016/0030-4018(84)90105-6.

[5] G. S. Edwards, S. J. Allen, R. F. Haglund, *et al.*, "Applications of Free-Electron Lasers in the Biological and Material Sciences," en, *Photochemistry and Photobiology*, vol. 81, no. 4, pp. 711–735, 2005, ISSN: 1751-1097, DOI: 10.1111/j.1751-1097.2005.tb01437.x.

[6] J. Ullrich, A. Rudenko, and R. Moshammer, "Free-Electron Lasers: New Avenues in Molecular Physics and Photochemistry," en, *Annual Review of Physical Chemistry*, vol. 63, no. Volume 63, 2012, pp. 635–660, May 2012, ISSN: 0066-426X, 1545-1593, DOI: 10.1146/annurev-physchem-032511-143720.

[7] P. H. Bucksbaum and N. Berrah, "Brighter and faster: The promise and challenge of the x-ray free-electron laser," *Physics Today*, vol. 68, no. 7, pp. 26–32, Jul. 2015, ISSN: 0031-9228, DOI: 10.1063/PT.3.2845.

[8] E. A. Seddon, J. A. Clarke, D. J. Dunning, *et al.*, "Short-wavelength free-electron laser sources and science: A review," en, *Reports on Progress in Physics*, vol. 80, no. 11, p. 115 901, Oct. 2017, ISSN: 0034-4885, DOI: 10.1088/1361-6633/aa7cca.

[9] G. Dattoli and F. Nguyen, "Free Electron Laser as a tool for fundamental quantum physics," *Nuclear Instruments and Methods in Physics Research Section B: Beam Interactions with Materials and Atoms*, Proceedings of the 7th International Conference Channeling 2016: Charged & Neutral Particles Channeling Phenomena, vol. 402, pp. 336–338, Jul. 2017, ISSN: 0168-583X, DOI: 10.1016/j.nimb.2017.03.044.

[10] H. N. Chapman, "X-Ray Free-Electron Lasers for the Structure and Dynamics of Macromolecules," en, *Annual Review of Biochemistry*, vol. 88, no. Volume 88, 2019,

pp. 35–58, Jun. 2019, ISSN: 0066-4154, 1545-4509, DOI: 10.1146/annurev-biochem-013118-110744.

[11] I. Matsuda and Y. Kubota, "Recent Progress in Spectroscopies Using Soft X-ray Free-electron Lasers," *Chemistry Letters*, vol. 50, no. 7, pp. 1336–1344, Jul. 2021, ISSN: 0366-7022, DOI: 10.1246/cl.200881.

[12] P. Vijayan, I. R. Willick, R. Lahlali, C. Karunakaran, and K. K. Tanino, "Synchrotron Radiation Sheds Fresh Light on Plant Research: The Use of Powerful Techniques to Probe Structure and Composition of Plants," *Plant and Cell Physiology*, vol. 56, no. 7, pp. 1252–1263, Jul. 2015, ISSN: 0032-0781, DOI: 10.1093/pcp/pcv080.

[13] T. Narayanan, H. Wacklin, O. Konovalov, and R. Lund, "Recent applications of synchrotron radiation and neutrons in the study of soft matter," *Crystallography Reviews*, vol. 23, no. 3, pp. 160–226, Jul. 2017, ISSN: 0889-311X, DOI: 10.1080/0889311X.2016.1277212.

[14] L. Mino, E. Borfecchia, J. Segura-Ruiz, C. Giannini, G. Martinez-Criado, and C. Lamberti, "Materials characterization by synchrotron x-ray microprobes and nanoprobes," *Reviews of Modern Physics*, vol. 90, no. 2, p. 025 007, Jun. 2018, DOI: 10.1103/RevModPhys.90.025007.

[15] Z. Gong and Y. Yang, "The application of synchrotron X-ray techniques to the study of rechargeable batteries," *Journal of Energy Chemistry*, vol. 27, no. 6, pp. 1566–1583, Nov. 2018, ISSN: 2095-4956, DOI: 10.1016/j.jechem.2018.03.020.

[16] "National synchrotron light source II: Conceptual design report," Brookhaven National Laboratory, Tech. Rep., 2006, [Online]. Available: https://www.bnl.gov/isd/documents/35598.pdf.

[17] "SPring-8-II conceptual design report," RIKEN SPring-8 Center, Tech. Rep., 2014, [Online]. Available: http://rsc.riken.jp/pdf/SPring-8-II.pdf.

[18] "PETRA III: A low emittance synchrotron radiation source. technical design report," Deutsches Elektronen-Synchrotron DESY, Tech. Rep., 2001, [Online]. Available: https://www.desy.de/~mpywar/Draftdir/PETRAIII/petra_tdr.pdf.

[19] "PETRA IV: The ultra-low emittance source - conceptual design report," Deutsches Elektronen-Synchrotron DESY, Tech. Rep., 2019, [Online]. Available: https://bib-pubdb1.desy.de/record/426140/files/DESY-PETRAIV-Conceptual-Design-Report.pdf.

[20] "ESRF EBS Design Report," European Synchrotron Radiation Facility, Tech. Rep., 2019, [Online]. Available: https://www.esrf.fr/files/live/sites/www/files/about/upgrade/documentation/Design%20Report-reduced-jan19.pdf.

[21] T. Fornek, "Advanced Photon Source Upgrade Project Final Design Report," en, Tech. Rep. APSU–2.01-RPT-003, 1543138, 153666, May 2019, APSU–2.01–RPT–003, 1543138, 153666, DOI: 10.2172/1543138.

[22] I. P. S. Martin, "Short pulse x-ray generation in synchrotron radiation sources," English, PhD thesis, Oxford University, UK, 2011, [Online]. Available: https://ora.ox.ac.uk/objects/uuid:9ac0bcc2-bedb-46d0-b95c-22f4741f45a0.

[23] S. Khan, "Ultrashort Pulses from Synchrotron Radiation Sources," en, in *Synchrotron Light Sources and Free-Electron Lasers: Accelerator Physics, Instrumentation and Science Applications*, E. J. Jaeschke, S. Khan, J. R. Schneider, and J. B. Hastings, Eds., Cham: Springer International Publishing, 2016, pp. 51–81, ISBN: 978-3-319-14394-1, DOI: 10.1007/978-3-319-14394-1_5.

[24] E. L. Saldin, E. A. Schneidmiller, and M. V. Yurkov, "Statistical properties of the radiation from SASE FEL operating in the linear regime," *Nuclear Instruments and Methods in Physics Research Section A: Accelerators, Spectrometers, Detectors and Associated Equipment*, vol. 407, no. 1, pp. 291–295, Apr. 1998, ISSN: 0168-9002, DOI: 10.1016/S0168-9002(98)00037-0.

[25] J. Rossbach, "New Linac Based Free Electron Laser Projects using Bright Electron Beams," 1996, DOI: 10.5170/CERN-1996-007.275.

[26] *The European X-ray free-electron laser: technical design report*, eng. Hamburg: DESY XFEL Project Group, 2006, ISBN: 978-3-935702-17-1, [Online]. Available: https://bib-pubdb1.desy.de/record/77248/files/european-xfel-tdr.pdf.

[27] S. Serkez, G. Geloni, S. Tomin, *et al.*, "Overview of options for generating high-brightness attosecond x-ray pulses at free-electron lasers and applications at the European XFEL," en, *Journal of Optics*, vol. 20, no. 2, p. 024 005, Jan. 2018, ISSN: 2040-8986, DOI: 10.1088/2040-8986/aa9f4f.

[28] N. Hartmann, G. Hartmann, R. Heider, *et al.*, "Attosecond time–energy structure of X-ray free-electron laser pulses," en, *Nature Photonics*, vol. 12, no. 4, pp. 215–220, Apr. 2018, ISSN: 1749-4893, DOI: 10.1038/s41566-018-0107-6.

[29] A. Malyzhenkov, Y. P. Arbelo, P. Craievich, *et al.*, "Single- and two-color attosecond hard x-ray free-electron laser pulses with nonlinear compression," *Physical Review Research*, vol. 2, no. 4, p. 042 018, Oct. 2020, DOI: 10.1103/PhysRevResearch.2.042018.

[30] J. Duris, S. Li, T. Driver, *et al.*, "Tunable isolated attosecond X-ray pulses with gigawatt peak power from a free-electron laser," en, *Nature Photonics*, vol. 14, no. 1, pp. 30–36, Jan. 2020, ISSN: 1749-4893, DOI: 10.1038/s41566-019-0549-5.

[31] P. Franz, S. Li, T. Driver, *et al.*, "Terawatt-scale attosecond X-ray pulses from a cascaded superradiant free-electron laser," en, *Nature Photonics*, vol. 18, no. 7, pp. 698–703, Jul. 2024, ISSN: 1749-4893, DOI: 10.1038/s41566-024-01427-w.

[32] C. Callegari, A. N. Grum-Grzhimailo, K. L. Ishikawa, K. C. Prince, G. Sansone, and K. Ueda, "Atomic, molecular and optical physics applications of longitudinally coherent and narrow bandwidth Free-Electron Lasers," *Physics Reports*, vol. 904, pp. 1–59, Apr. 2021, ISSN: 0370-1573, DOI: 10.1016/j.physrep.2020.12.002.

[33] R. Borrego-Varillas, M. Lucchini, and M. Nisoli, "Attosecond spectroscopy for the investigation of ultrafast dynamics in atomic, molecular and solid-state physics," en,

Reports on Progress in Physics, vol. 85, no. 6, p. 066 401, May 2022, ISSN: 0034-4885, DOI: 10.1088/1361-6633/ac5e7f.

[34] J. P. Cryan, T. Driver, J. Duris, *et al.*, "Chapter One - The development of attosecond XFELs for understanding ultrafast electron motion," in *Advances In Atomic, Molecular, and Optical Physics*, ser. Advances in Atomic, Molecular, and Optical Physics, L. F. DiMauro, H. Perrin, and S. F. Yelin, Eds., vol. 71, Academic Press, Jan. 2022, pp. 1–64, DOI: 10.1016/bs.aamop.2022.05.001.

[35] S. Krinsky, "Frequency Chirped SASE FEL," en, Tech. Rep. SLAC-PUB-9633, 812615, Jan. 2003, SLAC–PUB–9633, 812 615, DOI: 10.2172/812615.

[36] E. L. Saldin, E. A. Schneidmiller, and M. V. Yurkov, "Self-amplified spontaneous emission FEL with energy-chirped electron beam and its application for generation of attosecond x-ray pulses," *Physical Review Special Topics - Accelerators and Beams*, vol. 9, no. 5, p. 050 702, May 2006, DOI: 10.1103/PhysRevSTAB.9.050702.

[37] S. Serkez, O. Gorobtsov, D. E. Rivas, *et al.*, "Wigner distribution of self-amplified spontaneous emission free-electron laser pulses and extracting its autocorrelation," en, *Journal of Synchrotron Radiation*, vol. 28, no. 1, pp. 3–17, Jan. 2021, ISSN: 1600-5775, DOI: 10.1107/S160057752001382X.

[38] O. Chubar and P. Elleaume, "Accurate and efficient computation of synchrotron radiation in the near field region," en, vol. Vol. 1-3, 1998, pp. 1177–1179, [Online]. Available: https://accelconf.web.cern.ch/e98/PAPERS/THP01G.PDF.

[39] O. Chubar, "Simulation of emission and propagation of coherent synchrotron radiation wave fronts using the methods of wave optics," en, *Infrared Physics & Technology*, International Workshop on Infrared Microscopy and Spectroscopy with Accelerator-Based Sources, vol. 49, no. 1, pp. 96–103, Sep. 2006, ISSN: 1350-4495, DOI: 10.1016/j.infrared.2006.01.010.

[40] O. Chubar, L. Berman, Y. S. Chu, *et al.*, "Development of partially-coherent wavefront propagation simulation methods for 3rd and 4th generation synchrotron radiation sources," en, M. Sanchez del Rio and O. Chubar, Eds., San Diego, California, USA, Sep. 2011, p. 814 107, DOI: 10.1117/12.892812.

[41] O. Chubar, M. S. Rakitin, Y.-C. Chen-Wiegart, A. Fluerasu, and L. Wiegart, "Simulation of experiments with partially coherent x-rays using Synchrotron Radiation Workshop," en, in *Advances in Computational Methods for X-Ray Optics IV*, K. Sawhney and O. Chubar, Eds., San Diego, United States: SPIE, Aug. 2017, p. 38, ISBN: 978-1-5106-1233-4 978-1-5106-1234-1, DOI: 10.1117/12.2274481.

[42] R. Li and O. Chubar, "Memory and CPU efficient coherent mode decomposition of partially coherent synchrotron radiation with subtraction of common quadratic phase terms," en, *Optics Express*, vol. 30, no. 4, p. 5896, Feb. 2022, ISSN: 1094-4087, DOI: 10.1364/OE.452247.

[43] M. Glass and M. S. d. Rio, "Coherent modes of X-ray beams emitted by undulators in new storage rings," en, *Europhysics Letters*, vol. 119, no. 3, p. 34 004, Oct. 2017, ISSN: 0295-5075, DOI: 10.1209/0295-5075/119/34004.

[44] A. Singer, "Coherence properties of third and fourth generation X-ray sources Theory and experiment," Ph.D. dissertation, Germany, 2013, [Online]. Available: https://bib-pubdb1.desy.de/record/221096/files/desy-thesis-13-023.pdf.

[45] R. Khubbutdinov, "Statistical Properties of the X-ray Radiation at Large Scale Facilities," en, doctoralThesis, Staats- und Universitätsbibliothek Hamburg Carl von Ossietzky, 2022, [Online]. Available: https://ediss.sub.uni-hamburg.de/handle/ediss/9956.

[46] W. Freund, L. Fröhlich, S. Karabekyan, *et al.*, "First measurements with the K-monochromator at the European XFEL," en, *Journal of Synchrotron Radiation*, vol. 26, no. 4, pp. 1037–1044, Jul. 2019, ISSN: 1600-5775, DOI: 10.1107/S1600577519005307.

[47] A. Koch, W. Freund, J. Grünert, *et al.*, "Design and initial characterisation of X-ray beam diagnostic imagers for the European XFEL," en, S. G. Biedron, Ed., Prague, Czech Republic, May 2015, 95121R, DOI: 10.1117/12.2182463.

[48] P. H. van Cittert, "Die Wahrscheinliche Schwingungsverteilung in Einer von Einer Lichtquelle Direkt Oder Mittels Einer Linse Beleuchteten Ebene," de, *Physica*, vol. 1, no. 1, pp. 201–210, Jan. 1934, ISSN: 0031-8914, DOI: 10.1016/S0031-8914(34)90026-4.

[49] F. Zernike, "The concept of degree of coherence and its application to optical problems," en, *Physica*, vol. 5, no. 8, pp. 785–795, Aug. 1938, ISSN: 0031-8914, DOI: 10.1016/S0031-8914(38)80203-2.

[50] J. Goodman, "Some effects of target-induced scintillation on optical radar performance," *Proceedings of the IEEE*, vol. 53, no. 11, pp. 1688–1700, Nov. 1965, ISSN: 1558-2256, DOI: 10.1109/PROC.1965.4341.

[51] G. Geloni, E. Saldin, E. Schneidmiller, and M. Yurkov, "Fourier treatment of near-field synchrotron radiation theory," en, *Optics Communications*, vol. 276, no. 1, pp. 167–179, Aug. 2007, ISSN: 0030-4018, DOI: 10.1016/j.optcom.2007.03.051.

[52] "Terahertz Science at European XFEL," eng, European X-Ray Free-Electron Laser Facility GmbH, Schenefeld, Technical Note XFEL.EU TN-2018-001-01.0, 2018, [Online]. Available: https://xfel.tind.io/record/1564?ln=en&v=pdf.

[53] K. Peetermans, F. Lemery, W. Hillert, *et al.*, "STERN: Accelerator-based THz generation at XFEL," Optical Terahertz Science and Technology 2024, Marburg (Germany), 8 Apr 2024 - 12 Apr 2024, Apr. 8, 2024, [Online]. Available: https://bib-pubdb1.desy.de/record/607654.

[54] Z. Zhang, A. S. Fisher, M. C. Hoffmann, *et al.*, "A high-power, high-repetition-rate THz source for pump–probe experiments at Linac Coherent Light Source II," en, *Journal of Synchrotron Radiation*, vol. 27, no. 4, pp. 890–901, Jul. 2020, ISSN: 1600-5775, DOI: 10.1107/S1600577520005147.

[55] G. Geloni, V. Kocharyan, and E. Saldin, "Scheme for generating and transporting THz radiation to the X-ray experimental floor at the LCLS baseline," *arXiv:1108.1085 [physics]*, Aug. 2011, [Online]. Available: http://arxiv.org/abs/1108.1085.

[56] W. Decking, G. Geloni, V. Kocharyan, E. Saldin, and I. Zagorodnov, "Scheme for generating and transporting THz radiation to the X-ray experimental hall at the European XFEL," *arXiv:1112.3511 [physics]*, Dec. 2011, [Online]. Available: http://arxiv.org/abs/1112.3511.

[57] A. Naji, G. Stupakov, Z. Huang, and K. Bane, "Field analysis for a highly overmoded iris line with application to THz radiation transport," en, *Physical Review Accelerators and Beams*, vol. 25, no. 4, p. 043 501, Apr. 2022, ISSN: 2469-9888, DOI: 10.1103/PhysRevAccelBeams.25.043501.

[58] A. Naji and G. Stupakov, "Paraxial forward-scatter field analysis for a THz pulse traveling down a highly overmoded iris-line waveguide," en, *Physical Review Accelerators and Beams*, vol. 25, no. 12, p. 123 501, Dec. 2022, ISSN: 2469-9888, DOI: 10.1103/PhysRevAccelBeams.25.123501.

[59] J. W. Goodman, *Statistical optics* (Wiley classics library), en, Wiley classics library ed. New York: Wiley, 2000, ISBN: 978-0-471-39916-2 978-0-471-01502-4, [Online]. Available: https://www.wiley.com/en-sg/Statistical+Optics%2C+2nd+Edition-p-9781119009450.

[60] L. Mandel and E. Wolf, *Optical Coherence and Quantum Optics*. Cambridge University Press, 1995, ISBN: 978-0-521-41711-2, DOI: 10.1017/CBO9781139644105.

[61] R. Khubbutdinov, A. P. Menushenkov, and I. A. Vartanyants, "Coherence properties of the high-energy fourth-generation X-ray synchrotron sources," en, *Journal of Synchrotron Radiation*, vol. 26, no. 6, pp. 1851–1862, Nov. 2019, ISSN: 1600-5775, DOI: 10.1107/S1600577519013079.

[62] W.-Q. Hua, F.-G. Bian, L. Song, X.-H. Li, and J. Wang, "Hard X-ray optics simulation using the coherent mode decomposition of the Gaussian Schell model," en, *Chinese Physics C*, vol. 37, no. 6, p. 068 001, Jun. 2013, ISSN: 1674-1137, DOI: 10.1088/1674-1137/37/6/068001.

[63] W. Q. Hua, F. G. Bian, L. Song, Y. Wang, and J. Wang, "Application of Gaussian Schell-Model and Its Coherent Mode Decomposition on Hard X-Ray Synchrotron Radiation," in *2012 Symposium on Photonics and Optoelectronics*, May 2012, pp. 1–6, DOI: 10.1109/SOPO.2012.6270955.

[64] A. Singer and I. A. Vartanyants, "Modelling of partially coherent radiation based on the coherent mode decomposition," in *Advances in Computational Methods for X-Ray Optics II*, vol. 8141, International Society for Optics and Photonics, Sep. 2011, p. 814 106, DOI: 10.1117/12.893618.

[65] S. Reiche, "GENESIS 1.3: A fully 3D time-dependent FEL simulation code," en, *Nuclear Instruments and Methods in Physics Research Section A: Accelerators, Spectrometers, Detectors and Associated Equipment*, vol. 429, no. 1, pp. 243–248, Jun. 1999, ISSN: 0168-9002, DOI: 10.1016/S0168-9002(99)00114-X.

[66] H. P. Hong, X. Z. Cui, and D. Qiao, "An algorithm to simulate nonstationary and non-Gaussian stochastic processes," en, *Journal of Infrastructure Preservation and Resilience*, vol. 2, no. 1, p. 17, Dec. 2021, ISSN: 2662-2521, DOI: 10.1186/s43065-021-00030-5.

[67] H. Lajunen, A. T. Friberg, and P. Östlund, "Quasi-stationary plane-wave optical pulses and the van Cittert-Zernike theorem in time," en, *Journal of the Optical Society of America A*, vol. 23, no. 10, p. 2530, Oct. 2006, ISSN: 1084-7529, 1520-8532, DOI: 10.1364/JOSAA.23.002530.

[68] L. Ahad, I. Vartiainen, T. Setälä, A. T. Friberg, and J. Turunen, "Quasi-monochromatic modes of quasi-stationary, pulsed scalar optical fields," en, *Journal of the Optical Society of America A*, vol. 34, no. 9, p. 1469, Sep. 2017, ISSN: 1084-7529, 1520-8532, DOI: 10.1364/JOSAA.34.001469.

[69] G. Geloni, E. Saldin, E. Schneidmiller, and M. Yurkov, *Statistical Optics approach to the design of beamlines for Synchrotron Radiation*, en, Mar. 2006, [Online]. Available: http://arxiv.org/abs/physics/0603269.

[70] G. Geloni, E. Saldin, E. Schneidmiller, and M. Yurkov, "Transverse coherence properties of X-ray beams in third-generation synchrotron radiation sources," *Nuclear Instruments and Methods in Physics Research Section A: Accelerators, Spectrometers, Detectors and Associated Equipment*, vol. 588, no. 3, pp. 463–493, Apr. 2008, ISSN: 01689002, DOI: 10.1016/j.nima.2008.01.089.

[71] T. Young, "The Bakerian Lecture: Experiments and Calculations Relative to Physical Optics," *Philosophical Transactions of the Royal Society of London*, vol. 94, pp. 1–16, 1804, ISSN: 0261-0523, [Online]. Available: https://www.jstor.org/stable/107135.

[72] R. Hanbury Brown and R. Q. Twiss, "A Test of a New Type of Stellar Interferometer on Sirius," en, *Nature*, vol. 178, no. 4541, pp. 1046–1048, Nov. 1956, ISSN: 1476-4687, DOI: 10.1038/1781046a0.

[73] *Ocelot multiphysics simulation toolkit*, en, 2017, [Online]. Available: https://github.com/ocelot-collab/ocelot.

[74] "OCELOT as a Framework for Beam Dynamics Simulations of X-Ray Sources," eng, *Proceedings of IPAC17*, S. Tomin, I. Agapov, M. Dohlus, and I. Zagorodnov, Eds., 2017, [Online]. Available: https://accelconf.web.cern.ch/ipac2017/papers/wepab031.pdf.

[75] I. Agapov, G. Geloni, S. Tomin, and I. Zagorodnov, "OCELOT: A software framework for synchrotron light source and FEL studies," *Nuclear Instruments and Methods in Physics Research Section A: Accelerators, Spectrometers, Detectors and Associated Equipment*, vol. 768, pp. 151–156, Dec. 2014, ISSN: 0168-9002, DOI: 10.1016/j.nima.2014.09.057.

[76] T. Pfeifer, Y. Jiang, S. Düsterer, R. Moshammer, and J. Ullrich, "Partial-coherence method to model experimental free-electron laser pulse statistics," EN, *Optics Letters*, vol. 35, no. 20, pp. 3441–3443, Oct. 2010, ISSN: 1539-4794, DOI: 10.1364/OL.35.003441.

[77] E. L. Saldin, E. A. Schneidmiller, and M. V. Yurkov, *The Physics of Free Electron Lasers* (Advanced Texts in Physics), en. Springer Berlin Heidelberg, 2000, ISBN: 978-3-642-08555-0 978-3-662-04066-9, DOI: 10.1007/978-3-662-04066-9.

[78] K.-J. Kim, Z. Huang, and R. Lindberg, *Synchrotron Radiation and Free-Electron Lasers: Principles of Coherent X-Ray Generation*, en. Cambridge: Cambridge University Press, 2017, ISBN: 978-1-316-67737-7, DOI: 10.1017/9781316677377.

[79] P. Schmüser, M. Dohlus, J. Rossbach, and C. Behrens, *Free-Electron Lasers in the Ultraviolet and X-Ray Regime* (Springer Tracts in Modern Physics), en. Cham: Springer International Publishing, 2014, vol. 258, ISBN: 978-3-319-04080-6 978-3-319-04081-3, DOI: 10.1007/978-3-319-04081-3.

[80] A. Trebushinin, G. Geloni, S. Serkez, *et al.*, "Experimental Demonstration of Attoseconds-at-Harmonics at the SASE3 Undulator of the European XFEL," en, *Photonics*, vol. 10, no. 2, p. 131, Feb. 2023, ISSN: 2304-6732, DOI: 10.3390/photonics10020131.

[81] E. Schneidmiller and M. Yurkov, "Statistical properties of the radiation from SASE FEL operating in a post-saturation regime with and without undulator tapering," en, *Journal of Modern Optics*, vol. 63, no. 4, pp. 288–292, Feb. 2016, ISSN: 0950-0340, 1362-3044, DOI: 10.1080/09500340.2015.1035349.

[82] B. V. Ricketti, E. M. Gauger, and A. Fedrizzi, "The coherence time of sunlight in the context of natural and artificial light-harvesting," en, *Scientific Reports*, vol. 12, no. 1, p. 5438, Mar. 2022, ISSN: 2045-2322, DOI: 10.1038/s41598-022-08693-0.

[83] H. Mashaal, A. Goldstein, D. Feuermann, and J. M. Gordon, "First direct measurement of the spatial coherence of sunlight," EN, *Optics Letters*, vol. 37, no. 17, pp. 3516–3518, Sep. 2012, ISSN: 1539-4794, DOI: 10.1364/OL.37.003516.

[84] D. Zawischa, *Diffraction and Interference*, [Online]. Available: https://www.itp.uni-hannover.de/fileadmin/itp/emeritus/zawischa/static_html/diffraction.html.

[85] R. Bonifacio, L. De Salvo, P. Pierini, N. Piovella, and C. Pellegrini, "Spectrum, temporal structure, and fluctuations in a high-gain free-electron laser starting from noise," *Physical Review Letters*, vol. 73, no. 1, pp. 70–73, Jul. 1994, DOI: 10.1103/PhysRevLett.73.70.

[86] P. Pierini and W. M. Fawley, "Shot noise startup of the 6 nm SASE FEL at the TESLA test facility," *Nuclear Instruments and Methods in Physics Research Section A: Accelerators, Spectrometers, Detectors and Associated Equipment*, Proceedings of the 17th International Free Electron Laser Conference, vol. 375, no. 1, pp. 332–335, Jun. 1996, ISSN: 0168-9002, DOI: 10.1016/0168-9002(95)01221-4.

[87] E. L. Saldin, E. A. Schneidmiller, and M. V. Yurkov, "Simulation studies of 6 nm free electron laser at the TESLA test facility starting from noise," *Nuclear Instruments and Methods in Physics Research Section A: Accelerators, Spectrometers, Detectors and Associated Equipment*, Free Electron Lasers 1996, vol. 393, no. 1, pp. 157–161, Jul. 1997, ISSN: 0168-9002, DOI: 10.1016/S0168-9002(97)00450-6.

[88] M. Hogan, C. Pellegrini, J. Rosenzweig, *et al.*, "Measurements of High Gain and Intensity Fluctuations in a Self-Amplified, Spontaneous-Emission Free-Electron Laser," en, *Physical Review Letters*, vol. 80, no. 2, pp. 289–292, Jan. 1998, ISSN: 0031-9007, 1079-7114, DOI: 10.1103/PhysRevLett.80.289.

[89] D. C. Nguyen, R. L. Sheffield, C. M. Fortgang, J. C. Goldstein, J. M. Kinross-Wright, and N. A. Ebrahim, "Self-Amplified Spontaneous Emission Driven by a High-Brightness Electron Beam," en, *Physical Review Letters*, vol. 81, no. 4, pp. 810–813, Jul. 1998, ISSN: 0031-9007, 1079-7114, DOI: 10.1103/PhysRevLett.81.810.

[90] M. J. Hogan, C. Pellegrini, J. Rosenzweig, *et al.*, "Measurements of Gain Larger than 10 5 at 12 μm in a Self-Amplified Spontaneous-Emission Free-Electron Laser," en, *Physical Review Letters*, vol. 81, no. 22, pp. 4867–4870, Nov. 1998, ISSN: 0031-9007, 1079-7114, DOI: 10.1103/PhysRevLett.81.4867.

[91] J. Andruszkow, B. Aune, V. Ayvazyan, *et al.*, "First Observation of Self-Amplified Spontaneous Emission in a Free-Electron Laser at 109 nm Wavelength," *Physical Review Letters*, vol. 85, no. 18, pp. 3825–3829, Oct. 2000, DOI: 10.1103/PhysRevLett.85.3825.

[92] S. V. Milton, E. Gluskin, S. G. Biedron, *et al.*, "Observation of Self-Amplified Spontaneous Emission and Exponential Growth at 530 nm," *Physical Review Letters*, vol. 85, no. 5, pp. 988–991, Jul. 2000, DOI: 10.1103/PhysRevLett.85.988.

[93] V. Ayvazyan, N. Baboi, I. Bohnet, *et al.*, "Generation of GW Radiation Pulses from a VUV Free-Electron Laser Operating in the Femtosecond Regime," en, *Physical Review Letters*, vol. 88, no. 10, p. 104 802, Feb. 2002, ISSN: 0031-9007, 1079-7114, DOI: 10.1103/PhysRevLett.88.104802.

[94] M. Yabashi, K. Tamasaku, and T. Ishikawa, "Characterization of the Transverse Coherence of Hard Synchrotron Radiation by Intensity Interferometry," en, *Physical Review Letters*, vol. 87, no. 14, p. 140 801, Sep. 2001, ISSN: 0031-9007, 1079-7114, DOI: 10.1103/PhysRevLett.87.140801.

[95] M. Yabashi, K. Tamasaku, and T. Ishikawa, "Measurement of X-Ray Pulse Widths by Intensity Interferometry," en, *Physical Review Letters*, vol. 88, no. 24, p. 244 801, May 2002, ISSN: 0031-9007, 1079-7114, DOI: 10.1103/PhysRevLett.88.244801.

[96] J. Amann, W. Berg, V. Blank, *et al.*, "Demonstration of self-seeding in a hard-X-ray free-electron laser," en, *Nature Photonics*, vol. 6, no. 10, pp. 693–698, Oct. 2012, ISSN: 1749-4893, DOI: 10.1038/nphoton.2012.180.

[97] E. Allaria, D. Castronovo, P. Cinquegrana, *et al.*, "Two-stage seeded soft-X-ray free-electron laser," en, *Nature Photonics*, vol. 7, no. 11, pp. 913–918, Nov. 2013, ISSN: 1749-4893, DOI: 10.1038/nphoton.2013.277.

[98] S. Ackermann, A. Azima, S. Bajt, *et al.*, "Generation of Coherent 19- and 38-nm Radiation at a Free-Electron Laser Directly Seeded at 38 nm," *Physical Review Letters*, vol. 111, no. 11, p. 114 801, Sep. 2013, DOI: 10.1103/PhysRevLett.111.114801.

[99] S. Liu, W. Decking, V. Kocharyan, *et al.*, "Preparing for high-repetition rate hard x-ray self-seeding at the European X-ray Free Electron Laser: Challenges and opportunities," *Physical Review Accelerators and Beams*, vol. 22, no. 6, p. 060 704, Jun. 2019, DOI: 10.1103/PhysRevAccelBeams.22.060704.

[100] S. Liu, C. Grech, M. Guetg, *et al.*, "Cascaded hard X-ray self-seeded free-electron laser at megahertz repetition rate," en, *Nature Photonics*, vol. 17, no. 11, pp. 984–991, Nov. 2023, ISSN: 1749-4893, DOI: 10.1038/s41566-023-01305-x.

[101] S. Serkez, W. Decking, L. Froehlich, *et al.*, "Opportunities for Two-Color Experiments in the Soft X-ray Regime at the European XFEL," en, *Applied Sciences*, vol. 10, no. 8, p. 2728, Jan. 2020, ISSN: 2076-3417, DOI: 10.3390/app10082728.

[102] N. M. Lockmann, C. Gerth, B. Schmidt, and S. Wesch, "Noninvasive THz spectroscopy for bunch current profile reconstructions at MHz repetition rates," *Physical Review Accelerators and Beams*, vol. 23, no. 11, p. 112 801, Nov. 2020, DOI: 10.1103/PhysRevAccelBeams.23.112801.

[103] A. Trebushinin, G. Geloni, Y. Rakshun, and S. Serkez, "Gaussian random field generator for simulating partially coherent undulator radiation," en, *Optica*, vol. 9, no. 8, p. 842, Aug. 2022, ISSN: 2334-2536, DOI: 10.1364/OPTICA.460902.

[104] E. Wilson, *An Introduction to Particle Accelerators*, English. Oxford University Press, 2001, ISBN: 978-0-19-850829-8, DOI: 10.1093/acprof:oso/9780198508298.001.0001.

[105] R. D. Ruth, "An Introduction to Particle Accelerators," *Physics Today*, vol. 55, no. 8, p. 52, Aug. 2002, ISSN: 0031-9228, DOI: 10.1063/1.1510283.

[106] R. H. Brown and R. Q. Twiss, "Correlation between Photons in two Coherent Beams of Light," en, *Nature*, vol. 177, no. 4497, pp. 27–29, Jan. 1956, ISSN: 1476-4687, DOI: 10.1038/177027a0.

[107] T. Lensch and T. Wamsat, "A Fast Wire Scanner System for the European Xfel and Its Impact on Safety Systems," en, *Proceedings of the 17th International Conference on Accelerator and Large Experimental Physics Control Systems*, vol. ICALEPCS2019, 3 pages, 1.255 MB, 2020, ISSN: 2226-0358, DOI: 10.18429/JACOW-ICALEPCS2019-WEPHA086.

[108] V. Ginzburg, "On the radiation of microradiowaves and their absorbtion in the air," *Isvestia Akademii Nauk SSSR (Fizika)*, vol. 11, no. 2, p. 947, 1947.

[109] H. Motz, "Applications of the Radiation from Fast Electron Beams," *Journal of Applied Physics*, vol. 22, no. 5, pp. 527–535, May 1951, ISSN: 0021-8979, DOI: 10.1063/1.1700002.

[110] H. Motz, W. Thon, and R. N. Whitehurst, "Experiments on Radiation by Fast Electron Beams," *Journal of Applied Physics*, vol. 24, no. 7, pp. 826–833, Jul. 1953, ISSN: 0021-8979, DOI: 10.1063/1.1721389.

[111] K. W. Robinson, "Radiation Effects in Circular Electron Accelerators," *Physical Review*, vol. 111, no. 2, pp. 373–380, Jul. 1958, DOI: 10.1103/PhysRev.111.373.

[112] J. A. Clarke, *The Science and Technology of Undulators and Wigglers*. Oxford University Press, Jul. 2004, ISBN: 9780198508557, DOI: 10.1093/acprof:oso/9780198508557.001.0001.

[113] E. Levichev and N. Vinokurov, "Undulators and Other Insertion Devices," *Reviews of Accelerator Science and Technology*, vol. 03, no. 01, pp. 203–220, Jan. 2010, ISSN: 1793-6268, DOI: 10.1142/S1793626810000403.

[114] I. Lobach, "Statistical properties of undulator radiation: Classical and quantum effects," en, Ph.D. dissertation, The University of Chicago, Chicago, Illinois, Dec. 2021, [Online]. Available: https://lss.fnal.gov/archive/thesis/2000/fermilab-thesis-2021-27.pdf.

[115] D. Einfeld, J. Schaper, and M. Plesko, "Design of a diffraction limited light source (DIFL)," in *Proceedings Particle Accelerator Conference*, vol. 1, May 1995, 177–179 vol.1, DOI: 10.1109/PAC.1995.504602.

[116] G. Geloni, E. Saldin, E. Schneidmiller, and M. Yurkov, *Paraxial Green's functions in Synchrotron Radiation theory*, en, Feb. 2005, [Online]. Available: http://arxiv.org/abs/physics/0502120.

[117] D. F. Alferov, Y. A. Bashmakov, K. A. Belovintsev, E. G. Bessonov, and P. A. Cherenkov, "Ondulator as a source of electromagnetic radiation," English, *Part. Accel.; (United Kingdom)*, vol. 9:4, Jun. 1979, [Online]. Available: https://www.osti.gov/etdeweb/biblio/5801215.

[118] I. V. Bazarov, "Synchrotron radiation representation in phase space," en, *Physical Review Special Topics - Accelerators and Beams*, vol. 15, no. 5, p. 050 703, May 2012, ISSN: 1098-4402, DOI: 10.1103/PhysRevSTAB.15.050703.

[119] G. Geloni, E. Saldin, E. Schneidmiller, and M. Yurkov, "Undulator Radiation in a Waveguide," *Nuclear Instruments and Methods in Physics Research Section A: Accelerators, Spectrometers, Detectors and Associated Equipment*, vol. 584, no. 1, pp. 219–237, Jan. 2008, ISSN: 01689002, DOI: 10.1016/j.nima.2007.10.016.

[120] F. Lemery, M. Dohlus, K. Flöttmann, M. Ivanyan, M. Marx, and V. Tsakanov, "A Versatile THz Source for High-Repetition Rate XFELs," en, *Proceedings of the 39th Free Electron Laser Conference*, vol. FEL2019, 4 pages, 1.219 MB, 2019, DOI: 10.18429/JACoW-FEL2019-THP049.

[121] N. Stojanovic and M. Drescher, "Accelerator- and laser-based sources of high-field terahertz pulses," en, *Journal of Physics B: Atomic, Molecular and Optical Physics*, vol. 46, no. 19, p. 192 001, Sep. 2013, ISSN: 0953-4075, DOI: 10.1088/0953-4075/46/19/192001.

[122] A. Trebushinin, *Andre-trebushi/SRinWGuide*, Apr. 2023, [Online]. Available: https://github.com/trebushi/SRinWGuide.

[123] T. Tanaka and H. Kitamura, "SPECTRA: A synchrotron radiation calculation code," en, *Journal of Synchrotron Radiation*, vol. 8, no. 6, pp. 1221–1228, Nov. 2001, ISSN: 0909-0495, DOI: 10.1107/S090904950101425X.

[124] O. Chubar and N. Smolyakov, "Generation of intensive long-wavelength edge radiation in high-energy electron storage rings," en, in *Proceedings of International Conference on Particle Accelerators*, Washington, DC, USA: IEEE, 1993, pp. 1626–1628, ISBN: 978-0-7803-1203-6, DOI: 10.1109/PAC.1993.308540.

[125] G. Geloni, V. Kocharyan, E. Saldin, E. Schneidmiller, and M. Yurkov, "Theory of edge radiation," arXiv, Tech. Rep. arXiv:0808.1846, Aug. 2008, DOI: 10.48550/arXiv.0808.1846.

[126] M. Krasilnikov, Z. Aboulbanine, G. Adhikari, *et al.*, *First high peak and average power single-pass THz FEL based on high brightness photoinjector*, May 2024, DOI: 10.48550/arXiv.2405.19152.

[127] T. Tanikawa, S. Karabekyan, S. Kovalev, *et al.*, "A superradiant THz undulator source for XFELs," en, *Journal of Instrumentation*, vol. 14, no. 05, P05024, May 2019, ISSN: 1748-0221, DOI: 10.1088/1748-0221/14/05/P05024.

[128] B. Green, S. Kovalev, V. Asgekar, *et al.*, "High-Field High-Repetition-Rate Sources for the Coherent THz Control of Matter," en, *Scientific Reports*, vol. 6, no. 1, p. 22 256, Feb. 2016, ISSN: 2045-2322, DOI: 10.1038/srep22256.

[129] K. Floettmann, F. Lemery, M. Dohlus, M. Marx, V. Tsakanov, and M. Ivanyan, "Superradiant Cherenkov–wakefield radiation as THz source for FEL facilities," en, *Journal of Synchrotron Radiation*, vol. 28, no. 1, pp. 18–27, Jan. 2021, ISSN: 1600-5775, DOI: 10.1107/S1600577520014058.

[130] A. G. Fox and T. Li, "Resonant Modes in a Maser Interferometer," en, *Bell System Technical Journal*, vol. 40, no. 2, pp. 453–488, 1961, ISSN: 1538-7305, DOI: 10.1002/j.1538-7305.1961.tb01625.x.

[131] L. A. Vainshtein, "Open resonators for lasers," en, vol. 17, no. 3, pp. 1050–1067, 1963, [Online]. Available: http://jetp.ras.ru/cgi-bin/dn/e_017_03_0709.pdf.

[132] M.-S. Yeh, S.-G. Shiue, and M.-H. Lu, "First-order analysis of a three-lens afocal zoom system," *Optical Engineering*, vol. 36, no. 4, pp. 1249–1258, Apr. 1997, ISSN: 0091-3286, 1560-2303, DOI: 10.1117/1.601245.

[133] J. Goodman, *Introduction to Fourier Optics* (McGraw-Hill physical and quantum electronics series). W. H. Freeman, 2005, ISBN: 978-0-9747077-2-3, [Online]. Available: https://books.google.de/books?id=ow5xs_Rtt9AC.

[134] S. Serkez, "Design and Optimization of the Grating Monochromator for Soft X-Ray Self-Seeding FELs," en, Ph.D. dissertation, 2015, [Online]. Available: https://bib-pubdb1.desy.de/record/275967.

[135] *ATNF Daily Astronomy Picture*, [Online]. Available: https://www.atnf.csiro.au/daily-picture/2015/08/17/quantum-astronomy-and-stellar-imaging-2015/.